IN-SITU STRESS, PORE PRESSURE, AND HYDROCARBON MIGRATION AND ACCUMULATION IN SEDIMENTARY BASINS

A DISSERTATION

SUBMITTED TO THE DEPARTMENT OF GEOPHYSICS

AND THE COMMITTEE ON GRADUATE STUDIES

OF STANFORD UNIVERSITY

IN PARTIAL FULFILLMENT OF THE REQUIREMENTS

FOR THE DEGREE OF

DOCTOR OF PHILOSOPHY

Thomas Finkbeiner

September 1998

Abstract

An important concept for understanding fluid flow in hydrocarbon fields is that dynamic mechanisms governed by the stress state present drive oil and gas migration and accumulation. The principal goals in this dissertation are to constrain the full in-situ stress tensor and reservoir pore pressure conditions, identify hydrocarbon migration pathways, and test dynamic processes controlling fluid flow and rock deformation. For this purpose I analyze various types of downhole measurements from two hydrocarbon producing sedimentary basins.

In the Santa Maria Basin, on- and offshore California, stress orientations derived from borehole breakouts and inversion of earthquake focal plane mechanisms indicate a rather uniform stress field consistent with the regional trend. Analysis of borehole wall images reveal ubiquitous fractures and faults that exhibit great variations in orientation and occurrence. These variations can be correlated with changes of lithology and physical properties. Permeability appears to be enhanced in the vicinity of fractures and faults that are active and optimally oriented for failure in the current stress field.

In the South Eugene Island 330 field, Gulf of Mexico, drilling induced borehole breakouts, reveal least principal horizontal stress orientations, that are predominantly perpendicular to active normal faults. Minimum principal stress magnitudes show significant scatter revealing fracture gradients that cannot be correlated with previously published models from this area. Reservoir pore pressures are highly variable and range from hydrostatic to severely overpressured indicating compartmentalization and production induced depletion.

Reservoir depletion, pore pressures, and hydrocarbon column heights in individual reservoirs appear to be a function of stratigraphy. Shallow sands are hydrostatically pressured, well drained, and normally compacted. Oil and gas columns are long and controlled by a spill point. At intermediate stratigraphic levels, reservoir sands are undercompacted, moderately overpressured, and depletion induces stress changes that follow a stress path along which differential stresses strongly increase. Hydrocarbon columns are either small and dynamically constrained by reservoir bounding faults or long and controlled by a spill point. Deep sands exhibit small hydrocarbon columns and severe overpressured conditions near hydraulic fracturing or active faulting. The sand is extremely undercompacted and production appears to be accompanied by plastic and viscous deformation.

Acknowledgments

This is it! Six years of hard work at Stanford are coming to an end and I am about to deliver the final product, the Ph.D. dissertation. I would have never gotten so far without the help of a lot of people that not only provided scientific advice but also moral and spiritual support to keep me going in all these years. Now is the time to identify all those being responsible for what I am today and with what I am going to coin my name into Stanford's history. A good excuse for me in later times, when I can say: "Wasn't my fault!"

It was a very fortunate moment in my life when I first met my advisor Mark Zoback in 1991 in Karlsruhe University, Germany. Obviously, he instantly and miraculously saw a fruitful seed inside me that is worth a Ph.D. from Stanford. Ever since he provided incessant scientific, moral, and financial support to teach and guide me. With his door open, he always found a spare minute to hear my endless questions and demands or read manuscripts I had written in an attempt to describe my research results. Mark also helped to broaden my horizon by letting me go on field work to get my hands dirty in Tibet and Nevada and by having me participate in a summer internship with Amoco in Houston.

I am also very thankful to our collaborators in the South Eugene Island project - Peter Flemings and Beth Stump from Pennstate University. Peter assumed without hesitation the role of a co-advisor to me and provided a lot of help and support. Even when we went running he found the breath to talk science and he continued his support also after reading some of my draft papers (literally, I could hear him scream over from the East Coast!). Beth, a graduate student herself, diligently provided me with a lot of data and information - even at times when we were extremely busy preparing presentations for industrial meetings. Her "Okay, Thomas what do you want"-words after picking up the phone when I called her say it all.

Many people in the School of Earth Sciences helped me with the research I was pursuing: My committee members Lynn Orr, Amos Nur, Steve Graham, and Norm Sleep saw my work evolve as they sat with me through the oral exam, review sessions, and my Ph.D. defense. They provided good insight and useful comments. Colleen Barton and Dan Moos patiently answered many questions and got me started on computer and BHTV-digitizing equipments. I look forward working with them again very soon at GMI. With my student and office colleagues Carl, Wendy, David, Stacy, Balz, Stephanie, and Paul I grew into a very sociable group in which we helped each other with science and also learned how to celebrate birthdays during seminars (actually this habit was first introduced by one of our visiting scientists - many thanks, Pavel!), go on beer trains, and spent ski weekends in

Kirkwood. Of course, there are more people I am thankful to for many chats about science and other issues during coffee breaks and lunch sessions: Doron, Christine, Yizhaq, Mark, Tony, Ran, Tapan, Harold, Per, Matthias, Martin. Phil Farrell is not only our pangea-Guru around here but also a good resource when going hiking in the Sierra Nevada.

Of course, I would have been terribly stranded without our department administrators.Thanks to Linda, Jeanette, Laurie, and Marianne for your support and sympathy in guiding me through Stanford's jungles of bureaucracy and administration.

What would Stanford have been without the friends I made over the years? I think, a rather poor, colorless, monocultural, and boring experience. Thanks for the good times Christine, Ian, Karl-Heinz, Doron, Michal, Yizhaq, Gemma, Patti, Tony, Liz, Pen, Monique, Mark, all Martins and Tanjas, Radu, Stephan! While they never managed to beat the heavy German out of me, they crafted at least the rest of my character through endless and intense meetings at Yizhaq's parties, legendary Thursday Beers, sunny Borone sessions, dinners in the City and more. Ian, the Martins, Balz, and Stephan even had to put up with me as they unsuccessfully tried to outrun me on the Dish or tried to get rid off me in the dark wildernesses of Ventana and the Sierra Nevada.

An invaluable experience proofed to be the summer of 1994 in Tibet with the INDEPTH team. Yizhaq, Marin, the Michaels, Doug, Ian B., Larry, Simon, and others had to endure my endless moaning for which I earned the nickname "Finkweiner". The internship with Amoco in 1996 introduced me to Houston's corporate petroleum world and it was a very interesting and pleasant experience with Mike Mueller and Leon Thomsen as supervisors and Li Teng as a sympathizing colleague student also from Stanford.

I am very thankful to my American host family - the Wolfs. From the first minute of my arrival in 1992, Elizabeth and Hans provided a very comfortable environment that made me instantly feel at home. Throughout the years, we kept the contact, I became part of their family, and I met Annette - my "little-BIG sister".

My girl-friend Myraida has given me a lot of moral and spiritual support. Her presence in my life for the past 1 1/2 years made the way toward the degree a lot easier and smoother. Especially at times when the road seemed endless, steep and windy her loving care and beautiful smile gave me new energy and brought me back steaming up toward the summit.

Last but surely not least is my family in Germany. In particular for my parents and my brother Bernhard the separation has not always been easy and phone calls do not replace the scarce moments when the whole family can be together. Nonetheless, they bravely supported me morally and also finacially throughout all these years, never giving up the good spirit that it is only for my good to study at Stanford. I will always be thankful to them!

Table of Contents

List of Tables

List of Illustrations

CHAPTER 1

IN-SITU STRESS, PORE PRESSURE, AND HYDROCARBON MIGRATION AND ACCUMULATION IN SEDIMENTARY BASINS: INTRODUCTION

1.1 Introduction

Fluids play a vital role in crustal processes. In particular circulation of fluids has important effects on many earth phenomena ranging from transport of chemical constituents and heat to crustal deformation processes. One of the areas for which aspects of fluid migration and entrapment is of particular interest is the petroleum industry. Understanding why and how hydrocarbons move and what controls their entrapment and accumulation have been issues of preferred attention for many decades.

The pioneering work by Hubbert (1953) laid the foundation for understanding hydrocarbon migration in normally pressured (shallow) reservoirs (i.e. free-flow systems). As drilling went deeper into developing increasingly overpressured (i.e., pore pressures above hydrostatic) fields, Hubbert and Willis (1957) and Hubbert and Rubey (1959) progressed in applying Terzaghi's (1924) principle of effective stress to describe and quantify hydraulic fracturing and lowering the strength of thrust faults by reducing the basal friction. Powley (1990) and Hunt (1990) were the first to introduce and describe the concept of compartmentalization in sedimentary basins. Through careful analysis of downhole pressure measurements, they identified abrupt pore pressure transitions (vertically as well as laterally) to map areas of distinct pressure regimes within a single basins. These fluid compartments are bound by seals which in some cases follow the regional stratigraphy (i.e., shale layers) and in other cases coincide with fault zones that cut across stratigraphy. Hooper (1991) elaborated further on the roles of faults (in particular growth faults) for fluid migration. He concluded that flow along these faults is periodic and changes over time and in space depending on whether they are active or inactive thereby alternately providing seals for compartmentalization or pathways for fluid flow. This, and more recent work I introduce below, point towards the strong indication that understanding the relationship between the state of stress and faulting and pore pressure variations is vital for fluid flow processes in hydrocarbon bearing fields.

In my dissertation, I analyze various types of downhole measurements from two hydrocarbon producing sedimentary basins to apply and test some of the fundamental models and ideas pertaining to the state of stress, rock deformation, and fluid flow. The two basins are located in tectonically and geologically different regimes. The principal goals in this study are to constrain the full in-situ stress tensor and reservoir pore pressure conditions, identify hydrocarbon migration pathways, and infer processes controlling their accumulation. The benefits from this study will be to better understand the relationships between pore pressure and in-situ stress and the processes which control hydrocarbon accumulation and migration, as well as to better define the role of active faulting in oil

migration, and reservoir compaction and stress changes as a function of depletion.

One chapter in this dissertation (chapter 2) is devoted to the Santa Maria Basin, on- and offshore southern California. Located in a tectonically transpressive stress regime, this basin comprises the well consolidated and normally pressured Miocene Monterey Formation consisting of siliceous shale sequences of various diagenetic stages. The chapter mostly deals with the aspect of detecting pathways for fluid flow (i.e., fractures and faults) and their relationship to in-situ stress. The remaining four chapters (3 through 6) deal with a young hydrocarbon field located in a normal faulting environment on the outer continental shelf, offshore Louisiana in the Gulf of Mexico. This basin consists of unconsolidated and overpressured sand and thick shale sequences. In this study, I constrain the full in-situ stress tensor (chapter 3 and 4), identify reservoir compartments, establish a conceptual model for controlling maximum hydrocarbon column heights (chapter 6), and analyze compaction and stress changes as a result of depletion (chapter 5).

1.2 Santa Maria Basin, California

The Miocene age Monterey Formation is prime target for exploration and production of hydrocarbons in the Santa Barbara channel and further north along the coast offshore central California. Its siliceous rocks are not only an excellent source for oil and gas but also provide appropriate traps and reservoirs of high economic value. One important characteristic of the Monterey Formation is its generally high porosities but relatively low permeabilities (Isaacs, 1984). For this reason, fractures and faults are of great importance for hydrocarbon migration and production.

Veins, fractures and faults are abundant in the Earth's crust and they have long been known for their potential role of localizing fluid flow. However, not all of them are equally important. In fact, only a few fractures and faults are usually the primary fluid conduits for most of the flux in a given volume of rock (Long et al., 1991). Furthermore, faults can act as seals as well as conduits (Antonellini and Aydin, 1994) and Hooper (1991) pointed out that this can change over time or in space along the same fault plane. Therefore, identifying the fractures and faults that are specifically responsible for fluid flow is particularly important in stratigraphic sequences of low permeability like the Monterey Formation.

Barton et al. (1995, 1997) demonstrated that fluids preferentially flow along active faults optimally oriented in the current stress field for failure. These findings indicate that there exists a fundamental relationship between the in-situ state of stress, active fractures and faults, and fluid flow. While most of their examples involve areas comprised of crystalline rock, relatively few evidence has been gathered to date in sedimentary basins.

By studying the in-situ stress field, fractures and faults, and fluid flow in the Monterey Formation, offshore California, I test whether the hypothesis introduced above also applies in this sedimentary sequence.

Borehole televiewer data from four wells comprise the primary data set to detect fracture and faults. I correlate these with other types of well log data, drill stem tests, and stress orientation from greater depth (i.e., ~ 12 - 15 km) by inverting earthquake focal plane mechanisms. The primary goal is to look for potential relationships between stress, active faulting, and fluid flow. The results indicate a rather uniform stress field consistent with the regional trend. Fractures and faults are ubiquitous and exhibit great variations in orientation and occurrence that can be correlated with changes of lithology and physical properties. Permeability appears to be enhanced in the vicinity of fractures and faults that are active and optimally oriented for failure.

1.3 South Eugene Island 330 Field, Gulf of Mexico

The Gulf of Mexico region is a mature hydrocarbon province that has been the target of oil and gas exploration and production for almost a century. While early day activities of the oil industry were confined to the coastal regions, new technological advances allowed in recent years to push the exploration efforts further offshore, even into the deepwater province. Today, wells are being drilled in seawater depths reaching 3,000m resulting in extreme overpressured conditions. On the shelf, new technologies have enabled the petroleum industry to explore for small and previously often uneconomic plays.

Despite these technological advances, drilling and completion costs remain extremely high because of high risk and security factors for both human life and material. More research and technological progress are needed to better understand in-situ reservoir processes that affect drilling and completion and to further reduce the risks and expenses in the oil industry. For this reason, many scientists have invested great efforts to do extensive research in specific reservoirs but also on a regional scale. From the drilling engineering point of view, improved knowledge in controlling risk factors (specifically under severe overpressured conditions) related to sanding problems and loss of circulation and developing tools for stable wellbore design are of great importance - particularly in deepwater fields where drilling costs per well reach 20 million dollars and more.

Some of the issues that still require better understanding are related to in-situ pore pressure and its variations (i.e, compartmentalization), the state of stress, and the physical mechanisms that control them, in particular the ones that govern hydrocarbon migration and accumulation. In the North Sea, it has been observed empirically that holes are dry (i.e.,

no hydrocarbons present) below a certain threshold value of the minimum effective horizontal stress (the minimum principal stress minus the pore pressure) even though good reservoirs and traps existed. However, this effective stress threshold is not constant across the entire North Sea but rather shows a regional dependency. In the Central Graben, Gaarenstrom (1993) observed a threshold value of around 1,000 psi, whereas Borgerud and Svare (1995) report 3,000 psi for the Halten Terrace (Figure 1.1). If one were to apply the stress threshold value from the Halten Terrace as a decision criterion for drilling wells in the entire North Sea, then the reservoirs in the Central Graben with effective stresses between 3,000 psi and 1,000 psi would have been left unexploited.

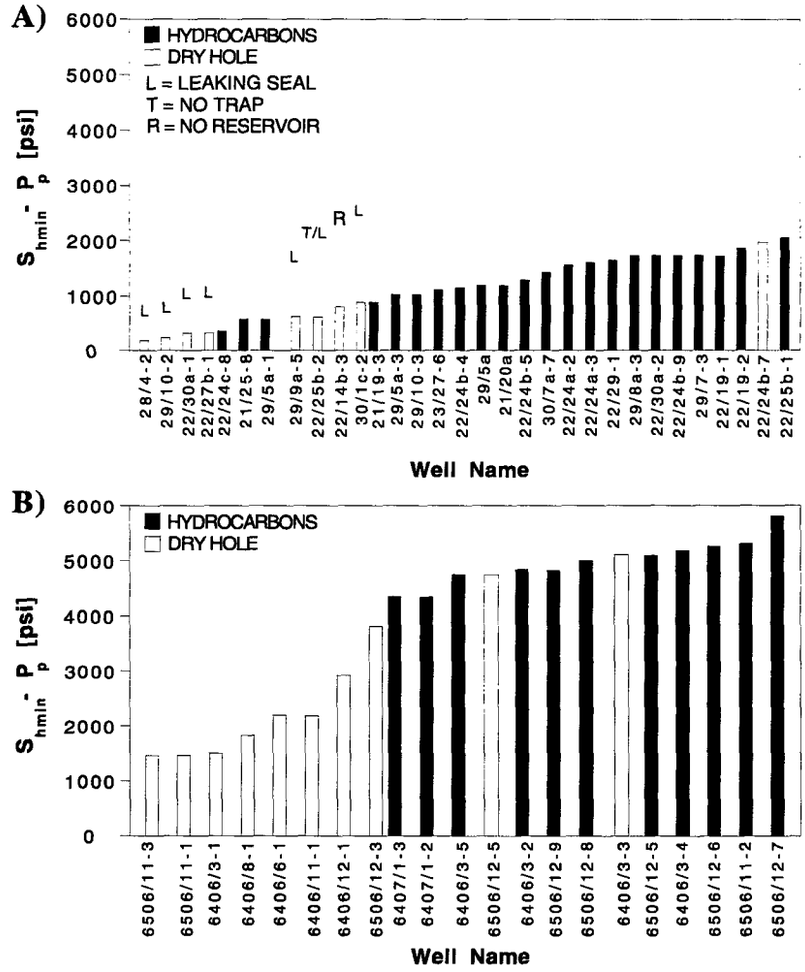

Figure 1.1: Dry and hydrocarbon bearing holes versus minimum effective horizontal stress in the North Sea. A) In the Central Graben (Gaarenstrom, 1993), dry holes are found in zones of effective stress below 1,000 psi. B) In the Halten Terrace (Borgerud and Svare, 1995), dry holes are found where the effective stress is generally below 3,000 psi.

For the South Eugene Island 330 field, offshore Gulf of Mexico, Flemings et al. (1996) demonstrated that hydrocarbon column heights and their associated buoyancy in reservoirs of severe overpressure are balanced by the vertical effective stress (Figure 1.2). Small hydrocarbon columns correlate with small effective stresses and severe overpressure, whereas large columns are found in zones of less overpressure and relative higher effective stresses. This observation suggests that the maximum amount of oil and gas stored in these reservoirs is in a state of dynamic equilibrium between pore pressure and stress.

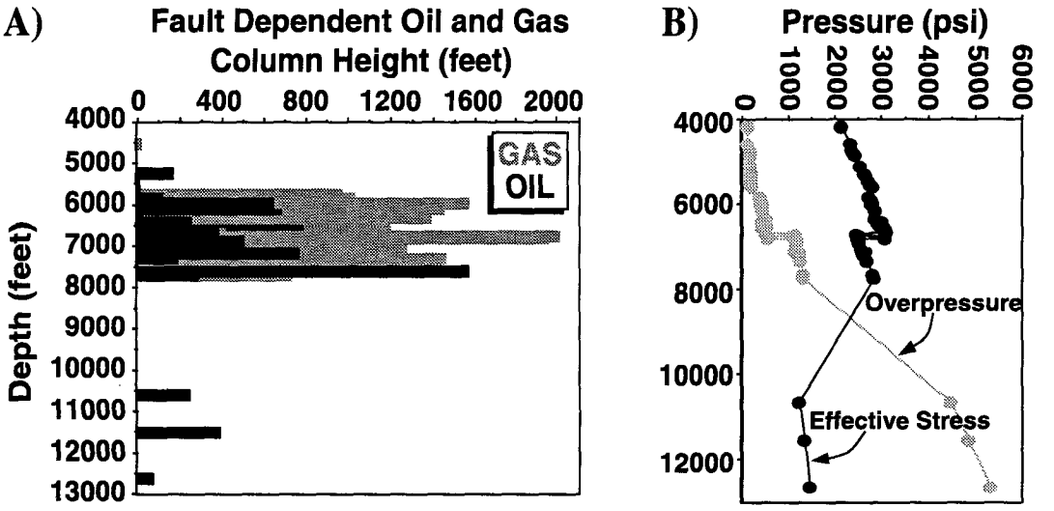

Figure 1.2: Hydrocarbon column heights versus depth in the South Eugene Island 330 field (A) and associated overpressures and effective stresses (B).

These two examples illustrate the need to study characteristics and variability of the state of stress and pore pressure in hydrocarbon fields to answer critical questions such as: How are pore pressure and stress related? How do fluids migrate in severely overpressured compartments? What controls hydrocarbon column height? Since many of the oil and gas reservoirs are surrounded by overpressured sequences of massive, low permeability shales, the question of how these fluids can migrate so efficiently over large distance is of particular interest as well. Also, what roles do faults play in this regard? For undercompacted and overpressured sands it is also important to understand how the state of stress changes with changing pore pressure. What mechanisms control reservoir deformation?

In chapters 3 through 6, I will focus on the South Eugene Island (SEI) 330 field, offshore Louisiana, in the Gulf of Mexico. This young hydrocarbon field is located on the outer continental shelf about 100 miles offshore Louisiana (Figure 1.3, inset). It has been the target of extensive exploration and production. Over 250 million barrels of oil and 2 tcf

of gas have been produced since its discovery in 1972 (Holland et al, 1992). These numbers make it one of the largest oil and gas producing fields in the US (Schuhmacher, 1993). In this study, I will focus specifically on the following issues:

- Determination of the full stress tensor and description of its variability at the reservoir scale
- Pore pressure and stress compartmentalization
- Stress control on hydrocarbon migration and accumulation in overpressured reservoirs and development of an appropriate model
- Reservoir deformation and compaction as a result of depletion

Geologically, the SEI 330 is a "classical" Plio-Pleistocene shelf minibasin dominated by deltaic deposition. It evolved by mobilization and extrusion of underlying salt sheets through gravitational loading of rapidly depositing and gulfward progressing sedimentary sequences (i.e., sand and shale). As a result of the salt evacuation process, the rapid sediment deposition and subsidence, and gravitational sliding on weak salt layers and overpressured shales a regional (down to the south) growth fault system developed that bounds the basin to the north and east (Alexander and Flemings, 1995). To the south, the minibasin is confined by an antithetic fault system (Figure 1.3). The basin fill reaches up to 4 km of alternating sand and shale sequences underlain by deep-water turbidites and salt sheets. High overpressure in the deeper buried Tertiary sediments was provoked by very high sedimentation rates dumping deep-water, low permeability shales on top of deep basin fan deposits, thus inhibiting dewatering and fluid migration of these sediments. As a result of processes related to the salt movements, the sediments were folded into rollover anticlines that provide ideal traps for oil and gas (Alexander and Flemings, 1995). Hydrocarbons are produced from over 25 Pliocene-Pleistocene sand layers that are segmented by faults into at least 100 structurally and stratigraphically individual reservoirs (Holland et al., 1992). As the hydrocarbons trapped within the reservoirs of the SEI field are much older than the young sediments, they are believed to have migrated vertically (perhaps also laterally) over significant distances relatively recently (Holland et al., 1992). Analysis of the normal fault system with respect to the pore pressure distribution shows that isobars are highly discontinuous across fault segments suggesting compartmentalization of individual reservoir pockets (pers. communication to P. Flemings). This indicates the importance of geologic structures on hydrocarbon entrapment and pressure gradient driven mechanisms for fluid flow.

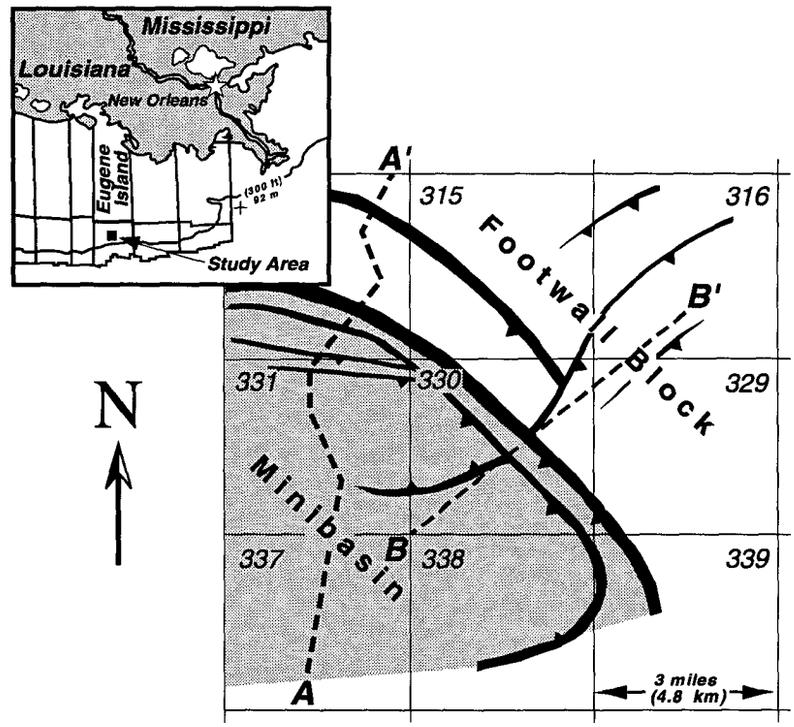

Figure 1.3: Basemap of the South Eugene Island 330 area showing 9 blocks with block 330 in the center. The major north-west trending growth normal fault system (black) bounds the minibasin, which is located on the hanging wall side (gray area). Dashed lines A-A' and B-B' mark the transects for the cross-sections in Figure 1.4.

Figure 1.4 displays two cross-sections trending N-S and NE-SW through the field (see Figure 1.3). These exhibit the main basin bounding growth fault system in the middle as it offsets sand reservoirs in the footwall (to the right) from those in the hanging wall (to the left). Note, that the structural relief across the fault system increases significantly with depth while individual sand reservoirs become less continuous. A typical characteristic of the growth faulting is the increasing stratigraphic offset with depth. For example, the OI sand is offset by approximately 2,000 feet while the underlying Lentic sand is offset by approximately 5,500 feet (Figure 1.4A).

Lithological properties are well documented by Holland et al. (1980, 1992). I present here a brief summary of the most important characteristics. Reservoir porosities are on average 30%. Permeabilities range from 10 md to over 6 darcys with 80% of the reservoirs having over 100 md and 20% over 1 darcy. All sands consist of relatively fine grained and well sorted quartzose to slightly arkosic arenites. Quartz is the predominant mineral (up to 89%) but feldspar and chert can represent as much as 25% of the bulk volume. Clay content is variable but minor never reaching more than 9% of the bulk matrix. However, the gross

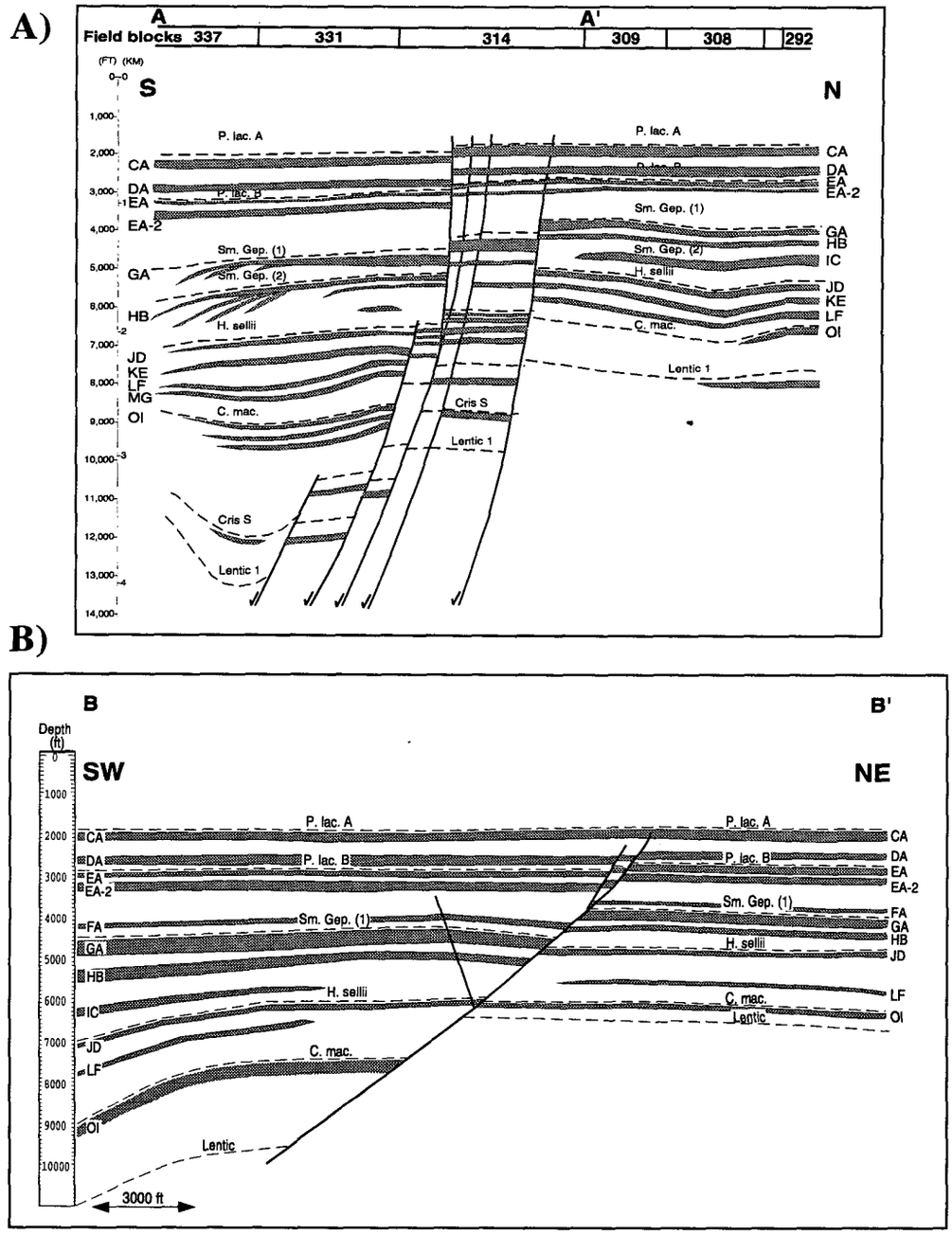

Figure 1.4: Cross-sections through the SEI 330 field. A) and B) show transects A-A' and B-B' respectively from Figure 1.3 (modified from Alexander and Flemings, 1995).

sedimentary sequence exhibits an increased shale to sand ratio with depth. Beneath the OI sands (Figure 1.4) the stratigraphy is largely shale dominated, and from the OI sands upward it is more sand-dominated. Pressures are closely tied to this stratigraphic architecture. In the shale-prone region, beneath the OI sands, severe overpressuring occurs.

Because the pressures follow these stratigraphic surfaces, and because there is significant offset across the growth fault at this depth, overpressures are much deeper in the hanging wall than in the footwall.

Lithological properties are well documented by Holland et al. (1980, 1992). I present here a brief summary of the most important characteristics. Reservoir porosities average about 30%. Permeabilities range from 10 md to over 6 darcys with 80% of the reservoirs having over 100 md and 20% over 1 darcy. All sands consist of relatively fine grained and well sorted quartzose to slightly arkosic arenites. Quartz is the predominant mineral (up to 89%) but feldspar and chert can represent as much as 25% of the bulk volume. Clay content is variable but minor never reaching more than 9% of the bulk matrix. However, the gross sedimentary sequence exhibits an increased shale to sand ratio with depth. Beneath the OI sands (Figure 1.4) the stratigraphy is largely shale dominated, and from the OI sands upward it is more sand-dominated. Pressures are closely tied to this stratigraphic architecture. In the shale-prone region, beneath the OI sands, severe overpressuring occurs. Because the pressures follow these stratigraphic surfaces, and because there is significant offset across the growth fault at this depth, overpressures are much deeper in the hanging wall than in the footwall.

1.3.1 Synopsis of chapters 3 through 6

In chapter 3, I compile and analyze pore pressure data and least principal stress measurements from minifracs in fracture completed reservoirs. The measurements show considerable variability in pore pressure and minimum principal stress and cannot be correlated with previously published fracture gradient models for this area. Pressure surveys indicate (severe) overpressures, compartmentalization, and depletion behavior that is dependent upon stratigraphy.

The main goal in chapter 4 is to constrain the full stress tensor in the SEI 330 field. I use caliper data from 38 dipmeter logs in vertical and highly deviated wells to identify drilling induced borehole breakouts. The orientation of the least principal horizontal stress, S_{hmin}, is predominantly perpendicular to the active growth faults, which is in agreement with an extensional, active normal faulting environment. The horizontal principal stresses are not equal, suggesting a non-isotropic state of stress. Furthermore, effective compressive rock strength appears to be a strong function of pore pressure.

In chapter 5, I investigate production related pressure transients in three stratigraphically different reservoir sands. The shallow sand is under hydrostatic conditions, well drained, and normally compacted. At intermediate stratigraphic levels, reservoir sands are undercompacted, moderately overpressured, and depletion induces a

stress change following a stress path that has been observed elsewhere. The deep sand exhibits severe overpressures and undercompaction. Production appears to be accompanied by plastic and viscous deformation.

In chapter 6, I introduce a conceptual dynamic capacity model to test whether pore pressures and hydrocarbon column heights in individual SEI reservoirs are controlled by the sealing capacity of the fault against which the sand abuts or hydraulic fracturing of the overlying shale or fault. The deepest reservoir sand is characterized by small hydrocarbon columns and pore pressure conditions near hydraulic fracturing or active faulting. At intermediate levels, I find hydrocarbon columns that are either small and in dynamic equilibrium with the reservoir bounding fault or that are long and static (i.e., pore pressures below criticality and probably controlled by a spill point). Shallow reservoirs exhibit long oil and gas columns that are also static and controlled by a spill point.

Chapter 2

RELATIONSHIP BETWEEN IN-SITU STRESS, FRACTURES AND FAULTS, AND FLUID FLOW IN THE MONTEREY FORMATION, SANTA MARIA BASIN, CALIFORNIA

This chapter was published with Colleen A. Barton and Mark D. Zoback as co-authors in the American Association of Petroleum Geologists Bulletin, v. 81, no. 12 (December 1997), pp. 1975-1999.

2.1 Abstract

I used borehole televiewer (BHTV) data from four wells within the on- and offshore Santa Maria Basin, California, to investigate the relationship between fracture distribution, orientation, and variation with depth and in situ stress. The analysis of stress-induced wellbore breakouts shows a uniform NE maximum horizontal stress (S_{Hmax}) orientation in each well. This direction is consistent with the S_{Hmax} direction determined from wellbore breakouts in other wells in this region, the NW trend of active fold axes, and kinematic inversion of nearby earthquake focal plane mechanisms.

In contrast to the uniformity of the stress field, fracture orientation, dip, and frequency vary considerably from well to well and within each well. With depth, fractures can be divided into distinct subsets on the basis of fracture frequency and orientation which correlate with changes of lithology and physical properties. While factors such as tectonic history, diagenesis, and structural variations have obviously influenced fracture distribution, integration of the in-situ stress and fracture data sets indicates that many of the fractures, faults, and bedding planes are active, small scale strike-slip and reverse faults in the current NE trending transpressive stress field. In fact, I observed local breakout rotations in the wells providing kinematic evidence for recent shear motion along fracture and bedding-parallel planes. Only in the onshore well do steeply dipping fractures strike parallel to S_{Hmax}. Drill stem tests from two of the offshore wells indicate that formation permeability is greatly enhanced in sections of the wells where fractures are favorably oriented for shear failure in the modern stress field. Thus, relatively small-scale active faults provide important conduits along which fluids migrate.

2.2 Introduction

Fractures and faults play an important role in controlling the hydraulic properties of rocks by providing permeable conduits for fluids. Conversely, the presence of fluids strongly influences deformation and rupture of rocks by controlling fluid pressure and geochemical properties within fractures and faults. However, not all fractures and faults contribute to fluid flow (Long et al., 1991) or are equally important for failure and deformation processes in the crust. Therefore, the study of orientation and distribution of fractures and faults and their relation to the current stress field along with their importance to fluid flow is of great interest.

In general, fracture-enhanced permeability depends on fracture density, orientation, and most importantly, hydraulic conductivity of the individual fractures and faults present.

This is especially crucial in hydrocarbon reservoirs with low matrix permeability where fractures are the primary pathways for oil and gas migrating from the source rocks into their reservoirs. Hence, it is important to discriminate hydraulically conductive from hydraulically non-conductive fractures and faults in order to increase the efficiency of oil production and reservoir development. By studying the distribution and orientation of these planar features, I seek to understand which types of fractures and faults are most important for fluid flow and their angular relationship to the regional stress field. In regard to crystalline rock, Barton et al. (1995) concluded that fractures and faults that are potentially active in the current stress field are most permeable. In this study, I investigate this hypothesis in sedimentary rocks of the Miocene Monterey Formation, California, where fractures are crucial features controlling hydrocarbon migration and diagenetic processes (e.g. Isaacs, 1984).

In this paper, I utilize borehole televiewer (BHTV) data to detect fractures and to constrain the orientation of the three principal stress axes from wellbore failure (breakout) occurrences. I then invert earthquake focal plane mechanisms for the principal stress tensor and compare the results with the breakout analysis. Finally, drill stem tests (DST) help to distinguish hydraulically conductive from hydraulically non-conductive fractures.

2.3 Background

The four wells I are investigating are located in the Santa Maria Basin, California. Three of them are offshore wells drilled by Chevron U.S.A. Inc. within the Point Arguello field (wells B and C) and near Point Sal in the San Miguel field (well A) (Figure 2.1). Well D, drilled by UNOCAL Corporation, is the only onshore well used in this study and is located near Santa Maria in the Orcutt field (Figure 2.1). The target interval for these wells were the oil reserves of the Monterey Formation, an enormous Miocene sedimentary unit that was deposited adjacent to the active continental margin into Neogene basins all along the California Coast. Miocene tectonics were dominated by transtensional faulting indicated by more or less N trending extensional structures in the offshore Santa Maria basin (Crain et al., 1985). Complex processes such as wrench-tectonism – involving transform-faulting – block rotation, and localized rifting had initiated the evolution of small and deep borderland sub-basins along the California margin (Graham and Williams, 1985), into which the sediments of the Monterey and younger formations were transported. These reflect major oceanographic changes in deep-water circulation, the paleoclimate, and centers of biosiliceous productivity (Behl and Garrison, 1994). The stratigraphy of the Monterey Formation essentially contains a basal calcareous facies such as limestone or

dolomite, a middle transitional phosphatic facies such as phosphatic shale, and a thick upper siliceous facies composed of diatomaceous rocks (Pisciotto and Garrison, 1981) (Figure 2.2).

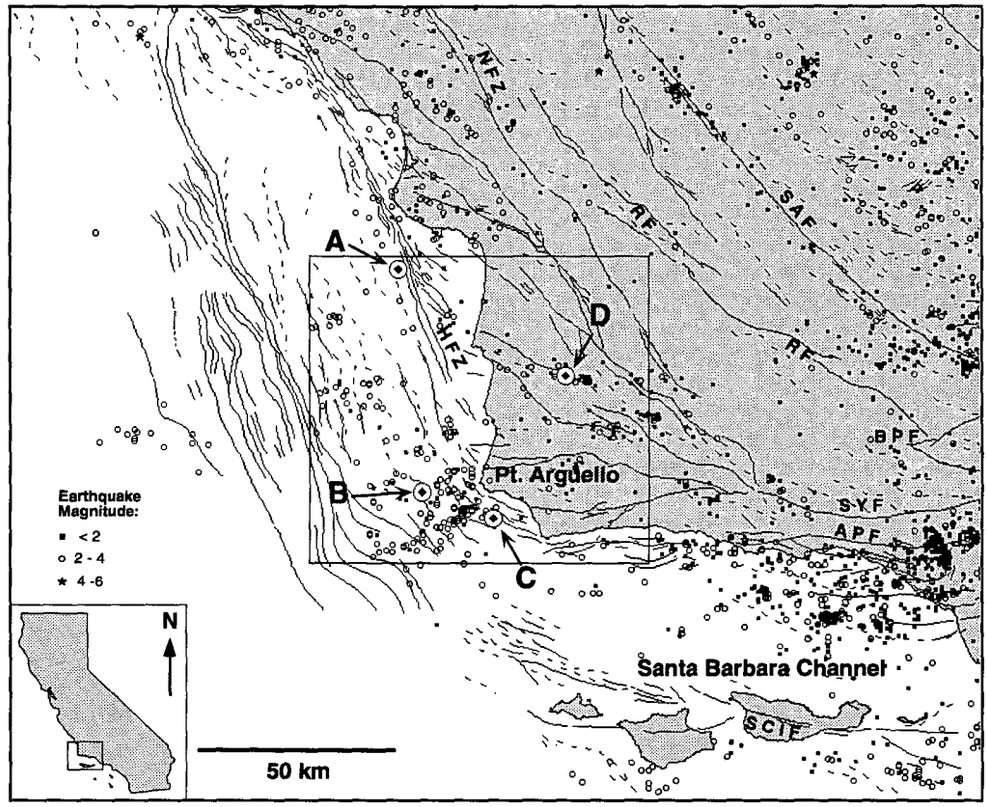

Figure 2.1: Basemap of study area (box) including location of wells studied in this analysis (A through D), surrounding background seismicity from 1987 to 1995 (Southern California Seismic Network Catalogue, U.S. Geological Survey field office, Pasadena), and folds (dashed lines) and Quaternary faults (< 1.6 Ma, solid lines) (from Jennings, 1975) (SAF: San Andreas Fault, RF: Rinconada Fault, BPF: Big Pine Fault, SYF: Santa Ynez Fault, APF: Arroyo Parida Fault, SCIF: Santa Cruz Island Fault, NFZ: Nacimiento Fault Zone, HFZ: Hosgri Fault Zone).

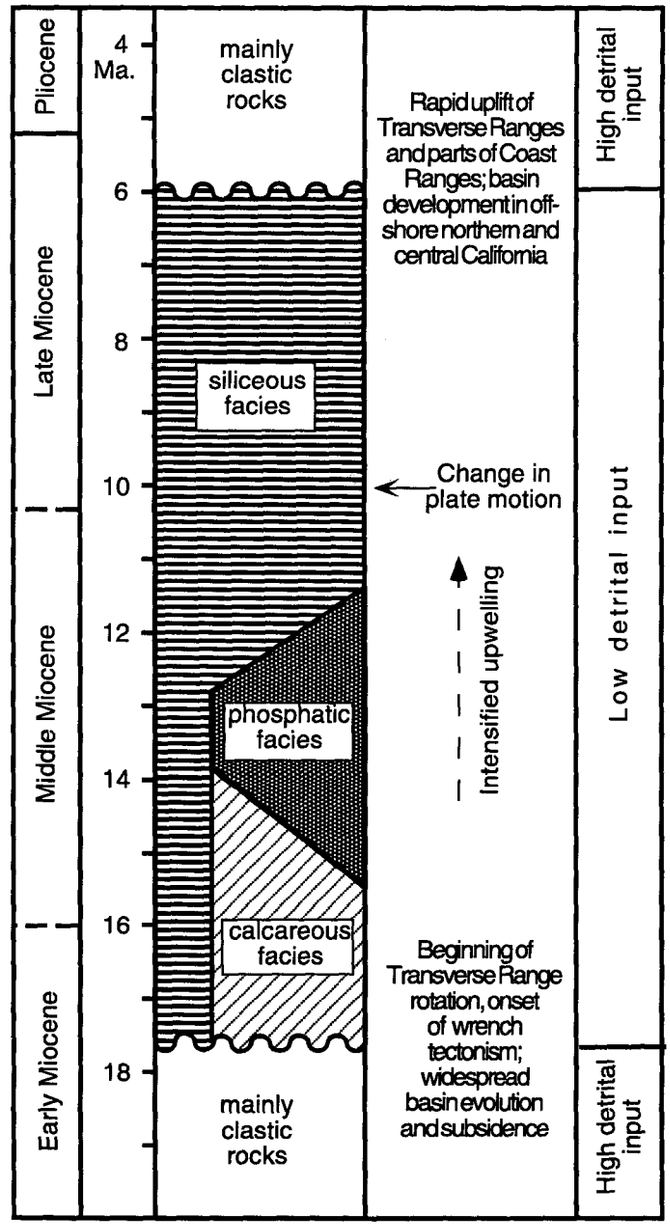

Figure 2.2: Generalized lithologic column of the Monterey Fm. (modified from Pisciotto and Garrison, 1981) showing qualitative time frame and amount of deposition during major tectonic events. The Monterey Formation was deposited between about 18 and 6 Ma under the influence of intense cold water upwelling, favoring the production of biogenic calcareous and siliceous facies.

Several aspects about the Monterey Formation are very characteristic and noteworthy: 1) it is both source and reservoir rock for hydrocarbons; 2) matrix porosity is quite high (10-30%), because of the abundant diatom content (however, matrix permeability is rather low

because of small grain sizes (Isaacs, 1984)); 3) the formation fluids typically are normal- or underpressured; 4) although fracture porosity is only a very small fraction of total porosity, the fractures are very permeable and therefore crucial for oil production (Isaacs, 1984); 5) its lithology has a high lateral and vertical variability. In general, outer basins had a relatively pure hemipelagic calcareous-siliceous sediment influx reflected by significant occurrences of cherts, whereas much more terrigenous sediments were deposited in medial and inner basins, which are void of chert phases (Graham and Williams, 1985; Behl and Garrison, 1994). High sedimentation rates for all these biogenic sediments introduced rapid increase in burial temperature and pressure favoring silica diagenesis and maturation of hydrocarbons.

By Pliocene time, extension ceased and the maximum principal stress direction rotated clockwise to its current NE orientations (Engebretson et al., 1985; Zoback et al., 1987; Zoback and Zoback, 1991), introducing a transpressional stress regime to coastal California, which has persisted to the present. This process uplifted the central California Coast Ranges and many basins were tectonically inverted changing to shallow and nonmarine sedimentation styles, depending on their proximity to the coast (Christiansen and Yeats, 1992). Jackson and Yeats (1982) divided this recent transpressive stress regime into a pre-Pleistocene gentle-folding stage and a post-Pleistocene phase involving intense shortening and rapid uplift. These tectonic forces have caused intense syn- and post-depositional folding and fracturing within the Monterey and younger formations, with major fold and fault axes generally striking NWN.

The study area is in a transitional region between the rapidly rotating block of the western Transverse Range to the south and the non-rotating area to the north. Namson and Davis (1990) describe this region as an active fold and thrust belt, typically involving fault-bend and fault-propagation faults. In addition, the San Andreas fault is influenced by the Big Bend south-east of the Santa Maria basin leading to changes in the regional stress pattern along the fault. These stress variations have been revealed by numerous studies of earthquake focal plane mechanisms and borehole breakouts (Zoback et al., 1987; Mount and Suppe, 1987). Localized variations of the horizontal principal stress orientations could be expected from similar localized variations in the region surrounding the Santa Maria basin.

2.4 Data and Methods of Analysis

For the three offshore wells, Chevron provided borehole televiewer (BHTV) and standard logging tool data such as dipmeter, sonic, gamma ray, resistivity, and

compensated neutron. Mudlogs, lithology descriptions, core analysis results, and formation permeability values from drill stem tests (DST) were also contributed. For onshore well D, only BHTV data were analyzed.

The borehole televiewer (BHTV) (first discussed by Zemanek et al., 1970) is a 360° circumferential acoustic imaging device that can be used to image stress-induced wellbore breakouts (described below) as well as fractures intersected by the borehole. Chevron and Unocal recorded the analog BHTV data II are utilizing here on video tape. Data quality is ranging from poor to excellent, depending on the well. After digitization, I performed a detailed analysis of both breakouts and fractures for each well utilizing software for interactive image analysis developed by Barton et al. (1991). I determined orientation, dip, and width of fractures and breakout widths and azimuths in order to investigate borehole shape and fracture characteristics with depth. For the fracture study, I considered the deviation of the wells from the vertical axis and corrected all of the measured fractures for borehole inclination.

The Pacific Gas and Electric Company (PG&E) provided a data set of earthquake focal mechanisms covering the southern Santa Maria Basin/Point Arguello area between 34°25' and 35°00' latitude (Figure 2.3A). Following the BHTV analysis, I used this data set to verify specifically the orientation and relative magnitude of the regional principal stress tensor in the study area by performing a focal mechanism stress inversion (FMSI). I compared this result with the resulting stress orientation obtained from the BHTV data analysis.

2.5 Orientation of Regional Stress Tensor

2.5.1 Breakout analysis

Stress-induced wellbore breakouts indicate the orientation of the principal horizontal stresses in the uppermost crust (Bell and Gough, 1979; Zoback and Zoback, 1980, 1991; Zoback et al., 1985; Plumb and Cox, 1987; Zoback et al., 1989). When the vertical stress (S_v) is nearly parallel to the axis of a vertical well, breakouts form in the direction of the minimum horizontal stress, S_{hmin}, where stress concentrations at the borehole wall exceed the rock strength. Mechanisms that describe the formation of these features are discussed

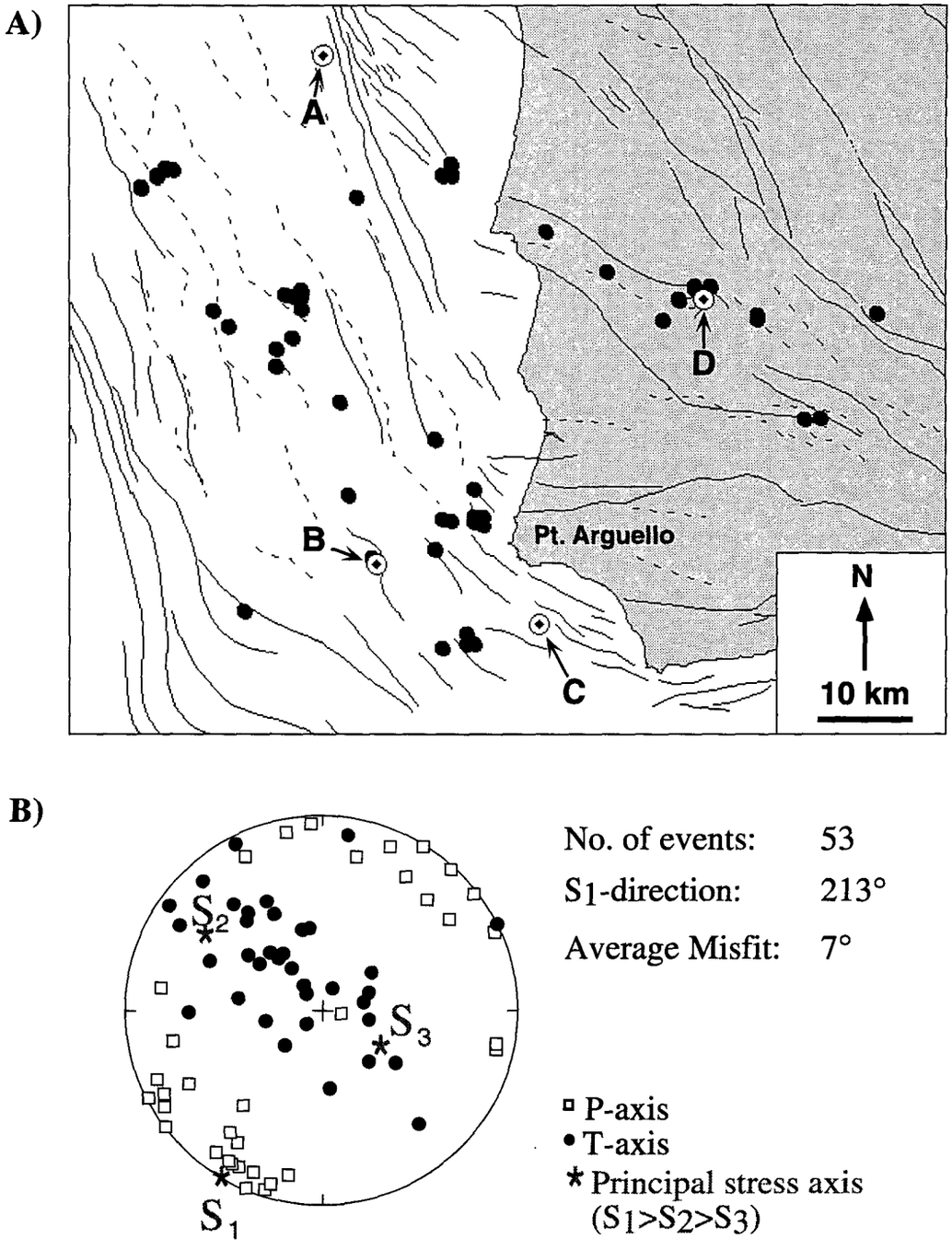

Figure 2.3: A) Spatial distribution of selected focal mechanisms (black, solid dots) in the Pt. Arguello region used for the stress inversion analysis. Also shown are relevant wells A through D (circles with diamonds), folds (dashed lines), and Quaternary faults (solid lines) (from Jennings, 1975). B) Lower hemisphere stereonet representation of P- and T-axis for selected earthquake events used in the stress inversion analysis. S_1, S_2, and S_3 denote resulting principal stress directions of best-fit stress tensor.

extensively in the literature (Bell and Gough, 1979; Zoback et al., 1985; Zheng et al., 1989). For each individual well, I used the following approach in order to identify and pick breakouts from the BHTV images: 1) two clearly discernible borehole elongations (i.e., low or even zero amplitudes and highly increased radii) with the necessary 180° spacing (Figure 2.4, right), 2) 5 cm-step analysis of borehole cross-sections over the potential breakout depth interval (Figure 2.4, left), and 3) independent azimuth and breakout width measurements on both sides of the well from the cross-sectional view. Since the well deviations are less than 10° in all wells, they should not affect breakout azimuths (Mastin, 1988). I omitted depth intervals with missing elongations on one side of the borehole (possibly due to off-centered tools or key seating). To obtain the mean direction and standard deviation of the least principal horizontal stress in each individual well, I analyzed the measurements following a statistical method developed by Mardia (1972). I plotted the results of this analysis in histograms of breakout azimuth versus cumulative occurrence (i.e., frequency) in order to identify the well-specific S_{Hmax} directions (Figure 2.5).

Well A, the northernmost well, was logged over a 628 m section and shows fair to good quality data. I picked breakouts, totaling a length of 20 m, mostly in the upper part of the well. These reveal a mean S_{hmin} direction of N143°E with a 13° standard deviation (Figure 2.5, well A). Hence, the mean S_{Hmax} orientation is N53°E. In the middle part of the logged depth interval, breakouts disappear. This could either result from higher natural fracture density below this depth and an associated decrease of stress concentration around the wellbore or lithology changes when the wellbore penetrates various and petrologically distinctly different members of the Monterey Formation; the latter corresponds with rock strength variations, that also influence breakout occurrence. Gross (1995) studied the change in mechanical failure as a function of lithology in the Monterey Formation intensely and found that local stresses and modes of failure (mode I versus shear mode) are different in hard (<9% weak minerals) versus soft (>22% weak minerals) beds in the Monterey formation. Well B, also located within the Point Arguello field, was logged over an interval of 508.5 m. Over long sections in the upper part of the well, the tool appeared to be off-centered to the East, resulting in larger radii (longer travel-times) to the West. In addition, the image often displayed repeated traces over short depth intervals (about 0.15 m - 0.3 m) indicating stick-slip motion of the tool in the wellbore. These logging conditions yield patchy looking images which can be misleading for breakout measurements. Because of their ambiguity, I did not use these features for stress analysis. In total, I only picked 125 breakouts, covering 3 m along the borehole and revealing a direction of N126°E for S_{hmin} – N36°E for S_{Hmax} – with a standard deviation of 13° (Figure 2.5, well B). Well C, within

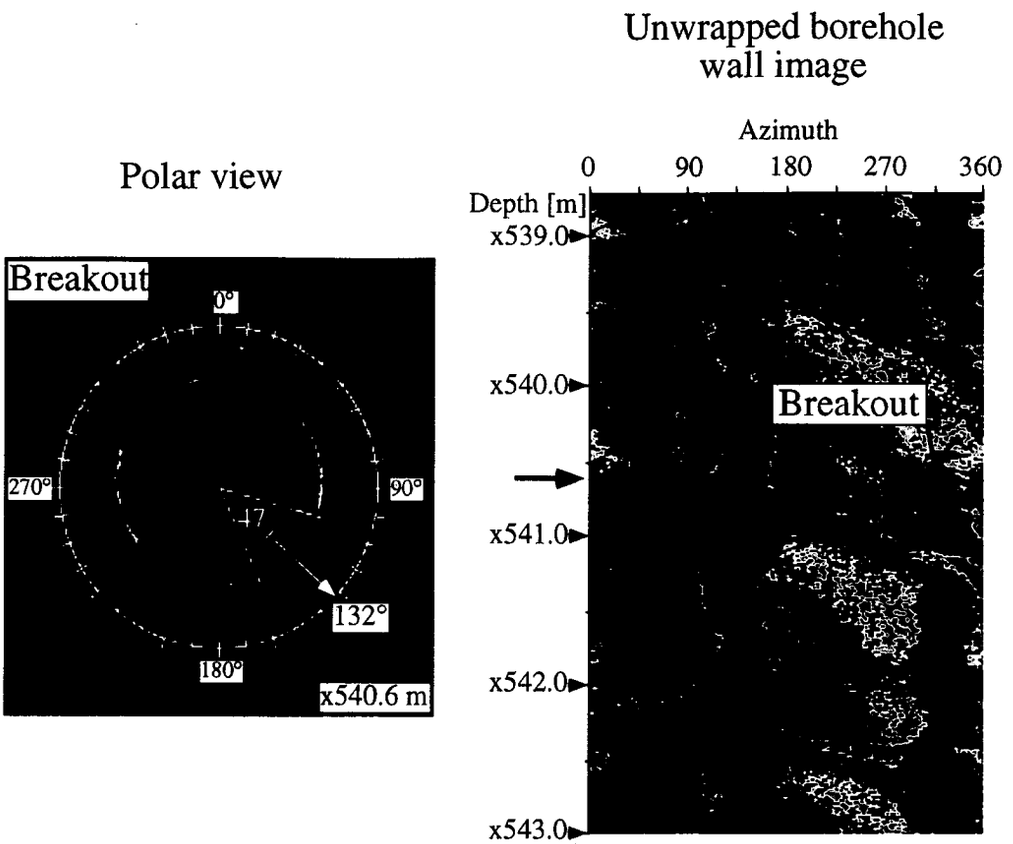

Figure 2.4: Typical breakout occurrence in well C. The unwrapped borehole wall image on the right displays the borehole radius as a function of azimuth and depth; it was converted from the acoustic wave travel-times (green/blue are smallest and orange/ black are largest radii). The breakout interval is clearly discernible as the two parallel, black, and vertical stripes with a spacing of roughly 180° (purple arrows). A cross-sectional polar view of the wellbore at x540.6 m depth (black arrow) is shown on the left. The two gaps in the borehole wall (purple arrow) correspond with the two black, parallel, and vertical stripes in the right image and are 180 ° apart - a necessary condition for breakout identification. The two white lines from the borehole center to its perimeter illustrate independent, one-sided breakout azimuth (132°) and width (47°) measurements.

the Point Arguello field, was logged over an interval of 640 m with data quality ranging from good to fair depending on the depth interval. Breakouts are abundant in the upper and lowermost part of the logged interval. In total, I took 5630 measurements covering a total depth interval of 107 m and yielding a mean orientation for S_{hmin} of N126°E with a standard deviation of 8°. This direction corresponds to a S_{Hmax} orientation of N36°E (Figure 2.5, well C). In the lower part of the upper breakout section, breakouts show a greater variance over short distances, which could be caused by small faults intersecting the wellbore (Shamir and Zoback, 1992; Barton and Zoback, 1994). In fact, I can correlate

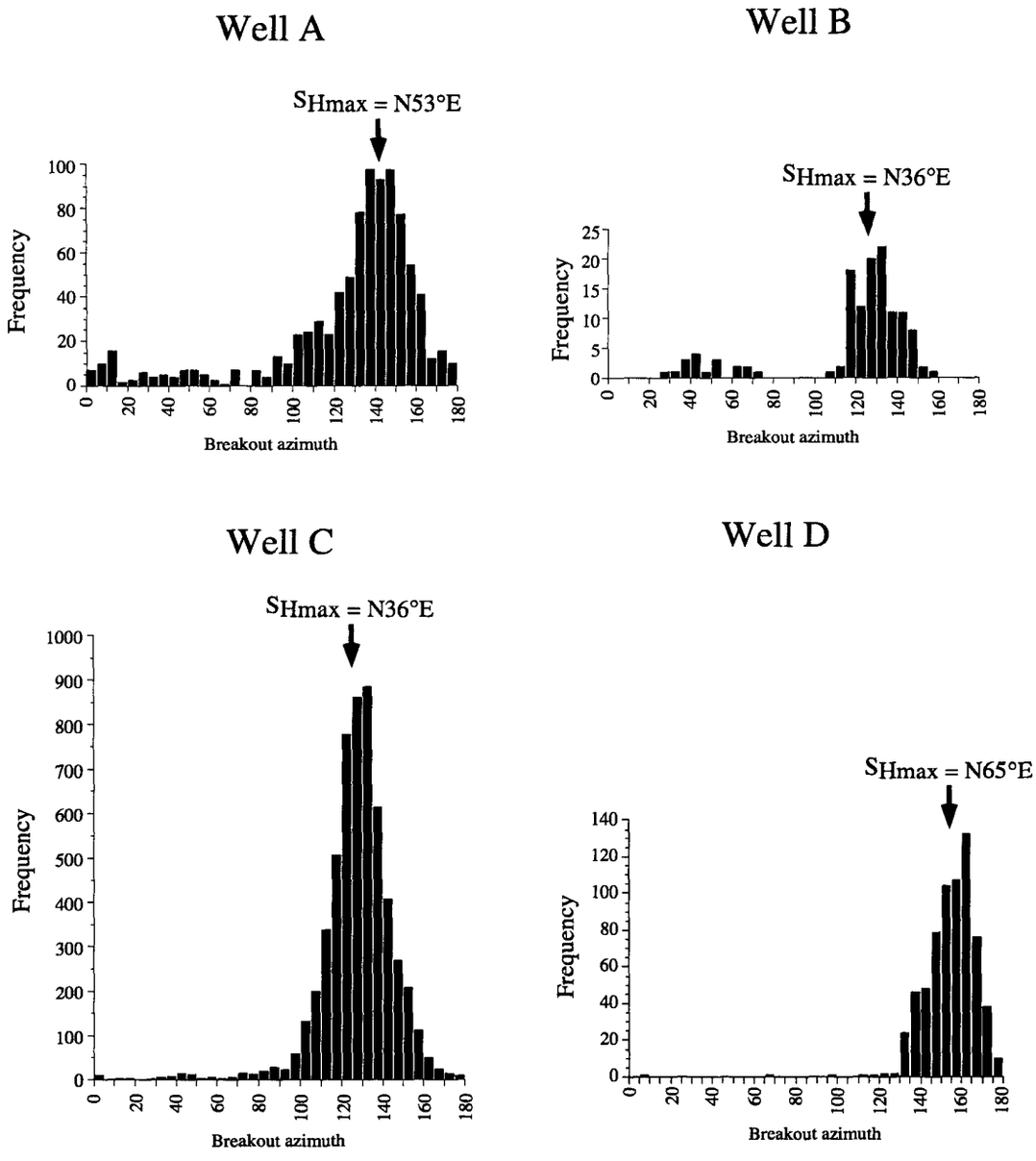

Figure 2.5: Breakout azimuth histograms for each well (A - C) present cumulative distribution of breakouts as a function of their orientation. This type of plot illustrates the variability and accuracy of the borehole-specific S_{Hmax} direction obtained through the picking process illustrated in Figure 2.4.

local breakout rotations (< 1 m) with planar features crossing the borehole, which most likely slipped in response to the raised fluid pressure caused by the drilling process (Shamir and Zoback, 1992). I will discuss the importance of this observation in relation to fracture type identification and active faulting further below. In the middle section of the well, breakouts vanish; I attribute this gap to lithological rock strength variations and local stress reduction (i.e., stress drop) caused by intense fracturing. Well D, within the onshore Orcutt

oilfield, was logged over 348 m. The data quality is excellent and I detected well-developed breakouts intermittently throughout the logged interval, covering a cumulative length of 17 m. The corresponding orientation of S_{Hmax} is 65° with a standard deviation of 6° (Figure 2.5, well D). Table 1 summarizes the results from the breakout analysis of the four wells outlined above.

TABLE 1. Summary of Stress Analyses from BHTV Data and Comparison with Results from the Focal Mechanism Stress Inversion (FMSI) in the Study Area.

Well	Average S_{Hmax}	Standard Deviation	Total Breakout Length [m]
A	N53°E	13°	20
B	N36°E	13°	3
C	N36°E	8°	107
D	N65°E	6°	17
Earthquake	$\sigma 1$ Direction	Average Misfit	Number of Events
FMSI	213°	7°	53

*Note the consistency with respect to the orientation of the maximum horizontal principal stress, S_{Hmax}, direction (see also Figure 2.Figure 2.6).

2.5.2 Stress inversion

For the stress inversion I used a methodology that is described by Gephart and Forsyth (1984) and Gephart (1990). It assumes stress in the region of interest is spatially and temporary uniform, and the observed slip direction marks the maximum shear stress direction on each fault plane. The inverse algorithm performs a grid search over possible stress models to find a best-fit uniform stress tensor with the smallest required total rotation of all fault planes about arbitrary rotation axes to match observed with predicted slip directions. The parameter

$$\mathbf{R} = \frac{\mathbf{S_2 - S_1}}{\mathbf{S_3 - S_1}} \qquad \text{Eqn. 2.1}$$

provides a measure for the relative stress magnitudes, where S_1, S_2, and S_3 denote the maximum, intermediate, and least principal stress, respectively.

For the study area I would expect two different styles of faulting: strike-slip and reverse. This constrains the parameter R as follows: For pure strike-slip faulting, S_v is the

intermediate principal stress S_2, while for pure reverse faulting, S_v is the least principal stress S_3. Since I observe a transpressive stress regime in the study area, I would expect S_v to be the least principal stress S_3; i.e.,

$$\mathbf{R} = \frac{\mathbf{S_2 - S_1}}{\mathbf{S_3 - S_1}} = \frac{\mathbf{S_{hmin} - S_{Hmax}}}{\mathbf{S_v - S_{Hmax}}} \qquad \text{Eqn. 2.2}$$

The earthquake focal mechanisms used in this analysis were recorded by the Central Coast Seismic Network operated through the Pacific Gas and Electric Company (PG&E). During the period from 1987 to 1994, 53 focal mechanisms were selected using only events with the highest levels of confidence. Since these are P-wave mechanisms calculated using the program FPFIT (Reasenberg and Oppenheimer, 1985), the selection criteria for each event were the following: (1) at least 15 different seismographic readings and (2) automated convergence with high confidence levels of the FPFIT-output. The locations of the 53 selected earthquake events are shown in Figure 2.5A. Their P- and T-axes distribution (Figure 2.5B) indicate reverse slip to strike-slip faulting (sub-horizontal P-axes and vertical to horizontal T-axes). The near-horizontal P-axes imply maximum compression in a NE-SW direction. For the inversion, I treated the focal mechanism data in two different ways. One was to assume that all events have more-or-less comparable precisions (i.e., equally weighted). The second way was to assume twice as much weight for the on- and near-shore events compared to the offshore events. Because of the station coverage of the seismographic network, I considered on- and nearshore focal mechanisms to be more reliable in the second approach. For both cases, I started the inversions on coarse search grids subsequently using finer grids to search more exactly in the vicinity where the first estimate on the principal stress orientations was obtained. The approach using the second assumption yielded the most reliable result (i.e., that with the smallest misfit). The orientation of the maximum principal stress S_1 was found to be N213°E with a plunge of 2° (Figure 2.7B and Table 1). The results for the orientations of the S_2 - and S_3 -axes were N304°E/26° and N119°E/64°, respectively (Figure 2.7B). However, it is important to note that the first assumption (giving all focal mechanisms equal weight) had almost identical results, implying that the stress tensor is not influenced by the differential weighing of the focal mechanisms. In both cases, the distribution of misfits for individual events did not suggest a non-uniform stress tensor, neither spatially nor temporally, which would possibly identify a distinct subset of earthquakes with a different stress tensor. The inversions yielded R-values between 0.4 and 0.6. Their uncertainty, however, was extremely high. Because the distribution of T-axes (ranging between horizontal and vertical) implies a

strike-slip/reverse faulting stress regime, I think the most reasonable result is that R is quite high; hence, $\mathbf{S_2 \cong S_3}$ (i.e. $\mathbf{S_{Hmax} > S_{hmin} \cong S_v}$), implying a transpressive stress regime.

2.5.3 Discussion

Figure 2.6 shows the orientation of the maximum horizontal stresses resulting from the stress inversion (black, bold arrow pair in the box) and the BHTV data breakout analysis (gray arrow pairs encompassing well symbols) along with the trend of mapped folds and faults, as well as results from other stress orientation analyses (fine gray symbols) (Zoback et al., 1987; Mount and Suppe, 1987) in the region around the study area. The box in the figure outlines the area in which the 53 slip events occurred that were used for the stress inversion. The maximum horizontal principal stress directions are principally consistent among the wells, follow the regional trend of NE maximum horizontal stress orientations (Zoback and Zoback, 1991) and are (sub-) orthogonal to the fold and Quaternary fault axes. Results on the S_{Hmax} orientation obtained from the extension direction of mode I tensile fractures in wellcore studies within the Point Arguello field (Sadler, 1990; Narr, 1991) agree well with my findings. The more locally-derived stress orientations in these studies follow the broader scale trend. However, the resulting S_{Hmax} orientations, especially for well D, which is located within the onshore Santa Maria basin (Figure 2.6), reveal slight deviations. These correlate with structural variations in the study area (Figure 2.6). Faults and folds at Well A are oriented to the north; near wells B and C their predominant orientation is toward the NW, and they strike easterly at Well D. I attribute these observations to the complex history of the Western Transverse Range block translation and rotation to the south and a non-rotating area to the north (Nicholson et al., 1992). Consequently, local tectonic, structural, and stress variations were introduced incorporating not only dextral, sinistral, and oblique reverse faulting but also local normal faulting (e.g. in the onshore Santa Maria basin) (Namson and Davis, 1990). These processes have been active since the Neogene and explain the deviations in modern breakout orientations.

Since the orientation of S_1 from the earthquake focal mechanism inversion follows the stress orientations observed in the wellbores, uniform compressive stress orientations persist throughout the crust to seismogenic depths (~12-15 km) (M. McLaren, pers. com., 1996). These different methods uniformly reflect the general transpressive stress regime that has dominated the evolution of the late Cenozoic fold and thrust belt in the southern Coast Ranges and the Santa Maria Basin (Page, 1981; Namson and Davis, 1990).

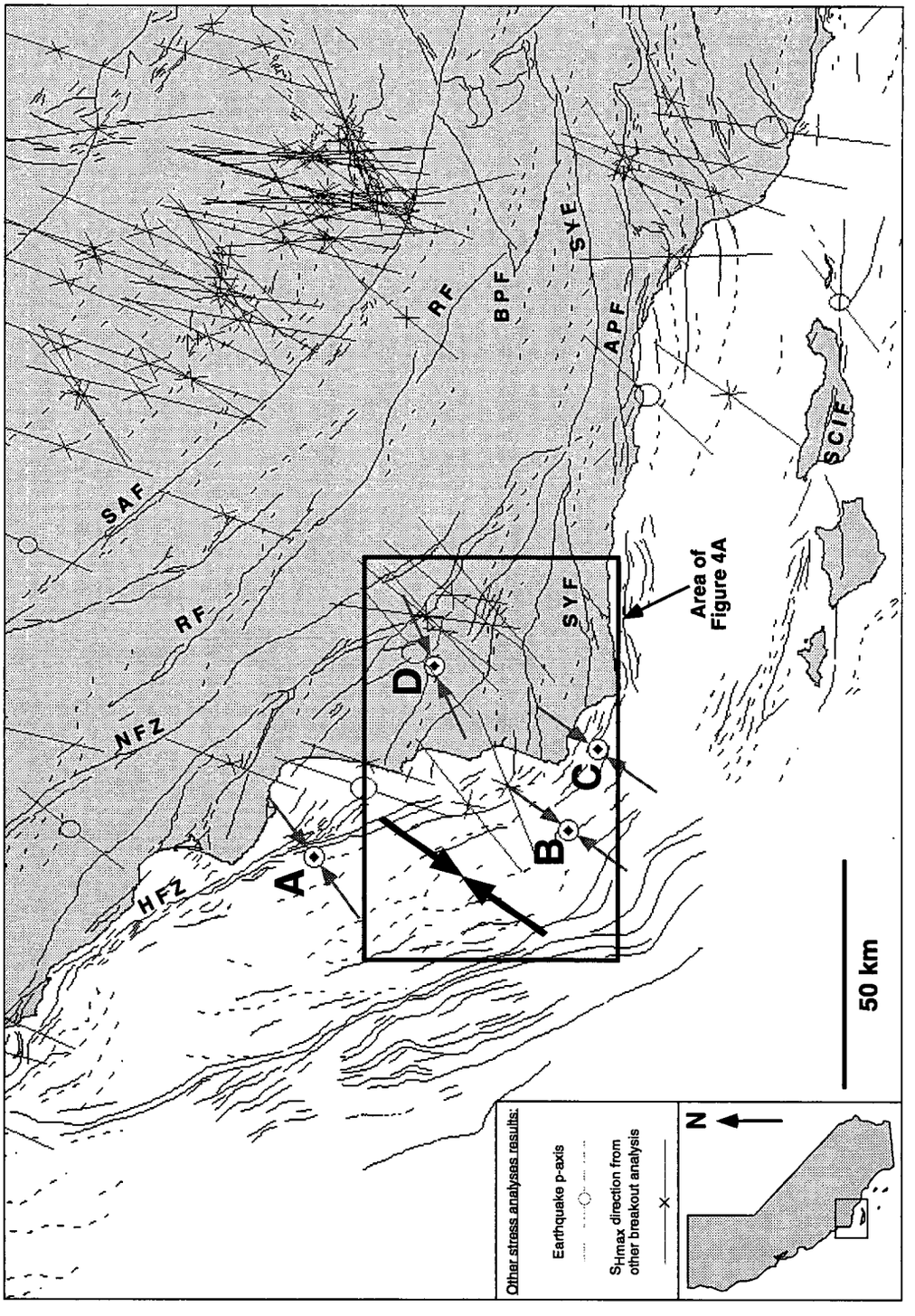

Figure 2.6: Basemap of study area showing location of wells (A - D) along with their mean S_{Hmax} directions obtained from breakout analysis (gray arrow pairs). Dark box and bold arrow pair constrain area of stress inversion analysis and resulting S_{Hmax} direction, respectively. Dark lines show folds (dashed) and faults (solid) (see Figure 2.1 for fault names). Fine gray symbols display world stress map data (Zoback, 1991).

2.6 Wellbore Fracture Analysis

Any dipping planar feature or structure detected by the borehole televiewer (such as a fracture, fault, or bedding plane) appears as a sinusoid in the image of the borehole wall (Figure 2.7). I determined azimuth, dip, and apparent aperture for all planar features imaged in the logs. However, many fractures have immeasurably small apparent apertures due to the limited resolution of the BHTV (Barton and Zoback, 1992). In practice, hairline cracks, which are quite common in the Monterey (Sadler, 1990; Gross, 1995, 1993; Gross and Engelder, 1995), and smooth bedding planes may escape detection by the borehole televiewer. Wellcores are best suited for a fine scale and detailed kinematic fracture analysis; unfortunately, this type of data was not available to us. The following results and discussions are based solely on the population of planar features observed in the BHTV images. These are macroscopic features with amplified apertures, called apparent apertures, likely to be caused by spalling associated with mechanical drilling effects.

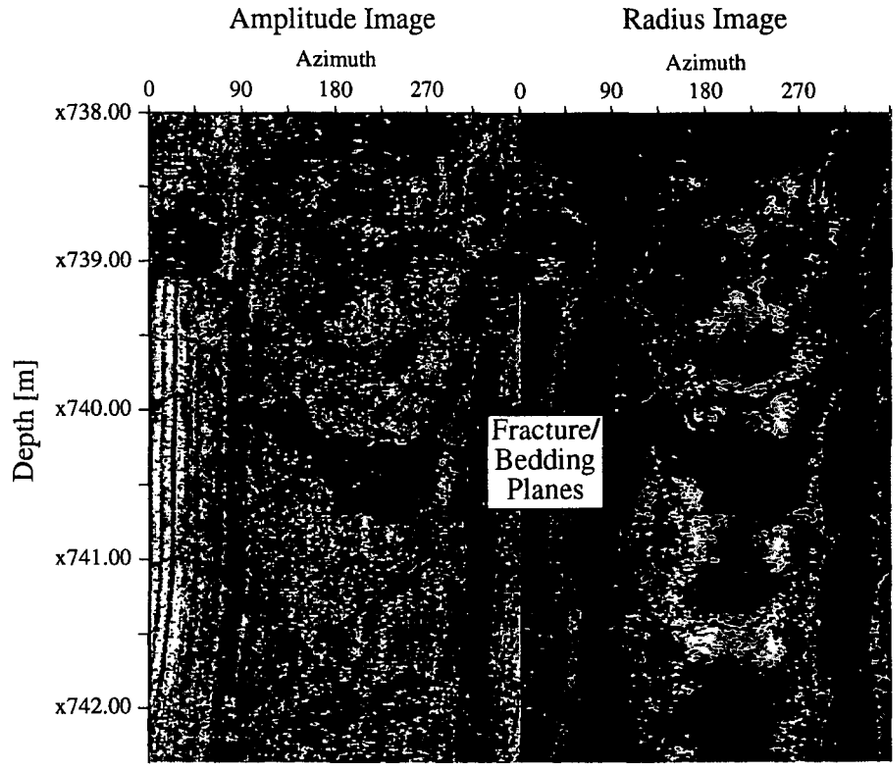

Figure 2.7: Representative BHTV image of well C. Left part shows acoustic wave amplitude image, where red and purple correlate with highest and lowest amplitudes, respectively. Right part displays corresponding acoustic wave travel-time image converted to borehole radii, where purple/blue are smallest and red/black are largest radii. Arrows point at two dipping planar features such as fractures, faults, or bedding planes, which are discernible in both images.

An important task of this study was to distinguish syndepositional features, such as bedding planes, from post-diagenetic structures, such as fractures and faults. I relied on the dipmeter logs available for these wells to determine bedding plane directions. The population of bedding planes was split into different depth intervals according to the distribution of planar features. I assumed that all planar features that have the same attitudes as the bedding planes within each of the individual depth intervals were bedding and interpreted the remaining planar features as fracture and fault planes distinct from bedding planes. While it may seem here that this treatment of the BHTV fracture data leads us to neglect bedding plane parallel-interbed slip surfaces (Narr, 1991), which commonly occur in chert beds, I present below a discussion of both sets of planar features as potential slip surfaces.

Although a coherent picture of the regional stress field persists in the study area, a complex distribution of fractures and bedding planes is observed. Fracture and bedding plane populations are composed of various orientations and, based on the BHTV data, I can divide them into distinct subsets on the basis of their frequency and predominant strike and dip directions. Some of the fracture subsets are extension cracks oriented parallel to the maximum horizontal stress S_{Hmax} (as will be shown later for well D); others are shear fractures (inferred from local breakout rotations at the fracture plane imaged by the BHTV tool), potentially active in the current stress field (including bedding-parallel slip planes); or cracks that are not related to the current stress field but rather to bedding planes, e.g., strike-perpendicular joints, cross joints, or bedding-parallel joints (Gross, 1995). These observations support the idea that markedly different factors influence the initiation and propagation of fractures (e.g., Stearns and Friedman, 1972).

2.6.1 Correlation of fractures with other well-log data

Because of the resolution limitations imposed by the BHTV-tool and the lack of wellcores, it is not worthwhile for us to discuss fracture origin and microscopic sedimentary features, such as hairline cracks or bedding plane related joints. I focus rather on broader scale correlations (i.e., fracture zones) using standard logging tools such as resistivity, gamma ray, neutron porosity, density, and sonic. These tools generally respond to changes in physical properties of the rocks penetrated by the wells. Figure 2.8 displays curves from well A as an example of pronounced correlations between standard well-logs, varying lithologic properties, and occurrences of fractures. The log data were smoothed twice within a moving window of 3 m, which reduces the spikiness but preserves the general character and scale of the curves. Note the increase in resistivity, gamma, and density associated with a general decrease in neutron porosity, and sonic slowness as the

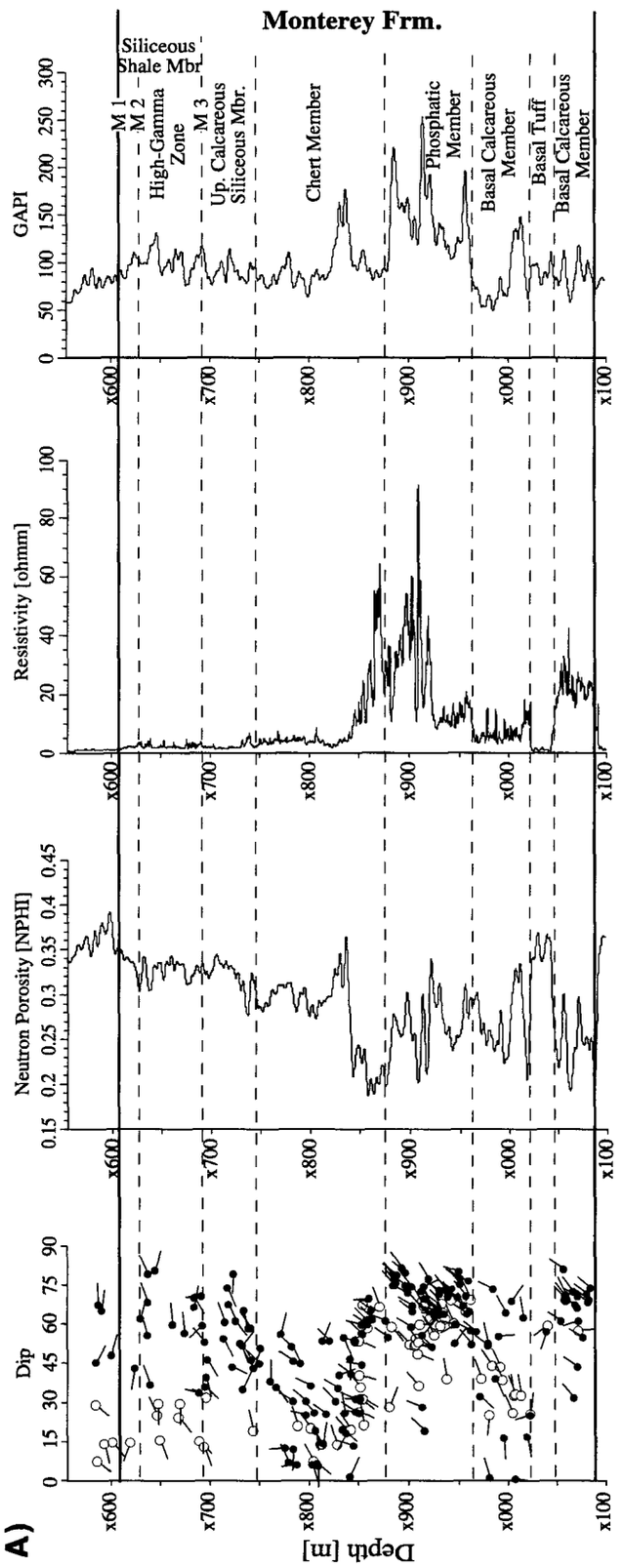

Figure 2.8: Correlation of fracture (solid tadpoles) and bedding plane (open tadpoles) distribution; the solid and open circles exhibit the dip, and the tails the down-dip, direction with responses from various standard logging tools in well A. A) Correlation with neutron porosity, resistivity, and gamma-ray data. B) Correlation with density and sonic data

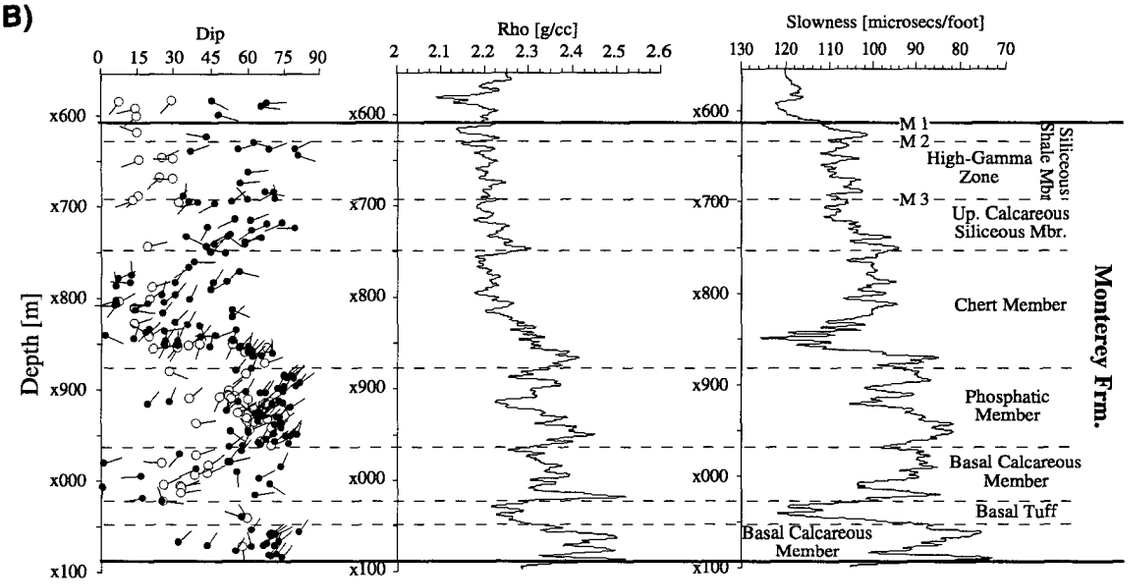

Figure 2.8: Continued.

fractures dip more steeply and strike predominantly perpendicular to S_{Hmax} in the lowermost chert, phosphatic, and lower basal calcareous members. A further comparison of fracture distribution in each well with major sequence stratigraphy (Figures 1.9 - 1.12) shows that different subsets of fractures tie with different lithologic units. This apparent lithology-dependent style of fracturing has been frequently observed in the Monterey Formation and is widely studied (Pisciotto and Garrison, 1981; Isaacs, 1984; Behl and Garrison, 1994). It is due either to diagenetic processes and the related embrittlement of diagenetically mature siliceous rocks (i.e., quartz as siliceous phase throughout the Point Arguello oil field (Crain et al., 1985), or to differences in physical toughness for different stratigraphic sequences (i.e., soft beds such as mudstones show widely spaced shear fractures as opposed to hard beds such as cherts and dolostones with an abundance of joints (Dunham, 1987; Gross, 1995)). Depth intervals with markedly organized patterns of fractures are more or less coherent with some standard logging tool responses (Figure 2.8), indicating that the degree and orientation of fracturing is related to different physical parameters of the formation.

2.6.2 Fracture and bedding plane orientation and potential slip surfaces

The orientations of the bedding planes (open tadpoles, Figures 1.9 - 1.11) obtained from the dipmeter data for the three offshore wells reveal that the dip distribution with depth is

quite moderate (< 40°) in the upper portions of the wells (approx. 250m). The dip then gradually increases with depth either to the top or close to the base of the Monterey chert

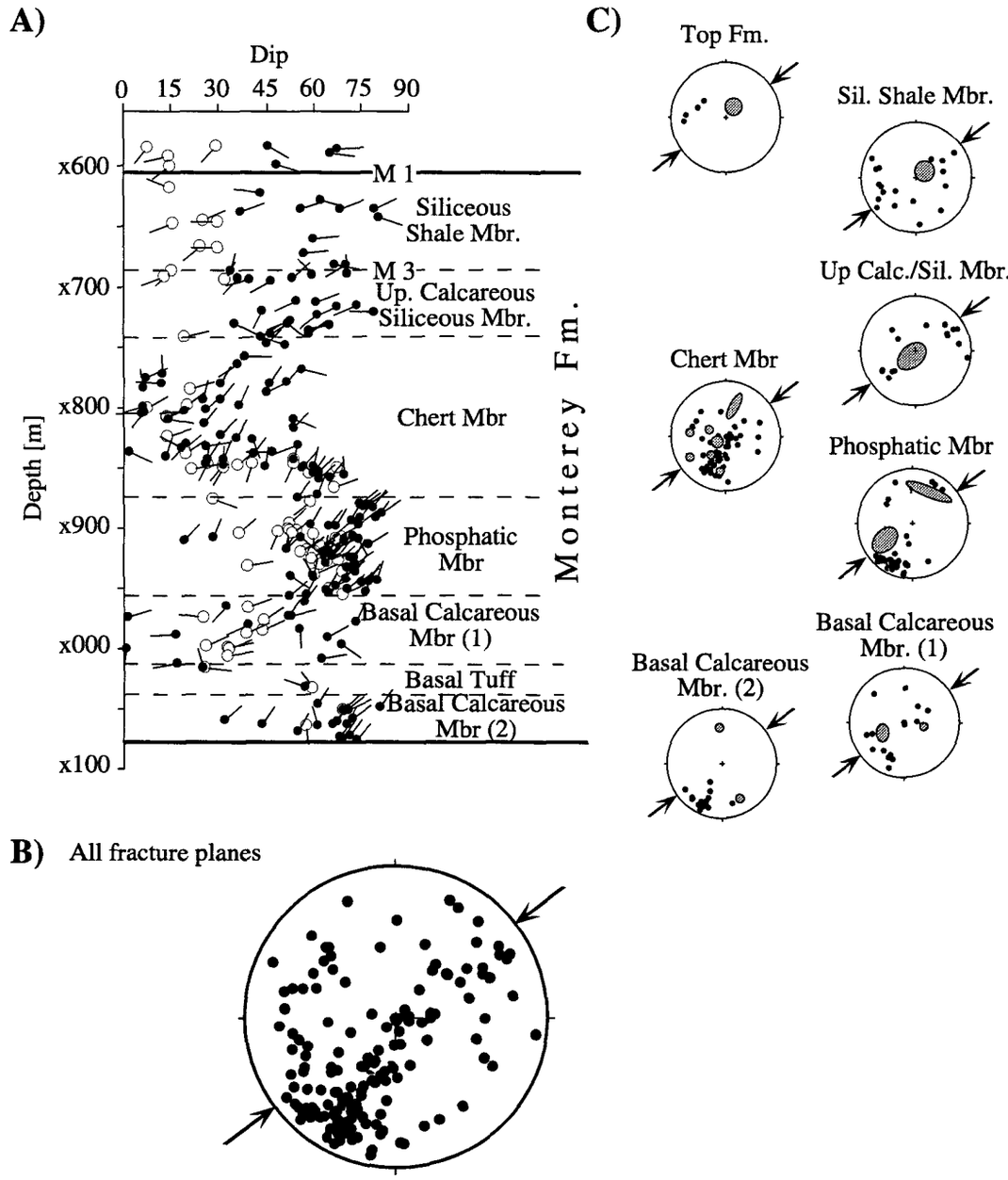

Figure 2.9: Fracture and bedding plane distribution and orientation in Well A. A) Tadpole representation of fractures (solid circles) and bedding planes (open circles) with depth including major sequence stratigraphy. B) Lower-hemisphere stereographic projections of poles to all fracture planes. C) Lower-hemisphere stereographic projections of poles to fracture planes (black dots) and bedding (gray areas) for individual lithologic sequences. The gray areas denote general orientation and distribution of bedding planes in this depth interval. Black arrows denote orientation of S_{Hmax} obtained from breakout analysis in this well.

member where the dips abruptly jump to higher values. Below, bedding planes occur less frequently and with more dispersed orientations. The scatter in orientation persists to the bottom of each well. Figures 1.9 - 1.11 show the trends of bedding plane orientations as both tadpole plots (parts A, open circles) and lower hemisphere stereographic representations (parts C, gray areas). These observations suggest that during the deposition of the Monterey chert member the character of sedimentation changed, resulting in changes of bedding plane orientations. The region around the Santa Maria basin was tectonically very active during the development of the San Andreas fault to the North; the former forearc basin and its associated accretionary complex were segmented into many smaller subbasins (Graham and Williams, 1985). This activity involved complex processes such as wrench-tectonism, transform faulting, and block rotation (Nicholson et al., 1994). These tectonic processes certainly had an important influence on depositional environments and sediment provenances. Soft sediment slumps commonly occurred during this period (S. Graham, pers. com., 1995), introducing additional variations in bedding plane attitudes. Hence, I expect significant variations in bedding plane characteristics.

The strikes of the bedding planes are predominantly NNE to NE in well B (gray areas in stereonets, Figure 2.10C), and NW in well C (gray areas in stereonets, Figure 2.11C), which matches results found by Narr (1991) from well-core analysis in adjacent wells of the same oil field less than 5 km away. Inferring from Narr (1991), I can conclude that the obvious rotation of bedding strikes from generally NE to NW was caused by the Point Arguello anticline, the main structure in the Point Arguello oil field, which was subject to tilting and changes in plunge. Because of the spatial proximity to wells B and C, I think the same or similar structures are responsible for bedding plane rotation between these two wells. In well A to the North, bedding strikes predominantly N to NW (Figure 2.9C). This observation differs from outcrop studies of the Monterey Formation at the shoreline in this area (Gross, 1995), and may be explained by the presence of folds and/or faults as compiled in a study by Tennysson et al. (1994). In the onshore well D, bedding was identified solely from the BHTV images since no dipmeter data were available. This is discussed in more detail below.

An analysis of the fracture and fault plane attitudes separately from the bedding shows a non-systematic distribution of fractures within each well and laterally among them. Figures 1.9 - 1.12, parts A, display the fracture planes as black tadpoles, while Figures 1.9 - 1.12, parts C, show lower hemisphere stereonet representation (black dots). Figures 1.9 - 1.12, parts B, represent poles to all fracture planes in lower hemisphere stereonets. Large variations in both dip and strike are obvious and in strong contrast to the uniform stress field observed from the breakout and focal mechanism inversion analysis. In well A, fracture

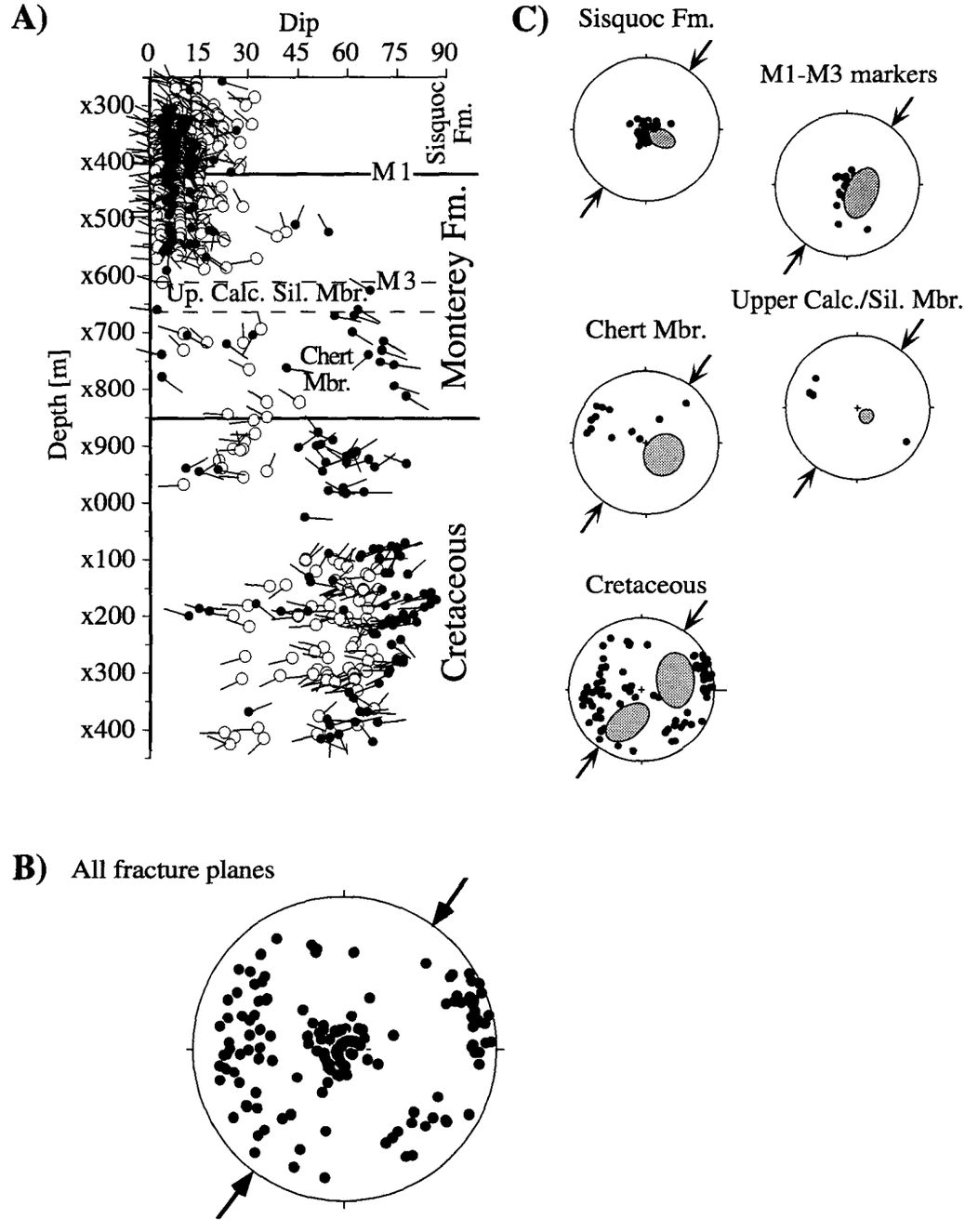

Figure 2.10: Fracture and bedding plane distribution and orientation in Well B. A) Tadpole representation of fractures (solid circles) and bedding planes (open circles) with depth including major sequence stratigraphy. B) Lower-hemisphere stereographic projections of poles to all fracture planes. C) Lower-hemisphere stereographic projections of poles to fracture planes (black dots) and bedding (gray areas) for individual lithologic sequences. The gray areas denote general orientation and distribution of bedding planes in this depth interval. Black arrows denote orientation of S_{Hmax} obtained from breakout analysis in this well.

strikes are generally perpendicular to S_{Hmax} with moderate to steep dips (Figure 2.9B). In the Upper Siliceous Calcareous Member, fracture strikes scatter with no predominant orientation. Within the Chert Member, however, fracture and fault dips range between sub-horizontal and sub-vertical; their strikes are oblique or orthogonal to S_{Hmax}. The Phosphatic Member, in contrast, shows a rather well organized fracture pattern with steep dip angles striking nearly orthogonal to S_{Hmax}. In well B, fractures have subhorizontal to shallow dips in the upper portion of the well (Figure 2.10A) (showing no change in character across the Sisquoc-Monterey boundary) and the dips then jump to higher values at the Upper Calcareous Siliceous Member. In this zone, only four fractures and faults were detected that strike parallel to S_{Hmax}. In the Chert Member below, steep dips persist with strikes mostly parallel to S_{Hmax} (Figure 2.10B). Within the Cretaceous, the lower portion of the well, fractures and faults are abundant and mainly strike oblique or perpendicular to S_{Hmax}. The dips of fractures and faults in well C are generally between 45° to 80° throughout the well, with highly variable strike orientations (Figure 2.11A). Fracture and fault density is considerably increased in the lower part of the Sisquoc Formation (between markers S5 and M1). In the Upper Calcareous Siliceous Member of the Monterey Formation, increased fracture frequency persists with strikes mostly oblique and perpendicular to S_{Hmax} (Figure 2.11B). In the Chert Member below, fewer fractures and faults were detected; these are generally oriented to S_{Hmax} in an oblique to perpendicular sense. While I can attribute the variability in fracture type and orientation in the offshore wells to changes in lithologies and physical properties as suggested above (e.g., Gross, 1995), Stearns and Friedman (1972) also provide explanations related to geologic structures. Fractures associated with folds and faults are commonly observed in outcrops and their origins are well understood. Given the complexity and ubiquity of folds and faults in my study area, structurally related fracturing is another feasibility for appreciable variability in fracture orientations. In fact, Narr (1991) explains differences in fracture spacing in the Point Arguello field with a change of plunge of a local fold, the main structure in the reservoir.

For onshore well D, dipmeter data was not available for discriminating between bedding and fractures and also not necessary, because BHTV data quality was excellent. The Monterey Formation is highly fractured over the logged interval and the BHTV data resolution is high enough for us to discriminate two general trends: moderately to steeply dipping fractures and subhorizontal bedding planes (Figures 1.12 and 1.13 left). The orientation of most steeply dipping fractures is approximately sub-parallel to the ambient stress field (determined by the breakout analysis) as indicated by the bold arrow pair (Figure 2.12B). Further, they do not seem to offset the subhorizontal set of bedding planes

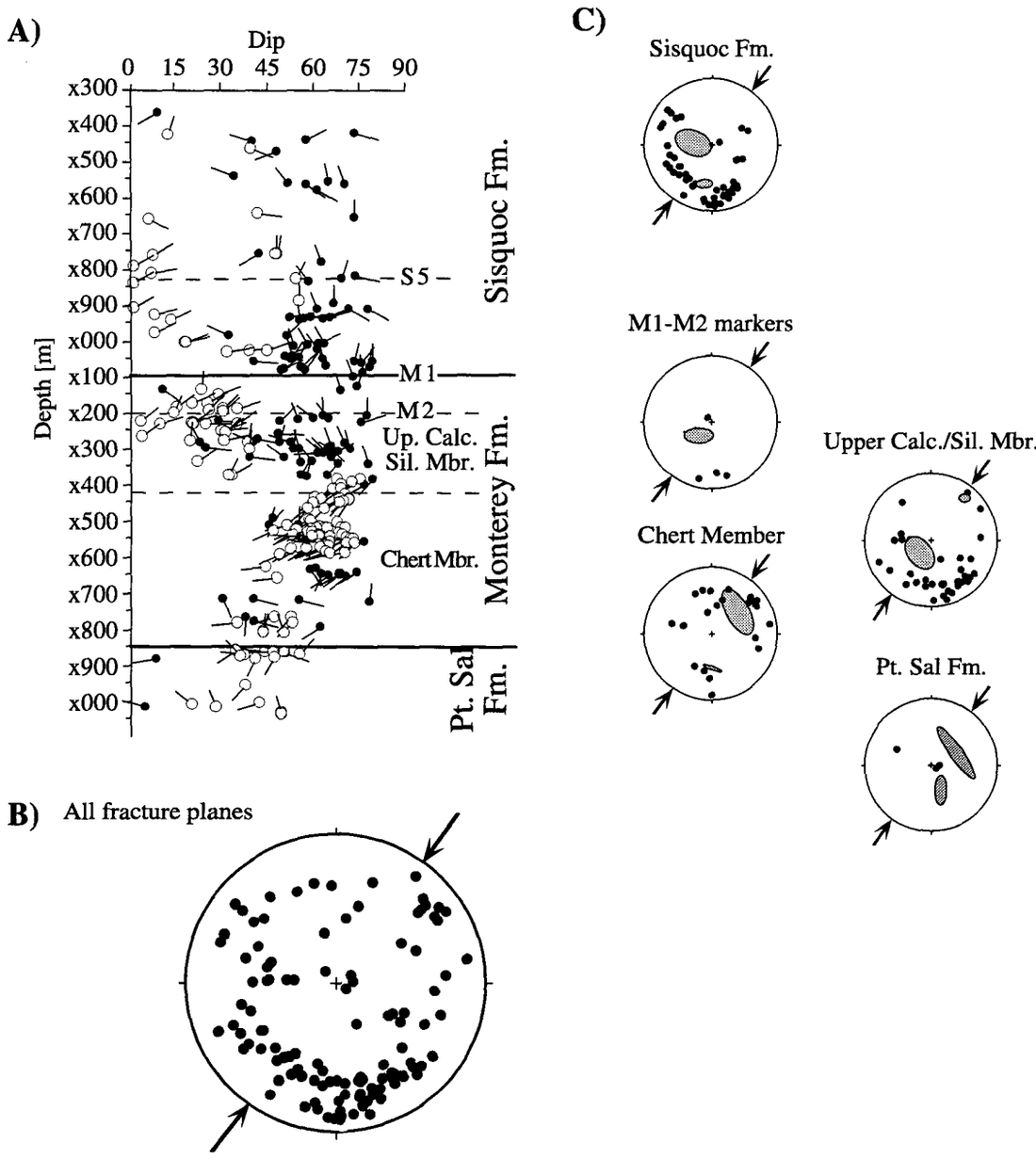

Figure 2.11: Fracture and bedding plane distribution and orientation in Well C. A) Tadpole representation of fractures (solid circles) and bedding planes (open circles) with depth including major sequence stratigraphy. B) Lower-hemisphere stereographic projections of poles to all fracture planes. C) Lower-hemisphere stereographic projections of poles to fracture planes (black dots) and bedding (gray areas) for individual lithologic sequences. The gray areas denote general orientation and distribution of bedding planes in this depth interval. Black arrows denote orientation of S_{Hmax} obtained from breakout analysis in this well.

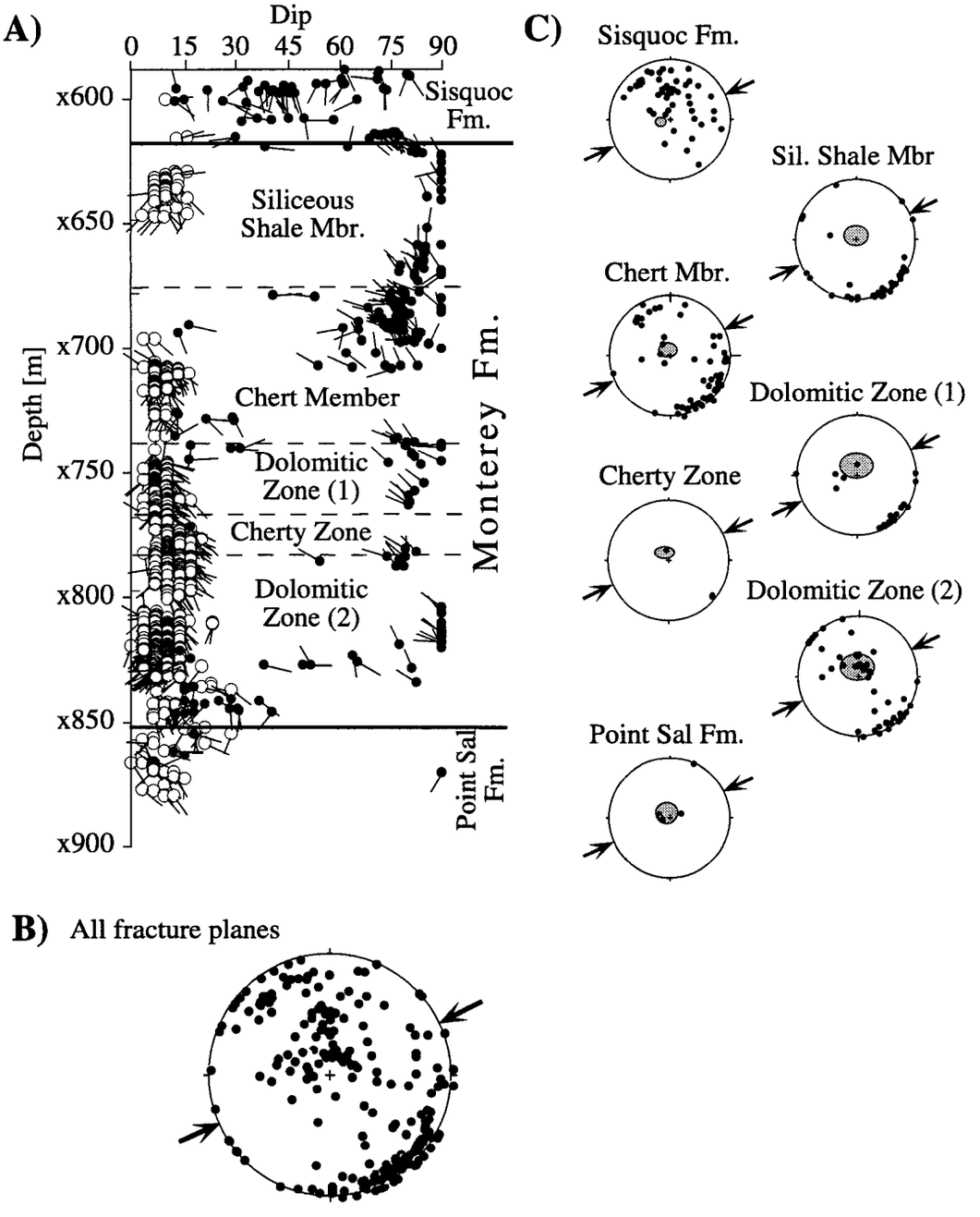

Figure 2.12: Fracture and bedding plane distribution and orientation in Well D. A) Tadpole representation of fractures (solid circles) and bedding planes (open circles) with depth including major sequence stratigraphy. B) Lower-hemisphere stereographic projections of poles to all fracture planes. C) Lower-hemisphere stereographic projections of poles to fracture planes (black dots) and bedding (gray areas) for individual lithologic sequences. The gray areas denote general orientation and distribution of bedding planes in this depth interval. Black arrows denote orientation of S_{Hmax} obtained from breakout analysis in this well.

(Figure 2.13, left). This implies that a subset of the population of steeply dipping fractures appears to have formed as Mode I fractures (perpendicular to S_3 in the S_1 - S_2 plane) within the ambient stress field. The depth distribution and orientations of fractures in well D are shown in Figure 2.12A. The relatively shallow dipping bedding planes and mostly steeply dipping fractures are easily distinguished (see also BHTV image, Figure 2.13). This observation prevails throughout the whole depth interval studied with the exception of the

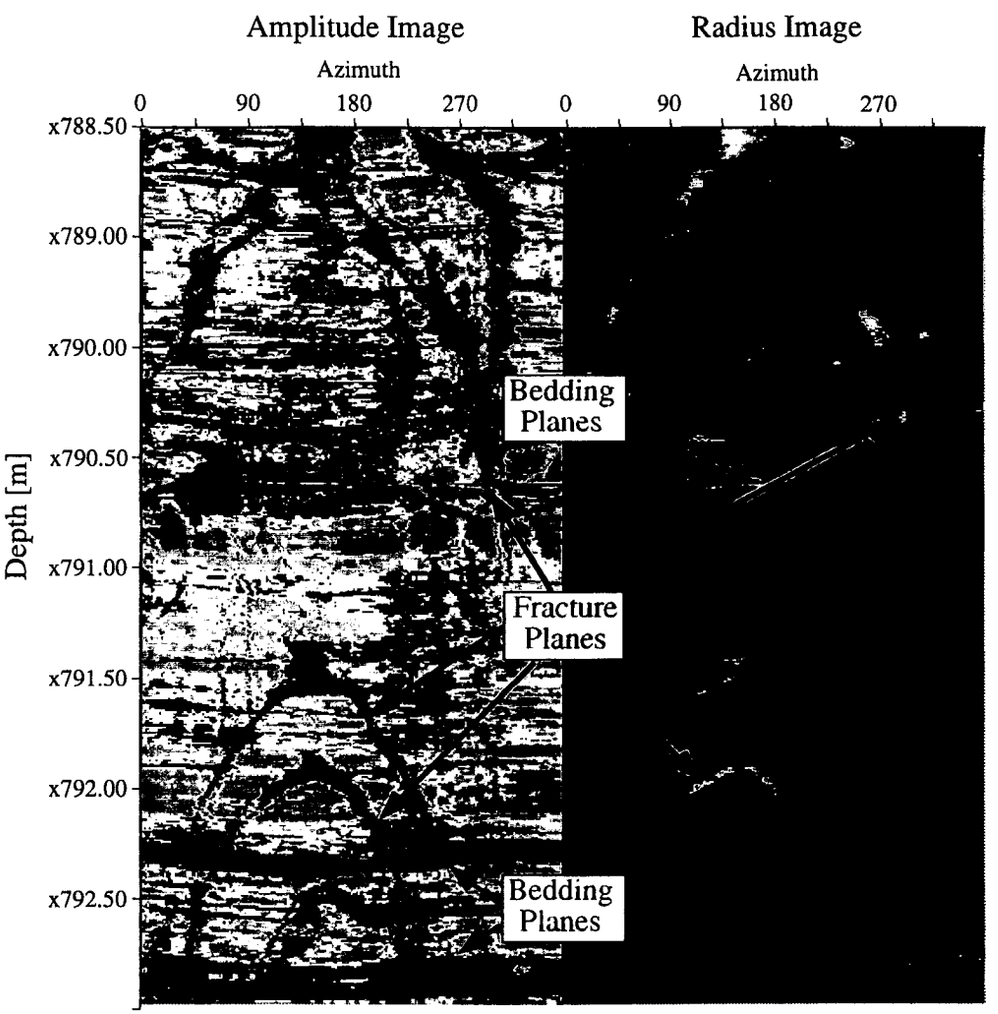

Figure 2.13: Representative BHTV image of Well D. Left: Acoustic wave amplitude image, where orange and purple correlate with highest and lowest amplitudes respectively. Right: Corresponding acoustic wave travel-time image converted to borehole radius, where purple/blue are smallest and yellow is largest radius. Black arrows point at representative steeply dipping fracture; red arrows point at bedding planes.

Sisquoc Formation. The fracture orientations observed in the Monterey Formation in this well are quite different from the three offshore wells in the sense that they are not obliquely or perpendicularly oriented to the local S_{Hmax} direction but rather parallel with primarily moderate to almost vertical dips striking to the NE. Structural interpretation of seismic and well-log data by Namson and Davis (1990) in the Orcutt field - the surrounding area of well D - shows the presence of the steeply dipping NE-trending, high angle Orcutt fault. The authors interpreted this faults as a normal growth fault, active during the Miocene and early Pliocene. In the late Cenozoic, this fault has experienced a period of slight reactivation as a thrust fault in association with the formation of the Orcutt anticline, which strikes NE to E at the location of well D. It is feasible, that the subset of steeply dipping and S_{Hmax}-parallel striking mode I fractures observed in this well are either structural relics associated with the transtensional faulting during the Neogene or be a manifestation of the bending processes in the sedimentary layers associated with folding in the current transpressional stress regime. Both mechanisms for fracture formation are well documented in the literature (e.g., Stearns and Friedman, 1972). In both cases, I would expect Mode I fractures to form parallel to the locally NE-striking Orcutt Fault and Orcutt Anticline. Since I only observe these fractures in the Monterey Formation (Figure 2.12) - the Sisquoc Formation above shows fracture attitudes that are different (i.e., moderate dips between 30° and 60° in south-easterly directions) - the former interpretation appears to be somewhat more plausible. However, it would be then merely fortuitous that the strike of the Mode I fractures is parallel to the current S_{Hmax} direction.

While the pattern and style of deformation in the study area is undoubtedly complex, the presence of earthquakes (Figure 2.1) is clear proof of ongoing faulting in the Santa Maria Basin region. In addition, I found evidence for recent slip along fracture and bedding planes in the BHTV images analyzed for this study. Figure 2.14 presents local breakout rotations in well C, that are associated with shear motion along small-scale faults. Shamir and Zoback (1992) and Barton and Zoback (1994) discuss in detail the evolution of these local rotations. Because of their short wavelength (< 1 m), I believe that these rotations are drilling induced local slip-events caused by bottom hole stress concentration or in response to increased pore fluid pressure around the wellbore during excess pumping while drilling (Shamir and Zoback, 1992). I think, this observation implies that many of the fracture and bedding planes are in fact potential slip surfaces (i.e., potentially active in the current stress field) and minor disturbances to the local stresses, such as changing fluid pressures while drilling, are sufficient to trigger small-scale rupture along these planes. Hence, the breakout rotations in the vicinity of the planes that slipped are a manifestation of the rupture-related local stress-drop and stress field change.

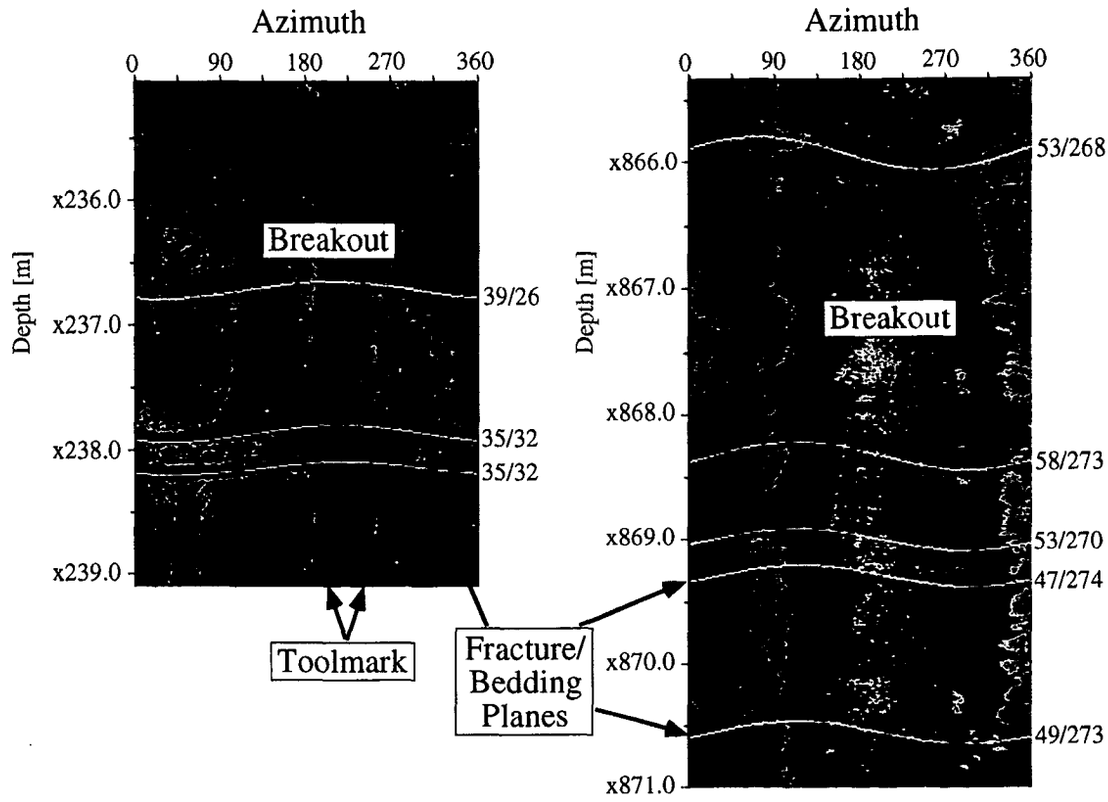

Figure 2.14: Breakout rotations caused by local slip along small-scale faults (i.e., bedding or fracture planes) that intersect well C (left and right images present two depth intervals within the Upper Calcareous Siliceous Member of the Monterey Formation and uppermost Point Sal Formation, respectively. They are the same type of unwrapped wellbore images as in Figure 2.3. Note the bending of breakouts as they approach the sinusoidal planes (highlighted as white lines). The left image illustrates how breakouts rotate and then vanish as they approach the upper fracture plane (x666.8 m), which is a result of slip related stress drop below the rock strength. The two black stripes running vertically through the image are tool marks caused by the drilling process; note, they do not obscure the breakouts or slip planes of interest. The right image shows various depth locations (e.g., x867.25 m, x867.75 m, or x868.0 m; white sinusoidal lines are not displayed), where breakout rotations occur without discernible fracture planes. These rotation were likely caused by faults that were not imaged by the BHTV-tool. The slip planes are annotated by two sets of numbers (e.g., 39/26), which denote dip and dip azimuth, respectively.

To elaborate further on the idea of potentially active fracture and bedding planes, I generated three dimensional Mohr diagrams (shear vs. effective normal stress normalized by the vertical stress) for the population of bedding planes (Figure 2.15A) and fractures (Figure 2.15B) imaged in each of the four wells. The purpose of these diagrams is to identify the planes, which have sufficient shear stress resolved in the current stress field, such that they could potentially slip. The diagrams were constructed by assuming two different cases for stress magnitude for comparison. The first case is

$$\mathbf{R} = \frac{\mathbf{S_2 - S_1}}{\mathbf{S_3 - S_1}} = 0.5 \qquad \text{Eqn. 2.3}$$

where $S_3 = S_v$, which is consistent with the results obtained from the earthquake stress inversion analysis discussed above. The second case is

$$\mathbf{R} = \frac{\mathbf{S_2 - S_1}}{\mathbf{S_3 - S_1}} = 0.9 \qquad \text{Eqn. 2.4}$$

to account for values I would usually expect in transpressive tectonic provinces (strike-slip/ reverse faulting), where $\mathbf{S_{Hmax} > S_{hmin} \cong S_v}$. To construct these plots, I assumed that preexisting faults are optimally oriented for failure as the ratio of shear to normal stress acting on their surfaces is close to a critical value beyond which rupture occurs (Byerlee, 1978; Jaeger and Cook, 1979). To compute the gradient of the maximum principal stress, I assumed a coefficient of friction of 0.8 (Byerlee, 1978) and hydrostatic pore pressure (which was observed). Similar to Barton et al. (1995), a portion of the fracture planes in each well plot within the failure lines, implying that these planes are potentially active in the current stress field and are likely to rupture. Intriguing, however, is the fact that the potential activity not only seems to apply to fractures (right sides in Figure 2.15), but also to bedding-parallel planes (left sides in Figure 2.15) since many of them are also optimally oriented for shear failure within the current stress field. In fact, the planes presented on the right image in Figure 2.14 were interpreted as bedding according to the dipmeter data used to distinguish between bedding and fractures planes; the ratios of shear to normal stress resolved on these bedding-parallel (Figure 2.14, right) and fracture (Figure 2.14, left) planes range from 0.54 to 0.75 for R=0.5 and from 0.66 to 0.75 for R=0.9, which indeed shows that they are potentially active in the current stress field. This observation further highlights the importance of bedding plane parallel slip surfaces in active deformation processes in this region, as suggested by Narr (1991). In the offshore wells (A - C), the poles to the critically stressed planes (bedding and fractures), which plot above the 0.6 failure line, are generally oriented from oblique to perpendicular to the maximum horizontal principal stress direction (S_{Hmax}) with moderate dips (see stereographic projections in Figure 2.15). I believe, that these features represent potentially active reverse and strike-slip faults. In the onshore well D, critically stressed planar features are pre-

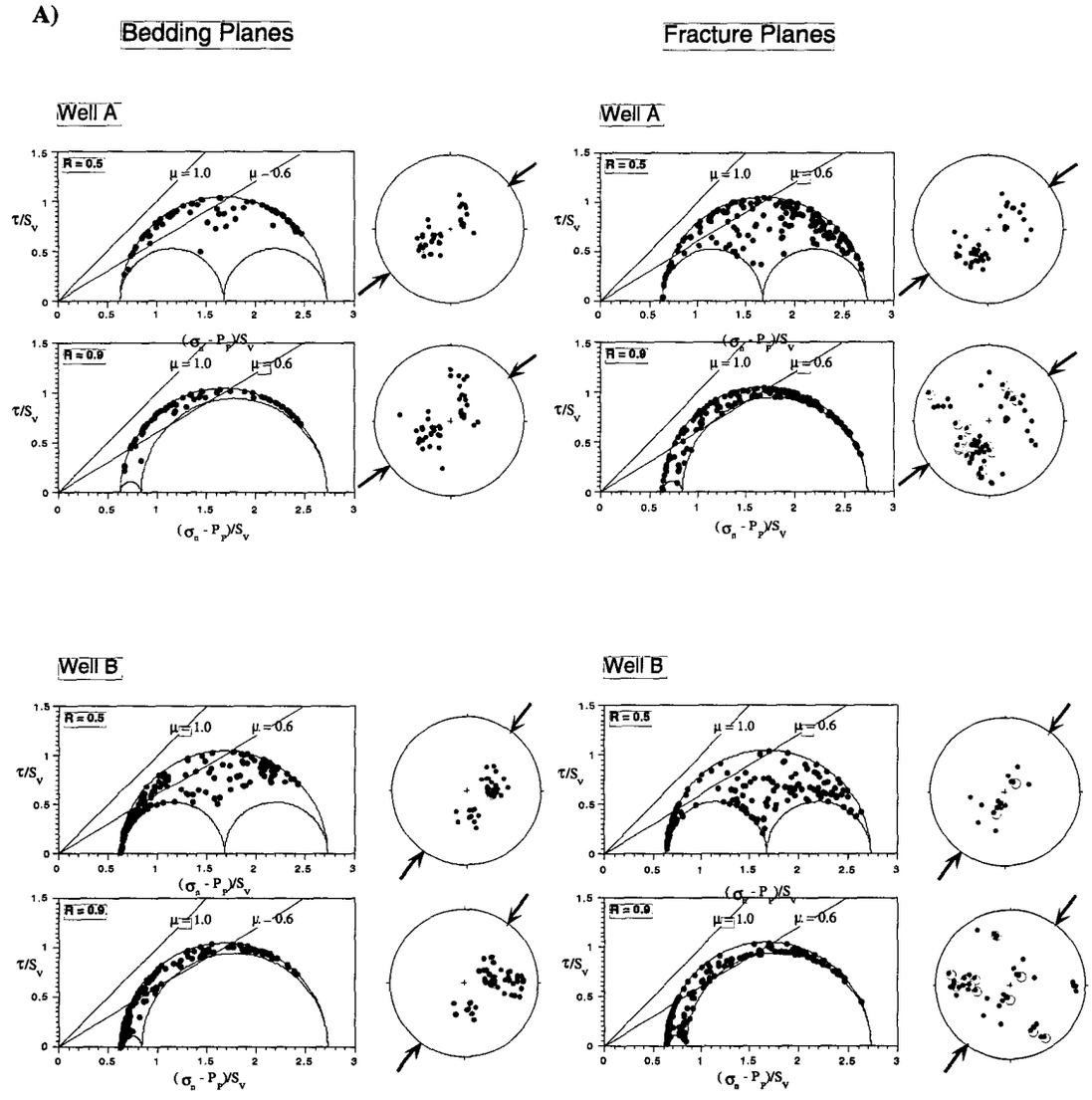

Figure 2.15: Normalized shear versus effective normal stress for all planar features (refer to Jaeger and Cook, 1979, p. 28, for details of construction of these diagrams); Coulomb failure lines (black straight lines) for two different coefficients of frictions μ are representative for most crustal rocks. The diagrams show bedding (left) and fracture planes (right) separately for two different scenarios: i) R = 0.5, ii) R = 0.9. Lower-hemisphere stereographic projections to the right of each Mohr diagram present poles to critically stressed fracture or bedding planes. Black arrow pairs denote S_{Hmax} direction as found from BHTV analysis in each well. A) Wells A and B. B) Wells C and D.

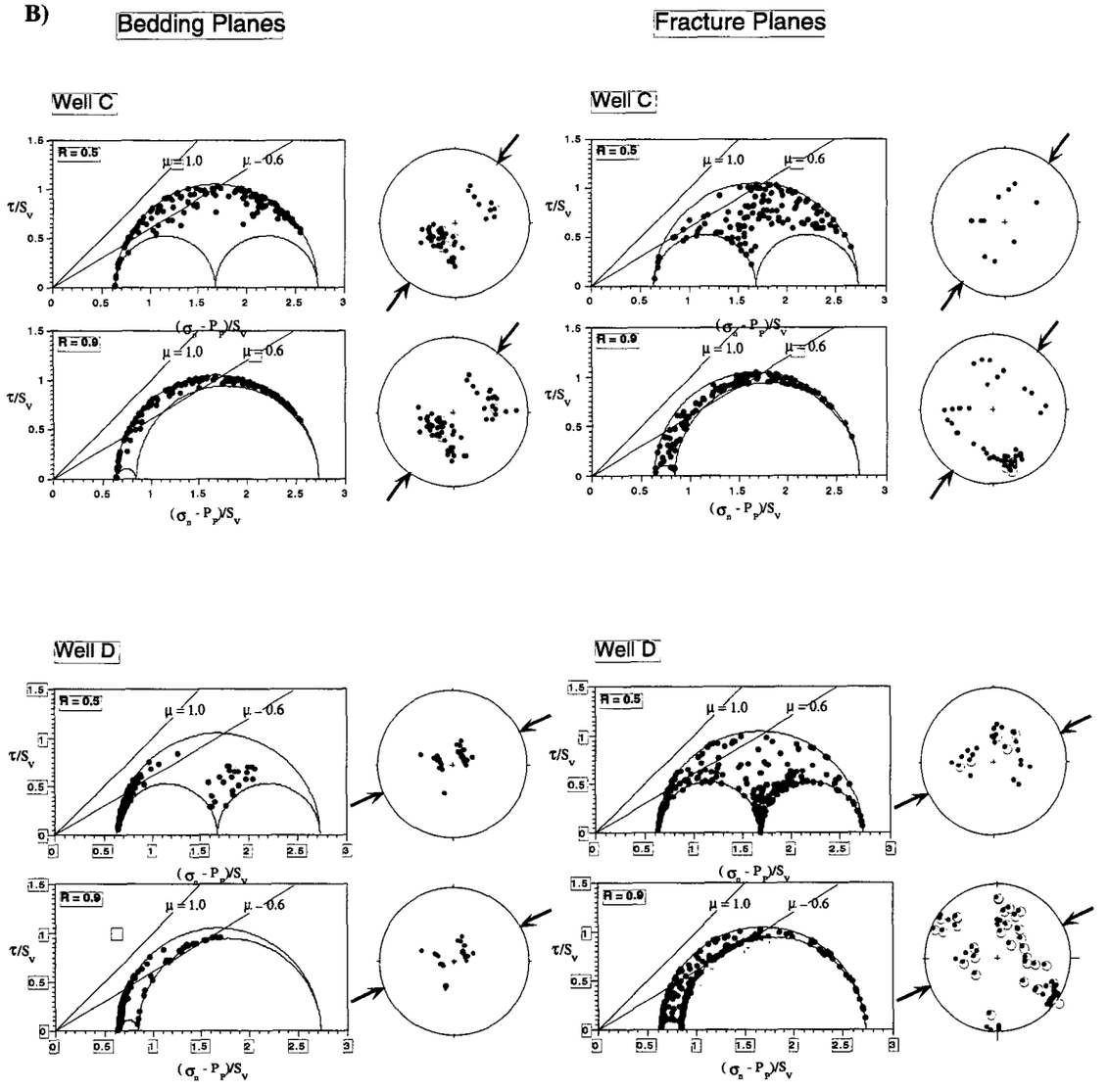

Figure 2.15: Continued.

dominantly oriented oblique to S_{Hmax} with mostly sub-horizontal to moderately steep dips. The population of these planes in the well has different orientations than the steeply dipping and S_{Hmax}-parallel striking fractures discussed above; only for R=0.9 are a subset of these fractures with a specific range of azimuths potentially active. It is likely that this observation is further evidence for the currently passive nature of these Mode I fractures, which were formed during the Neogene, while fractures with shallower dips and S_{Hmax}-oblique strikes are more favorably oriented for failure in the current stress field.

Comparing both scenarios of Mohr diagrams for any given well (Figure 2.15), one

notices that the number of critically stressed planes is larger when R = 0.9 (transpressive stress regimes in which $S_2 \sim S_3$), because the lower bound stress circle plots above the failure line. Although the orientation of these planes is more dispersed, the general direction – from oblique to perpendicular to S_{Hmax} – observed in case A (R = 0.5) still prevails. Dip angles, however, appear to be mostly moderate. This comparison of both scenarios implies that the result from the earthquake stress inversion analysis, although different from my expectations, does not obscure my interpretation of the occurrence and orientation of potentially active faults within the current stress regime.

2.7 Relation to fluid flow

As mentioned above, the Monterey Formation has very low matrix permeability and fractures are crucial for providing pathways for oil production. This issue has been frequently addressed in outcrop and well studies that discuss both qualitatively and quantitatively the occurrence and orientation of fractures most likely involved in fluid flow (e.g., Sadler, 1990; Narr, 1991; Crain et al., 1985; Isaacs, 1984). For my study, drill stem test (DST) data and information from mudlog and core analysis reports are used in conjunction with the fracture analysis to investigate the relationship between fluid migration paths and the current stress field.

DST data from various depth zones within the BHTV data analysis intervals were provided for two of the offshore wells - A (Figure 2.16A) and C (Figure 2.16B). In well A, seven tests determined formation permeability successfully, whereas only two test values are reported in well C. Formation permeabilities from DST tests do not provide a means of pointing out individual fractures and their permeability values; rather, they give the average permeability of the whole DST interval. Figures 1.16 shows depth versus permeability of the relevant DST tests (highlighted in gray). These are correlated with lower hemisphere stereonet representations of poles to fracture and bedding-parallel planes (in Figure 2.16 stereonets on the left show all planes, while the stereonets on the right focus solely on critically stressed planes) in each interval. Unfortunately, DST data are not perfect indicators of formation permeability and one can only use them as first order approximations (lost circulation material or acid added to the drillmud can mask the true formation permeability). However, I nonetheless believe that these data indicate generalized patterns between fluid flow and the distribution of fractures and bedding-parallel features.

DST permeability in well A (Figure 2.16A) is quite low within DST-interval 8 (0.1 mD) (Siliceous-Shale member); although the test interval is thick (more than 200 feet), the frac-

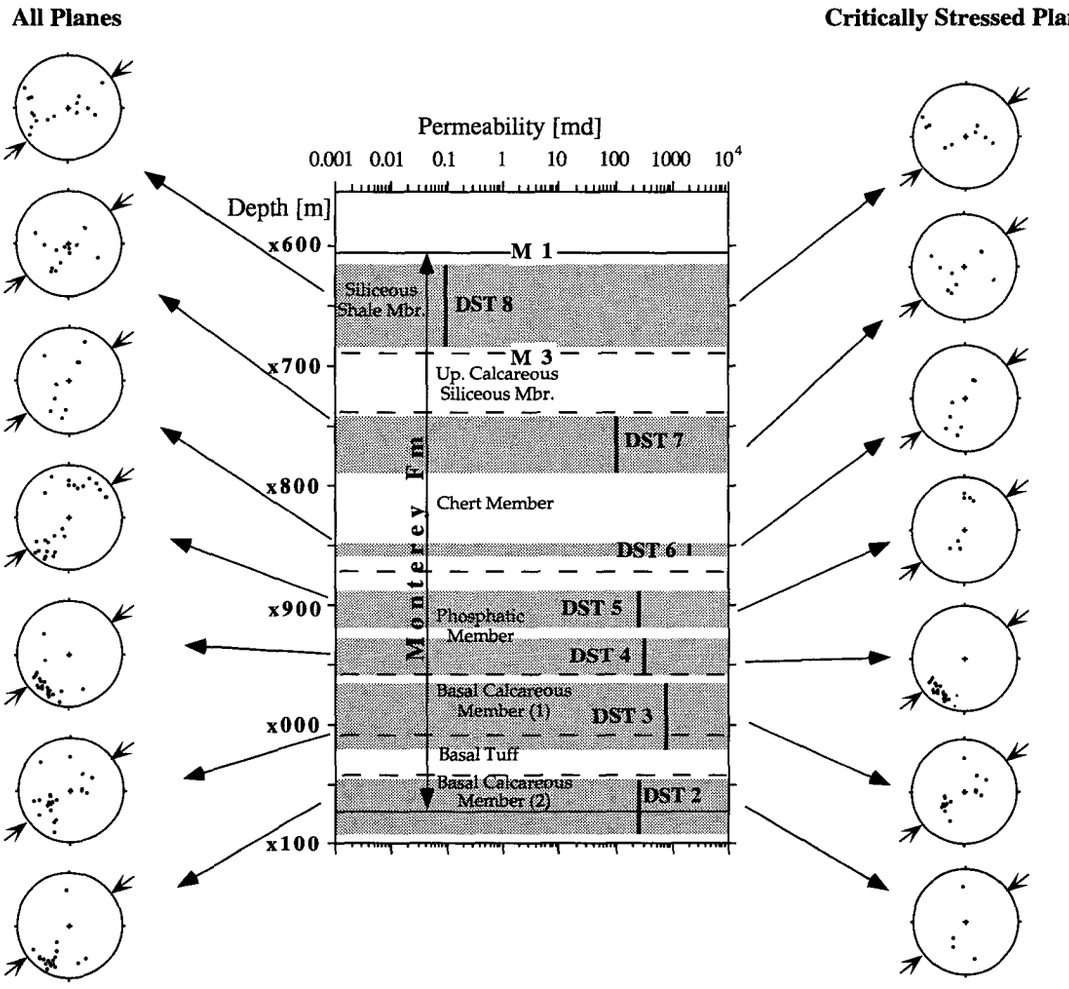

Figure 2.16: Formation permeability obtained from drill stem tests (DST) compared with lower hemisphere stereonet projections of poles to fracture and bedding-parallel planes, as in Figures1.10 and 1.12, for all planes (left) and only critically stressed planes (right) for A) well A and B) well C. Gray zones bound relevant DST intervals. Black arrows indicate S_{Hmax} direction obtained from breakout analysis in each well. Note that formation permeability varies over four orders of magnitude.

ture and bedding-parallel planes in this interval do not seem to contribute to fluid flow. In contrast, lower in the well within the Chert, Phosphatic, and Basal Calcareous members (DST-intervals 2 through 7), high permeability values are observed (100 - 2,100 mD). It is striking that DST 6, with the smallest depth coverage and the lowest fracture and bedding-parallel plane population, shows the highest permeability (2,100 mD), which is roughly four orders of magnitude larger compared to DST-interval 8. This suggests that only a few or even single planar features may be the sole responsible contributors to fluid migration in certain depth zones. In well C, permeability values between both DST tests vary by over an

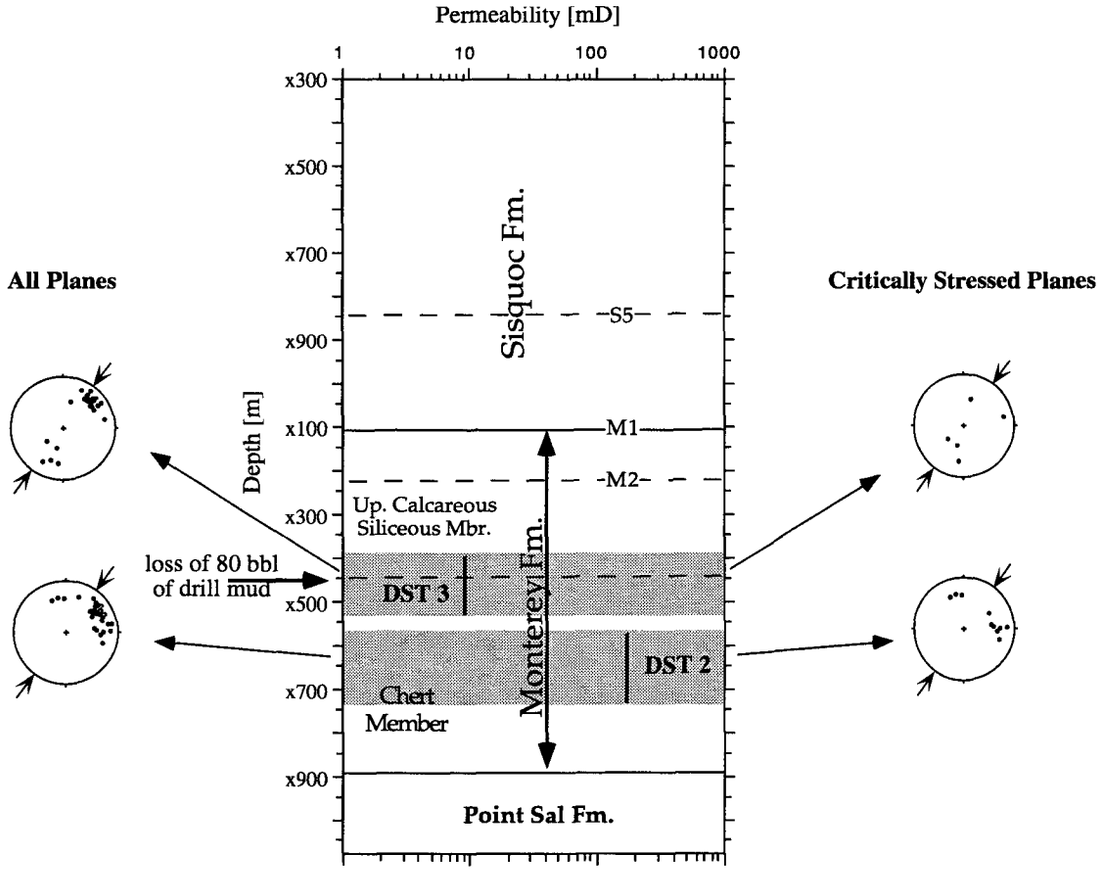

Figure 2.16: Continued.

order of magnitude (Figure 2.16B). DST 2 was conducted within the Chert member yielding 170 mD, whereas the DST 3 interval is at the transition between Upper Calcareous Siliceous and Chert members, showing 9 mD as the formation permeability.

In all DST depth intervals, most fracture and bedding-parallel planes strike perpendicular or oblique to S_{Hmax} and have moderate to steep dips, as indicated by the stereonet projections accompanying each DST result (Figure 2.16). Clearly, not only fracture planes are important as permeable fluid conduits, but I must also consider bedding plane parallel features. In well C (Figure 2.16B), comparison of orientations shows that more planes (fractures as well as bedding-parallel planes) are critically stressed in the lower interval (DST 2) than in the upper (DST 3). Referring to Barton et al. (1995), I think this observation may imply that in the Monterey Formation, critically stressed shear planes are responsible for fluid flow. Inferring from my discussion above, I can conclude that these are either reverse or strike-slip faults. This conclusion includes bedding-parallel planes, since they are also favorably oriented for failure in the current stress field (Figure 2.15).

Focusing on well A (Figure 2.16A), I observe that permeability values are either similar or differ by one order of magnitude, with the exception of DST 8, which differs by four orders of magnitude. In the short DST-interval 6, where the highest permeability was observed, nearly all fracture and bedding-parallel planes are critically stressed. This zone includes the lowermost part of the Chert Member, where the fracture planes dip most steeply and persistently strike sub-perpendicular to S_{Hmax}. Bedding planes in this interval have moderate dips and are also oriented nearly orthogonal to the principal maximum horizontal stress direction. These observations suggest that reverse faults provide highly permeable fluid migration paths in this depth interval of the Monterey Formation. A similar interpretation may also apply to DST-interval 3 (second highest formation permeability), where most fracture and bedding-parallel planes are also critically stressed. However, the fracture population in this depth zone of the well (Basal Calcareous Member) is much less organized in orientation than in the DST-interval 6, which may explain the reduced permeability value. The reason for lower permeabilities within the other test intervals (DST 2, 4, 5, 7, and 8) could be the smaller percentage of critically stressed planes and their increased scatter in dip and orientation.

To explain the low permeability value for DST 8 in well A (Figure 2.16A) – despite the fact that fracture and bedding-parallel planes are well oriented for failure in the current stress field – I must discuss another important factor controlling permeability. Gross (1995), Behl and Garrison (1994), Isaacs (1984), Pisciotto and Garrison (1981), and others have shown that the mechanical behavior of the Monterey Formation is a function of lithology. Soft rocks, such as shales or opal-A, deform more plastically; hard rocks, such as dolostones or cherts, are brittle. Hence, the ability of softer and more ductile shales to keep fractures open as a means to provide fluid migration paths is potentially reduced compared with more brittle rocks.

In addition to the DST data, results from core analysis of well C within the Upper Calcareous Siliceous Member and the Chert Member describe the presence of many hairline cracks, which show fresh oil stains. These small, Mode-I joints obviously could not be detected by the borehole televiewer due to its limited resolution and the quality of data recorded in these wells. The question of whether larger and detectable fractures or small hairline joints act as major fluid conduits may be evaluated by using information from mudlogs for this well. Near the bottom of the Upper Calcareous Siliceous Member, where two steeply dipping fractures striking perpendicular to S_{Hmax} (presumably thrust faults) were detected, 80 bbl of drillmud were lost during drilling (Figure 2.16B). Intuitively, it is unlikely that small hairline cracks controlled by bedding planes are responsible for this instantaneous loss of circulation fluids. Moreover, the core analysis report describes one

foot wide zones of highly fractured rubble in the upper chert member striking perpendicular to S_{Hmax}. These were interpreted as fault gouge. Large features such as these are imaged by the borehole televiewer, which appears to match my observations. These sources of information further suggest that larger-scale faults predominantly contribute to fluid flow.

In contrast, information about apparent fracture aperture obtained through the BHTV image analysis does not provide any further explanation of permeability differences over orders of magnitude in different depth intervals. Obviously, the aperture values do not necessarily account for hydraulic apertures needed for substantial amounts of fluid flow.

2.8 Conclusions

Breakout analysis from borehole televiewer data in four wells located in the producing fields of the Santa Maria Basin (on- and offshore) shows a NE orientation for the maximum principal horizontal stress, S_{Hmax}, which is consistent with regional stress data and NW-SE trending fold axes in central California. In addition, results from focal plane inversion analysis, which yielded a similar stress orientation, indicates that this consistency persists throughout the seismogenic zone of the crust. Analysis of fractures in these wells, in contrast, reveals that fracture orientation and frequency vary markedly within each well and laterally among them. In each well, fractures can be divided into distinct subsets on the basis of fracture frequency and predominant strike and dip directions. These subsets of fractures correlate with changes of lithology, indicating that the degree of fracturing is related to tectonic history, diagenesis, and structural variations. Using dipmeter data, I separated bedding-parallel planes from fractures and faults within the three offshore wells and analyzed both types of planes independently from each other. Three dimensional Mohr analysis of these planar features suggests that a large percentage of both bedding planes and fracture and fault planes are critically stressed (i.e., they are favorably oriented for failure within the current stress field). Thus bedding-parallel slip plays an important role in active deformation processes within this region. According to their orientation and dip-angles, these planar features are potentially active reverse or strike-slip faults. In fact, I observed local breakout rotations in the wells, that correlate with fracture and bedding planes, providing kinematic evidence for recent shear motion along these planes. In addition, earthquake activity in the region of the study area is a further demonstration for active shear deformation and faulting processes. Only in one well, the onshore well D, do steeply-dipping fractures strike parallel to S_{Hmax}, implying that they are Mode I extension fractures.

To establish relationships between fracture orientation and fluid flow, I used drill stem

test data (DST) results provided for two of the offshore wells. These data showed evidence that formation permeability is enhanced at depth intervals with brittle lithologies and critically-stressed fracture and bedding planes that strike perpendicular or oblique to S_{Hmax}. This result implies that the strike-slip and reverse faults penetrated by the wells play an important role in providing fluid migration paths in these low-permeability rocks.

2.9 Acknowledgments

I wish to thank Tom Zalan of the Chevron U.S.A. Production Co. for providing the offshore well-data, Unocal Corporation for providing the data on the onshore well, and Marcia McLaren from Pacific Gas and Electric Company for providing the earthquake focal mechanisms used in the stress inversion analysis. I appreciate the comments and helpful discussions from Daniel Moos, Steve Graham, and Lev Vernik. This research was financially supported by the Stanford Rock & Borehole Geophysics Project (SRB).

CHAPTER 3

LEAST PRINCIPAL STRESS AND PORE PRESSURE IN SAND RESERVOIRS OF THE SOUTH EUGENE ISLAND 330 FIELD, GULF OF MEXICO

3.1 Abstract

From the South Eugene Island 330 (SEI 330) field, offshore Gulf of Mexico, I compiled and analyzed pore pressure data and least principal stress measurements from minifracs in fracture completed reservoirs. The measurements show considerable variability in pore pressure (P_p) and minimum principal stress ($S_3 = S_{hmin}$). S_{hmin} values range from half the overburden (S_v) to roughly 99% of S_v. Pore pressures vary from sub-hydrostatic to nearly 95% of lithostatic. Because the majority of the minifracs were conducted in reservoirs with appreciable production induced depletion, the measured stresses need to be corrected. I applied two methods to correct for the depletion effect: (i) a poroelastic model based on laboratory derived Poisson's ratio (ν) of 0.3, and (ii) the effective reservoir stress path (i.e., $A = \Delta S_{hmin}/\Delta P_p$) with a value of 0.81 for one of the reservoir sands.

In general, whether I consider observations from undepleted sands or sands with appreciable pressure declines and stress changes, the resulting pore pressures and stresses show effective stress ratios, K, that scatter significantly and do not correlate with previously published fracture gradient models for this area. The lower-bound value of K is 0.33, which corresponds to the expected value for Coulomb failure for a coefficient of friction of 0.6 in normal faulting environments. However, in some sands K approaches unity, thus indicating an essentially isotropic stress field. Hence, the data indicate a highly variable state of stress that cannot be simply related to depth or pore pressure, but appear to reflect a complex interaction between deformational processes and material properties. Correlating K with sonic and gamma ray logs reveals only a very weak dependency of K on sonic Vp, which could be suggestive of time dependent creep beavior as observed in laboratory measurememnts.

Analysis of the pressure surveys show uniform pore pressure reduction over time for most reservoir compartments. This indicates hydraulically contiguous compartments that correlate with seismically interpreted fault blocks. In the deepest reservoir sand, however, I observe a non-uniform pressure reduction behavior within individual fault blocks implying more complex compartmentalization possibly on a sub-fault block scale.

3.2 Introduction

For many hydrocarbon producing fields around the world, there exists a large body of publications that attempts to predict fracture gradients as a function of depth to drill optimally stable and safe wellbores. In general, a vast quantity of different types of data (e.g., formation integrity tests, leak-off tests, loss-circulation reports) from different

locations is being compiled by various authors to derive and predict a regional fracture gradient trend. The papers published for the Gulf Coast (e.g., Matthews and Kelly, 1967; Althaus, 1977; Pilkington, 1978; Brennan and Annis, 1984) provide a good example for the different types of least principal stress compliations and fracture gradient predicitions that may exist. In addition, there has been growing evidence recently that hydrocarbon accumulation and migration are closely linked to the tectonic stress field. Gaarenstrom et al. (1993) recognized for the Central North Sea that retention capacity and trapping integrity of individual pressure cells are controlled by the bounding faults and the local in-situ stress field. Similarly, Grauls and Baleix (1994) attributed the efficiency of hydrocarbon transfer between pressure compartments along and across faults in a sedimentary basin in South-East Asia to be a fundamental function of in-situ stresses. These examples point towards a potentially close relationship between pore pressure and stress. Therefore, accurate determination of pore pressures, in-situ state of stress, and rock properties is critical for addressing engineering issues such as borehole stability and sand production as well as for understanding dynamic constraints on hydrocarbon migration and fracture permeability.

In this study, I focus on pore pressure survey and fracture completion data from reservoir sands of the South Eugene Island (SEI) 330 field (see Chapter 1 for geologic background). Fracture completions have become popular in poorly consolidated sediments only in recent years; therefore, relatively little data of this kind exists. The availability of minifrac data from fracture completions and pore pressure history data from pressure surveys from the SEI 330 field provides an unique opportunity to accurately characterize in-situ least principal stresses and pore pressures in the hydrocarbon producing sand reservoirs. There are three clear advantages of this study over previous studies of this type in the Gulf coast region: (1) The least principal stress data I use come from minifracs conducted in sands whereas previous studies derived stress data from low quality leak-off tests that were predominantly measured in shales. (2) The stress measurements in my study were taken in the same reservoir sands in which pore pressures were measured whereas previous compilations often compare stress data from shales with pore pressure data from sands. (3) All of my data come from the same field (and often even the same well) whereas previous publications reflect regional compilations. Furthermore, pore pressure history data from numerous production wells allow me to quantify production related pore pressure reduction and associated stress changes. Since many of the minifracs were carried out in reservoirs sands that showed significant pore pressure decline, I anticipated associated stress changes due to poroelastic effects.

First, I compile all available data from the SEI 330 field. In reservoirs with substantial pressure decline, I then attempt to restore initial pore pressure and stress conditions. Subsequently, I compare the results with previously published fracture gradient models from the Gulf Coast. Finally, I try to correlate the observed state of stress and pore pressures with well-log data (i.e., sonic and gamma) to explain potential variability.

3.3 Stress and Pore Pressure Data

3.3.1 Minifractures

Twenty fracture completions from 17 production wells from both the minibasin and the footwall side of the SEI 330 field provide data on the least principal stress. Figure 3.1 shows a basemap of the field and locates the respective wells that were fracture completed. I used the pressure records from mini-fracture tests, which are conducted prior to the actual fracture treatment, to derive the bottomhole closure pressure. I considered this value to represent the magnitude of the least principal stress ($S_3 = S_{hmin}$) since it is obtained from the late stage pressure record after the well was shut-in and the pressure has bled off to the critical point where it can no longer keep the mini-fracture open (Figure 3.2). At this stage of the minifrac test, pumping has ceased and the fracture has propagated into the formation away from the hole. Thus, fracture initiation, near wellbore and fluid related friction effects have dissipated and the pressure should more or less reflect the current least principal stress in the reservoir. Closure pressure values are then derived from Horner and $\sqrt{t}$ -plots using the transient pressure responses recorded during the mini-fracture test. At least two values for closure pressure were generally obtained in one test, one for each method. In case an additional step-rate test was run, two more values for S_{hmin} were available. This enabled me to define upper and lower bounds for this parameter. Figure 3.3 exhibits an example of a pressure-time curve and a $\sqrt{t}$ -plot for one of the fracture completed wells in the footwall side of the main growth fault system. Table A1 (see Appendix) summarizes the data from the 20 minifrac tests.

Pore pressure values are generally measured before the minifracture test after perforation. As described in more detail below, I quality controlled these values with pore pressure history records, which were in fair to good agreement and required adjustments in 13 wells of up to 545 psi (see Table 1 below).

3.3.2 Pressure Surveys

A comprehensive data base of pressure surveys from over 80 production wells in the SEI 330 field was available for my study. The surveys were conducted over two decades of production history and closely monitor the production related pore pressure evolution throughout the entire SEI 330 field. From the beginning of their operations, pore pressure measurements have been taken periodically in individual wells and can be integrated into pore pressure histories for individual reservoir compartments. Analysis of this integrated data base allows me to calibrate pore pressures obtained from minifracs during fracture completions and to address issues related to reservoir compartmentalization and production

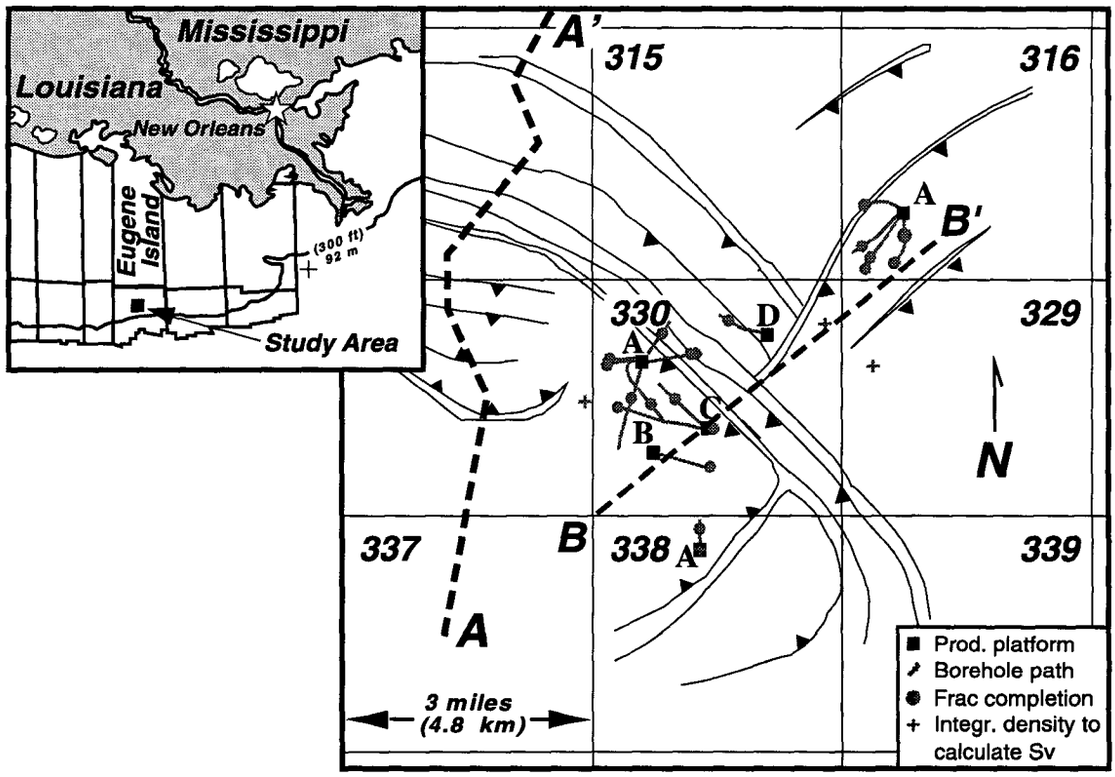

Figure 3.1: Basemap with trajectories of fracture completed wells (gray). The gray dots mark the exact location of the minifractures along the wellpaths (gray). Production platforms are shown as black squares labeled alphabetically for each field block. The gray crosses locate the four wells for which I integrated density logs to calculate overburden values, Sv. The map is a schematic structure map of the stratigraphic OI-1 sand level (see figure 1.4). The major north-west trending growth normal fault system bounds the minibasin, which is located on the hanging wall side. The black triangles point towards the relative down-thrown side of a normal fault. A-A' and B-B' mark the transect of the two cross sections in Figure 1.4.

induced pore pressure depletion. Because each well is shut-in for a certain period of time prior to the measurement, the production related local pressure depression around the well

can equilibrate to some extent and the resulting pore pressure value is a close lower bound to the real pore pressure in the reservoir at the time of the survey.

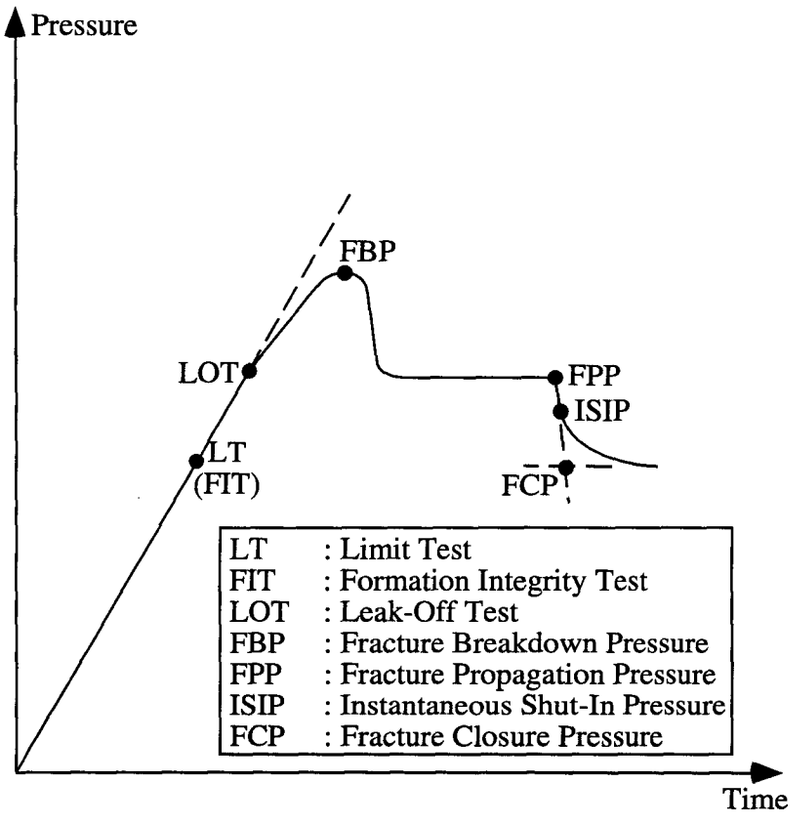

Figure 3.2: Bottomhole pressure versus time in a typical minifracture test (modified from Gaarenstroom et al., 1993).

Pore pressure data in an individual reservoir compartment need to be corrected to a common datum, because pressure surveys were carried out in multiple wells at varying depths. In order to accurately determine fluid pressures at a specific datum, precise knowledge of in-situ fluid density is critical. I integrated reservoir temperatures and API gravities from the pressure survey reports using formulas published by Batzle and Wang (1992) to calculate the in-situ, live fluid density (i.e., taking dissolved gas into consideration). Comparing my results with calculations carried out by Pennzoil, which used PVT analysis, showed extremely good agreement with errors in fluid density of 5% or less. When calibrating and adjusting pore pressures from minifrac tests during fracture completions, I used the most recent (relative to the date of the minifrac) pressure surveys from the same reservoir fault block. As shown in Table A1, pore pressures for the minifracs needed to be adjusted in the case of 13 wells. These adjustments were minor to fair in magnitude with a maximum value of 545 psi in case of the OI-1 FB-C reservoir. Figure 3.4

displays an example of pore pressure data from the LF sand in fault block B to illustrate the following: (i) pore pressure decline as a result of production (Figure 3.4A), (ii) how pore pressures derived from fracture completions were adjusted to those from pressure surveys (Figure 3.4A), and (iii) how pressure values corrected to a specific datum using the live oil density method compare to Pennzoil's pressure data (Figure 3.4B).

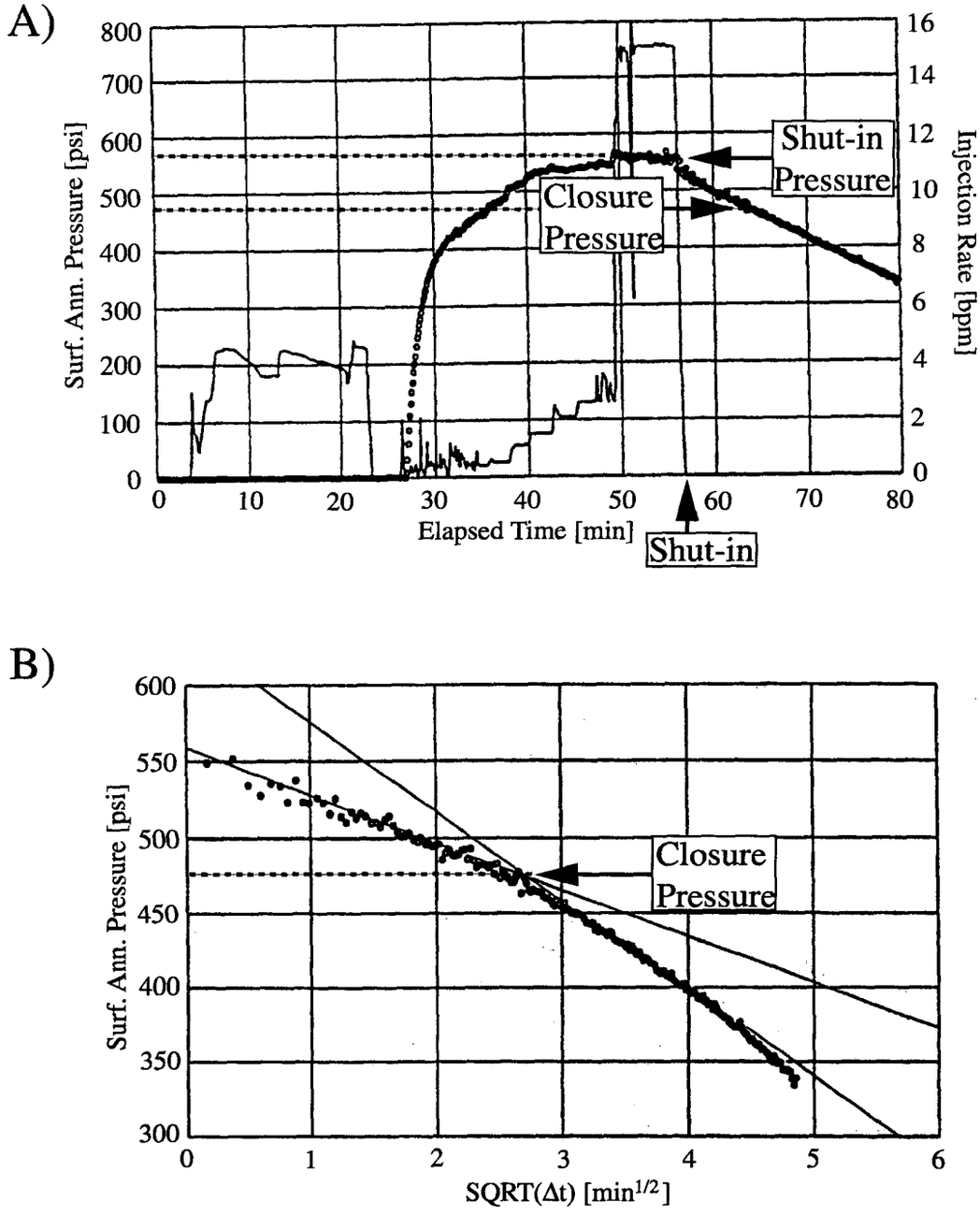

Figure 3.3: Minifracture in well 316/A-3ST displaying shut-in and closure pressures on (A) pressure-time curve and (B) $\sqrt{t}$ -time curves. Modified graphs from Pennzoil.

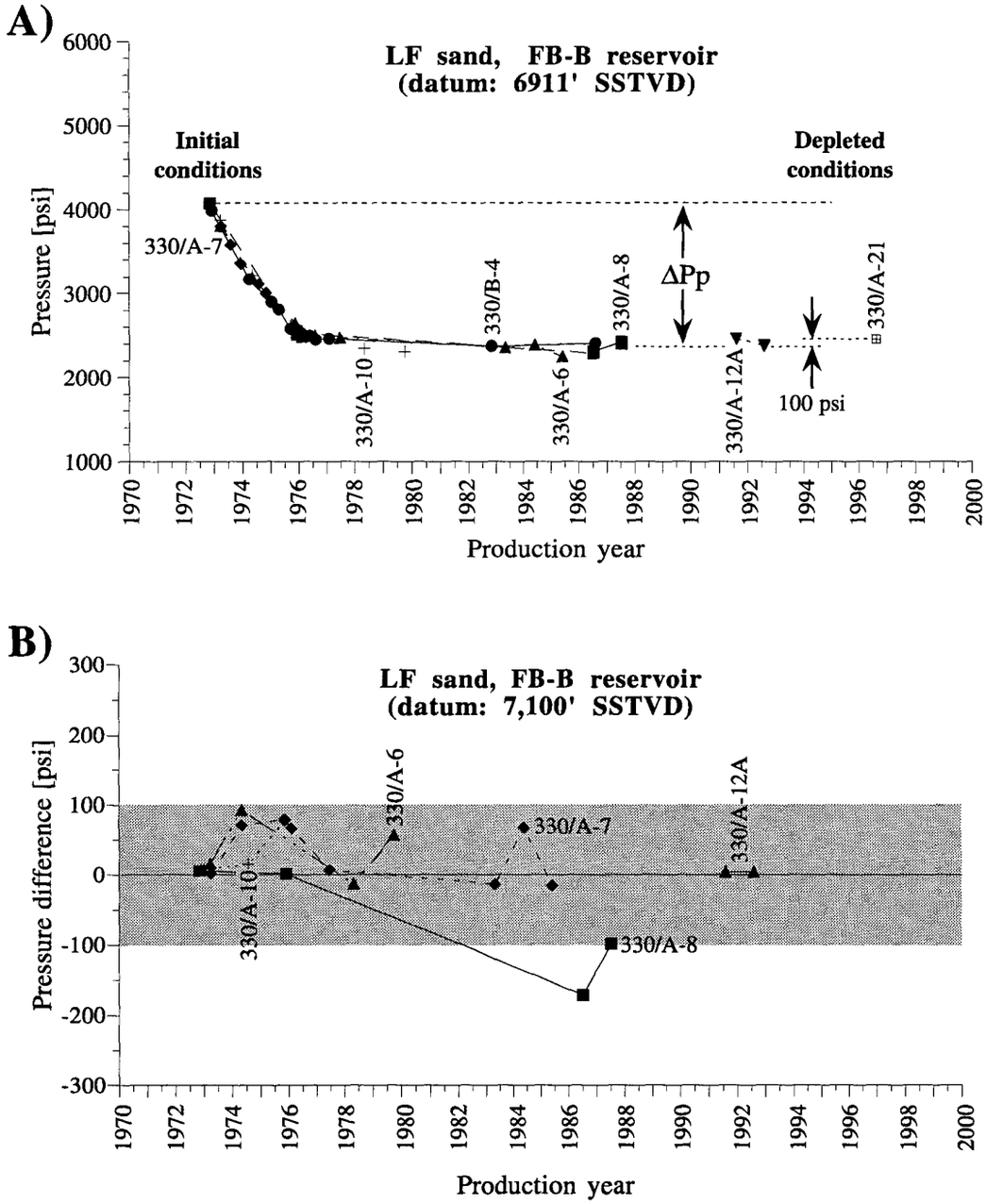

Figure 3.4: Pore pressure surveys from 7 productions wells in LF sand, FB-B reservoir. A) Pore pressure history showing pore pressure decline (ΔPp) due to production. The data were corrected to a datum of 6911 ft. SSTVD, which corresponds to the fracture completion depth in this reservoir. Notice the uniform pore pressure decline. The open box with the cross exhibits the pore pressure measured prior to the minifrac in well 330/A-22. This value is adjusted (by 100 psi as labeled) to the most recent pressure survey in well 330/A-12A carried out in 1992 (inversed, black triangle). B) Comparison of calculated reservoir pore pressures using the live oil density method with Pennzoil's pressure data (derived from PVT analysis). The gray box outlines a pressure difference of ±100 psi, which corresponds to an error of approx. 4%.

3.3.3 Overburden

Another requirement for this analysis is accurate knowledge of the overburden stress. The overburden stress was calculated using integrated density logs because I expected low overburden gradients in the SEI 330 field due to undercompaction and overpressure effects at depth. Four wells were chosen to represent the overburden gradient with depth (two from the minibasin side and two from the footwall side; see Figure 3.1). Figure 3.5 displays the calculated density gradients as a function of depth. In the depth range of interest (i.e., from

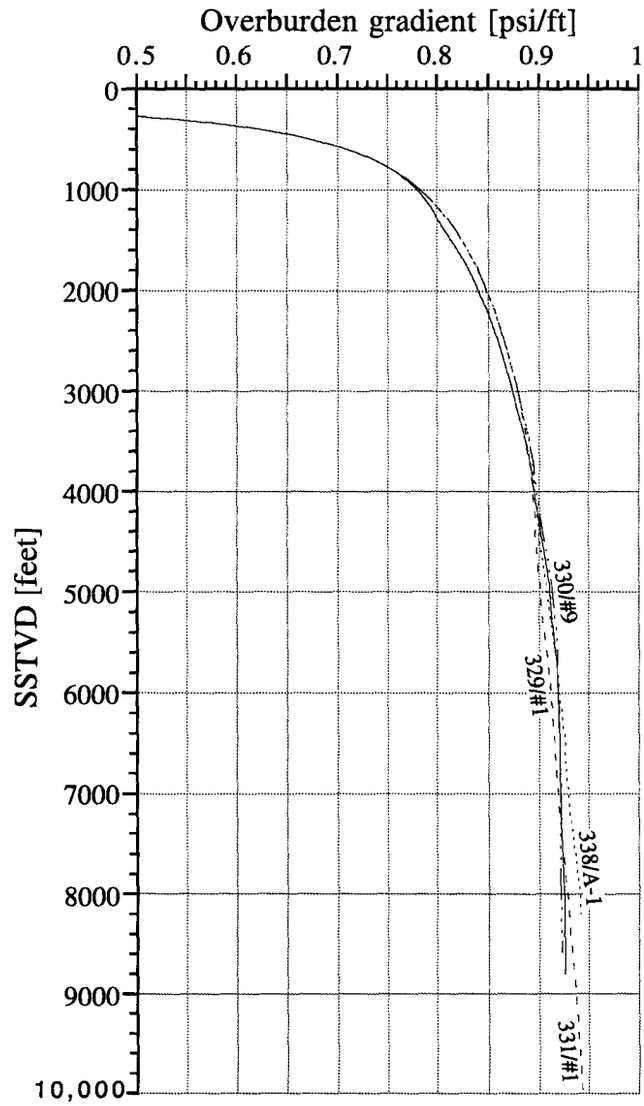

Figure 3.5: Overburden gradients for four wells used in to calculate the overburden (Sv) at fracture completion depths in the SEI 330 field. Note for comparison the often assumed constant gradient of 1 psi/ft.

4,800 ft. to 7,700 ft.) all four curves essentially overlay showing an average overburden gradient of approximately 0.919 psi/ft. This is considerably lower than the often assumed constant gradient of 1 psi/ft (e.g., Althaus, 1977).

3.4 Reservoir pore pressures and states of stress

3.4.1 Effect of production on pore pressures and least principal stresses

The values for pore pressure and S_{hmin} (Table A1) are displayed in Figure 3.6 as a function of depth and exhibit large variations. I attribute this observation to the fact that despite their spatial proximity within the same field (Figure 3.1), individual reservoir compartments with varying pressure and stress characteristics are complied in this graph. These compartments are either separated by normal faults or pinching out sand lenses within the basin proper (see cross-section in Figure 1.4). In general, the least principal stress varies from 66% to almost near lithostatic (i.e., 99%) and pore pressures range from

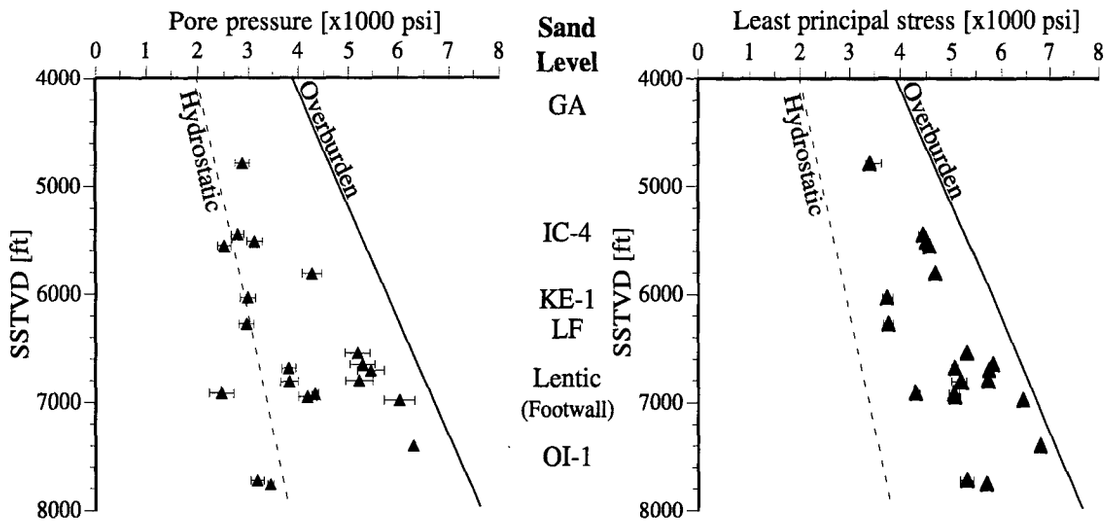

Figure 3.6: Average minimum principal stress, Shmin, (A) and average pore pressure (B) as derived from fracture completions. Error bars denote upper and lower bounds (often masked by symbol). For both plots the overburden was derived from integrated density logs. Hydrostatic pore pressure was calculated with a constant brine gradient of 0.465 psi/ft. The seawater depth in the field is 248 feet. The figure also displays the approximate depth of various sand levels (compare with cross-section, Figure 1.4).

sub-hydrostatic (i.e., 37%) to 95% of S_v. Hydrostatic or even sub-hydrostatic pore pressures correspond with low S_{hmin} values, while high pore pressures correlate with least principal

stresses that are close to the overburden. This apparent link suggests an intrinsic relationship between pore pressure and the least principal stress. Likewise, Flemings et al. (in prep.) observed in a nearby well of the SEI 330 field that with increasing overpressure the total stresses ($S_2 = S_{Hmax}$, $S_3 = S_{hmin}$) approach the overburden ($S_1 = S_v$) in a non-linear fashion while differential and effective stresses decrease. The increase of overpressure with depth is a common phenomenon in the Gulf Coast region because it reflects processes of rapid sediment loading and poorly drained conditions of alternating sand and thick shale sequences resulting in compaction disequilibrium (Dickinson, 1953; Traugott, 1997). Quite surprising, however, is the observation of hydrostatic or even sub-hydrostatic pore pressure conditions at depths of over 5,000 feet SSTVD. Because most of the wells were fracture completed only very recently in reservoirs that had been under production for up to 25 years, I believe that the pore pressures measured reflect depleted reservoir conditions at the time of fracture completion. Therefore, these pore pressures and stresses do not represent the reservoir's unperturbed (i.e., initial) state and require to be restored. I address the issues of compartmentilization, depletion behavior, and required corrections next.

3.4.2 Reservoir depletion

The pressure survey data available for this study allow me to investigate pore pressure histories for most producing reservoirs in the SEI 330 field. Therefore, I can address issues related to compartmentalization, depletion behavior, hydraulic reservoir communication across faults, hydrocarbon column heights, and production related pore pressure changes. In this section, I focus on the latter issue because it is important for identification of reservoir stress paths and restoration of the initial states of stress. All former issues are presented in detail in chapters 5 and 6 of this thesis.

The pore pressure surveys show that a large number of fracture completed reservoirs have experienced (partly significant) depletion due to intensive hydrocarbon production. The pressure transients of different reservoirs exhibit very different behaviors and appear to be a function of the stratigraphic level of the sand (see chapter 5). Figures 3.4A and 3.7A through C present four examples of characteristic transient pore pressure behavior in the SEI 330 field from three fracture completed reservoirs. The cross-section in chapter 1 (Figure 1.4) helps to locate their relative structural and stratigraphic positions. As indicated, the pressure values in each of the reservoirs come from various pressure surveys in different wells, hence, they were datum corrected to be able to compare them.

The KE-1 (Figure 3.7A) and LF (Figures 3.4A and 3.7B) sands are moderately overpressured ($0.62 < \lambda < 0.65$; Table A2) and show uniform pressure declines of approximately 700 psi and 2000 psi respectively. The late stage flattening at pressure levels

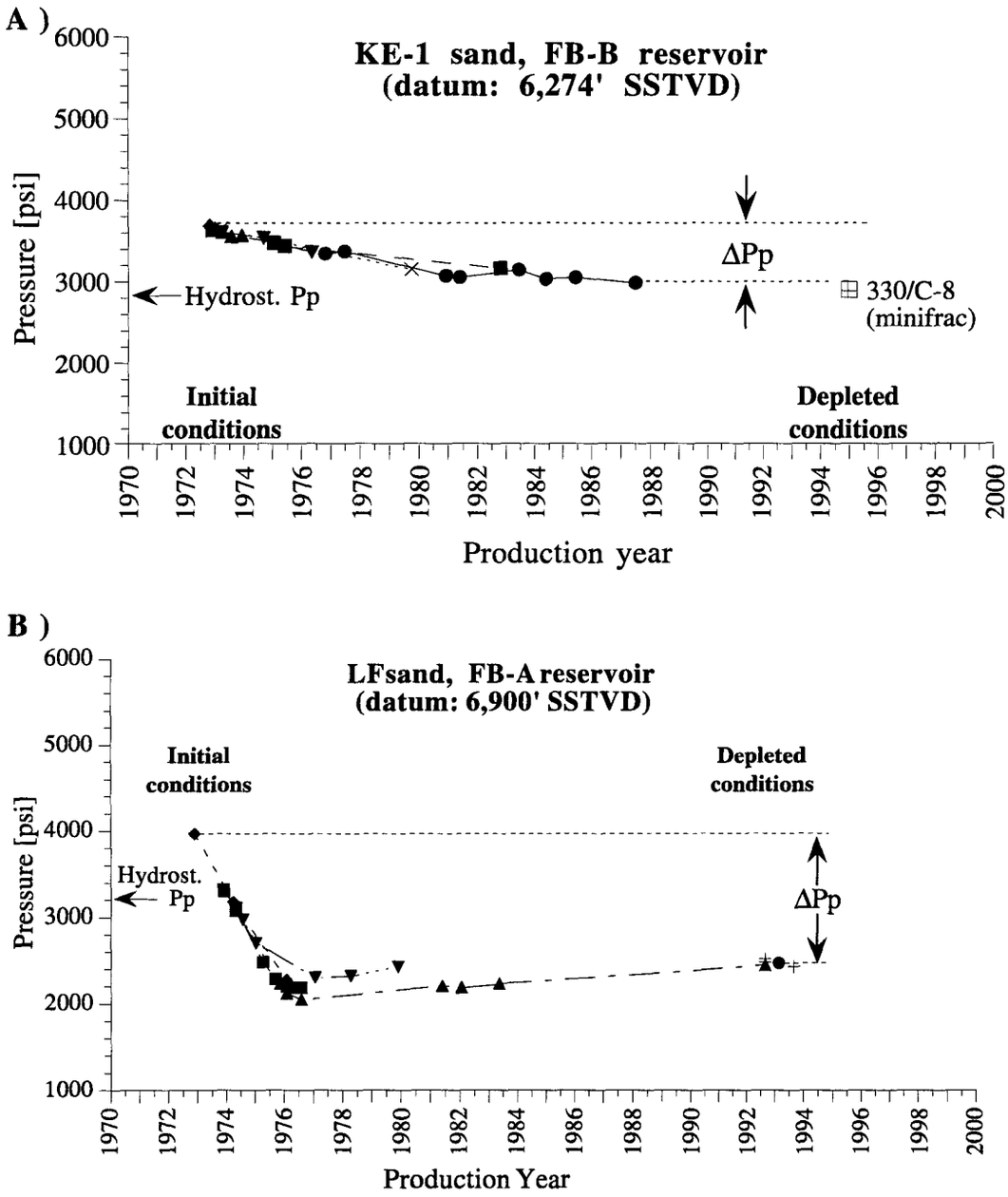

Figure 3.7: Pore pressure depletion in three different reservoir compartments of the SEI 330 field. The data in each of these examples were corrected to a specific datum (as indicated) to be able to compare pore pressures from different wells (displayed by different symbols). Pore pressures from corresponding minifracs are shown with open-crossed squares. The arrows at the depth axes indicate hydrostatic pore pressure (0.465 psi/ft) at the corresponding datum. A) KE-1 sand, FB-B reservoir from the minibasin side. B) LF sand, FB-A reservoir from the minibasin side. C) L-1 sand, FB-C reservoir from the footwall side.

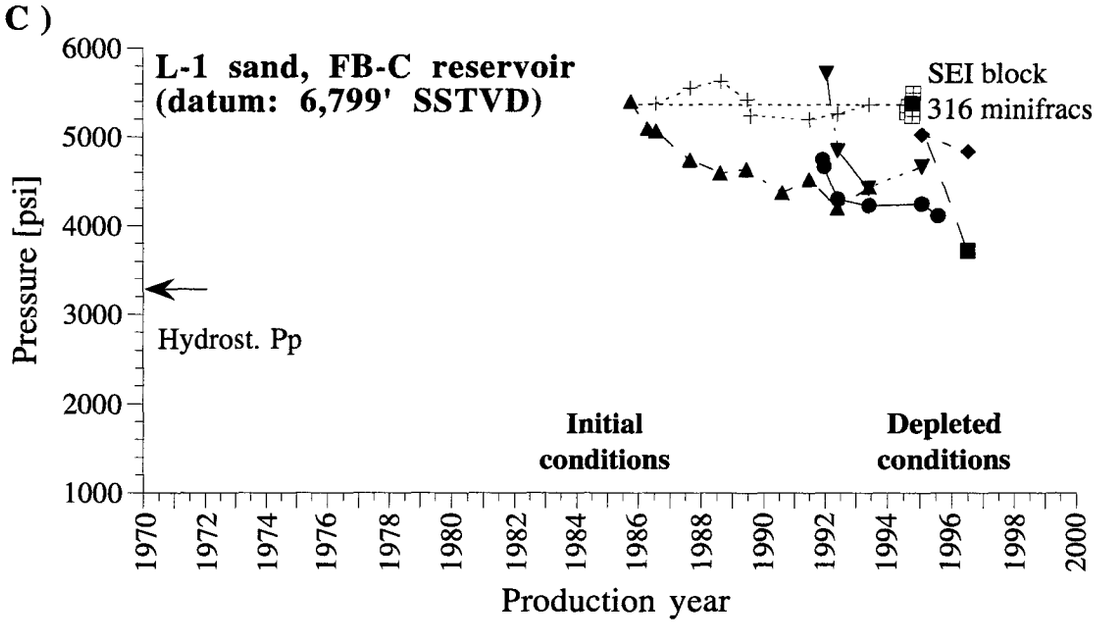

Figure 3.7: Continued.

that are (sub-)hydrostatic indicates that the reservoirs have reached an equilibrium most probably with their ambient aquifers. The remarkable uniform depletion behavior in all three reservoirs indicates internal, hydrological contiguous compartments that coincide with seismically interpreted fault bounded fault blocks. In contrast, the Lentic-1 (or L-1) sand (Figure 3.7C) reveals severe overpressured conditions ($\lambda > 0.8$; Table A2) and strong, non-uniform pressure depletion over ~10 years of production. This behavior suggests undrained reservoir conditions and possible compartmentalization on a sub-fault block scale. Additionally, I observe the following: (i) pore pressures in one of the wells surveyed (crosses in Figure 3.7C) essentially maintain their initial value; (ii) pore pressures measured at the time of the minifracs indicate the same values when compared with the earliest (i.e., initial) pore pressure measurement available for this sand. Given (i) and (ii), there is evidence that the production related pore pressure change is zero. In chapter 5, I discuss the possible underlying compaction mechanism that gives rise to this type of behavoir.

In summary, the production related pressure transients exhibit different behaviors as a function of the stratigraphic level of the reservoir. Intermediate reservoirs are moderately overpressured and exhibit uniform pressure depletions between 700 psi and 2,000 psi. The deep L-1 sand is severely undercompacted and overpressured. Non-uniform pressure transients within the same fault block indicate sub-compartmentilization. In fact, the data suggest that there has been no pore pressure change despite production.

3.4.3 Depletions corrections and stress paths

Because of the apparent intrinsic interdependence between pore pressure and stress observed in Figure 3.6, I also expect stress changes to accompany the observed fluid pressure reduction (Segall and Fitzgerald, 1998). Since all fracture completions were carried out at a later stage in the production histories of the SEI 330 sands, the least principal stresses do not reflect the undepleted (i.e., initial) conditions and need to be corrected. Estimating the change of least principal stress with the change of pore pressure (i.e., the stresspath) is generally a difficult task, especially for the poorly consolidated and highly overpressured sediments of the SEI 330 field. This raises the question of how the reservoir sands compact as hydrocarbons are being produced. While I also study this issue in chapter 5, I introduce and present here the results of two ways that appear most plausible to me in order to correct for the effects of depletion.

First is a method that is based on results from laboratory experiments and the assumption of a constitutive law for mechanical compaction. Chang and Zoback (1998) conducted drained, uniaxial compaction tests on core samples from well 316/A-12 (the footwall side of the basin bounding growth fault system; see Figure 3.1) under zero lateral strain conditions and measured an average static Poisson's ratio (υ) of 0.3. Although visco-elastic creep was observed in the core plugs over short time scales, and although other publications address the issue of non-linear elastic or even plastic stress relaxation in sedimentary rocks over geologic times (e.g. Holbrook, 1995), I assume for this correction method that on the scale of the SEI 330 reservoirs and over the time-span during which oil and gas have been produced from the field (i.e., max. 20 years), the sediments respond primarily elastic to the hydrocarbon production. Engelder and Fischer (1994) derived a formula that accounts for the change of horizontal stress, ΔS_h, with a change in pore pressure, ΔP_p, using simply the equations of linear elasticity under the assumption of zero later strain:

$$\Delta S_h = \alpha \frac{1-2\upsilon}{1-\upsilon} \Delta P_p \qquad \text{Eqn. 3.1}$$

where α denotes Biot's coefficient. I assume $\alpha \sim 1$ because of the unconsolidated nature of the reservoir sands the modulus of the solid constituents (excluding pores) is probably much larger than that of the bulk sand (including pores) (i.e., $K_s >> K_b$). Since the reservoirs are believed to exhibit a high aspect ratio of length over width, the overburden S_v does not change. Using the value of 0.3 for υ as determined by Chang and Zoback (1998) in equation 3.1, the change of stress amounts to $\Delta S_h = 0.571 \cdot \Delta P_p$.

The second method bypasses the assumption of a constitutive compaction law for these soft sediments. I carefully searched leak-off test (LOT) data from wells drilled into initially undepleted reservoir sands and found one LOT carried out in the LF FB-B reservoir that obviously fractured the sand reservoir. Given the S_{hmin} magnitudes from the LOT and minifrac, I can calculate ΔS_h that corresponds to ΔP_p in this particular reservoir compartment (Figure 3.8). The ratio of ΔP_p and ΔS_h defines the stress path parameter A (Addis et al., 1996):

$$A = \frac{\Delta S_h}{\Delta P_p} \qquad \text{Eqn. 3.2}$$

Parameter A presents the effective reservoir behavior under loading conditions (i.e., increase of effective stress as the pore pressure is drawndown) and a characteristic reservoir rheology. Note, A does not impose any boundary conditions on the physical behavior of the reservoir. Because I consider only two points along this stress path (initial state and depleted state at some later time), any intermittent time or pressure dependent compaction behavior is averaged out and the actual stress path of the reservoir is neglected. In case of the LF FB-B reservoir, the value for A is 0.81. This value is similar to results found by Engelder and Fischer (1994) and Teufel et al. (1991). Because this is the only LOT I found in an undepleted reservoir of all the reservoirs studied, I assume the same value for A for the remaining reservoir sands with significant depletion history (i.e., they follow the same stress path) to restore their state of stress.

In order to calculate the least principal horizontal stress change, I used the pressure survey data to extract current and initial pore pressures within individual reservoir compartments and calculate ΔP_p. Figures 3.4A and 3.7B and C serve as examples. Using equations 3.1 and 3.2, I then calculated the associated least principal stress change and added it to the S_{hmin} value from the minifrac test to obtain the unperturbed (i.e., prior to hydrocarbon production) S_{hmin} magnitude. Table A2 (see Appendix) summarizes production related pore pressure changes and associated restored stress values. Notice, since there is no obvious pore pressure change with production in the Lentic sand (Figure 3.7C) there is consequently no least principal stress change.

Figure 3.9 illustrates the effect of production related pore pressure and stress correction to initial (i.e., undepleted) conditions. In this figure, pore pressures and least principal stresses are normalized by the overburden, S_v, which removes the explicit depth effect and yields a dimensionless plot. The diagrams also show lines for three common rock

mechanical models: (i) The hydrofrac failure limit at which the pore pressure equals the least principal stress and natural hydraulic fracturing occurs (Hubbert and Willis, 1957; Nur

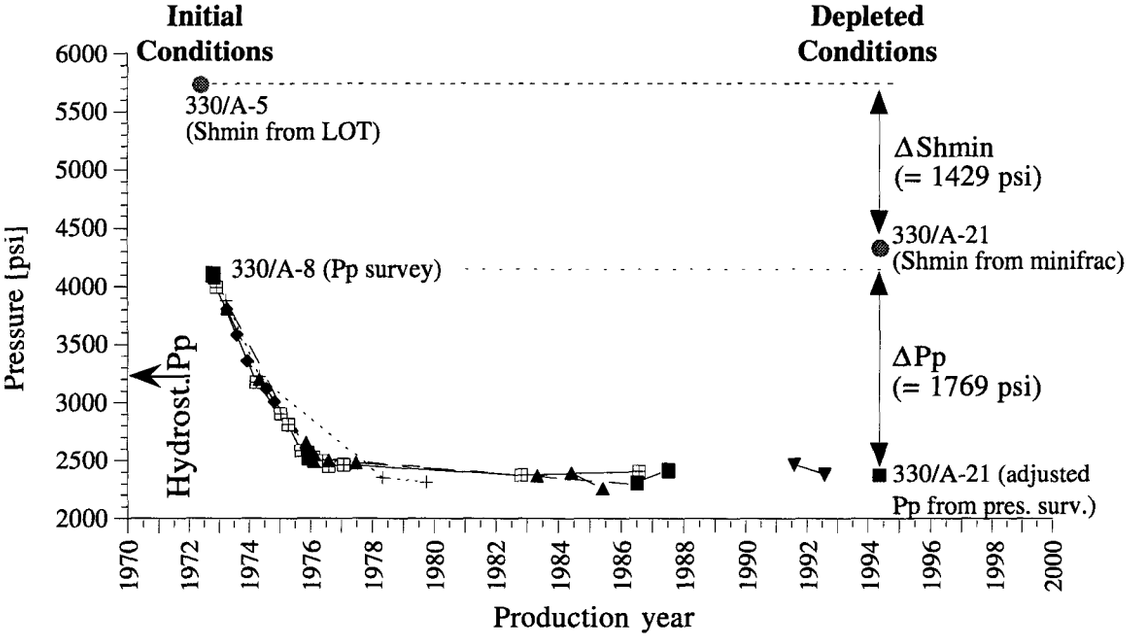

Figure 3.8: Pore pressure history from pressure surveys in 7 wells and least principal stress data (LOT and minifrac) from two wells drilled into the LF FB-B sand reservoir. The pore pressure data were corrected to a datum of 6911 ft. SSTVD. For reference, I display the hydrostatic pore pressure (arrow) with a gradient of brine (0.465 psi/ft).

and Walder, 1990). (ii) Frictional failure (i.e., Coulomb failure) for a coefficient of friction (μ) of 0.6 (Zoback and Healy, 1984, 1992). According to this model, the state of stress is in frictional equilibrium with pre-existing, optimally oriented shear planes and faults (Jaeger and Cook, 1971; Byerlee, 1978). (iii) The isotropic stress state for which $S_3 = S_1$ (i.e., $S_{hmin} = S_v$). Note, that the lines for (i) and (ii) converge as pore pressure increases.

As Figure 3.9A and B show, depending on the magnitude of ΔP_p the correction generally brings the reservoirs either closer or right on to an isotropic stress state (i.e., $S_{hmin}/S_v = 1$). For the first correction method (i.e., with $\nu = 0.3$; Figure 3.9A), the slope of the stress path is less steep than the frictional failure line for $\mu = 0.6$. Hence, the corrected state of stress in the reservoirs is not only more isotropic but also closer or in frictional equilibrium. In case of the second method (i.e., with A = 0.8; Figure 3.9B), the stress path slope is steeper than the frictional failure line distancing the corrected reservoir stress states further from frictional failure but bringing them even closer to stress isotropy compared to the previous method. Because the resulting stress state in case of one well (OI-1/FB-C) is actually above the isotropic stress line (Figure 3.9B), I think that the assumption of a similar

A value for all SEI 330 reservoirs is incorrect (i.e., too high) for this sand. Since I consider S_v as the maximum principal stress in the normal faulting environment of the SEI field, the ratio S_{hmin}/S_v can never be greater than 1. Stratigraphically, the OI-1 sand is the deepest and oldest sand of all reservoirs that need to be corrected for depletion. It was deposited in a different sedimentation cycle than the shallower sands (Alexander and Flemings, 1995) and, therefore, exhibits variations in composition, pore pressure, and compaction conditions. Hence, a different value for A (i.e., smaller than 0.81) appears to me quite plausible. Similarily, three sands in Figure 3.9A are driven below the frictional failure line toward hydraulic fracturing by the depletion correction using $\nu = 0.3$. Because these are the shallow and relatively clean KE-1 sands, I would expect a steeper stress path (i.e., smaller ν) than the one predicetd using the laboratory measured value for Poisson's ratio. These two last observations reveal the problem of the very limited data available to restore the initial state of stress in the fracture completed reservoirs. This requires me to assume a similar value for A or υ for all depleted reservoirs that require stress correction.

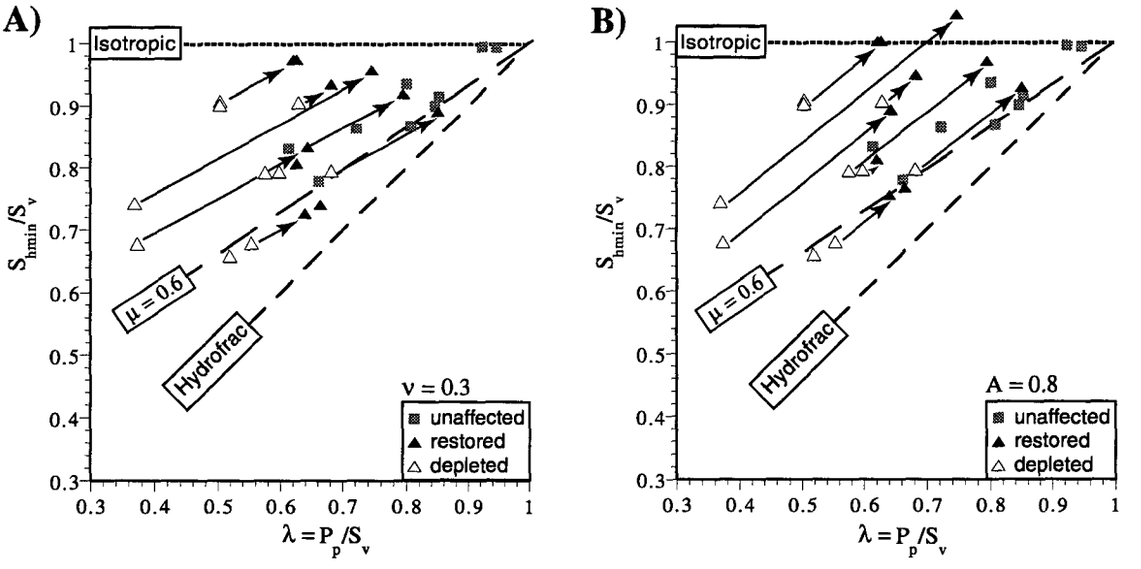

Figure 3.9: Normalized least principal stress versus normalized pore pressure. The diagrams display depleted conditions as open triangles, restored conditions as black triangles, and reservoirs unaffected by production as gray squares. Arrows indicate individual stress paths (i.e., connect depleted and restored conditions in an individual reservoir). Hydraulic fracturing, frictional failure for a coefficient of friction (μ) of 0.6, and the isotropic stress state are shown as dashed lines. (A) The original state of stress was calculated using the assumption of zero lateral strain in the SEI 330 field. (B) The original state of stress was restored using the stress path parameter A.

In general, the stress path derived from the lab measurements on Lentic cores is less steep than the one derived from the field observation in the LF sand (Figure 3.9). I think, there are two possible explanations for this difference: (i) the LF and Lentic sands are from two different stratigraphic levles with profound variations in sand consolidation and pore pressure. As a result, production induced compaction and stress change vary also. (ii) Consistent with Teufel et al. (1991), field data generally show steeper stress paths than lab measurememnts because of different boundary conditions (BC). While a strict zero lateral strain BC can be maintained in the lab, a combined stress-strain BC is probably more likely in the field. The OI-1and KE-1 cases show that, additionally, the BC in the field probably vary between different reservoirs resulting in variable stresspaths vary as well. Nonetheless, I believe the two methods presented most likely serve as upper and lower bound and the effective stress path for each reservoir sands lies somewhere in between.

3.4.4 Initial reservoir conditions

In Figure 3.10, I display the restored (i.e., initial) pore pressures in two different ways: A) pore pressure versus depth to compare it with Figure 3.6A and B) normalized pore pressures (i.e., $\lambda = P_p/S_v$) as a function of depth to better illustrate overpressured conditions in individual, undepleted sand reservoirs. As with the depleted reservoir pore pressures, initial pore pressures show significant scatter ranging from slightly to severely overpressured conditions (i.e., λ = 0.58 to λ = 0.95). However, in spite of the large variations, the data suggest to follow one of three trend lines depending upon structural position and stratigraphic level in the field. While the structural position of the footwall reservoirs (i.e., the Lentic sands) is quite shallow, stratigraphically they are the deepest sands and characterized by relatively high shale contents, limited continuity, and poorly drained conditions (because they were rapidly buried and are overlain by thick shale sequences). As a consequence, the λ trend line (Figure 3.10B) indicates moderate to severe overpressures. In contrast, stratigraphically shallower sands within the minibasin exhibit less overpressure because they are more continuous, relatively clean, and characterized by better drainage (Holland et al., 1992). In particular the shallowest reservoirs are only mildly overpressured. Deeper minibasin sands are less well drained and consequently exhibit moderately overpressured conditions.

In Figure 3.11, I converted the production restored stress data to effective stress ratio, K, which is simply calculated by taking the ratio of the effective least horizontal stress, σ_{hmin} (S_{hmin} - P_p) over the effective overburden stress, σ_v (S_v - P_p):

$$K = \frac{\sigma_{hmin}}{\sigma_v} \qquad \text{Eqn. 3.3}$$

Notice, for comparison I also display K values for depleted reservoir conditions in the two figures.

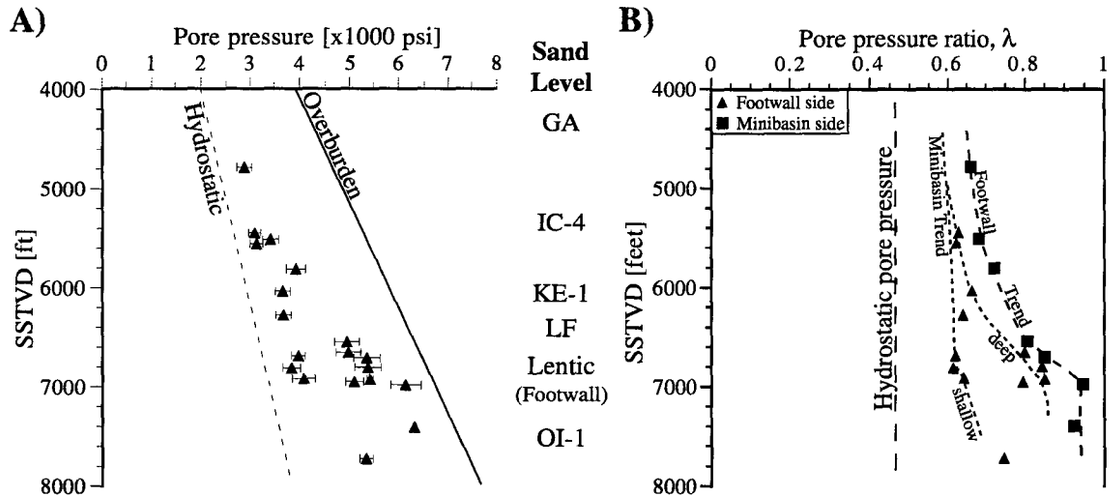

Figure 3.10: Undepleted (i.e., restored) pore pressures in SEI 330 reservoirs that were fracture completed. For both plots, the overburden was derived from integrated density logs. Hydrostatic pore pressure was calculated with a constant brine gradient of 0.465 psi/ft. The seawater depth in the field is 248 feet. The figure also displays the approximate depth of various sand levels (compare with cross-section in Figure 1.4). A) Pore pressure versus SSTVD. Error bars denote upper and lower bounds. B) Normalized pore pressure (λ=Pp/Sv) versus SSTVD. Reservoirs from within the minibasin and the footwall side are denoted as black triangles and black squares respectively. Pore pressure trends for hydrostatic conditions, the footwall side, and shallow and deep sand levels in the minibasin are displayed as dashed lines.

Based on previous studies, I would expect K to increase with depth (Althaus, 1977; Breckels and vanEekelen, 1982; Brennan and Annis, 1984; Mathews and Kelly, 1967; Pilkington, 1978). However, my data show no clear correlation but rather scatter, regardless whether I consider depleted (open triangles) or both initial (black squares and gray triangles) conditions (i.e., ν=0.3 and A=0.8). For the two initial states, I find the majority of the data to be limited by two bounds: (1) K = 0.32 and (2) K = 1. The first value corresponds to frictional faulting theory for a coefficient of friction (μ) of 0.6 (as introduced above):

$$K = \frac{\sigma_{hmin}}{\sigma_v} = \left(\sqrt{\mu^2 + 1} + \mu\right)^{-2} \qquad \text{Eqn. 3.4}$$

The second value relates to an isotropic stress state in which all differential stresses in the reservoir sands have dissipated comparable to an ideal fluid. K = 1 is also the upper bound in a region of normal faulting (like the SEI 330 field), where the overburden, S_v, is the maximum principal stress.

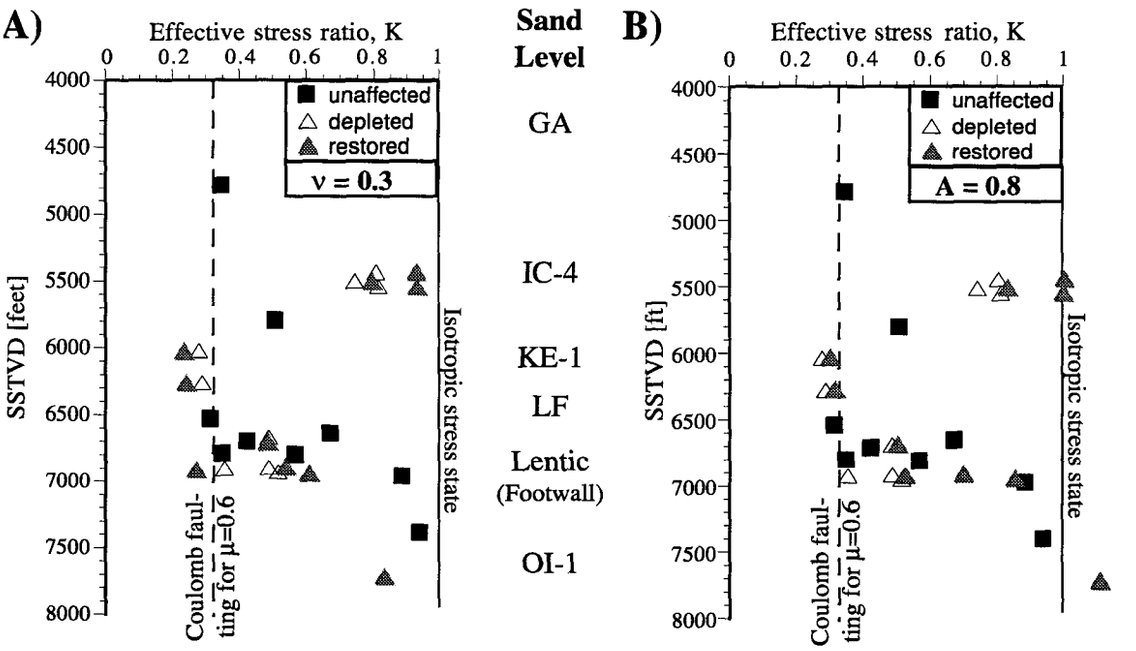

Figure 3.11: Effective stress ratio, K, versus SSTVD for depleted (open triangles), restored (gray triangles) and unaffected sand reservoirs in fracture completed wells of the SEI 330 field. "Unaffected" refers to negligible pore pressure reduction. The two dashed lines show the bounds for Coulomb frictional faulting (K=0.32) and isotropic stress state (K=1). A) State of stress was restored using a value of Poisson's ratio (ν) of 0.3. B) The state of stress was restored using a value for the stresspath parameter A (ΔSh/ ΔPp) of 0.8.

A large number of other studies have shown that the state of stress in most rock types encountered in the upper, brittle part of the Earth's crust is in frictional equilibrium for μ = 0.6 (e.g., Zoback and Healy, 1984, 1992; Barton et al., 1995; Brudy et al., 1997). In contrast, the stress data from the SEI 330 field suggest that frictional equilibrium for μ = 0.6 may only act as a lower bound and the majority of the sand reservoirs are, in fact, characterized by lower differential stresses (i.e., more isotropic state of stress). Figure 3.12 displays the undepleted conditions in normalized least principal stress versus normalized pore pressure space. Regardless of whether I consider measurements corrected for

depletion with A = 0.8 or ν = 0.3, I can conceptually characterize the initial reservoir conditions with the following three classifications: (i) Sands that follow the frictional failure line for μ = 0.6. (ii) Near isotropic stress states (i.e., zero differential stress) implying almost no strength comparable to a fluid. (iii) Intermediate conditions indicating reduced strength and low differential stresses. Apparently, the Coulomb model is not appropriate for

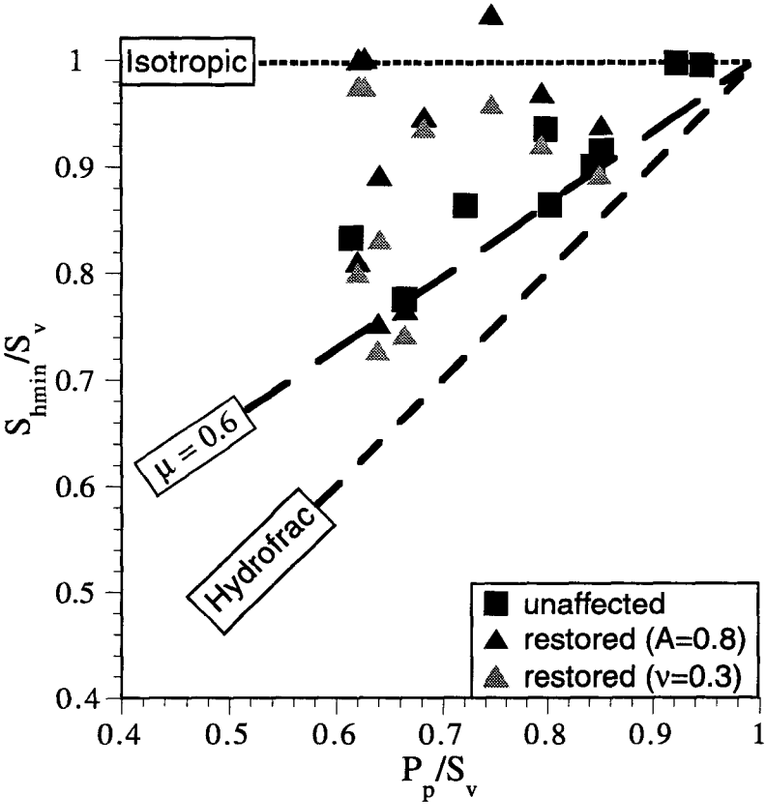

Figure 3.12: Normalized least principal stress versus normalized pore pressure for restored (i.e., undepleted) reservoir conditions. Black triangles display data restored using the stress parameter method with A=0.8, gray triangles show restored data with the laboratory derived Poisson's ratio of ν=0.3. Black squares represent data of reservoirs unaffected by depletion.

the majority of the reservoir sands (i.e. they are not deforming in a manner described by frictional failure), which favors the idea of either weak sediments (i.e., μ values that are considerably lower than 0.6) or mechanisms that allow to dissipate differential stresses. In fact, laboratory measurements by Chang and Zoback (1998) on unconsolidated sediments from the same field have shown time-dependent visco-elastic creep and stress relaxation (i.e., dissipation of differential stress). In a later section of this chapter, I try to verify the ideas derived from the laboratory measurements by integrating stress data with material properties obtained from well-logs.

3.4.5 Comparison with other fracture gradient models

Comparing the South Eugene Island data with three common fracture gradient regressions from the Gulf of Mexico (Althaus, 1977; Breckels and van Eekelen, 1982; Brennan and Annis, 1984) (Figure 3.13) demonstrates that there is no obvious correlation with either the depleted or the initial pore pressures and stresses. I think, this mismatch is the result of the stress and pore pressure data being exclusively from within sand reservoirs in one specific Gulf Coast field. The three representative compilations, in contrast, are empirical regressions based on regional stress data mostly measured in shales. In fact, for most of the data points the regressions overpredict the stress magnitudes (i.e., S_{hmin}) in the sands, which is in agreement with the idea that stresses in shales are generally higher. However, the trend of the regressions could also indicate creep behavior in shales as similarily observed in sands by Chang and Zoback (1998). Since the creep was attributed to the presence of clay, shales can have even lower differential stresses than sands because of their higher clay content.

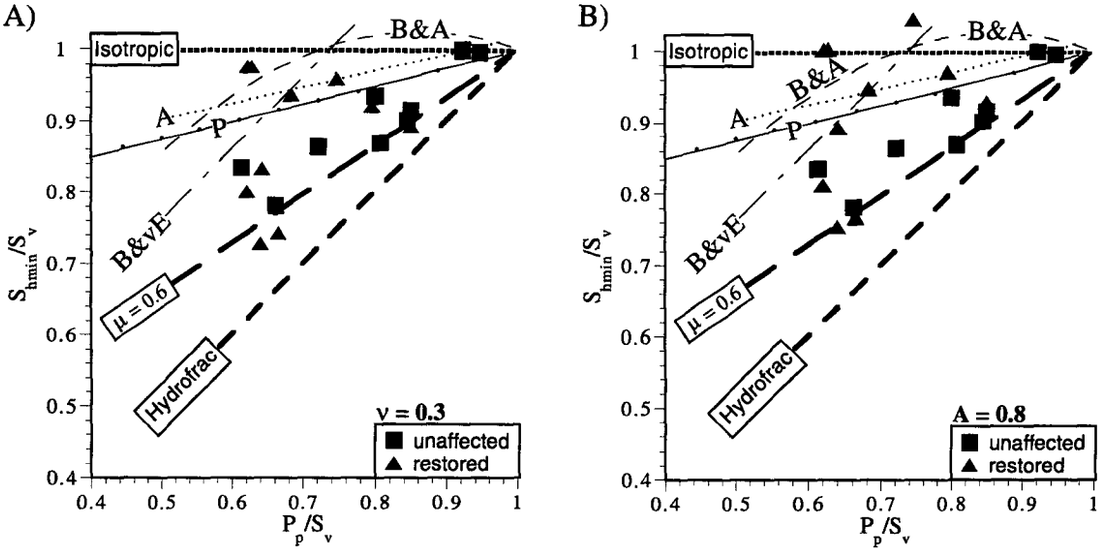

Figure 3.13: Normalized least principal stress versus normalized pore pressure for initial (i.e., undepleted) reservoir conditions. Hydrofrac, frictional faulting, and isotropic stress state lines are shown dashed. The four different fracture gradient regressions were calculated for a reference depth of 6,500 ft. SSTVD and an average overburden gradient of 0.92 psi/ft. A: Althaus (1977); B&vE: Breckels and vanEekelen (1982); B&A: Brennan and Annis (1984); P: Pennzoil (unpublished data). A) State of stress was restored using a value of Poisson's ratio (ν) of 0.3. B) The state of stress was restored using a value for the stresspath parameter A (ΔSh/ΔPp) of 0.8.

Among themselves, the regressions also show no obvious match. I attribute this to the fact that they are not only based on various regional data but also on different data types for

stress determination. For example, Breckels and vanEekelen (1982) primarily used formation integrity tests (FITs), which are ambiguous for least principal stress determination since the reservoir is not fractured. Althaus (1977) and Brennan and Annis (1984) used circulation losses and leak-off tests (LOTs) respectively. While these tests usually cause the sedimentary rock to fail, it is not clear whether they reflect the breakdown, propagation, closure, or some intermittent pressure, which can be very different.

In summary, I think the regressions prove not to be useful in predicting least principal stresses in sand reservoirs of the SEI 330 field. Regardless of whether I consider depleted (not shown in Figure 3.13) or initial (i.e., depletion corrected) conditions, the SEI 330 data exhibit significant scatter which implies that stresses in these reservoir sands cannot be related to depth or pore pressure by a simple relation. From my point of view, the SEI 330 data rather reflect a complex interaction between deformational processes (i.e., varying stress/strain boundary conditions) and material properties.

3.5 Correlation of stress with material properties

In the previous section, initial as well as depleted reservoirs conditions in the fracture completed sands have shown significant scatter in the state of stress (i.e., effective stress ratio, K). Essentially independent of pore pressure, structural, or stratigraphic position, the reservoir sands can experience either stress isotropy, are in frictional fequilibrium, or show intermediate stress states. In this section, I analyze well-log data (i.e., gamma ray and sonic) within the fracture completed reservoir sand intervals in order to identify a potential correlation of material properties with the state of stress. Based on the fact that unconsolidated, overpressured, and clay bearing sands have shown viscous creep in laboratory experiments (Chang and Zoback, 1998), I would expect to find a trend by cross-plotting sonic velocity or gamma ray versus K. These expectations are based on the idea that with increasing gamma (i.e., shale content) and decreasing sonic velocity (i.e., degree of undercompaction) the state of stress should be more isotropic (i.e., the effective stress ratio K approaches unity). In turn, high K values should also reflect a state of compaction disequilibrium (i.e., low velocity due to high porosity), severe overpressures, and high gamma as a result of insufficient drainage due to increased shale volume fractions.

3.5.1 Well-log data

Given various types of well-log data from about 30 wells, I selected 8 wells that penetrated the fracture completed reservoir compartments (i.e., fault blocks) and had good

quality data of the following types: gamma ray, compressional sonic velocity, resistivity, and bulk density. Three out of the eight wells were actually fracture completed in the following reservoirs: OI-1/FB-C (well 330/A-22), LF/FB-B (well 330/A-21), and L-1/FB-C (well 316/A-12). Hence, the reservoir properties recorded by the well-logs in these reservoirs directly correlate with the stress state obtained from the fracture completions. For all remaining reservoirs, I assume that the properties recorded by the well-logs and the state of stress measured in the minfracs do not change within the same reservoir compartment and, therefore, can be correlated. With the help of structure maps I obtained reservoir penetration depths and identified the fracture completed reservoir intervals on the logs from which I extracted the relevant data. As an example, Figure 3.14 shows the reservoir intervals penetrated by well 330/A-21. This log does not show the Lentic sand since it is the deepest reservoir in the SEI 330 field and was not penetrated by this well. The data used for the Lentic analysis come from wells in SEI block 316 located in the footwall of the minibasin bounding growth fault system (Figure 3.1). For the log data from any given reservoir interval, I ran statistical analyses for gamma ray and sonic velocity logs to determine their average values and standard variations. Table A3 lists mean values of sonic Vp, gamma ray, and density logs of the eight relevant wells. Error ranges come from statistical standard deviations, which ranged generally between 3% and 7%.

Sonic velocity

Acoustic velocities are primarily a good indicator for porosity. Measurements by Wyllie et al. (1956, 1958) already revealed simple, monotonic relationships between velocity and porosity. Extensive research has been done ever since (see Mavko et al., 1998, for a review on the most important models). Because overpressured sediments are often associated with compaction disequilibrium, acoustic velocity measurements can be used to predict effective stresses and, subsequently, pore pressure (e.g., Hart et al., 1995; Stump et al., in prep.). Following the ideas presented in these publications, I would thus expect to find a trend that inversely relates sonic velocities with observed overpressures and effective stresses.

In Figure 3.15, I display four cross-plots of stress or pressure versus sonic Vp. Figures 3.15A and B show overpressure (i.e., pore pressure in excess of hydrostatic) and effective vertical stress, respectively. Both graphs exhibit trends as I would expect for the unconsolidated sediments of the field. Firstly, overpressure increases with decreasing Vp (Figure 3.15A). Unless secondary fluid generation mechanisms are operative, overpressured reservoir sands can usually be characterized by relatively high porosity and undercompaction (Bowers, 1994; Hart et al., 1995). Hence, as I would expect, this trend

suggests insufficient drainage of pore fluids associated with compaction disequilibrium. Secondly, effective vertical stress increases with increasing sonic Vp (Figure 3.15B). This trend reflects the mechanical reduction of porosity with increasing compaction (i.e., burial). Thus, high velocities coincide with low porosities and low overpressures as the sediment grains support most of the load (i.e., high effective stresses) and low velocities, in turn, present undercompacted and overpressured reservoirs with relatively high porosities.

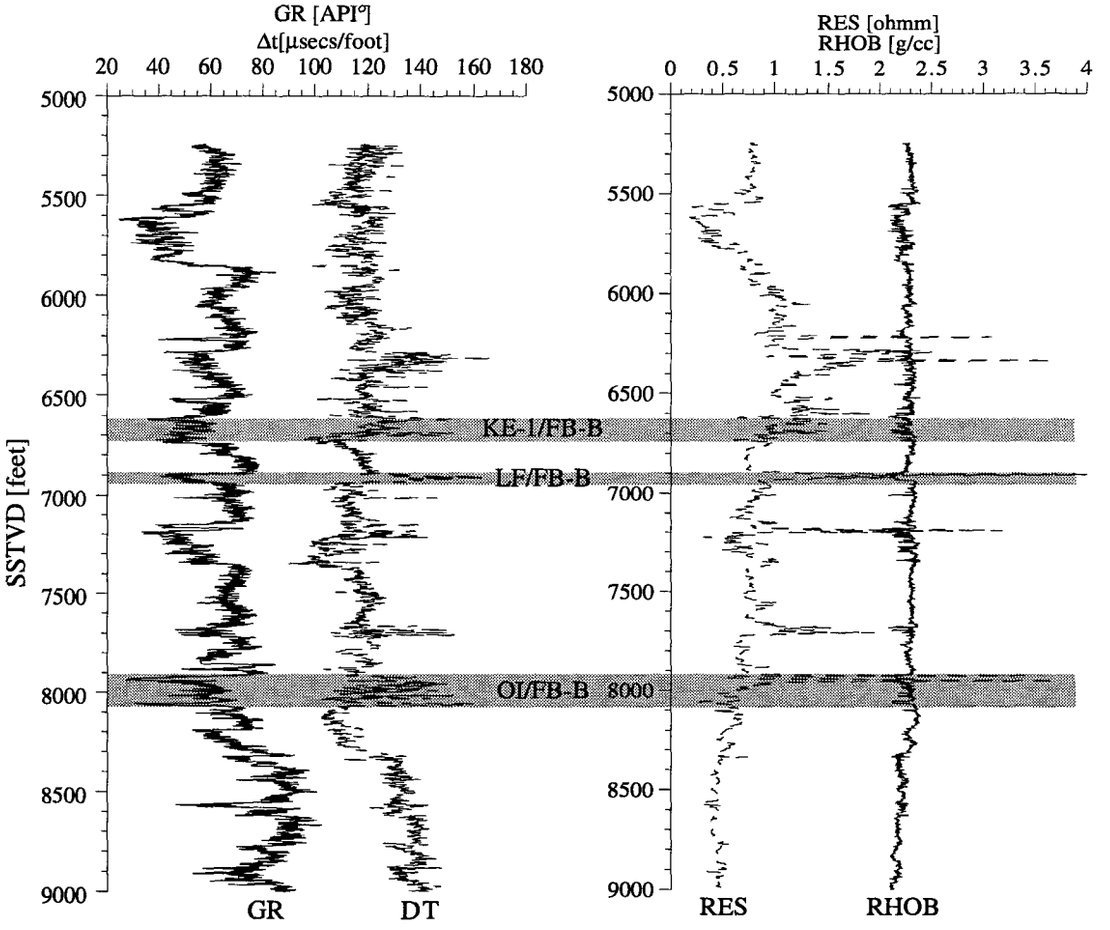

Figure 3.14: Well-log data from well 330/A-21 including four depth intervals of reservoirs sands that were fracture completed (gray boxes). Gamma ray and sonic Δt are displayed on the left; resistivity and bulk density are on the right.

In contrast, effective horizontal stress data (Figure 3.15C) scatter and show no obvious trend as a function of sonic Vp. The effective least principal stress appears not to be a simple function of porosity and overpressure unlike the effective vertical stress. Therefore, predicting horizontal stresses in SEI 330 reservoir sands with sonic log data seems not feasible and models imposing zero lateral strain boundary conditions to predict horizontal

stresses appear not applicable. Similarly, effective stress ratio, K (Eqn. 3.3), exhibits no clear correlation with sonic velocity (Figure 3.15D) which is due to the scatter in effective horizontal stress. Perhaps, there appears to be a weak trend in the sense that reservoirs with

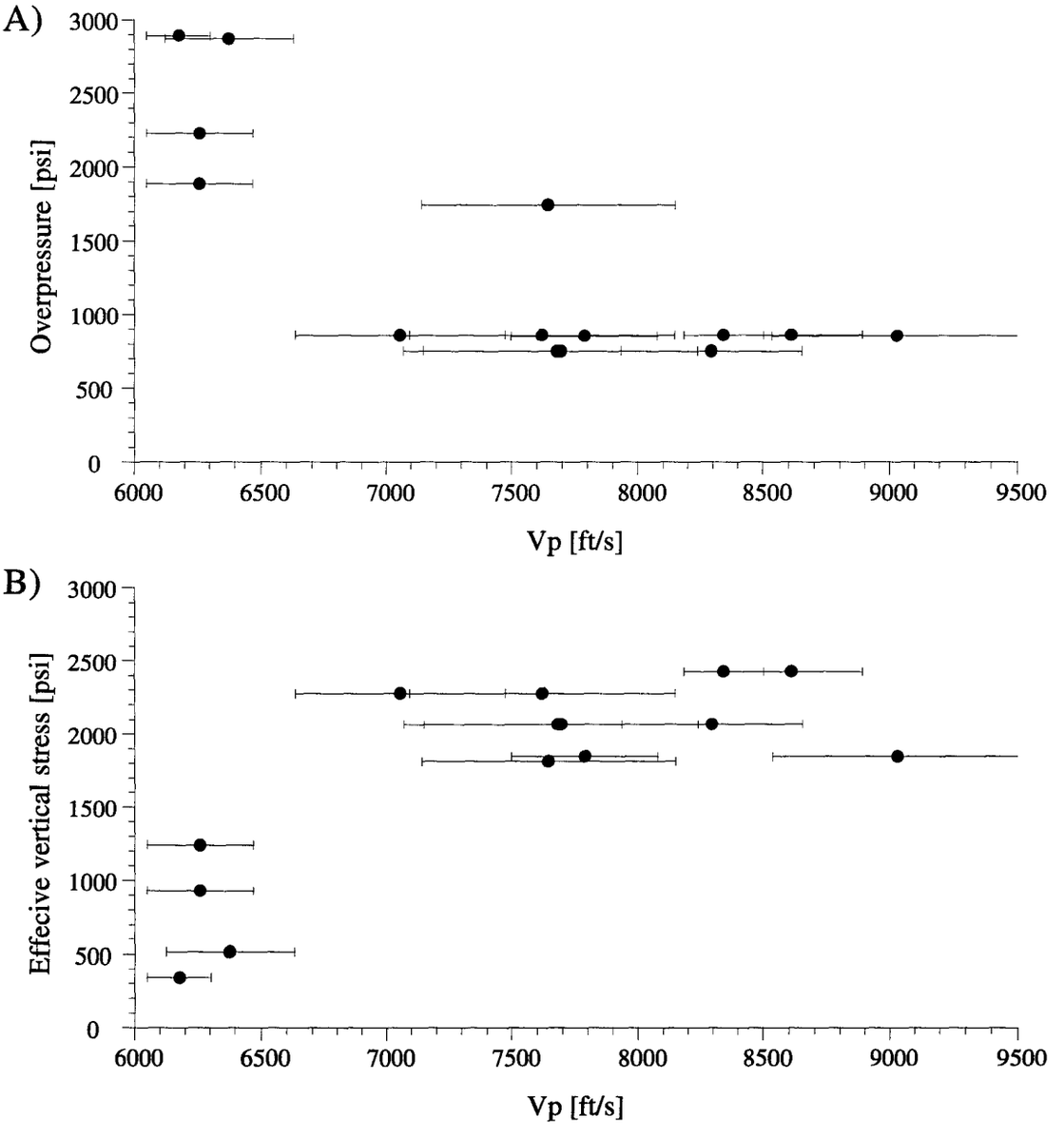

Figure 3.15: Mean compressional sonic velocity (Vp) versus (A) overpressure (i.e., pore pressure in excess of hydrostatic), (B) effective vertical stress, (C) effective horizontal stress, and (D) effective stress ratio K. The dashed lines in (D) represent an isotropic stress state where all principal effective stresses are equal, and the Coulomb criterion for a coefficient of friction (μ) of 0.6.

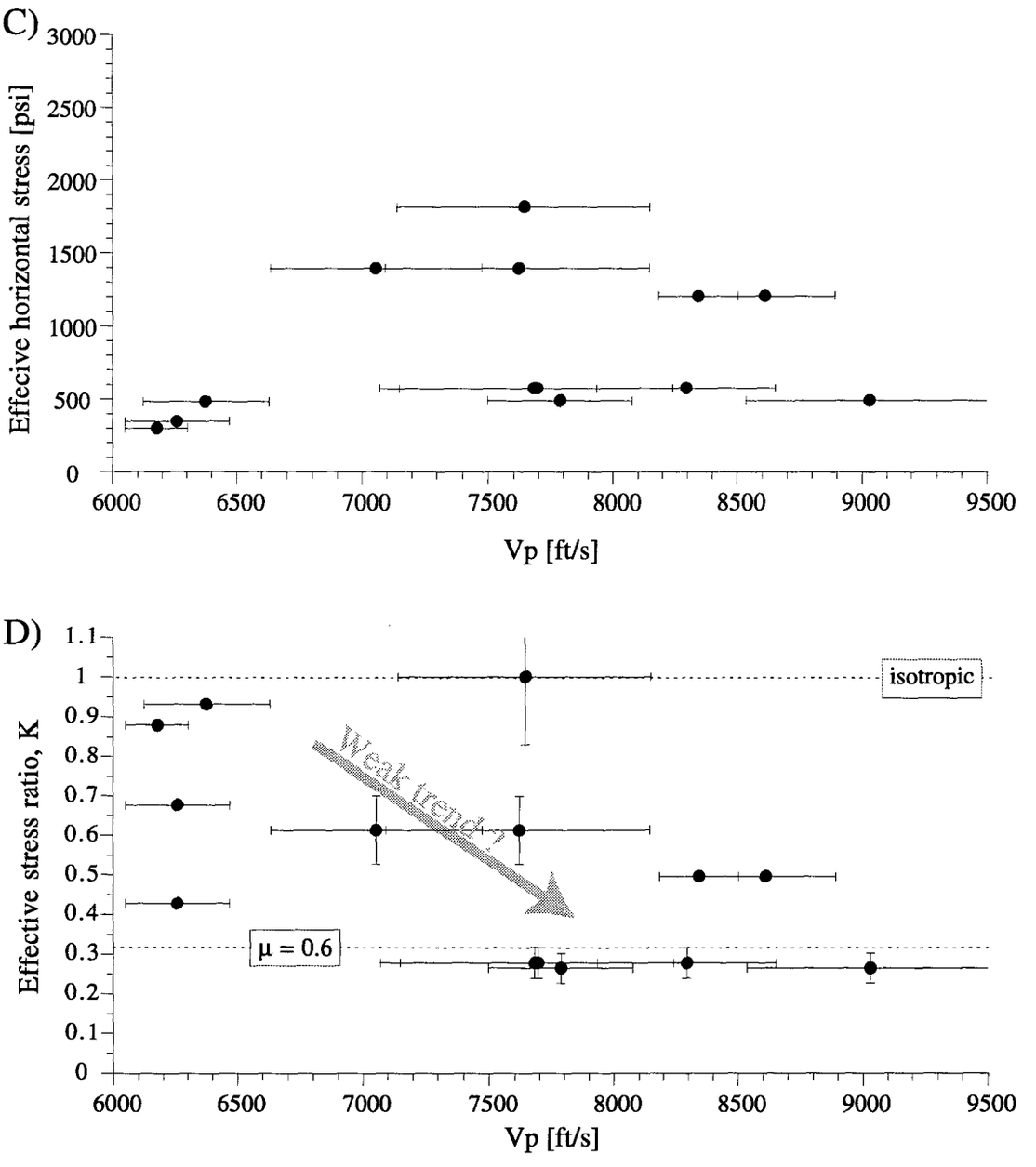

Figure 3.15: Continued.

higher Vp values tend to have lower effective stress ratios and vice versa (shown as gray arrow in Figure). This observation may be a hint that overpressured and underconsolidated reservoirs dissipate differential stresses (i.e., creep) and approach an isotropic stress state as observed by Chang and Zoback (1998) in laboratory measurements on Lentic core from the SEI 330 field.

Gamma ray

A number of publications have postulated that creep (i.e., time dependent strain) is an important deformation mechanism for compacting sedimentary basins (Holbrook and Maggiori, 1993; Ostermeier, 1993; Scott et al., 1998). Chang and Zoback (1998) attribute their observed visco-elastic behavior and time dependent stress relaxation to small amounts (~10%) of intergranular clay. Therefore, I want to test with gamma ray logs whether there exists a correlation between the presence of shale (i.e., clay) and the observed stresses in the fracture completed SEI 330 reservoirs. In other words, if viscous creep as described by Chang and Zoback (1998) is the responsible mechanism for the observed state of stress in the SEI 330 reservoirs then sands with high K values should have high gamma and vice versa.

Plotting overpressure and effective vertival stress as a function of gamma (Figures 3.16A and B) shows a clear trend in the sense that overpressure decreases and effective vertical stress increases as gamma increases. This correlation is somewhat surprising as I would expect the opposite trend (i.e., high gamma values at high overpressures and low effective stress) because as a function of depth and overpressure in the SEI 330 field the volume fraction of shale increases relative to the volume fraction of sand (Alexander and Flemings, 1995). However, the described volume fractions in this publication refer to the gross volume in the field and not to individual reservoirs. In fact, all SEI 330 reservoirs are relatively clean independent of their stratigraphic position in the field (Holland et al., 1992). In other words, the net amount of shale increases relative to the net amount of sand as a function of depth simply because the thickness of the shale layers separating the sand reservoirs increases. Because with depth the relatively clean sand reservoirs are increasingly undercompacted and overpressured, the trend in gamma values in Figures 3.16A and B may also reflect a relative increase in porosity (i.e., undercompaction) if I assume a constant amount of shale. To further explore this idea I cross-plotted in Figure 3.17 GR versus Vp. This plot exhibits an increase in gamma with increasing sonic velocity. This trend may suggest the postulated porosity and relative gamma effect due to the unconsolidated nature of the SEI 330 reservoir sediments. In other words, as velocity increases the sands compact and porosity decreases which increases the relative amount of shale. I want to emphasize again that this conclusion is based on the assumption of relative clean and well sorted sands, which were described by Holland et al. (1992) and Alexander and Flemings (1995).

Figures 3.18A and B show effective horizontal stress and K as a function of gamma. Like with sonic velociy, the effetive horizontal stress does not exhibit the same porosity effect as the effective vertical stress but rather scatters (Figure 3.18A). As a result, K

scatters as well and shows no real trend. From these observations, I conclude that the measured gamma values do not account for the scatter in the state of stress observed in the SEI 330 reservoirs.

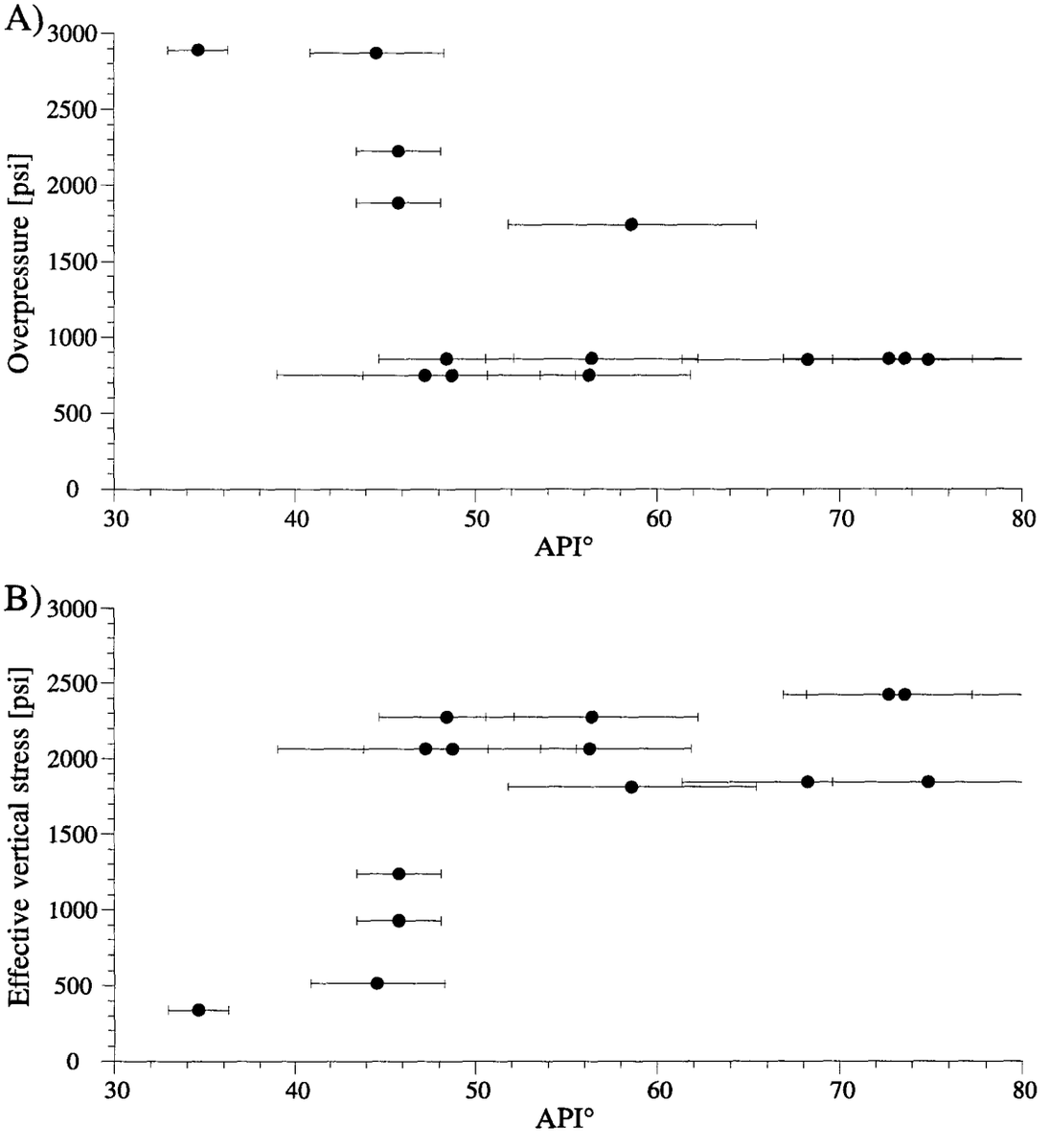

Figure 3.16: Mean gamma ray versus (A) overpressure (i.e., pore pressure in excess of hydrostatic) and (B) effective vertical stress for the fracture completed reservoirs listed in Table A3.

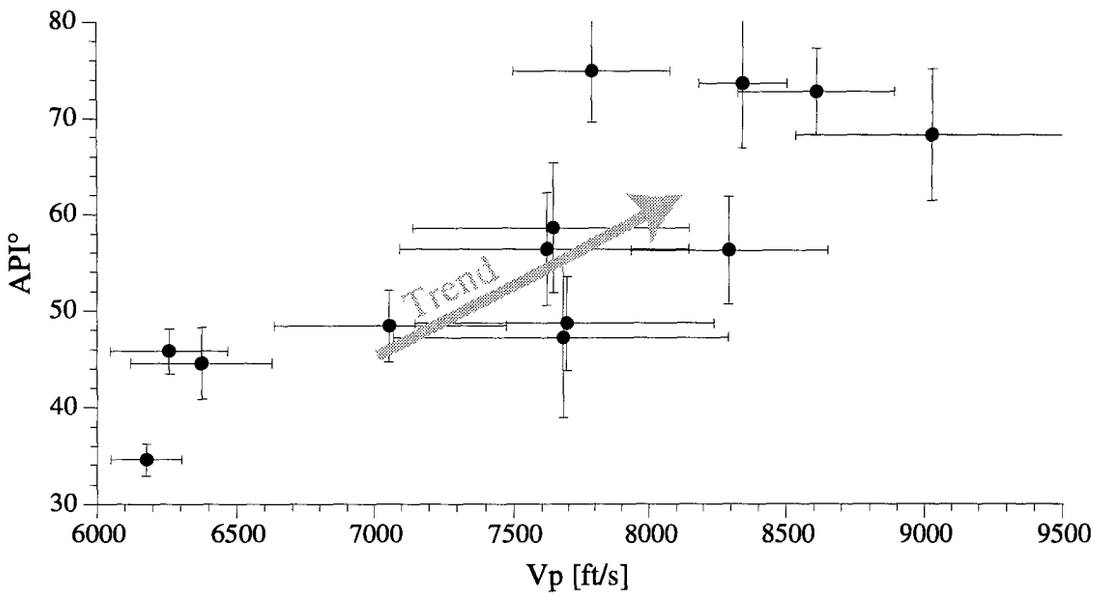

Figure 3.17: Mean gamma ray versus mean sonic velocity for the fracture completed reservoirs listed in Table A3.

3.5.2 Summary

Correlation of sonic and gamma ray log data with overpressure and effective stresses indicates a porosity trend for both data types. With increasing overpressure and associated undercompaction (i.e., porosity increase) both sonic Vp and gamma decrease. On the other hand, with increasing effective vertical stress (i.e., burial) both gamma and Vp increase wich suggests to reflect the relative mechanical reduction of porosity.

In contrast, effective horizontal stress and effective stress ratio, K, do generally not reflect any obvious correlation with sonic Vp or gamma. However, there may be a weak dependency of K to sonic Vp in the sense that reservoirs with higher sonic Vp exhibit somewhat lower K values (i.e., higher differential stresses). In general, though, it appears that the effective horizontal stress, hence K, cannot be easily determined with these log measurements because they either do not capture the viscuous creep and time dependent stress relaxation as observed in the laboratory or other factors influence K such as varying stress/strain boundary conditions or different types of rheology.

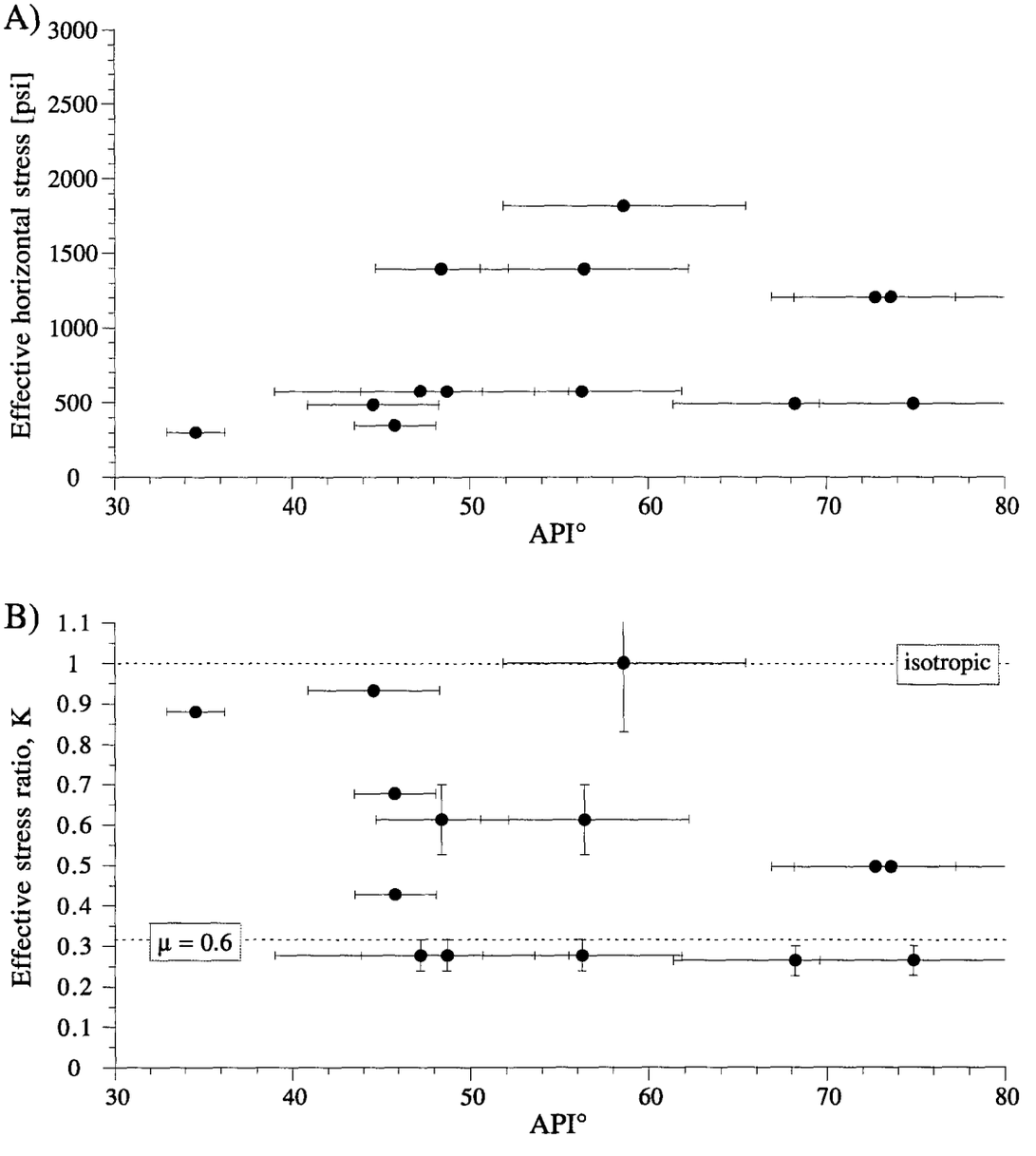

Figure 3.18: Mean gamma ray versus (A) effective horizontal stress, and (B) effective stress ratio K for the fracture completed reservoirs listed in Table A3. The dashed lines in (A) represent an isotropic stress state where all principal effective stresses are equal, and the Coulomb failure for a coefficient of friction (μ) of 0.6.

3.6 Conclusions

From the South Eugene Island 330 (SEI 330) field, offshore Gulf of Mexico, I compiled and analyzed pore pressure data and least principal stress measurements from minifracs of

fracture completed wells. The measurements were made over a depth range of 4800 ft. to 7700 ft. SSTVD (sub-sea true vertical depth) and show considerable variability in pore pressure (P_p) and minimum principal stress ($S_3 = S_{hmin}$). S_{hmin} values within sands and shales range from half the overburden (S_v) to roughly 99% of S_v. Pore pressures vary from sub-hydrostatic to nearly 95% of lithostatic.

Since the majority of the minifracs were conducted in sands with appreciable production induced depletion, the measured stresses do not reflect the original stress states in the reservoirs prior to hydrocarbon production and, thus, need to be corrected. I applied two methods to correct for the depletion effect: (i) a poroelastic model based on laboratory derived Poisson's ratio (v) of 0.3, and (ii) an effective stress path model for which I determined the change of horizontal stress with the change of pore pressure (parameter A) in the LF reservoir sand to be 0.81. For all other reservoirs that required depletion correction, I assumed the same stress path.

In general, whether I consider observations from undepleted sands or sands with appreciable pressure declines and stress changes, the resulting pore pressures and stresses show effective stress ratios, K, that scatter significantly and do not correlate with previously published fracture gradient models for this area. The lower-bound value of K is 0.33, which corresponds to the expected value for Coulomb failure for a coefficient of friction of 0.6 in normal faulting environments. However, in some sands K approaches unity, thus indicating an essentially isotropic stress field. Hence, the data indicate a highly variable state of stress that cannot be simply related to depth or pore pressure, but appears to reflect a complex interaction between deformational processes and material properties. Correlating K with sonic and gamma ray logs reveals only a very weak dependency of K on sonic Vp, which could be suggestive of time dependent creep beavior as observed in laboratory measurememnts.

Analysis of the pressure surveys show uniform pore pressure reduction over time for most reservoir compartments. This indicates hydraulically contiguous compartments that correlate with seismically interpreted fault blocks. In the deepest reservoir sand, however, I observe a non-uniform pressure reduction behavior within individual fault blocks implying more complex compartmentalization possibly on a sub-fault block scale.

3.7 Acknowledgments

I would like to thank Pennzoil, Shell, Texaco, and Chevron for generously providing the data used in this analysis. Peter B. Flemings and Beth B. Stump provided invaluable help and suggestions during the preparation and revision of this manuscript. This project is

funded by the Gas Research Institute under contract number 5095-260-3558 and the Stanford Rock and Borehole Geophysics (SRB) Consortium.

3.8 Appendix

TABLE A1: Pore pressures (Pp) from minifracs and pressure surveys, least principal horizontal stress (Shmin; from minifrac closure pressures), and overburden (Sv) from SEI 330 fracture completions. The fluid densities (ρlive) are the average applied specific live oil densities from pressure surveys taken in wells drilled into corresponding sand reservoirs. The table lists the footwall reservoirs first, followed by the shallow and deep minibasin reservoirs.

Well	Sand reservoir	SSTVD [ft]	Pp (minifrac) [psi]	Pp (pres. surv.) [psi]	Shmin [psi]	Sv [psi]	ρlive [psi/ft]
330/D-7	KE-1/FB-EB	4787.3	2892.0	2888.0	3394.0	4360.0	0.263
316/A-11	OI/FB-A	5811.3	4296.0	3922.0	4690.0	5433.1	0.312
316/A-3ST	L-1/FB-A	7406.3	6316.0	6316.0	6799.0	6833.8	0.344
316/A-10	L-1/FB-C	6547.3	5200.0	4943.0	5310.0	6122.8	0.309
316/A-1ST	L-1/FB-C	6654.3	5300.0	4982.0	5823.0	6223.7	0.309
316/A-12A	L-1/FB-C	6714.3	5468.0	5349.0	5747.0	6280.2	0.309
316/A-12A	L-1/FB-C	6805.3	5239.0	5379.0	5727.0	6364.8	0.309
316/A-12	L-5/FB-C	6985.0	6034.0	6137.0	6439.0	6480.0	0.222
330/A-10ST	IC-4/FB-B	5515.3	3144.0	3144.0	4520.0	4999.6	0.343
330/A-10ST	IC-4/FB-B	5449.3	2803.0	2485.0	4456.0	4935.6	0.343
330/A-8ST	IC-4/FB-B	5557.3	2539.0	2539.0	4570.0	5040.4	0.343
330/C-12	KE-1/FB-A	6037.3	2998.0	3055.0	3735.0	5508.9	0.299
330/C-8	KE-1/FB-B	6280.3	2976.0	2976.0	3770.0	5740.3	0.314
338/A17	LF/FB-A	6688.7	3829.0	3829	5078.0	6397.9	0.331
330/A-21	LF/FB-B	6911.3	2472.0	2373.0	4305.0	6355.5	0.340
330/B-10ST	NH/FB-A	6951.4	4199.2	3676.0	5079.3	6406.1	0.313
330/C-18	NH/FB-B	6811.3	3839.0	3839.0	5199.0	6251.5	0.273
330/A-22	OI-1/FB-C	7727.3	3187.0	2642.0	5306.0	7151.9	0.255
330/A-20ST	OI-4/FB-E	6923.3	4350.0	4350.0	5062.0	6367.0	0.303

TABLE A2:Depleted (depl.) and restored (rest.) pore pressures and associated corrections of the state of stress for the two different methods explained in the text.

Struct./ strat. position	Reservoir	SSTVD [feet]	Depl. Pp [psi]	Rest. Pp [psi]	ΔPp [psi]	Rest. Sh (A=0.8) [psi]	Rest. Sh (ν=0.3) [psi]	λ initial	K (A = 0.8)	Sh/Sv (A = 0.8)	K (ν = 0.3)	Sh/Sv (ν = 0.3)
Foot-wall	KE-1/FB-EB	4787.3	2888	2888	0	3394	3394	0.662	0.344	0.778	0.344	0.778
	OI/FB-A	5811.3	3922	3922	0	4690	4690	0.722	0.508	0.863	0.508	0.863
	L-1/FB-A	7406.3	6316	6316	0	6799	6799	0.924	0.933	0.995	0.933	0.995
	L-1/FB-C	6547.3	4943	4943	0	5310	5310	0.807	0.311	0.867	0.311	0.867
	L-1/FB-C	6654.3	4982	4982	0	5823	5823	0.800	0.677	0.936	0.677	0.936
	L-1/FB-C	6714.3	5349	5349	0	5747	5747	0.852	0.427	0.915	0.427	0.915
	L-1/FB-C	6805.3	5379	5379	0	5727	5727	0.845	0.353	0.900	0.353	0.900
	L-5/FB-C	6985.0	6137	6137	0	6439	6439	0.947	0.880	0.994	0.880	0.994

TABLE A2: Continued.

Struct./ strat. position	Reservoir	SSTVD [feet]	Depl. Pp [psi]	Rest. Pp [psi]	ΔPp [psi]	Rest. Sh (A=0.8) [psi]	Rest. Sh (ν=0.3) [psi]	λ initial	K (A = 0.8)	Sh/Sv (A = 0.8)	K (ν = 0.3)	Sh/Sv (ν = 0.3)
Mini-basin, shallow	IC-4 /FB-B	5515.3	3144	3415	271	4737	4675	0.683	0.834	0.947	0.795	0.935
	IC-4 /FB-B	5449.3	2485	3097	612	4946	4806	0.627	1.005	1.000	0.929	0.974
	IC-4/FB-B	5557.3	2539	3135	596	5047	4910	0.622	1.003	1.000	0.932	0.974
	KE-1/FB-B	6280.3	2976	3673	697	4328	4168	0.640	0.317	0.754	0.239	0.726
	KE-1/FB-A	6037.3	3055	3662	607	4221	4082	0.665	0.302	0.766	0.227	0.741
	LF/FB-A	6688.7	3829	3971	142	5192	5159	0.621	0.503	0.811	0.490	0.806
	LF/FB-B	6917.3	2373	4079	1706	5670	5279	0.642	0.699	0.892	0.527	0.831
Mini-basin, deep	NH/FB-A	6951.4	3676	5096	1420	6215	5890	0.795	0.854	0.970	0.606	0.919
	NH/FB-B	6811.3	3839	3839	0	5199	5199	0.614	0.564	0.832	0.564	0.832
	OI-1/FB-C	7727.3	2642	5338	2696	7463	6845	0.746	1.171	1.044	0.831	0.957
	OI-4/FB-E	6923.3	4350	5415	1065	5914	5670	0.850	0.524	0.929	0.268	0.891

TABLE A3: Initial pore pressure and stress data derived from pressure histories, integrated density logs, and minifracs in fracture completed sand reservoirs. Pp* denotes overpressure (i..e., above hydrostatic). K_{mean} and $\sigma hmin_{mean}$ were derived from depletion corrected stress data. Average values from sonic, gamma ray, and density log data come from wells penetrating the corresponding reservoirs.

Structural position	Reservoir	Average depth [SSTVD]	Well fracture completed	Pp (init) [psi]	Pp* [psi]	σv (init.) [psi]	K mean	σhmin mean [psi]	Well logged	Vp [ft/s]	GR	RHOB [g/cc]
Footwall	L-1/FB-A	7406	316/A-3ST	6316	2872.1	517.80	0.933	483	316/A-13	6375.9	45	2.1560
	L-1/FB-C	6654	316/A-1ST	4982	1887.8	1241.7	0.677	348	316/A-12	6259.4	46	2.2812
	L-1/FB-C	6714	316/A-12A	5349	2226.9	931.20	0.427	348	316/A-12	6259.4	46	2.2812
	L-5/FB-C	6985	316/A-12	6137	2889.0	343.00	0.880	302	316/A-12	6177.0	35	2.0099
Hangingwall	KE-1/FB-A	6037	330/C-12	3662	854.66	1846.9	0.265	489.1	330/B-13	9030.2	68	2.0787
	KE-1/FB-A	6037	330/C-12	3662	854.66	1846.9	0.265	489.1	330/C-19	7787.6	75	2.2442
	KE-1/FB-B	6280	330/C-8	3673	752.66	2067.3	0.278	574.79	330/A-21	7694.7	49	2.2357
	KE-1/FB-B	6280	330/C-8	3673	752.66	2067.3	0.278	574.79	330/A-22	8293.9	56	2.1780
	KE-1/FB-B	6280	330/C-8	3673	752.66	2067.3	0.278	574.79	331/#1	7681.1	47	2.1529
	LF/FB-A	6688	338/A-17	3971	860.95	2426.7	0.496	1204.3	330/B-13	8343.8	74	2.1832
	LF/FB-A	6688	338/A-17	3971	860.95	2426.7	0.496	1204.3	330/C-19	8609.6	73	2.2904
	LF/FB-B	6917	330/A-21	4079	862.46	2276.5	0.613	1395.4	330/A-21	7054.7	48	2.1440
	LF/FB-B	6917	330/A-21	4079	862.46	2276.5	0.613	1395.4	331/#1	7620.2	56	2.1498
	OI-1/FB-C	7727	330/A-22	5338	1744.8	1813.9	1.001	1816.1	330/A-22	7644.7	59	2.0900

CHAPTER 4

CHARACTERIZATION OF THE FULL STRESS TENSOR IN THE SOUTH EUGENE ISLAND 330 FIELD, OFFSHORE GULF OF MEXICO

4.1 Abstract

Dipmeter caliper logs from 38 different wells in the South Eugene Island (SEI) 330 field are used to identify stress-induced wellbore breakouts and to constrain in-situ stress orientation and magnitude. I applied rigorous and conservative criteria to maintain high levels of confidence and reliability in the analysis. The caliper data analysis yielded elongations of fair to good quality (poor quality data would not have passed through my strict selection criteria) in 21 wells that could be considered stress-induced breakouts. Least principal horizontal stress orientations in near-vertical wells (deviation < 20°) exhibit a relatively consistent picture for stress orientation in the SEI-330 field. While the stress directions vary spatially in between fault blocks, the orientation of the least principal horizontal stress, S_{hmin}, is predominantly perpendicular to the active growth faults. This is in agreement with a general extensional environment that is dominated by active normal faulting. Constraining the magnitude of the maximum horizontal stress (S_{Hmax}) in 2 wells with appreciable inclination (> 20°) is again consistent with a normal faulting state of stress in which the overburden S_v is the maximum principal stress (i.e., $S_v \geq S_{Hmax} \geq S_{hmin}$). The horizontal principal stresses are not equal, suggesting a non-isotropic state of stress. The pore pressure (P_p) conditions at each breakout depth in these two wells indicate severe overpressures (λ = 0.74, 0.95), where the least principal effective stress approaches zero. The effective compressive rock strength, C_0, varies by one order of magnitude and is below average values reported in the literature. I believe that this reflects poor sediment consolidation under undrained conditions.

4.2 Introduction

Knowledge of the in-situ state of stress in hydrocarbon producing fields is vital not only for borehole stability and sand production (e.g., Cooper, 1994) but also fluid migration (e.g., Barton et al., 1995) and fracture completion design (Economides and Nolte, 1989). For this reason, determination of the in-situ stress tensor has recently received a lot of attention in many hydrocarbon producing areas around the world (e.g., North Sea (Fejerskov, 1994; Brudy, 1998; Wiprut and Zoback, 1998), Scotian Shelf (Yassir and Bell, 1994), Gulf of Mexico (Zerwer and Yassir, 1994)). One way to determine the stress field is to measure the geometry of or image the wellbore wall after a well was drilled. It is well known that in response to the ambient stress field wellbore walls can fail leading to the development of characteristic features when the hoop stress around the borehole exceeds the rock strength in either compression to form breakouts (i.e., stress induced symmetrical

elongations; e.g., Bell and Gough, 1979; Zoback et al, 1985) or tension to form tensile fractures (e.g., Aadony, 1990; Brudy and Zoback, 1993). Furthermore, using numerous observations of breakouts and/or tensile fractures in both vertical and inclined wells along with pore pressure data, Peska and Zoback (1995) and Zoback and Peska (1995) demonstrated that it is possible to constrain the full stress tensor (i.e., magnitude and orientation) and place bounds on mudweight and effective compressive rock strength.

In this study, I comprehensively investigate and characterize the maximum principal horizontal stress (S_{Hmax}) based on integration of fracture closure pressure, pore pressure, and observation of borehole breakouts from dipmeter caliper logs in the South Eugene Island (SEI) 330 field, offshore Gulf of Mexico (see chapter 1 for a geologic overview). By implementing these various measurements and observations into a number of models (the mathematical and physical basis for these models are described in Peska and Zoback, 1995, and Zoback and Peska, 1995), I constrain both rock strength and the unknown components of the stress tensor, typical the magnitude of S_{Hmax}.

First, I will carefully describe the conditions how to analyze and interpreted borehole elongations from caliper data to avoid pitfalls and misinterpretations. Then, I try to explain the resulting stress orientations in the SEI field in view of geologic structures at different stratigraphic levels and the overall tectonic regime. Finally, I attempt to constrain orientation and magnitude of S_{Hmax} using independent observations of pore pressure, the overburden stress (S_v), and the least principal horizontal stress (S_{hmin}).

4.3 Dipmeter logs and breakout interpretation

Dipmeter tools are frequently used in the petroleum industry to obtain stratigraphic information (e.g., bedding plane orientation) and to perform structural analysis (e.g., identification of unconformities or attitudes of fault planes) of the reservoir rocks in the pay zone. Because these tools acquire microresistivity values measured at the borehole wall, direct contact of the tool-pad electrodes with the borehole wall is required (Figure 4.1). For this reason, dipmeter tool arms - there are commonly four orthogonal arms - are hydraulically forced against the borehole wall. With this tool arrangement, borehole diameter can be mechanically recorded during the logging operation and, hence, yield useful and continuous information on borehole diameter, shape, and orientation over the logged interval. In general, as the tool is pulled up it can freely rotate given a borehole that is in-gauge. When the tool encounters an enlargement, however, rotation ceases and the diameter recordings of the two orthogonal caliper pairs differ (Plumb and Hickman, 1985)

(Figures 4.2A-E). By applying rigorous criteria (see below), the caliper data can be used to identify borehole breakouts for analysis of the state of stress.

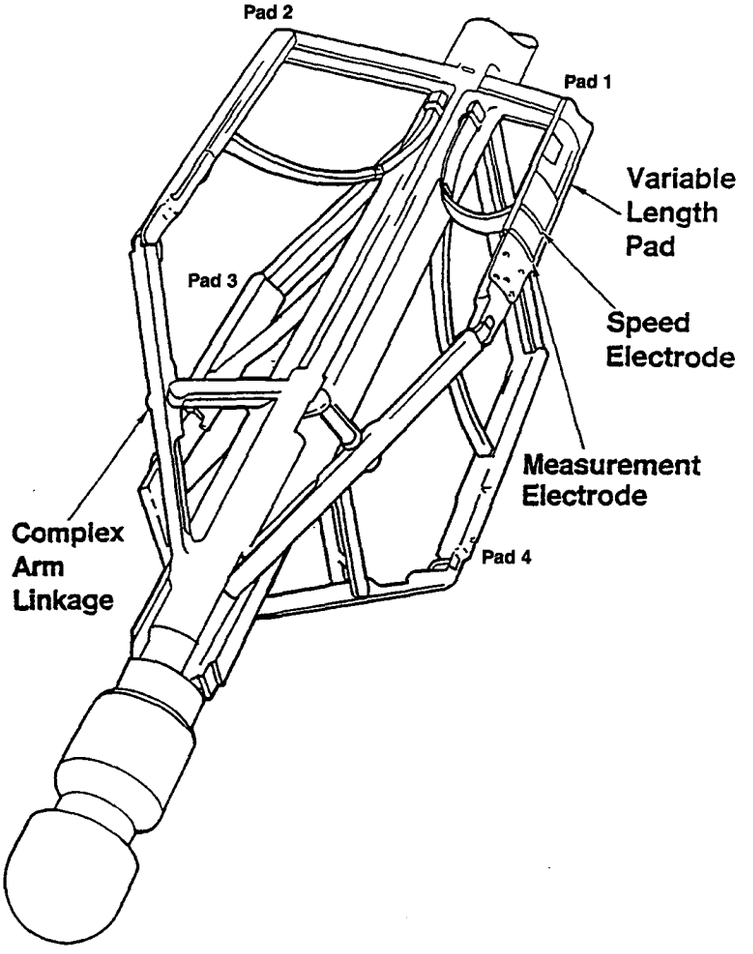

Figure 4.1: Schematic illustration of a 4-arm dipmeter tool (from Schlumberger, 1986). Note the four orthogonal caliper pads. Each opposite caliper pair (i.e., C1-3 and C2-4) measures diameter across the hole.

Stress-induced wellbore breakouts indicate the orientation of the maximum principal horizontal stress (S_{Hmax}) in the uppermost crust (Bell and Gough, 1979; Zoback and Zoback, 1980, 1991; Zoback et al., 1985; Plumb and Cox, 1987; Zoback et al., 1989). When the vertical stress (S_v) is nearly parallel to the wellbore, breakouts form in the direction of the minimum principal horizontal stress (S_{hmin}), where stress concentrations at the borehole wall exceed the rock strength (C_0). Mechanisms that describe the formation of these features are discussed extensively in the literature (e.g. Bell and Gough, 1979; Zoback et al., 1985; Zheng et al., 1989). In inclined wells, where the borehole axis is not

parallel with any of the principal stresses, the location of the breakouts around the wellbore rotates and does not indicate the true orientation of S_{hmin}. Observation of these breakouts from various nearby wells, however, can be utilized to determine not only stress tensor orientation but also principal stress magnitudes (Peska and Zoback, 1995).

Because of their frequent use, dipmeter logs and, hence, caliper data are abundantly available for most hydrocarbon producing provinces and, therefore, allow one to conduct detailed stress analysis over large areas using state-of the art software tools. In order to identify breakout intervals from the caliper data, certain criteria have to be met which provide a means to distinguish them from other borehole enlargements such as washouts or key seat. These two latter features (Figures 4.2C-E) are a result of the drilling process and occur frequently in inclined wells that penetrate poorly compacted and/or overpressured sediments such as the shales and sands encountered at greater depth in EI-330. Key-seats are easily misinterpreted as breakouts since they occur due to wear at the high-side of the hole by the drillpipe resulting in directional enlargements parallel to the hole-azimuth (HAZ, the direction of the well) while the orthogonal caliper pair can remain in-gauge (Figure 4.2D and 4.3A). For this reason, it is absolutely necessary to follow strict guidelines because misidentifications can lead to erroneous interpretations, hence, deceiving results for the state of stress. The criteria for interpreting an enlarged borehole interval as a breakout interval are as follows:

- Cessation of tool rotation resulting in a constant pad-1 azimuth (Figure 4.2E).
- Steady and continuous enlargement of one caliper pair, while the second pair is in-gauge with the bitsize (Figures 4.2B and E).
- The diameter difference between enlarged and in-gauge caliper pair is at least 1 inch.
- The enlarged caliper pair is not parallel with the hole-azimuth (HAZ); in other words, if pad1-azimuth (P1AZ, direction of the tool's pad1, see Figure 4.1) is parallel to HAZ, then caliper pair 2-4 (C2-4) must be enlarged in order to be a breakout; in turn, caliper pair 1-3 (C1-3) must be enlarged to be a breakout if P1AZ is at 90 or 270 degrees from HAZ (Figures 4.2E).

The fourth point is particularly critical and requires careful analysis of the data because it helps to distinguish between breakouts and key seats. Many case studies reported in the literature in the past but also more recently have shown that by applying less rigorous criteria (i.e., specifically by relaxing the third criterion listed above) for selecting and categorizing breakouts drastically increases the potential for interpreting other types of

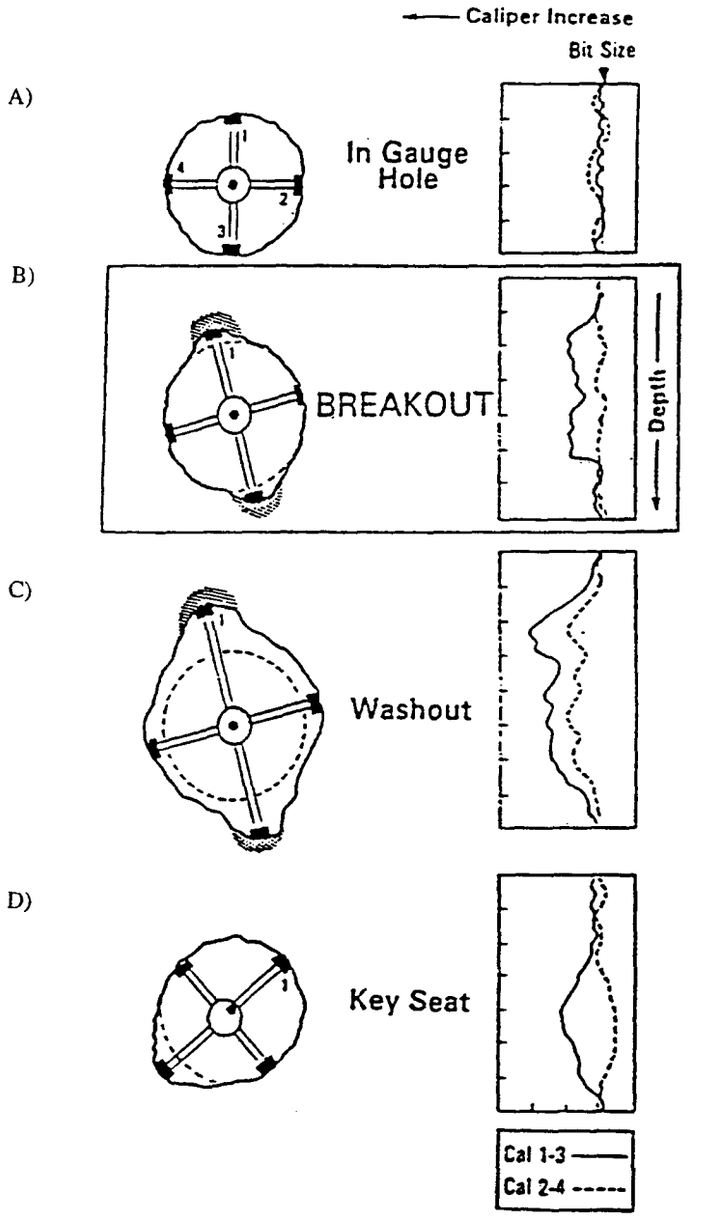

Figure 4.2: Illustration of typical caliper log data and various elongations as detected by a 4-arm caliper tool (from Plumb and Hickman, 1985). A: Cross-section (left) of an in gauge hole with a nearly circular shape (i.e., no elongations); both caliper pairs record more or less a diameter that is equal to the bit size of the hole (right). B: Borehole breakout with one caliper pair locked into the elongation (cross-section on left); this results in a diameter recording that is larger than the bit size (right); the second pair records a diameter approximately equal to the bit size. C: Borehole washout where both caliper pairs record diameters that are significantly larger than the bitsize. D: Cross-section (left) of key seat, which is a one sided borehole wall elongation in an inclined well; because one caliper pair records a larger diameter while the second is in gauge (right), this feature can easily be interpreted as a breakout and data monitoring caliper and borehole orientations are required to resolve this ambiguity.

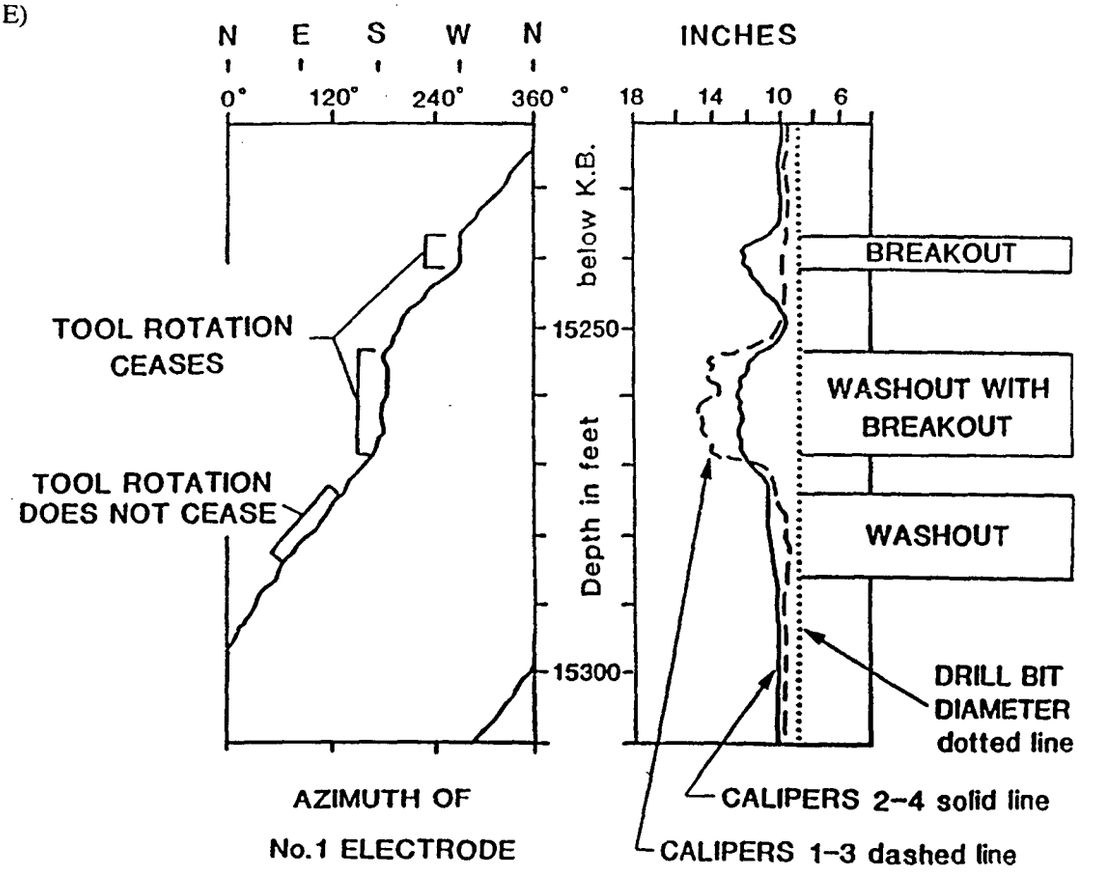

Figure 4.2: (Continued). E: Caliper orientation vs. depth (left) and diameter vs. depth (right) of breakouts and washouts; notice, how caliper orientation data can facilitate resolving the ambiguity between true, stress-induced borehole breakouts and other types of borehole elongations.

borehole elongations as breakouts. This results in questionable and ambiguous stress orientations and large spatial variations (e.g., Yassir and Zerwer, 1997). Also, vertical or near-vertical wells are commonly thought not to be subject to key seating. Only very recently, however, analysis of North Sea data have shown that key seat is even likely to occur ubiquitously in wells with less than 5 degree inclination (own unpublished observation).

For this reason all borehole enlargements I found and analyzed including those from vertical or near-vertical wells, were subject to the set of criteria outlined above. Figure 4.4A is a typical example of key-seat encountered in the suite of dipmeter logs and illustrates the problem discussed above. I believe that it is absolutely necessary to apply rigorous selection criteria for breakouts. These guarantee high levels of confidence when attempting

to understand and predict stress related mechanisms for hydrocarbon accumulation and migration.

4.4 South Eugene Island data set

I was able to analyze caliper data from 38 dipmeter logs acquired in South Eugene Island (SEI) blocks 316, 330, 338, and 339 (Figure 4.3). I present a detailed listing of the various caliper logs, the log type, the depth interval covered, and comments regarding the analysis in Table A1 in the appendix. Table A2 summarizes breakout occurrences for each well if any were observed.

The caliper data were generally provided on two tracks (Figures 4.4A and B): the two orthogonal bit sizes (C1-3 and C2-4) are plotted on one track along with a gamma ray (GR) log supplementing the acquisition. The second track displays borehole drift (i.e., HAZ, P1AZ, and borehole inclination INC) as tadpoles with two tails of different length. The short tail indicates P1AZ, while the long tail shows HAZ. In contrast to the continuous caliper curves, the tadpoles cannot be presented continuously over the logged intervals, thus, requiring a certain spacing in between. This presentation style has the disadvantage that there is no information on borehole drift at potential breakout intervals if they occur in between two adjacent borehole drift tadpoles. This problem became particularly obvious in well EI 338/A-21ST4 where I found a tadpole spacing of 100 ft. (see Table A1).

I estimate that the accuracy with which caliper data can be read from paperlogs is on the order of 15 degrees for angular parameters (i.e., INC, P1AZ, and HAZ) and within the range of 0.2 inches for the caliper diameters (i.e., C1-3 and C2-4). These errors have to be added to the general standard deviations of the resulting breakout data.

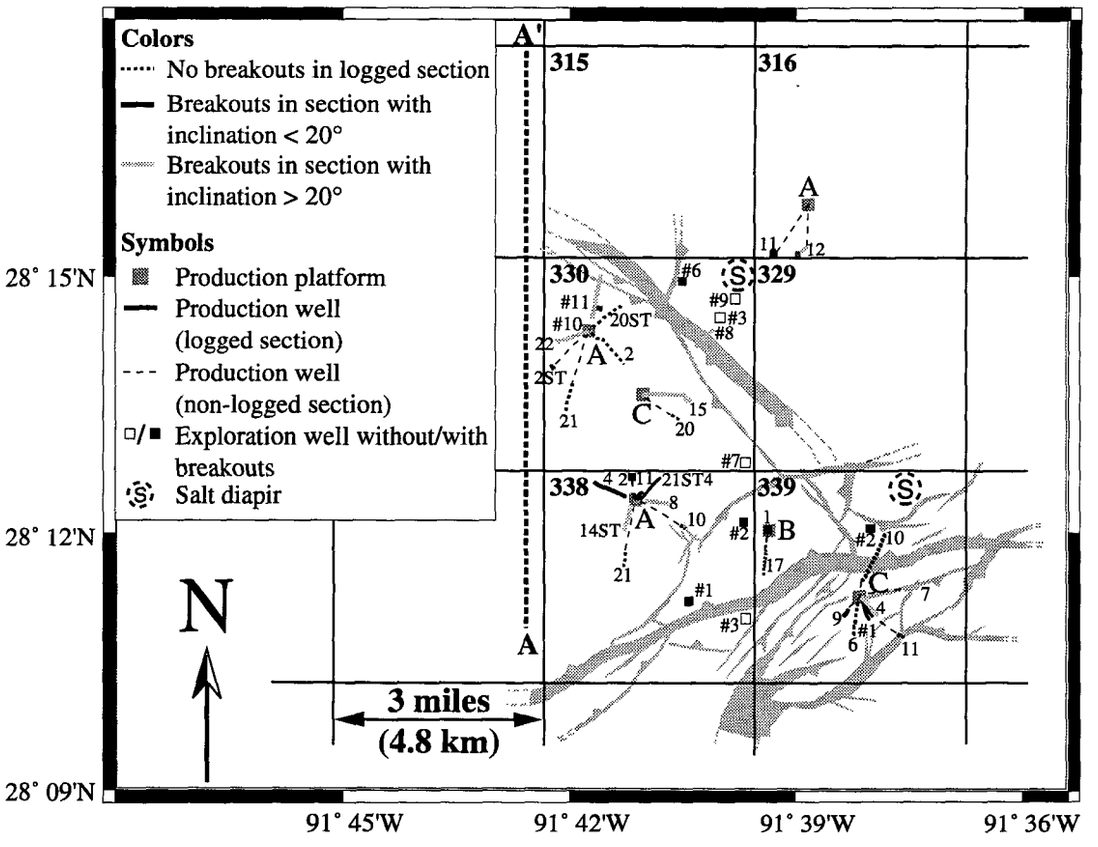

Figure 4.3: Basemap showing dominant structures of study area at level of GA-sand (refer to Figure 1.4) and trajectories of wells with available dipmeter logs. The thick, dashed line A-A' shows the approximate trend of the cross-section in Figure 1.4. This map was generated by combining Pennzoil's (blocks 329 and 330) and Texaco's (blocks 338 and 339) depth structure maps from 3-D seismic data interpretations of the GA sand level to obtain maximum structural coverage of the area. The map marks in black the intersections of basin bounding normal faults, which are vertical projections of the fault plane, with the GA horizon; the sides of relative downthrown sand sections are indicated with black triangles along the fault plane. Dashed lines mark inferred continuation of the faults. Locations of platforms, exploration wells, and borehole paths were obtained from Texaco's and Pennzoil's deviation data. The location of two salt diapirs was obtained from Alexander and Flemings (1995).

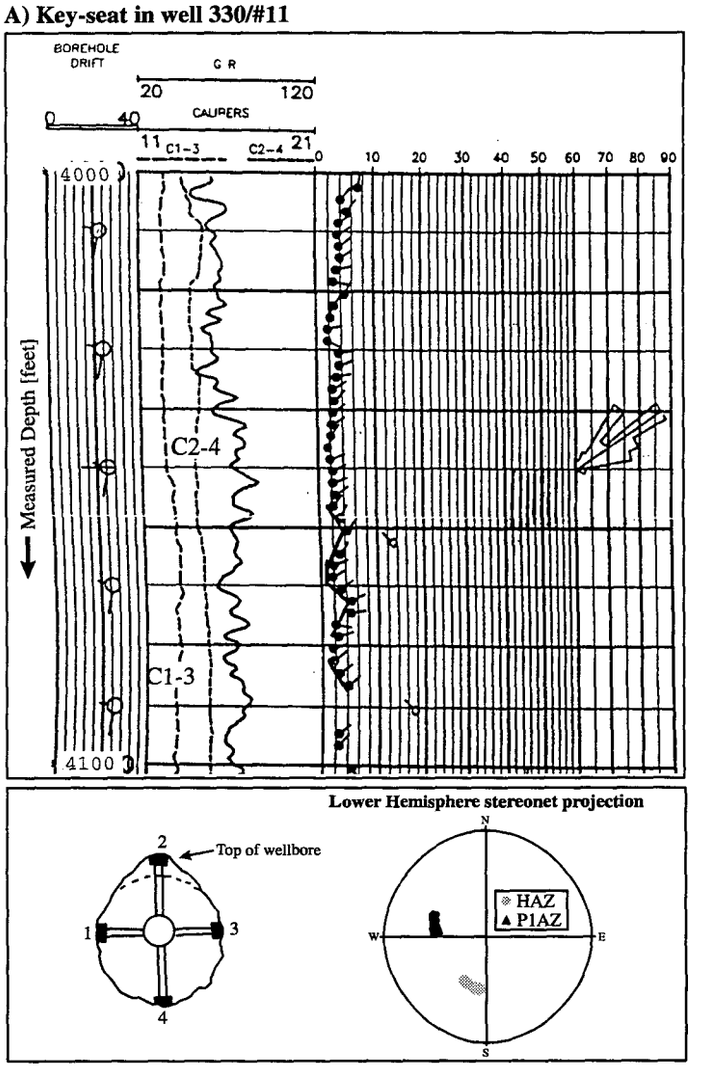

Figure 4.4: A: Examples of a typical key-seat in well 330/#11. The upper boxes display typical 4-arm dipmeter logs analyzed in this study. The track on the left shows borehole drift in tadpole style: the body indicates well-inclination, the short and long tails display P1AZ and HAZ respectively. The next track exhibits caliper size of caliper pairs C1-3 (long dash) and C2-4 (short dash). The solid line is the gamma ray (GR) log. The lower boxes show a schematic wellbore cross-section with caliper numbers on the left and on the right are lower hemisphere stereonet projections of wellbore (HAZ) and pad-1 (P1AZ) azimuths. Note, that P1AZ and HAZ are orthogonal (see stereonet) with C2-4 as the larger caliper; hence, the well is elongated in direction of its deviation (i.e., approx. N190E), where key-seats occur.

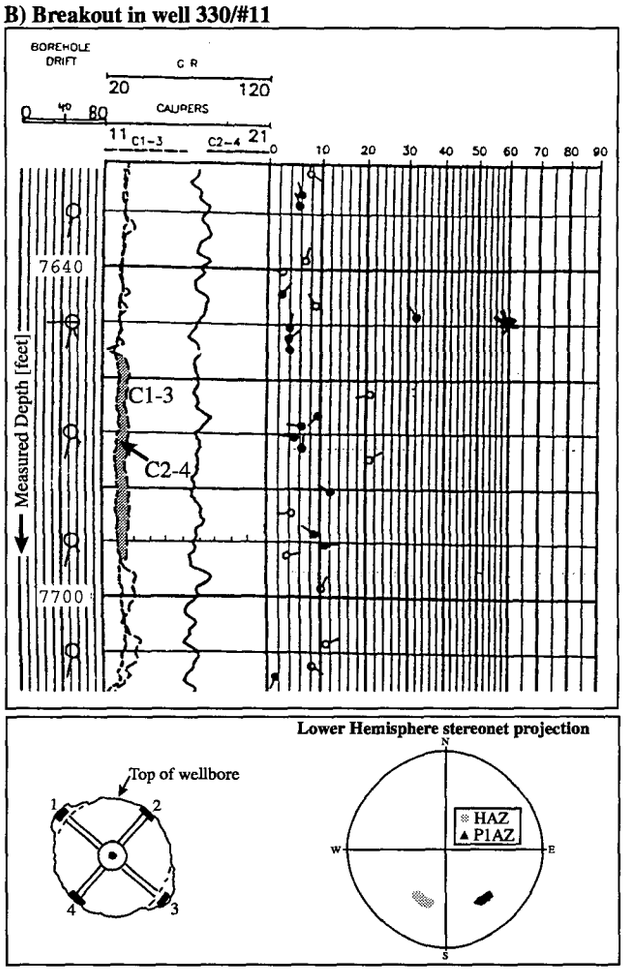

Figure 4.4: (Continued). B: Examples of a typical breakout (marked in gray) in well 330/#11. The upper boxes display typical 4-arm dipmeter logs analyzed in this study. The track on the left shows borehole drift in tadpole style: the body indicates well-inclination, the short and long tails display P1AZ and HAZ respectively. The next track exhibits caliper size of caliper pairs C1-3 (long dash) and C2-4 (short dash). The solid line is the gamma ray (GR) log. The lower boxes show a schematic wellbore cross-section with caliper numbers on the left and on the right are lower hemisphere stereonet projections of wellbore (HAZ) and pad-1 (P1AZ) azimuths. Note, P1AZ and HAZ are neither parallel nor orthogonal but at approx. 30 degrees from each other (see stereonet below); since C1-3 is larger than C2-4, the breakout is at P1AZ (i.e., approx. N160E).

4.5 Results and findings

Table A2 shows that only a small number of relatively reliable breakouts I observed in the caliper data from the 38 wells. I rank the quality of the selected breakouts to be fair or good because poor quality elongations would not pass through my rigorous selection

criteria described earlier. However, by means of the world stress map criteria (WSM; Zoback and Zoback, 1991) the observed breakout intervals receive, with a few exceptions, a low quality ranking (i.e., D or E). This low ranking is a reflection of the sparse and short (a few tens of feet on average) breakout intervals observed within the wells studied. I believe, the following three explanations for the limited and low quality data (by means of the WSM criteria) are most plausible: (i) the hoop stress around the wells is too low to exceed the compressive rock strength (i.e., S_{Hmax} - S_{hmin} is small and the rock is not failing to form breakouts), (ii) key seats and/or washouts are sufficiently ubiquitous to entirely mask stress induced breakouts (Figure 4.4A), or (iii) breakouts have formed but were not wide enough to be detected by the pads of the dipmeter tools. Revisiting Table A1, one notices that wells with no observed breakouts are either in-gauge (i.e., vertical wells) or contaminated by potential key seats because they were deviated. Since I think that the criteria applied to the borehole elongations observed are sufficiently rigorous and conservative, I am sure that any identified breakout (Figure 4.4B) truly reflects the state of stress in the EI area (in spite of the low ranking by the WSM criteria) and I will use them in the following analysis.

The observed breakout intervals occur over a fairly wide depth range (i.e., between 1600 ft. and 8130 ft. sub-sea total vertical depth, SSTVD) corresponding to the hydrostatically pressured HB and the hard-geopressured Lentic sand levels (Figure 1.4). It is important to note that breakouts can occur in deep, severely overpressured sediments. To find an explanation, I need to consider and compare two competing factors. Generally stresses rapidly increase with depth eventually reaching magnitudes at which compressive borehole failure occurs (Moos and Zoback, 1990). If, in addition, the rock is overpressured, like in the Gulf of Mexico, its strength is reduced due to undercompaction. This state of unconsolidation enhances the potential for compressive failure at the borehole wall and, therefore, breakouts are even more likely to occur. However, at the same time total differential stresses (i.e., S_{Hmax} - S_{hmin}), which control the magnitude of the hoop stress around the borehole wall, become very low at severe overpressures, because both the least and maximum horizontal principal stresses approach the overburden. Hence, the hoop stress around the borehole wall may fall below the compressive rock strength decreasing the likelihood for breakouts occurrence. Obviously, in the wells studied the former two factors appear to have dominated and favored breakout development in the deep, overpressured zone. Because sediments cored from reservoirs at this level show essentially no cementation (pers. com. to P. Flemings), a very low rock strength appears to be the responsible factor which allows even small differential stresses to cause compressive borehole wall failure.

4.6 Stress orientation

4.6.1 Overview

Depending on the inclination of the boreholes, there are two different ways to get the orientation of the stress tensor from wellbore breakout observations. In near-vertical wells with inclinations less than 20°, breakout directions indicate directly the orientation of the least principal horizontal stress (S_{hmin}) as described above. In highly deviated wells (i.e., inclinations greater than 20°), in contrast, breakouts rotate away from the S_{hmin} direction (Mastin, 1988) obscuring the true principal horizontal stress directions. However, stress orientation can be obtained from this type of breakouts given independent sources for S_{hmin} and pore pressure (P_p) (e.g., Peska and Zoback, 1995). While I devote an entire section below to discuss the latter issue in detail, I summarize the results for both approaches in the following paragraphs of this section. In Table A2 I indicate the wells with an appreciable amount of inclination (i.e., greater than 20°) with a star in the first column to distinguish them from the near-vertical wells (no star). However, in the following figures, I display the stress orientations for two highly inclined wells (316/A-12 and 330/A-22, see Table A2) because only in these two cases, the breakouts occurred in sand intervals for which I had independent and reliable pore pressure and stress data available to constrain the full stress tensor.

Plotting the stress orientations from each individual well on a structure map enables me to compare these with the general structure in the SEI field and the resulting S_{hmax} direction found in another study in this area by Zoback and Peska (1995). Note, that I assume that the overburden (S_v) is a principal stress axis. I think that this may be a reasonable assumption because vertical fractures were observed in the core (Losh, in press) and formation micro imager (FMI) data (Peska and Zoback, 1995) from the Pathfinder well, which is located within the same area (well 330/A20ST in Figure 4.3).

4.6.2 Expectations on the state of stress

In the context of Anderson's faulting theory (Anderson, 1937) principal stresses in extensional regions are approximately horizontal, less in magnitude from the vertical stress, and cause active faults to slip, which are oriented more or less perpendicular to S_{hmin}, the least principal horizontal stress. In this context, the least principal stress direction helps to distinguish between currently active and inactive faults by literally pointing towards the former. I would expect this to hold true also in the extensional environment of the Gulf of Mexico. In fact, Zoback and Peska (1995) conducted a detailed stress analysis of good

quality data in the Pathfinder well (well 330/A20ST in Figure 4.2) and demonstrated that the S_{hmin} direction is perpendicular to the major growth fault suggesting that it is active and dominates the stress field in its vicinity.

Because of the extremely variable geologic structures (both laterally and vertically), the presence of salt diapirs, and the spatially dispersed data throughout the field, I examine the resulting S_{hmin} directions in three different structural levels (GA, LF, and Lentic sands, Figure 1.4). Figures 4.5A-C display the resulting stress directions obtained from breakouts in wells with less than 20° inclination in red and from breakouts in wells with an inclination greater than 20° in green. Note, the arrows point outwards in the direction of S_{hmin}, which is also the azimuth of the mean breakout direction.

4.6.3 GA Sand

The GA sand (Figure 4.5A) is the shallowest sand studied (4,150 ft. to 5,500 ft. SSTVD). It is characterized by near-hydrostatic pore pressures (i.e., $\lambda = P_p/S_v = 0.465$) and the values for the effective stress ratio, K (σhmin/σv), range from 0.46 to 0.61. At this structural level, there are two major fault sequences: (i) the regional, NW-SE striking growth fault through block 330 and (ii) the counterregional, SW-NE striking fault through blocks 338 and 339. Also, the map shows many smaller scale normal faults resulting in a rather complex structural distribution of the SEI field. See Alexander and Flemings (1995) for a more detailed discussion on structure and stratigraphy. The borehole breakout orientations are varied but suggest that the S_{hmin} directions are perpendicular to the main basin bounding growth fault system. Particularily in the south, S_{hmin} directions are more or less perpendicular to the NE-SW striking main normal fault. In well 339/B-1 the stress orientations are dominated by the more distant NW-SE striking main basin bounding growth fault. I believe that the minor faults close to those two wells are currently inactive and do not contribute to the state of stress in the field. This explanation has the interesting aspect that the resulting S_{hmin} directions from my breakout study would always point in the direction of active faults which are also believed to be potential hydrocarbon migration pathways (e.g., Hooper, 1991; Barton et al., 1995). The stress orientation observed in the north of block 330 (well 330/#6) could be induced either by the small fault splay to the east of the main fault or perhaps by the salt diapir in the northeast corner of block 330. I believe these strong variations in stress orientations could be an indication of relatively low horizontal stress anisotropy.

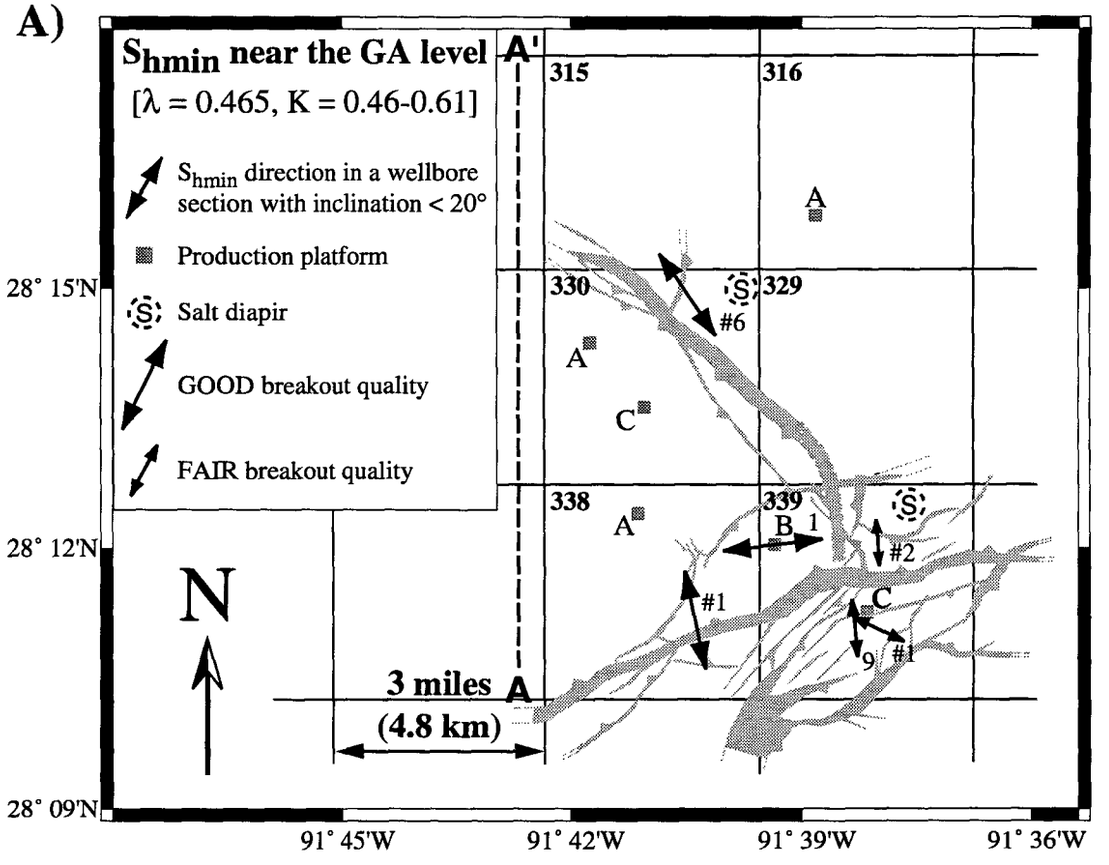

Figure 4.5: A: Basemap of the GA sand horizon displaying S_{hmin} directions resulting from the borehole breakout observations. We only display fair and good quality breakouts because lower quality data are not considered in this study. Dashed line A-A' shows approximate transsect of cross-section from Figure 1.4. Refer to Figure 4.3 for well trajectories, location of exploration wells, and how these maps were generated.

4.6.4 LF Sand

The LF sand (Figure 4.5B) is the intermediate sand studied (6,000 ft. to 7,600 ft. SSTVD) and characterized by moderate overpressures (i.e., $\lambda = 0.64$). K ranges from 0.71 to 0.75. The structural maps show the main basin bounding growth fault sequence along with some minor antithetic normal faults. The inferred southward extension of the main growth fault into block 339 (dashed in the figure) is based on maps shown by Alexander and Flemings (1995). Three wells exhibit S_{hmin} directions that are (sub-)perpendicular to the nearest normal fault, which is in agreement with my expectations. In block 338, the stress orientation in the well that is furthest to the west appears not to be influenced by the smaller scale, proximal normal faults but rather the distant main basin bounding fault

system. Perhaps, in this case, the minor fault is inactive and does not contribute to the current state of stress and, hence, may also not be important to fluid flow.

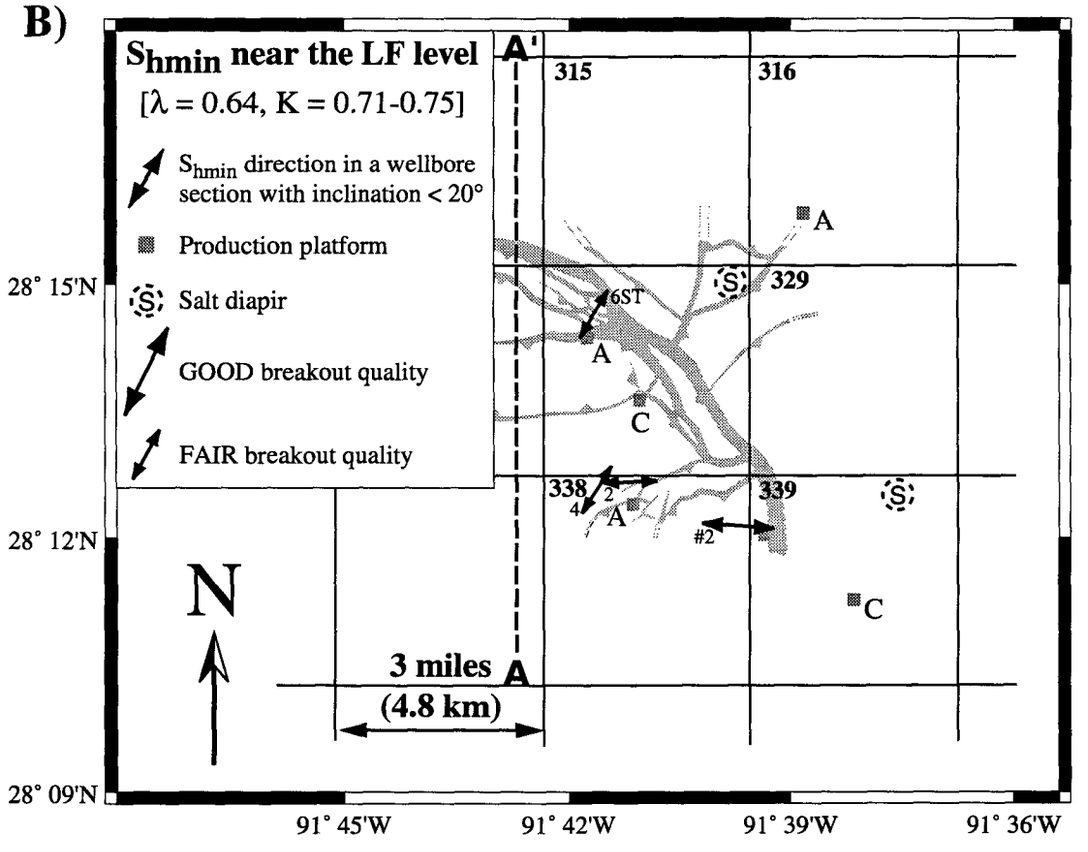

Figure 4.5: (Continued). B: Basemap of the LF sand horizon displaying S_{hmin} directions resulting from the borehole breakout observations. We only display fair and good quality breakouts because lower quality data are not considered in this study. Dashed line A-A' shows approximate transsect of cross-section from Figure 1.4. Refer to Figure 4.3 for well trajectories, location of exploration wells, and how these maps were generated.

4.6.5 Lentic Sand

The Lentic sand (Figure 4.5C) is the deepest reservoir in the SEI field (6,500 ft. to 11,200 ft. SSTVD) and characterized by extremely overpressured conditions (i.e., $0.85 < \lambda < 0.95$), which is also reflected in the values for K (0.74 - 0.84). The structural map portrays a very complex picture of normal faults at this level. However, the main basin bounding growth fault striking through block 330 and an antithetic normal fault through blocks 315 and 316 are still obvious.

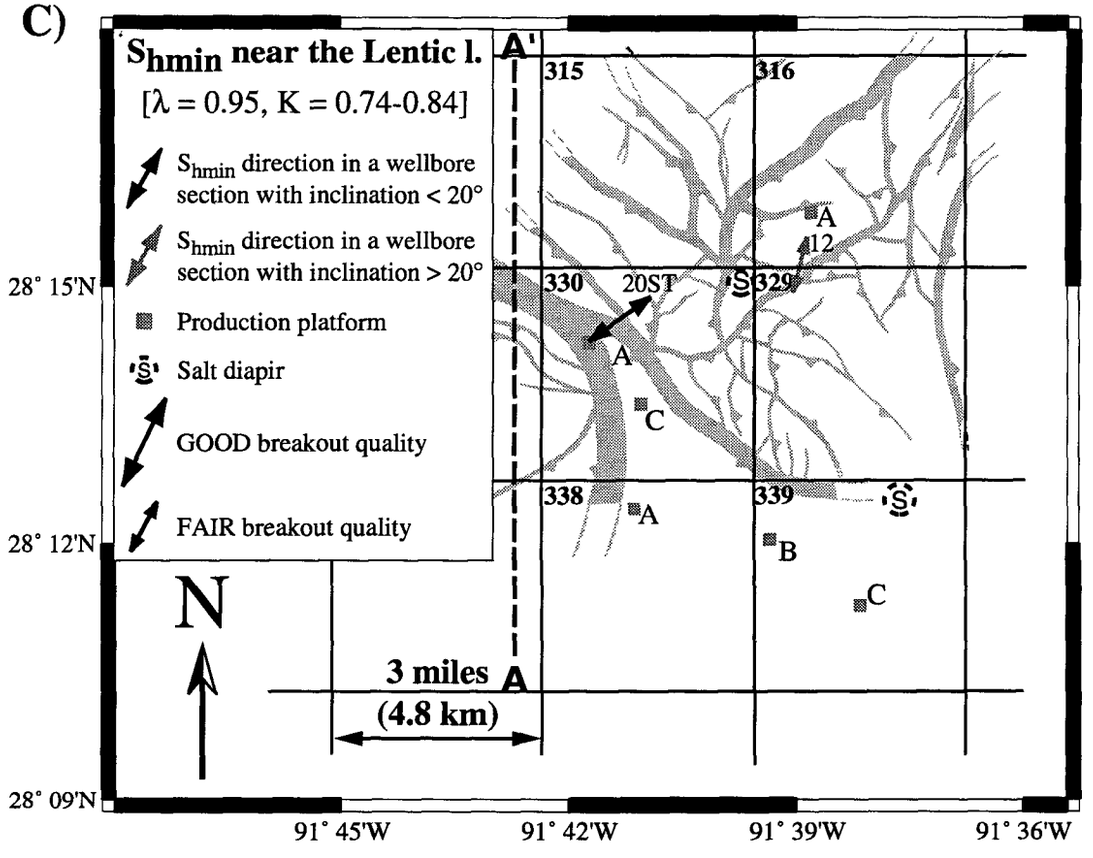

Figure 4.5.: (Continued). C: Basemap of the Lentic sand horizon displaying S_{hmin} directions resulting from the borehole breakout observations. We only display fair and good quality breakouts because lower quality data are not considered in this study. Derivation of stress direction in the highly inclined 316/A-12 well is described in detail below. The stress direction in the Pathfinder well (well 330/20ST) (Zoback and Peska, 1995) is shown for reference. Dashed line A-A' shows approximate transsect of cross-section from Figure 1.4. Refer to Figure 4.3 for well trajectories, location of exploration wells, and how these maps were generated.

The S_{hmin} directions of well A20ST (Pathfinder well) (Zoback andPeska, 1995) in block 330 is perpendicular to the main normal fault as I would expect. In contrast, S_{hmin} in the inclined well in block 316 (A-12, gray arrow) parallels an antithetic normal fault. It remains unclear to me why there exists such a discrepancy in the orientation of S_{hmin} between the two proximal wells in block 316 given their similar stratigraphy and pore pressure conditions. Perhaps, the near isotropic state of stress in this severely overpressured environment that allows localized stress perturbations to be responsible for seemingly random breakout orientations.

4.6.6 Summary

The results presented above show that the state of stress in the SEI field is characteristic of an active normal faulting environment, where, in general, the least principal stress is perpendicular to the main basin bounding and smaller scale normal faults. However, I can identify appreciable variations induced by either salt diapirs or relatively small horizontal stress anisotropy, which could be similar to results published by Yassir and Zerwer (1997). In some cases, the stress orientation may also reflect the influence of more distant faults because proximal faults could be inactive. This suggests that the observed S_{hmin} directions always point towards the currently active faults because they dominate the local state of stress in their vicinity. Since the active faults are also believed to provide pathways for fluid flow (e.g., Hooper, 1991; Barton et al., 1995), the stress directions obtained from this study could also point towards potential migration pathways in the SEI field. Currently inactive faults, in contrast, do not influence the state of stress in the area and are also considered to be unimportant for fluid flow. The results hold for three different stratigraphic levels with extremely high structural variability and are also independent of pore pressure conditions, which vary between hydrostatic and severely overpressured. This conclusion is also consistent with results from the stress analysis in the Pathfinder well (Zoback and Peska, 1995) and with Anderson's faulting theory (Anderson, 1937) as described above.

4.7 Constraining the full stress tensor and compressive rock strength

4.7.1 Overview

In this section I attempt to constrain the full stress tensor and rock strength (i.e., effective uniaxial compressive rock strength, C_0) from wellbore failure in deviated boreholes by using specific stress models that were described in detail by Peska and Zoback (1995) and Zoback and Peska (1995). Similar to the analysis in the Pathfinder well (well 330/A-20ST in Figure 4.3) (Zoback and Peska, 1995), I utilize borehole breakout observations in inclined wells (i.e., inclination >20°) in association with independent pore pressure, least principal stress, and maximum principal stress measurements in order to determine S_{Hmax} magnitude and C_0. As mentioned above, two wells qualify for this type of analysis (330/A-22 and 316/A-12, see Table A2) because in these two cases, the observed breakouts occurred in reservoir sands for which I have independent and accurate least principal stress magnitude (S_3) data from minifrac measurements available.

4.7.2 Assumptions and in-situ pore pressure and stress values

For this analysis I assume that the effective stress ratio [$K = (S_{hmin}-P_p)/(S_v-P_p)$] (Finkbeiner et al., 1996) is constant between the depth of the stress/pore pressure measurements and the depth of the observed breakout, and that the overburden (S_v) is a principal stress axis. Again, this latter assumption is based on the fact that vertical fractures were detected in the core of the Pathfinder well (well 330/A-20ST in Figure 4.3) (Losh, in press) and FMI logs (Peska and Zoback, 1995). Hence, the problem of constraining the full stress tensor is reduced to two unknowns: magnitude and orientation of S_{Hmax}. Table A3 summarizes the input parameters and modeling results of the stress tensor analysis for the two highly deviated wells. I obtained the overburden (S_v) by integrating density logs. Note, at the breakout depths in the two wells I observe severely overpressured conditions with λ=0.74 in well 330/A-22 and λ=0.96 in well 316/A-12 (Table A3).

4.7.3 Parameters and modes for constraining the full stress tensor

The input consists of assumed and in-situ measured values of various parameters at the observed breakout depth. These parameters are: wellbore azimuth (Azi) and deviation (Dev), pore pressure (P_p), mudweight (P_m; assumed to be equal to P_p), least principal horizontal stress (S_{hmin}; from minifrac), coefficient of internal friction (IntFric; assumed to be 1), Poisson's ratio (PoisRat; assumed to be 0.25; although the analysis is essentially independent of this parameter), breakout azimuth (aziBO) measured counterclockwise from the bottom of the well in a coordinate frame that has one principal axis parallel-downward to the borehole axis. For the breakout width (wBO) I assumed a minimum value of at least 20° (otherwise the dipmeter tool would not have detected the breakout) and a maximum value of 90°, which corresponds to half of the wellbore's circumference that has failed in compression (any larger value for wBO would lead to a washout which I would discard from the analysis). Because breakout width is a function of compressive rock strength (Zoback et al., 1985; Vernik and Zoback, 1992), the two bounding wBO values enable me to deduce lower and upper bound for C_0.

Given these input parameters, constraining the stress tensor can be carried out in two different modes:

(i) ranges of maximum principal horizontal stress magnitudes (S_{Hmax}) and orientations (aziSH); this requires the specification of a magnitude value for S_{hmin} from an independent measurement (e.g., minifrac, leak-off test, or formation integrity test).

(ii) ranges of S_{hmin} and S_{Hmax} magnitudes, which requires specification of stress ori-

entation from an independent observation (i.e., from a breakout observed in a near-vertical well nearby).

After performing a grid search in between these different stress ranges, the outputs render possible stress tensor values for aziSH versus S_{Hmax} in case (i) and S_{hmin} versus S_{Hmax} in case (ii) that are consistent with the observed borehole breakouts. These results are gray color coded as a function of critical C_0 values for which compressive borehole failure would occur under conditions consistent with the in-situ observations.

4.7.4 Constraining S_{Hmax} magnitude

Figure 4.6 shows results of mode (i) runs. The gray areas indicate all possibilities of S_{Hmax} magnitudes and azimuths plus the associated C_0 values so that breakouts can occur that are consistent with the given borehole deviation and stress and pore pressure data at the observed breakout depths. Given that S_v and S_{hmin} were obtained from independent data and the assumption that the S_v is a principal stress, I can find the two missing stress components (i.e., S_{Hmax} magnitude and azimuth) in the following way in case of well 330/A-22 (Figure 4.6A): the grayish area pinches out towards 7,125 psi and S_v is an upper bound; therefore, S_{Hmax} ranges from 7,125 psi to 7,549 psi at azimuths from 145° to 170°, which constrains the full stress tensor. Effective rock strength, C_0, in this case, ranges from approximately 3,300 psi to 3,700 psi. I determined the stress tensor for well 316/A-12 in a similar fashion (Figure 4.6B and Table A3).

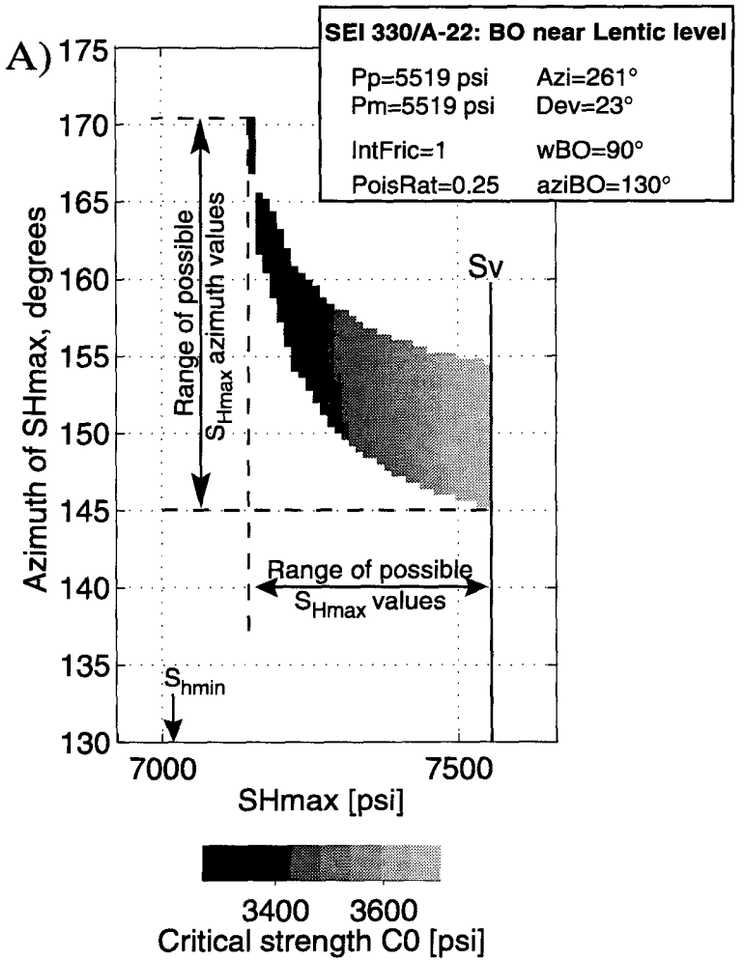

Figure 4.6: A: Well 330/A-22 near the Lentic sand. Resulting ranges of S_{Hmax} magnitudes and orientations and associated compressive strength values, C_0, from stress tensor modeling consistent with breakout occurrence and in-situ pore pressure and stress conditions. The annotated values for S_{hmin} and S_v come from independent measurements and provide lower and upper bounds respectively to determine S_{Hmax} magnitude and orientation. Notice, this plot presents the result for a breakout width (wBO) of 90° (assumed maximum); corresponding results for wBO=20° (assumed minimum), which only affect the value of for C_0, are shown in Table A3. The abbreviation "BO" in the legend stands for breakout.

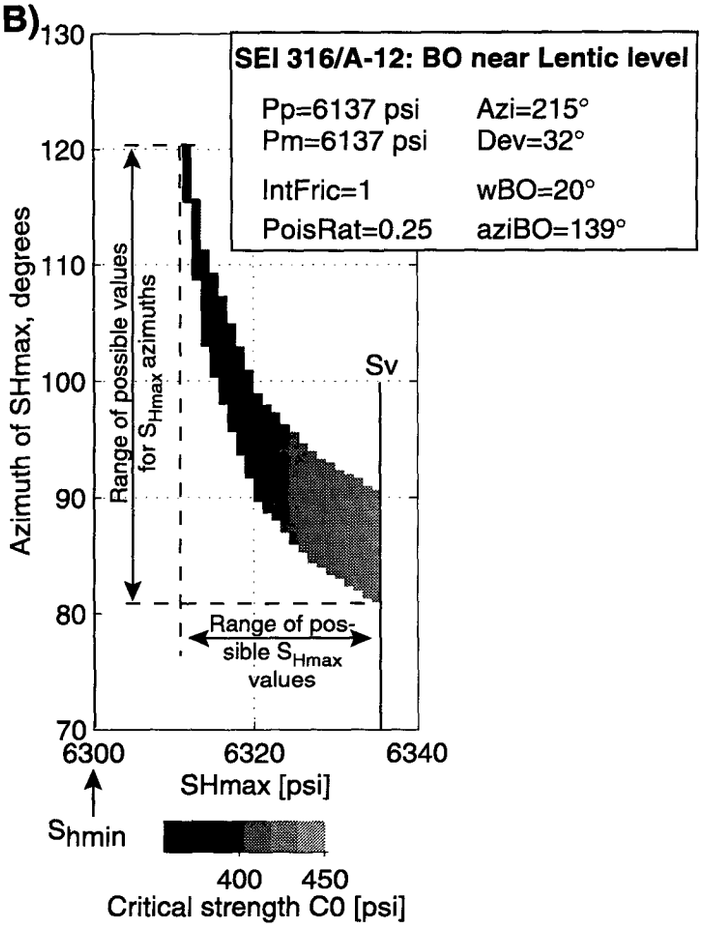

Figure 4.6: (Continued). B: Well 316/A-12 near the Lentic sand. Resulting ranges of S_{Hmax} magnitudes and orientations and associated compressive strength values, C_0, from stress tensor modeling consistent with breakout occurrence and in-situ pore pressure and stress conditions. The annotated values for S_{hmin} and S_v come from independent measurements and provide lower and upper bounds respectively to determine S_{Hmax} magnitude and orientation. Notice, this plot presents the result for a breakout width (wBO) of 20° (assumed minimum); corresponding results for wBO=90° (assumed maximum), which only affect the value of for C_0, are shown in Table A3. The abbreviation "BO" in the legend stands for breakout.

Since I already discussed the resulting stress orientations in Figs. 4.5A - C, I focus in the following paragraph on the stress magnitudes. Figures 4.7A and B show plots from mode (ii) runs. In these cases, the gray areas represent possible combinations of C_0 and stress magnitudes for breakouts to occur that are consistent with the in-situ observations. Since these figures plot stress on both axis, they do not provide any further information on S_{Hmax} azimuths, but can be used to constrain S_{Hmax} magnitudes by specifying S_{Hmax} orientations obtained independently from breakout observations in nearby wells (noted in

the labels of Figures 4.7A and B). Using S_{hmin} and S_v magnitudes as previously, I can demonstrate that the S_{Hmax} magnitude is bound by intersecting the dashed S_{hmin} lines with the gray areas. I find for the S_{Hmax} magnitudes the following values: a range from 7,180 to 7,300 psi in case of well 330/A-22 (Figure 4.7A) and ~ 6,315 psi in case of well 316/A-12 (Figure 4.7B). As the figures in both cases also show, the S_v magnitude plots to the right of the gray areas indicating that it is the maximum stress. Because I assume that S_v is a principal stress, I can identify S_{Hmax} as the intermediate principal stress, S_2, and S_{hmin} as the least principal stress, S_3. The results from these two figures confirm a normal faulting environment where $Sv \geq SHmax \geq Shmin$.

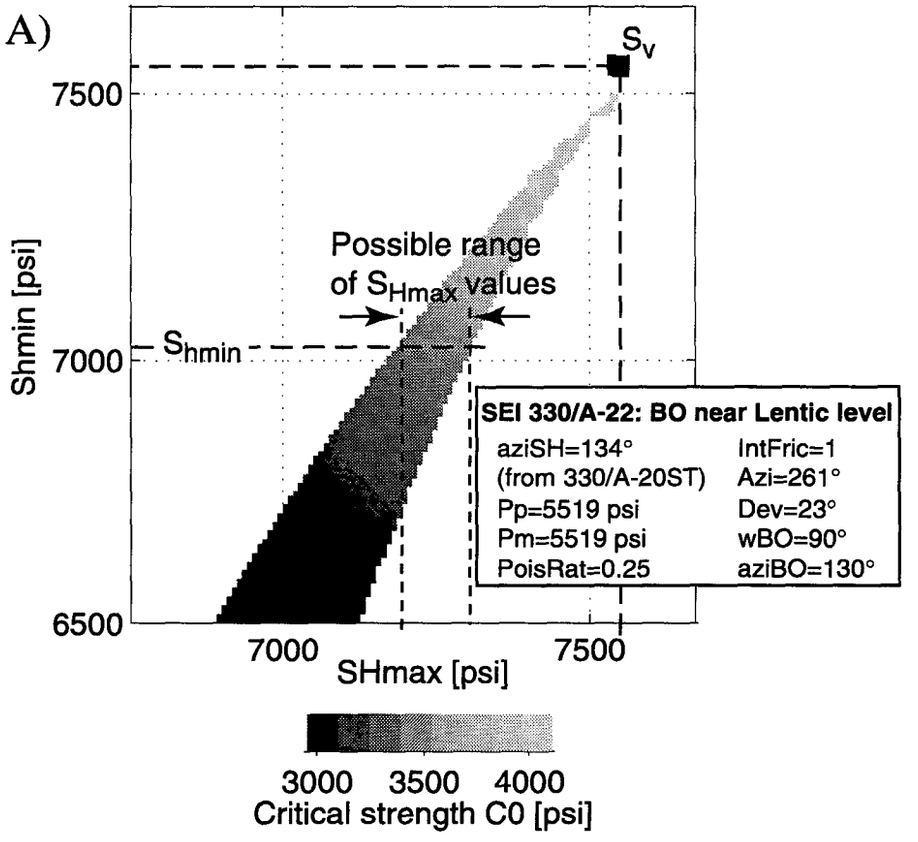

Figure 4.7: A: Well 330/A-22 near the Lentic sand. Resulting S_{Hmax} magnitude and associated compressive strength values, C_0, from stress tensor modeling consistent with breakout occurrence and in-situ pore pressure and stress conditions. The annotated values for S_{hmin} and S_v come from minifrac and density log measurements respectively and provide lower and upper bounds to determine S_{Hmax} magnitudes. The independent S_{Hmax} orientation is from well 330/A-20ST (Pathfinder; Zoback and Peska, 1995). Notice, this plot presents the result for a breakout width (wBO) of 90° (assumed maximum); corresponding results for wBO=20° (assumed minimum), which affect the value of C_0, are shown in Table A3.

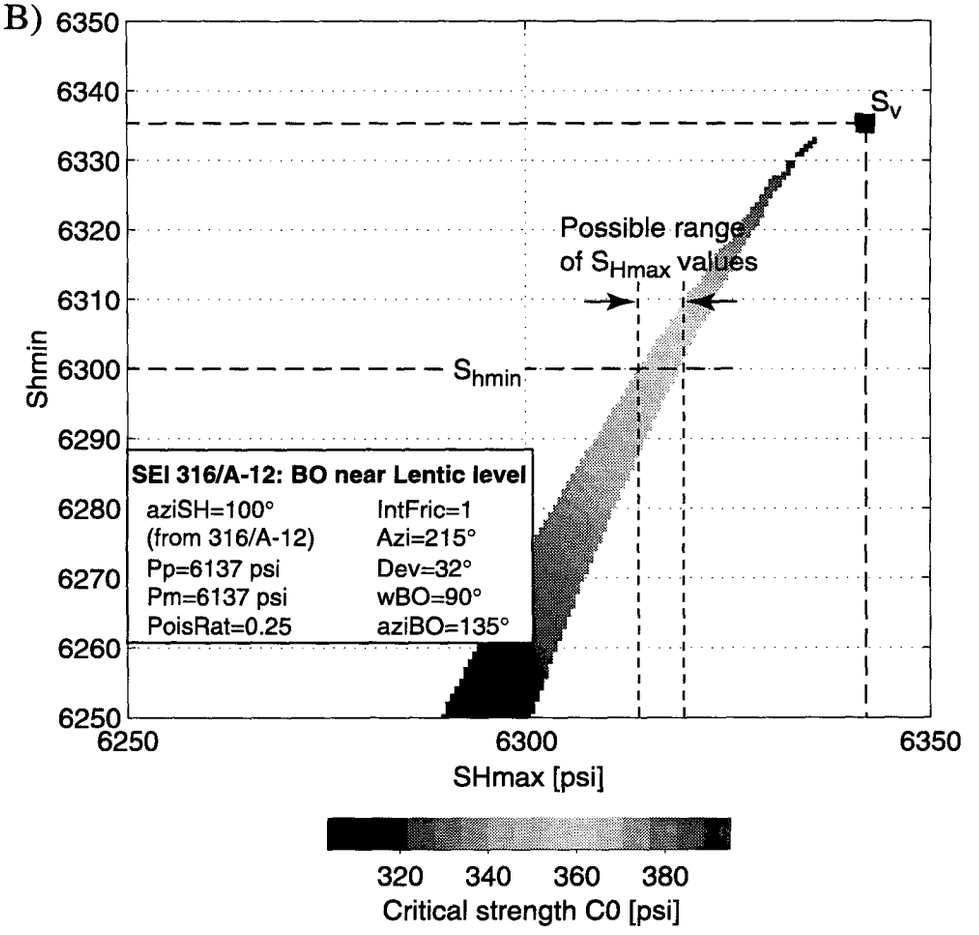

Figure 4.7: (Continued). B: Well 316/A-12 near the Lentic sand. Resulting S_{Hmax} magnitude and associated compressive strength values, C_0, from stress tensor modeling consistent with breakout occurrence and in-situ pore pressure and stress conditions. The annotated values for S_{hmin} and S_v come from minifrac and density log measurements respectively and provide lower and upper bounds to determine S_{Hmax} magnitudes. The independent S_{Hmax} orientation is from the same well at shallower depth and near vertical inclination. Notice, this plot presents the result for a breakout width (wBO) of 90° (assumed maximum); corresponding results for wBO=20° (assumed minimum), which affect the value of C_0, are shown in Table A3.

4.7.5 Implications for the state of stress in the SEI field

An important result is that S_{hmin} and S_{Hmax} values are not equal even at depths of severe overpressure. This finding clearly indicates that the state of stress in the SEI field is not isotropic and differential stresses can exist in the principal horizontal stress plane. This is a particularly interesting point because it is commonly assumed that S_{hmin} equals S_{Hmax} in the Gulf of Mexico. This assumption resulted in the use of uniaxial strain models to predict stresses and to describe fracture gradients in reservoir sands (e.g. Daines, 1982). In fact,

considering that breakouts did form in the SEI field is in itself sufficient evidence that differential principal horizontal stresses have to exist for the development of hoop stress around the wellbore; this is a necessary condition for stress induced breakouts to form. Nevertheless, the variations in the stress orientations seen at the GA level (Figure 4.5A) and in other studies (Yassir and Zerwer, 1997) suggest that the overall horizontal stress anisotropy is relatively small.

4.7.6 Implications for rock strength in the SEI field

Constraining the stress tensor from Figures 4.6 and 4.7 also provides values of effective uniaxial compressive rock strength, C_0 (Table A3). Knowledge of C_0 greatly facilitates the assessment of borehole stability in deviated wells given in-situ pore pressure and stress conditions. I find that in the two cases considered the values for C_0 vary by approximately one order of magnitude and are below the average range of effective compressive strengths for sands (Lockner, 1995). I attribute this to the overpressured conditions in-situ. Especially in case of the extremely overpressured Lentic sand C_0 is very low (~ 350 psi). This is consistent with the previous argument: in spite of the near isotropic stress state and the, consequently, almost vanishing hoop stress around the borehole, the effective rock strength had to be sufficiently low for breakouts to form. This low C_0 value not only reflects the undrained conditions (i.e., vanishing effective stresses) and poor sediment consolidation in-situ but also implies that minor load changes (e.g., caused by production related pore pressure drawdown) could induce failure. As a result, wellbores may become very unstable possibly leading to borehole wall collapse and sand production. In terms of reservoir behavior, nearly zero effective stresses accompanied by very low compressive rock strength imply that the sediments are in a state of incipient failure and become 'leaky' (i.e., are characterized by increased permeability) (Grauls and Baleix, 1994).

4.7.7 Summary

I constrained the full stress tensor in two highly deviated wells (i.e., inclination > 20°) of the SEI field using breakout observations that occurred in sands along with independent information on in-situ pore pressure and stress. As expected, the results indicate an active normal faulting environment in which the overburden is the maximum principal stress (i.e., $Sv \geq SHmax \geq Shmin$). In addition, the state of stress in the principal horizontal stress plane appears to be anisotropic (i.e., $SHmax \neq Shmin$). I also obtained values of uniaxial compressive rock strength, C_0, and find that under moderate to severe overpressures C_0 is highly variable (by one order of magnitude) but below average rock strength values

reported in the literature. This suggests that the sediments in the environment of approaching zero effective stress are highly susceptible for compressive failure potentially leading to wellbore collapse and poor reservoir sealing, which can result in enhanced permeability and fluid leakage.

4.8 Conclusions

Rigorous and conservative analysis of caliper logs from 38 different wells in the SEI-330 field yielded elongations in 21 wells that I consider stress-induced breakouts. These breakouts can be characterized by fair to good quality (poor quality data would not have passed through the strict selection criteria). Plotting the stress directions from breakouts in 12 near-vertical wells (deviation < 20°) on a basemap exhibits a relatively consistent picture for stress orientation in the SEI-330 field. While the stress directions vary spatially in between fault blocks, the orientations of the least principal horizontal stress, S_{hmin}, are predominantly perpendicular to the minibasin growth fault trends. This is in agreement with the fact that the state of stress in the SEI-330 field is extensional and dominated by active normal faulting. If, in fact, active faults are pathways for fluid migration, then the observed S_{hmin} directions could be used as a tool to point out the faults that currently conduct hydrocarbons. However, I also observed considerable scatter, that I attribute to relatively low horizontal stress anisotropy and inactive faults suggestive that do not play an important role in the current in-situ stress field.

Observation of wellbore breakouts in sand intervals from two wells with appreciable inclination (> 20°) is suitable to constrain the magnitude of the maximum horizontal stress (S_{Hmax}) and effective uniaxial compressive rock strength (C_0). The in-situ pore pressures at each breakout depth in the two wells indicate highly overpressured conditions ($\lambda = 0.74$, 0.94). Nonetheless, the results are again consistent with my expectations and indicate a normal faulting state of stress in which the overburden S_v is the maximum principal stress (i.e., $Sv \geq SHmax \geq Shmin$). The horizontal principal stresses are not equal, suggesting a non-isotropic state of stress. The effective rock strength, C_0, varies by one order of magnitude and is below average values reported in the literature. I believe that this reflects poor sediment consolidation under undrained conditions suggesting a state of incipient failure potentially leading to leaky sediments (i.e., enhanced permeability) in hydrocarbon reservoirs and stability problems in boreholes (e.g., sand production).

4.9 Acknowledgments

I would like to thank Pennzoil, Shell, Texaco, and Chevron for generously providing the data used in this analysis. Peter B. Flemings and Beth B. Stump provided invaluable help and suggestions during the preparation and revision of this manuscript. This project is funded by the Gas Research Institute under contract number 5095-260-3558 and the Stanford Rock and Borehole Geophysics (SRB) Consortium.

4.10 Appendix

Table A1

Table A1: List of analyzed caliper logs from 38 wells in blocks 316, 330, 338, and 339 of the South Eugene Island field (MD: Measured Depth; SSTVD: Sub-Sea Total Vertical Depth; FMS: Formation Micro Scanner; FMI: Formation Micro Imager; BO: breakout)

Well	Log Type	Depth Interval		Geographic Location (Long., Lat.)		Comments
		MD [ft]	SSTVD [ft]	Interval Top	Interval Bottom	
EI 316/A-11	Dipmeter	7600 - 8700	6089.7 - 7166.0	-91.6547, 28.2541	-91.6551, 28.2537	short BO intervals; rest in-gauge or keyseat
EI 316/A-12	FMI	7400 - 7520 7670 - 8230	6414.7 - 6520.0 6640.9 - 7119.5	-91.6490, 28.2544	-91.6492, 28.2541	short BO intervals; no indication for bitsize short BO intervals; no indication for bitsize
EI 330/#3	Dipmeter	3299 - 5399	3299.0 - 5399.0	-91.6660, 28.2409	-91.6661, 28.2409	no BOs; in-gauge
EI 330/#6	Dipmeter	1191 - 3501 3266 - 3501 3587 - 3717 4150 - 5292 9954 - 10,094 9868 - 10,005 9990 - 10,041	1190.5 - 3501.0 3265.5 - 3501.0 3587.0 - 3716.5 4149.5 - 5292.0 9953.5 - 10,093.5 9868.0 - 10,005.0 9989.5 - 10,041.0	-91.6730, 28.2490	-91.6730, 28.2490	two short BO intervals, rest in-gauge; vertical well no BOs, in-gauge; vertical well no BOs, in-gauge; vertical well no BOs, in-gauge; vertical well no BOs, in-gauge; vertical well no BOs, in-gauge; vertical well no BOs, in-gauge; vertical well
EI 330/#7	Dipmeter	3000 - 3800 5000 - 6500	2899.0 - 3699.0 4899.0 - 6399.0	-91.6607, 28.2134	-91.6607, 28.2134	no BOs; in-gauge no BOs; in-gauge
EI 330/#8	Dipmeter	1000 - 3500 3500 - 5900	899.0 - 3303.1 3303.1 - 5326.3	-91.6684, 28.2398	-91.6721, 28.2362	three intermittent BO intervals; rest keyseat or in-gauge no BOs, key-seat throughout
EI 330/#9	Dipmeter	3600 - 8700	3193.2 - 7990.4	-91.6630, 28.2470	-91.6630, 28.2470	no P1AZ indicated, useless
EI330/#10	Dipmeter	6084 - 6767 6089 - 6768	6084.0 - 6766.5 6088.5 - 6768.0	-91.6950, 28.2390	-91.6950, 28.2390	no deviation data; no Bos, calipers in-gauge no deviation data; no BOs, calipers in-gauge
EI 330/#11	Dipmeter	4000 - 7810	3893.0 - 7196.3	-91.6932, 28.2504	-91.6952, 28.2418	BOs at bottom; rest keyseat or in-gauge
EI 330/A-2	Dipmeter	5860 - 6660	5860.0 - 6660.0	-91.7035, 28.2327	-91.7036, 28.2325	no BOs; washouts or key-seat; near vertical
EI 330/A-2ST	Dipmeter	7000 - 7700	6449.7 - 6749.5	-91.6950, 28.2390	-91.6880, 28.2330	no BOs; dubious enlargements, most likely key-seat
EI 330/A-6ST	Dipmeter FMS	5560 - 7350 7280 - 7930	4745.8 - 7116.0 6456.0 - 6816.4	-91.6944, 28.2441	-91.6941, 28.2448	short BO intervals no P1AZ indicated, useless

Table A1: (Continued) List of analyzed caliper logs from 38 wells in blocks 316, 330, 338, and 339 of the South Eugene Island field (MD: Measured Depth; SSTVD: Sub-Sea Total Vertical Depth; FMS: Formation Micro Scanner; FMI: Formation Micro Imager; BO: breakout)

Well	Log Type	Depth Interval		Geographic Location (Long., Lat.)		Comments
		MD [ft]	SSTVD [ft]	Interval Top	Interval Bottom	
EI 330/A-21	Dipmeter	9500 - 13,700	8382.5 - 11,970.7	-91.6993, 28.2291	-91.7008, 28.2233	no BOs, key-seat throughout
EI 330/A-22	Dipmeter	7800 - 8800	7357.7 - 8290.9	-91.7017, 28.2375	-91.7028, 28.2373	one BO interval; rest keyseat or in-gauge
EI 330/C-15	Dipmeter	3952 - 4853 4801 - 5864 5800 - 6840 5803 - 6871 7171 - 7899	3951.5 - 4853.0 4800.5 - 5864.0 5799.5 - 6840.0 5802.5 - 6871.0 7170.5 - 7899.0	-91.6840, 28.2270	-91.6730, 28.2260	no BOs, calipers in-gauge no BOs, calipers in-gauge, appear to be in casing two BOs, rest in-gauge no BOs, calipers in-gauge, appear to be in casing no BOs, calipers in-gauge, appear to be in casing
EI 330/C-20	Dipmeter	7380 - 8130	6102.9 - 6821.9	-91.6775, 28.2232	-91.6757, 28.2222	no BOs, key-seat throughout
EI 338/#1	Dipmeter	3500 - 6550 5050 - 7250 7200 - 7550 7300 - 8300	3500.0 - 6550.0 5050.0 - 7250.0 7200.0 - 7550.0 7300.0 - 8300.0	-91.6850, 28.2070	-91.6850, 28.2070	good BO intervals; rest in-gauge some short BOs; long interval with useless C2-4 caliper no BOs; in-gauge no BOs; in-gauge
EI 338/#2	Dipmeter	6000 - 6300 6000 - 7150 6900 - 7250 7750 - 8650	5908.0 - 6208.0 5908.0 - 7058.0 6808.0 - 7158.0 7658.0 - 8558.0	-91.6610, 28.2020	-91.6610, 28.2020	no BOs; keyseat; tool rotates in enlargement BO at bottom; mostly keyseat no BOs; keyseat throughout no BOs; one long ambiguous enlargement, keyseat
EI 338/#3	Dipmeter	4020 - 4400 4000 - 5700	4020.0 - 4400.0 4000.0 - 5700.0	-91.6610, 28.1820	-91.6610, 28.1820	no BOs; vertical well; caliper pairs in-gauge no BOs; vert. well; dubious enlargements, HAZ rotating
EI 338/A-2	Dipmeter	5750 - 7100 6900 - 7100 7100 - 8350 8000 - 8350	5379.6 - 6725.0 6525.1 - 6725.0 6725.0 - 7973.7 7624.4 - 7973.7	-91.6859, 28.2109	-91.6861, 28.2112	no BOs; in-gauge6525.1 - 6725.0 no BOs; in-gauge short BO intervals; otherwise mostly in-gauge short BO intervals; otherwise mostly in-gauge

Table A1: (Continued) List of analyzed caliper logs from 38 wells in blocks 316, 330, 338, and 339 of the South Eugene Island field (MD: Measured Depth; SSTVD: Sub-Sea Total Vertical Depth; FMS: Formation Micro Scanner; FMI: Formation Micro Imager; BO: breakout)

Well	Log Type	Depth Interval		Geographic Location (Long., Lat.)		Comments
		MD [ft]	SSTVD [ft]	Interval Top	Interval Bottom	
EI 338/A-4	Dipmeter	3100 - 3900 3800 - 4800 4800 - 5800 5700 - 6750 6750 - 7750 7750 - 8000 7750 - 9250	2897.1 - 3578.4 3494.2 - 4336.7 4336.7 - 5182.2 5097.0 - 6010.9 6010.9 - 6937.2 6937.2 - 7170.3 6937.2 - 8404.2	-91.6875, 28.2072	-91.6947, 28.2100	no BOs; keyseat one BO; otherwise mostly keyseat no BOs; abundant keyseat; partly in-gauge no BOs; abundant keyseat; partly in-gauge no BOs; abundant keyseat; partly in-gauge no BOs; keyseat throughout short BO intervals; mostly keyseat
EI 338/A-8	Dipmeter	4000 - 7700	3772.3 - 7051.0	-91.6833, 28.2065	-91.6780, 28.2060	good BO intervals; rest keyseat or in-gauge
EI 338/A-10	Dipmeter	8500 - 10,000 10,000 - 10,150	7290.6 - 8684.4 8684.4 - 8834.6	-91.6755, 28.2018	-91.6745, 28.2013	no BOs; strange caliper traces, appear to be all keyseat no BOs; keyseat throughout
EI 338/A-11	Dipmeter	3100 - 4300	2876.0 - 3852.7	-91.6850, 28.2070	-91.6800, 28.2110	no BOs; keyseat throughout
EI 338/A-14ST	Dipmeter	4970 - 8980	4871.4 - 8326.2	-91.6863, 28.2055	-91.6881, 28.2007	one BO interval; rest keyseat or in-gauge
EI 338/A-21	Dipmeter	7410 - 8800	5693.9 - 6764.7	-91.6877, 28.1965	-91.6881, 28.1936	no BOs; only key-seat
EI 338/A-21ST4	Dipmeter	3610 - 7100	3499.9 - 6763.2	-91.6857, 28.2068	-91.6838, 28.2082	lots of potentially good BOs, but tadpoles which indicate P1AZ, HAZ, DEVI, and INC are too sparse
EI 339/#1	Dipmeter	2700 - 4450 4550 - 5000 4950 - 5250 5000 - 7000	2628.0 - 4378.0 4478.0 - 4928.0 4878.0 - 5178.0 4928.0 - 6928.0	-91.6360, 28.1880	-91.6330, 28.1840	no BOs; either keyseat or in-gauge no BOs; keyseat throughout no BOs; keyseat throughout intermittent, short BO intervals; rest keyseat or in-gauge
EI 339/#2	Dipmeter	2700 - 4100 4100 - 5300 5250 - 5850	2630.0 - 4030.0 4030.0 - 5230.0 5180.0 - 5780.0	-91.6350, 28.2030	-91.6350, 28.2030	one BO interval; rest in-gauge no BOs; in-gauge no BOs; in-gauge
EI 339/B-1	Dipmeter	2900 - 3950 3800 - 4950 4950 - 5950	2900.0 - 3950.0 3800.0 - 4950.0 4950.0 - 5950.0	-91.6563, 28.2009	-91.6563, 28.2009	some good developed BOs; rest in-gauge; vertical well no BOs; vertical well; caliper pairs in-gauge no BOs; vertical well; caliper pairs in-gauge

Table A1: (Continued) List of analyzed caliper logs from 38 wells in blocks 316, 330, 338, and 339 of the South Eugene Island field (MD: Measured Depth; SSTVD: Sub-Sea Total Vertical Depth; FMS: Formation Micro Scanner; FMI: Formation Micro Imager; BO: breakout)

Well	Log Type	Depth Interval		Geographic Location (Long., Lat.)		Comments
		MD [ft]	SSTVD [ft]	Interval Top	Interval Bottom	
EI 339/B-17	Dipmeter	3250 - 3800 3700 - 4700 4450 - 4700 4450 - 6100 5950 - 6750	2873.2 - 3310.2 3231.2 - 4016.0 3820.4 - 4016.0 3820.4 - 5123.1 5004.9 - 5645.2	-91.6565, 28.1979	-91.6571, 28.1921	data problems; continuous enlargement throughout the whole ogged section; data cannot be interpreted as BO
EI 339/C-1	Dipmeter	9650 - 10,550	9573.0 - 10473.0	-91.6359, 28.1885	-91.6359, 28.1885	no BOs; in-gauge
EI 339/C-4	Dipmeter	5100 - 6550 6100 - 6550	4786.2 - 6108.4 5698.4 - 6108.4	-91.6343, 28.1856	-91.6333, 28.1843	three BO intervals; otherwise mostly in-gauge no BOs; keyseat throughout
EI 339/C-6	Dipmeter	1250 - 2600 4150 - 4350 5200 - 6950	1156.0 - 2500.5 3855.1 - 4008.3 4656.0 - 5950.1	-91.6364, 28.1885	-91.6374, 28.1813	no BOs; in-gauge no BOs; keyseat throughout no BOs; keyseat throughout
EI 339/C-7	Dipmeter	5600 - 5900 5600 - 6950	3893.6 - 4076.0 3893.6 - 4636.3	-91.6266, 28.1893	-91.6231, 28.1896	no BOs; keyseat throughout one BO interval at bottom; rest keyseat
EI 339/C-9	Dipmeter	4200 - 5250	3755.8 - 4586.4	-91.6382, 28.1855	-91.6393, 28.1841	three BO intervals; rest in-gauge or keyseat
EI 339/C-10	Dipmeter	3200 - 4550 4300 - 4650 4400 - 6250 6000 - 7000 7000 - 7900	2865.7 - 3720.2 3557.9 - 3784.5 3623.2 - 4779.5 4633.5 - 5217.6 5217.6 - 5792.0	-91.6352, 28.1908	-91.6304, 28.1999	no BOs; either keyseat or in-gauge no BOs; keyseat throughout no BOs; keyseat throughout no BOs; keyseat throughout no BOs; in-gauge
EI 339/C-11	Dipmeter	7300 - 7500 7300 - 8550	5469.1 - 5632.3 5469.1 - 6530.5	-91.6276, 28.1806	-91.6258, 28.1797	no BOs; in-gauge no BOs; either keyseat or in-gauge

Table A2

Table A2: Observed breakout (BO) intervals for individual wells. BO length refers to the length of each breakout interval. HAZ, INC, P1AZ, C1-3, C2-4, and BOAZ refer to borehole azimuth, borehole inclination, pad-1 azimuth, caliper 1-3 diameter, caliper 2-4 diameter, and breakout azimuth respectively. Mean breakout azimuth (Mean BOAZ) and standard deviation (ST.D.) were calculated from individual breakout orientations observed in each well. Q describes our quality ranking (g: good; f: fair). Wells marked with a star (*) have inclinations of greater than 20° and could potentially be used to constrain SHmax magnitude.

Well	Depth Interval SSTVD [ft]	Geographic Location [long, lat]	Nearest Reservoir Sand	BO Length [ft]	HAZ	INC	P1AZ	C1-3 [inch]	C2-4 [inch]	BOAZ	Mean BOAZ	St.D.	Q
EI 316/A-12 *	6845.5 - 6893.4	-91.6495, 28.2538	L-5	47.9	215	32	257	<C2-4	>C1-3	N167E	N172E	4	f
	6963.6 - 7026.8	-91.6496, 28.2536	L-5	63.2	212	32	266			N176E			
	7052.6 - 7057.7	-91.6497, 28.2535	L-5	4.9	214	32	262			N172E			
EI 330/#6	1640.0 - 1660.0	-91.6730, 28.2490	n/a	20	225	0	260	9.5	11.0	N150E	N145E	7	g
	1950.0 - 1970.0	-91.6730, 28.2490	n/a	20	210	0	230	9.5	11.0	N140E			
EI 330/#8 *	2420.3 - 2667.7	-91.6684, 28.2398	n/a	247.4	88	22	150	10.0	12.0	N60E	N60E	0	g
	2709.9 - 2780.1	-91.6686, 28.2397	n/a	70.2	107	25	150	9.5	12.0	N60E			
EI 330/A-6ST	6157.7 - 6172.6	-91.6941, 28.2447	JD	14.9	17	7	210	11.0	9.8	N30E	n/a	n/a	f
EI 330/A-22 *	8092.6 - 8138.8	-91.7027, 28.2374	OI-5	46.2	261	23	330	8.2	9.3	N60E	n/a	n/a	g
EI 330/C-15 *	4300.2 - 4308.2	-91.6788, 28.2265	GA-5	8.0	160	22	100	7.5	9.5	N10E	N15E	7	g
	4314.2 - 4354.2	-91.6786, 28.2265	GA-5	40.0	170	22	110	7.5	10.0	N20E			

Table A2: (Continued) Observed breakout (BO) intervals for individual wells. BO length refers to the length of each breakout interval. HAZ, INC, P1AZ, C1-3, C2-4, and BOAZ refer to borehole azimuth, borehole inclination, pad-1 azimuth, caliper 1-3 diameter, caliper 2-4 diameter, and breakout azimuth respectively. Mean breakout azimuth (Mean BOAZ) and standard deviation (ST.D.) were calculated from individual breakout orientations observed in each well. Q describes our quality ranking (g: good; f: fair). Wells marked with a star (*) have inclinations of greater than 20° and could potentially be used to constrain SHmax magnitude.

Well	Depth Interval SSTVD [ft]	Geographic Location [long, lat]	Nearest Reservoir Sand	BO Length [ft]	HAZ	INC	P1AZ	C1-3 [inch]	C2-4 [inch]	BOAZ	Mean BOAZ	St.D.	Q
EI 338/#1	3650.0 - 3694.0	n/a	n/a	44.0	325	3	260	11.8	14.0	N170E	N167E	22	g
	4305.0 - 4345.0	n/a	n/a	40.0	10	3	165	13.0	11.0	N170E			
	4355.0 - 4415.0	n/a	n/a	60.0	25	3	270	11.5	14.0	N180E			
	4445.0 - 4460.0	n/a	GA-5	15.0	359	3	220	11.5	13.0	N130E			
	4570.0 - 4580.0	n/a	GA-5	10.0	20	3	265	11.5	13.0	N175E			
	4870.0 - 4930.0	n/a	n/a	60.0	65	3	190	13.0	11.0	N190E			
	5228.0 - 5250.0	n/a	n/a	22.0	330	3	100	11.0	12.0	N190E			
	5400.0 - 5540.0	n/a	n/a	140.0	310	3	160	13.5	11.5	N160E			
EI 338/#2	6888.0 - 6908.0	-91.6617, 28.2025	n/a	20.0	125	7	185	8.0	9.5	N95E	N93E	8	f
	6944.0 - 7014.0	-91.6617, 28.2025	n/a	70.0	115	10	85	10.0	8.0	N85E			
	8133.0 - 8168.0	-91.6618, 28.2024	m/a	35.0	90	11	190	7.0	8.5	N100E			
EI 338/A-2	7070.9 - 7130.9	-91.6860, 28.2111	LF	60.0	350	2	15	6.8	8.0	N105E	N87E	19	f
	7389.7 - 7419.7	-91.6860, 28.2111	n/a	30.0	10	3	60	7.5	6.5	N65E			
	7612.4 - 7652.3	-91.6860, 28.2111	OI-1	39.9	0	2	180	6.5	7.5	N90E			
EI 338/A-4	3663.1 - 3713.8	-91.6888, 28.2077	n/a	50.7	295	34	75	13.0	15.5	N165E	n/a	n/a	f
	7578.9 - 7594.7	-91.6945, 28.2099	n/a	15.8	305	12	20	9.0	8.0	N20E	N32E	9	
	7634.1 - 7644.0	-91.6945, 28.2099	n/a	9.9	305	12	40	9.0	8.0	N40E			
	7693.6 - 7737.2	-91.6945, 28.2099	n/a	43.6	305	11	215	9.0	8.0	N35E			
EI 338/A-8 *	4846.8 - 4900.8	-91.6820, 28.2063	GA-5/HB-1	54.0	51	36	26	13.7	12.8	N26E	N39E	11	g
	4985.6 - 5065.2	-91.6818, 28.2062	GA-5/HB-1	79.6	50	36	30	14.1	13.1	N30E			
	5143.2 - 5212.7	-91.6815, 28.2062	n/a	69.5	54	36	37	14.0	13.0	N37E			
	6338.9 - 6372.6	-91.6794, 28.2061	n/a	33.7	52	36	31	14.9	13.6	N31E			
	6398.0 - 6469.8	-91.6793, 28.2061	n/a	71.8	56	38	15	14.1	13.1	N15E			
	6469.8 - 6609.1	-91.6792, 28.2061	JD	139.3	62	41	31	15.2	13.6	N31E			
	6718.9 - 6795.3	-91.6789, 28.2060	KE	76.4	79	46	51	16.0	12.8	N51E			

Table A2: (Continued) Observed breakout (BO) intervals for individual wells. BO length refers to the length of each breakout interval. HAZ, INC, P1AZ, C1-3, C2-4, and BOAZ refer to borehole azimuth, borehole inclination, pad-1 azimuth, caliper 1-3 diameter, caliper 2-4 diameter, and breakout azimuth respectively. Mean breakout azimuth (Mean BOAZ) and standard deviation (ST.D.) were calculated from individual breakout orientations observed in each well. Q describes our quality ranking (g: good; f: fair). Wells marked with a star (*) have inclinations of greater than 20° and could potentially be used to constrain SHmax magnitude.

Well	Depth Interval SSTVD [ft]	Geographic Location [long, lat]	Nearest Reservoir Sand	BO Length [ft]	HAZ	INC	P1AZ	C1-3 [inch]	C2-4 [inch]	BOAZ	Mean BOAZ	St.D.	Q
EI 338/A-14ST *	7688.8 - 7778.2	-91.6877, 28.2016	n/a	89.4	198	26	247	9.2	8.3	N67E	n/a	n/a	f
EI 339/#1	5178.0 - 5198.0	-90.5501, 28.1935	n/a	20.0	275	5	210	8.0	9.0	N120E	N113E	26	f
	5446.0 - 5458.0	-90.5501, 28.1935	n/a	12.0	295	3	190	8.0	9.0	N100E			
	5528.0 - 5538.0	-90.5501, 28.1935	n/a	10.0	300	3	210	7.5	8.5	N120E			
EI 339/#2	3040.0 - 3050.0	-91.6353, 28.2035	n/a	10.0	140	2	355	12.0	10.0	N175E	n/a	n/a	f
EI 339/B-1	3071.0 - 3291.0	-91.6563, 28.2009	n/a	220.0	225	1	165	10.5	12.0	N75E	N82E	10	g
	3081.0 - 3291.0	-91.6563, 28.2009	n/a	210.0	272	1	340	11.0	13.0	N70E			
	3541.0 - 3871.0	-91.6563, 28.2009	n/a	330.0	57	2	82	12.5	10.5	N82E			
	3601.0 - 3871.0	-91.6563, 28.2009	n/a	270.0	250	1	180	11.0	12.5	N90E			
	4251.0 - 4401.0	-91.6563, 28.2009	GA-5	150.0	276	2	5	11.0	12.0	N95E			
EI 339/C-4 *	5388.8 - 5441.4	-91.6338, 28.1850	n/a	52.6	145	26	240	9.5	11.0	N150E	N152E	3	f
	5475.9 - 5631.6	-91.6337, 28.1849	n/a	155.7	145	27	245	9.5	11.0	N155E			
	5936.1 - 5959.4	-91.6334, 28.1844	n/a	23.3	145	27	240	10.0	11.5	N150E			
EI 339/C-7 *	4591.8 - 4603.6	-91.6234, 28.1896	n/a	11.8	120	62	85	10.5	13.5	N152E	n/a	n/a	g
EI 339/C-9	4077.3 - 4107.9	-91.6387, 28.1847	n/a	30.6	220	33	175	13.5	10.0	N175E	N173E	3	f
	4254.2 - 4283.8	-91.6390, 28.1844	n/a	29.6	225	30	170	13.0	10.0	N170E			
	4509.4 - 4528.6	-91.6392, 28.1842	GA-5	19.2	240	19	195	11.0	10.0	N195E	n/a	n/a	

Table A3

Table A3: Input parameters and stress tensor modeling results for two deviated wells. Abbreviations: SSTVD - sub-sea total vertical depth, BOAZ - borehole azimuth, INC -inclination, K - effective stress ratio, λ (= Pp/SV) - normalized pore pressure, C_0 - effective compressive rock strength, AZ - azimuth.

Well	Mean BOAZ (Table A2)	Mean INC	Available S_{hmin} Measurement			At Observed Breakout Depth					Results from Stress Modeling at Observed Breakout Depth		
			Type	SSTVD [ft]	Calc. K	SSTVD [ft]	S_V psi]	S_{hmin} [psi]	P_p [psi]	λ	Mean S_{hmin} AZ	S_{Hmax} [psi]	C_0 [psi] (wBO=20° /90°)
EI 316/A-12	N172E	32	Minifrac	6985.0	0.90	6985	6335	6300	6137	0.96	N190° E (±15°)	6315 (±15)	350 / 350 (±50 / ±50)
EI 330/A-22	N60E	23	Minifrac	7727.3	0.74	8116	7549	7018	5519	0.73	N67° E (±7°)	7250 (±100)	3900 / 3350 (±300 / ±150)

CHAPTER 5

PRODUCTION RELATED RESERVOIR DEPLETION AND ASSOCIATED EFFECTS IN THE SOUTH EUGENE ISLAND 330 FIELD, GULF OF MEXICO

5.1 Abstract

Production related pressure depletion in three stratigraphically distinct reservoir sands of the South Eugene Island (SEI) 330 field exhibit significant variations. With production shallow sands experience hydrostatic conditions, appear to be well drained, and normally compacted. At intermediate stratigraphic levels, reservoir sands are undercompacted and moderately overpressured. With production, pore pressures decline drastically suggesting that the sand grains are capable of supporting the induced differential stresses. The change in the least horizontal stress with changing pore pressure is 0.81 implying an increase of differential stresses. Multiple wells that penetrate the same sand within the same fault block exhibit uniform pressure changes indicating a hydraulically continuous compartment. The sand in the deepest stratigraphic level is severely undercompacted and overpressured. Non-uniform pressure changes suggest compartmentalization on a sub-fault block scale. Pore pressures in this sand either maintains its initial value in a given well or decreases and then increases again. Laboratory measurements indicate that increasing differential stress resulting from production may cause plastic and viscous deformation at the effective stress levels of the deep reservoirs.

5.2 Introduction

Hydrocarbon production from oil and gas fields can significantly reduce the pore pressure in a reservoir if no adequate pressure support is provided naturally by an aquifer (feeding the reservoir), a gas cap (expanding as the fluids are being produced) or through water injection. If the reservoir is poorly consolidated and overpressured the sediments can compact during production and, as a consequence, change permeability and due to poroelastic effects, the state of stress within and around the reservoir (Teufel et al., 1991; Engelder and Fischer, 1994; Segall and Fitzgerald, in press). Depending on the state of consolidation and material properties of the reservoir sands, compaction can either be elastic, plastic, or a combination of both. As a result of the sediment compaction and the accompanying stress changes the pore pressure in the reservoir can be maintained or even increased driving production. Furthermore, the hoop stress around wells penetrating the compacting reservoirs changes, potentially leading to wellbore stability problems such as sand production. General well and fracture completion designs for boreholes being drilled into already depleted sands need to account for these stress changes to adjust mudweights, wellpaths, and fracture gradients accordingly.

The importance of these issues has greatly increased in recent years since many wells are now being drilled horizontally and in often extremely overpressured reservoirs in which minor pore pressures variations could induce significant changes in mechanical reservoir behavior. While the amount of reliable and high quality data is still sparse, a number of recent publications have addressed production induced reservoir compaction behavior, associated stress paths, and matrix permeability changes for a few hydrocarbon producing fields along the Gulf Coast and in the North Sea (e.g., Salz, 1977; Teufel et al., 1991; Engelder and Fischer, 1994; Santarelli et al., 1998).

In this chapter, I present production related pore pressure depletion curves in three reservoir sands from the South Eugene Island (SEI) 330 field. For a general geologic overview of the SEI field refer to chapter 1. Specifically, I focus on the differences in depletion behavior in order to assess variations of sediment compaction and possible associated stress changes (i.e. stresspath) within a single field. The pore pressure data I use come from pressure surveys taken in over 80 production wells located in blocks 330 and 316 of the SEI field (see Figure 1.4). The three reservoir sands are the GA-2 (shallow level), the LF (intermediate level), and the Lentic (deep level) (see cross-section in Figure 1.4). I describe and discuss each sand individually in stratigraphic order. In each case, I first provide a brief depositional and lithologic description. Subsequently, I present the pore pressure survey data, from which I compile depletion curves for each reservoir undergoing production. As described in chapter 3 (section 3.3.2), I followed a method published by Batzle and Wang (1992) to correct pore pressure measurements from various wells in each reservoir to a given datum (usually the center depth of perforation in case one of the wells was fracture completed). Finally, I discuss the pressure history and its impact on potential stress changes and sand compaction behavior.

5.3 GA-2 sand

5.3.1 Overview

The upper stratigraphic level I study is the GA-2 sand, one of the youngest and shallowest producing reservoirs in the field (see cross-section in Figure 1.4). The average depth to its top is about 4,400 ft. sub-sea true vertical depth (SSTVD). This sand interval was deposited in fluvial channels and at the deltaic mouth during sea level lowstands when the shelf was above sea level (Alexander and Flemings, 1995). The sand can be quite massive (up to 400ft.) and is comprised of relatively fine grains with little cement (Holland et al., 1992). Structurally, the GA-2 sand is highly continuous divided only by the main basin bounding

growth fault into footwall and minibasin side (Figure 5.1). Production is mainly controlled by a strong water drive from the aquifer below. The logs in Figure 5.2 indicate that the sediments surrounding the GA-2 contain relatively little shale (GR-track) and they lay on a normal compaction trend (Δt-track) implying sufficient drainage for the pore fluids to escape as the sediments are being buried.

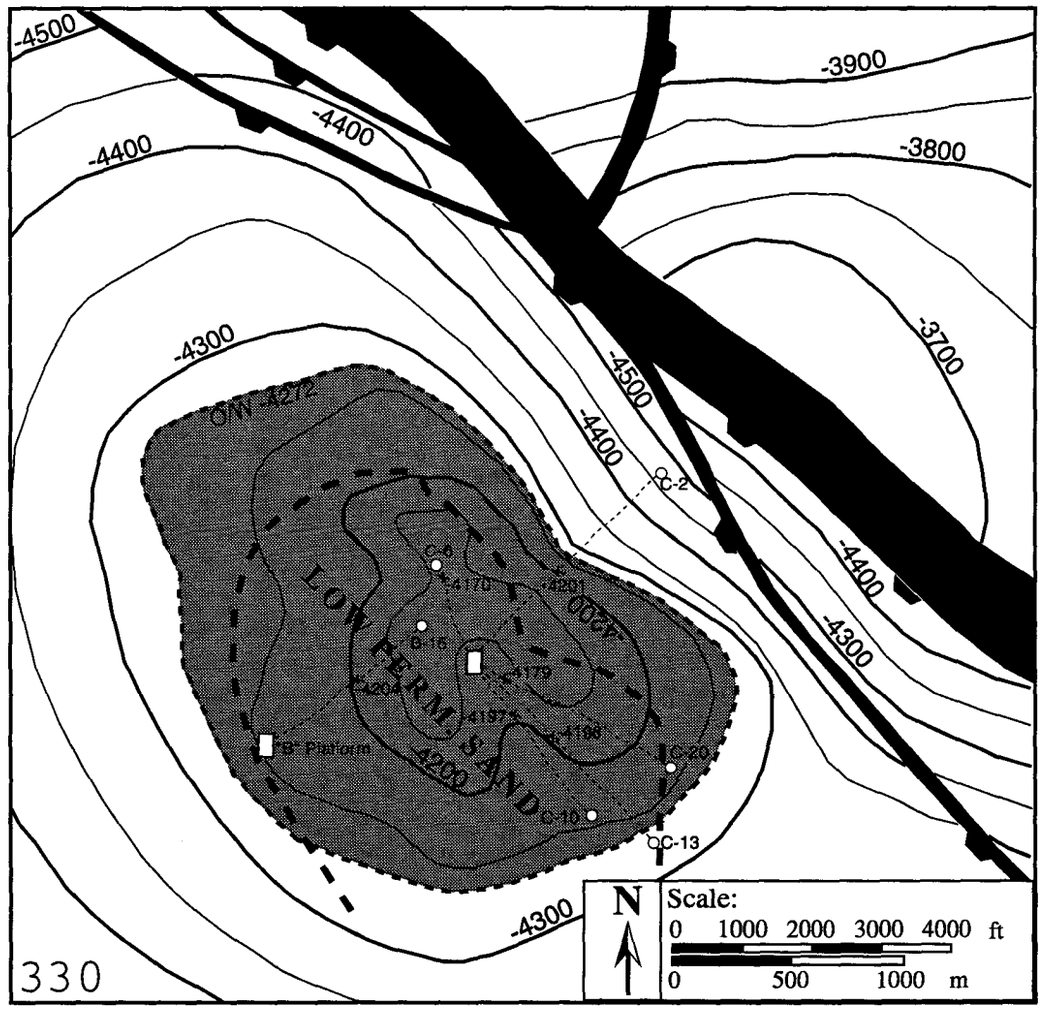

Figure 5.1: Structure map of the GA-2 sand in SEI fault block 330. Depth contours are in feet SSTVD. Wellpaths of boreholes (thin dashed lines) from which we obtained pore pressure data were drilled from platforms B and C (shown as white rectangles). The points of reservoir penetration are indicated as crosses along wellpaths. Medium dashed line displays the interpreted oil-water contacts (O/W). The associated depth intervals in the reservoir filled with oil are shown in gray. Thick dashed line exhibits assumed permeability contrast. This structure map was generated from Pennzoil's 3-D seismic data interpretations. The normal faults are vertical projections of the fault plane onto the Lentic horizon; the sides of relative downthrown sand sections are indicated with black symbols along the fault plane. Locations of platforms, exploration wells, and borehole paths were obtained from Pennzoil's deviation data.

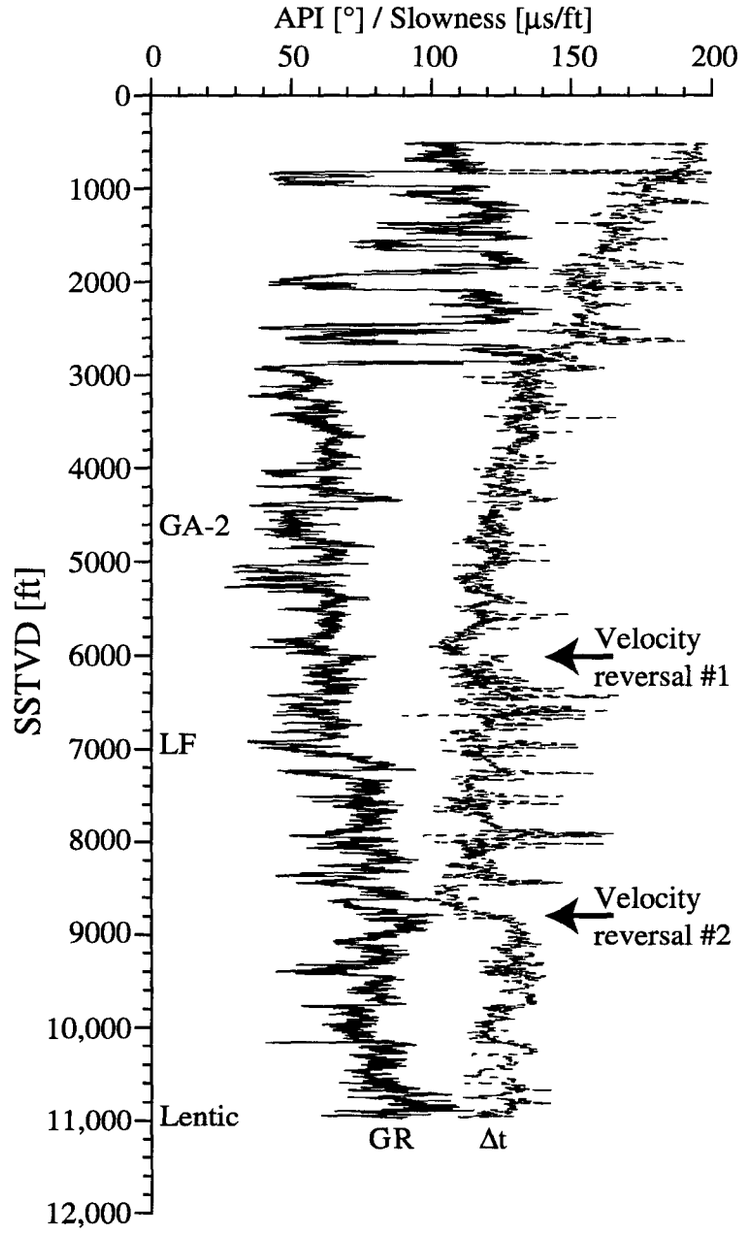

Figure 5.2: Gamma ray (GR, left track) and sonic log (Δt, right track) of well 331/#1. The depths (in SSTVD) where the well penetrates the four reservoirs presented in the study are labeled accordingly. Along the sonic log, notice the normal compaction trend (<5400 ft. SSTVD), the first velocity reversal (~6,000 ft. SSTVD), and the second velocity reversal (~ 8,800 ft. SSTVD) indicating compaction disequilibrium and overpressured conditions (Bowers, 1994; Hart et al., 1995).

5.3.2 Pressure history

Figure 5.3 displays production induced pressure evolution in the GA-2 sand as compiled from 5 production wells. Initially, the reservoir pressure was slightly above hydrostatic (i.e., ~about 250 psi). In February of 1995 cumulative production accounted for almost 30 mbbls of liquids (oil and water), and 13 mmcf of gas. Despite oil production the pressure-time curve is rather flat indicating insignificant pressure decline from slightly above to approximately equal to hydrostatic levels (assuming brine with an equivalent density of 0.465 psi/ft). Because pore pressures are essentially hydrostatic and the reservoir shows rather small depletion, I consider the GA-2 sand a normally compacting reservoir (as seen from the sonic log) with aquifer support that is in communication to the surface. Furthermore, the sand appears to be well drained, i.e. fluids can freely escape at any time during loading and compaction. In other words, the grains of the GA-2 sand support the load of the overburden and production does not induce any stress changes on the system.

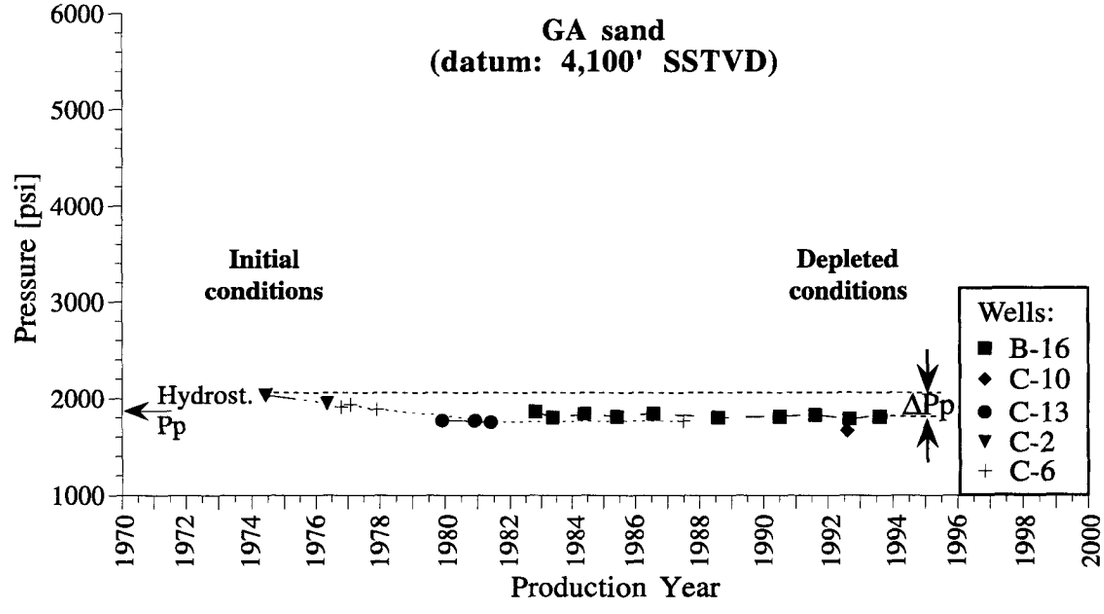

Figure 5.3: Pore pressure depletion in the GA-2 reservoir. The graph is compiled with pressure surveys from 5 different wells (as labeled) and corrected to a datum of 4,100 ft. SSTVD. The change in pore pressure, ΔPp, is 250 psi. The reference hydrostatic pore pressure was calculated using an equivalent gradient of 0.465 psi/ft.

5.4 LF sand

5.4.1 Overview

The LF is representative of the intermediate stratigraphic level. It was deposited in a shallow deltaic environment (Alexander and Flemings, 1995) and is characterized by moderate overpressures. This is also expressed in the sonic log, where the sand lies below the first velocity reversal (indicating a deviation from the normal compaction trend) (Figure 5.2). The LF is very fine grained, extremely clean, and cementation is more uniform compared to other reservoir sands (Holland et al., 1992). Hydrocarbons are produced through a combination of gas-cap expansion and aquifer drive from below. The thickness of the LF sand increases towards the west but is only up to 100 ft. in SEI blocks 330 and 331. Its top is between 6,200 ft. and 7,500 ft. SSTVD on average. Within the minibasin (SEI blocks 330 and 331), the LF sand is offset by subsidiary faults sub-dividing it into several fault blocks (FB). Figure 5.4 displays the structure map of the JD sand, which was deposited above the LF during the same sedimentation cycle (Figure 1.4). The structures at this stratigraphic level are very similar to those of the LF sand and therefore an adequate representation (no digital structure map is available for the LF sand).

5.4.2 Pressure history

Production from the LF sand has been quite significant. By February 1995 cumulative production was almost 15 mbbls of liquids and just over 15 mmcf of gas in FB-B, and over 6 mbbls of liquids and over 8.5 mmcf of gas in FB-A. Figure 5.5 displays the corresponding pressure histories. Initial pore pressure conditions indicate moderate overpressures (λ = 0.59 and 0.64). The sand can be characterized by compaction disequilibrium and undrained reservoir fluids that support a fraction of the overburden load. As a consequence of production, both reservoirs experienced drastic, but uniform pressure declines between 1,500 and 1,800 psi. In FB-A, the pore pressures drops to about 2,000 psi and then exhibits a late stage "recovery" of approximately 400 psi to 2,400 psi. In FB-B pore pressures decline and then remain essentially constant at about 2,400 psi. The approximately flat nature of both curves suggests an equilibrium state between the compartments and the aquifer feeding the LF sand. Note also that the late stage equilibrium pore pressure of 2,400 psi in both LF reservoirs is about 800 psi below hydrostatic. I interpret this fact to be the result of the isolating nature of the compartmentalization resulting from the lack of communication with the surface.

The uniform depletion behavior in each of the two reservoirs indicates that the production induced pressure changes spread pervasively through this sand in each fault block. Thus, fault blocks A and B, which were interpreted from seismic data, coincide with two hydrologically continuous compartments (i.e. bounded by subsidiary faults). Furthermore, initial and final pore pressures are approximately equal and the shape of the depletion curves look essentially similar. It is likely, that the two compartments are in hydraulic communication across the fault block bounding normal fault. Alexander and Handshy (1998) came to the same conclusion with a geochemical analysis of the pore fluids in the SEI 330 reservoirs. In fact, the pressure "recovery" seen in fault block A corresponds to an increase in pressure to that in fault block B.

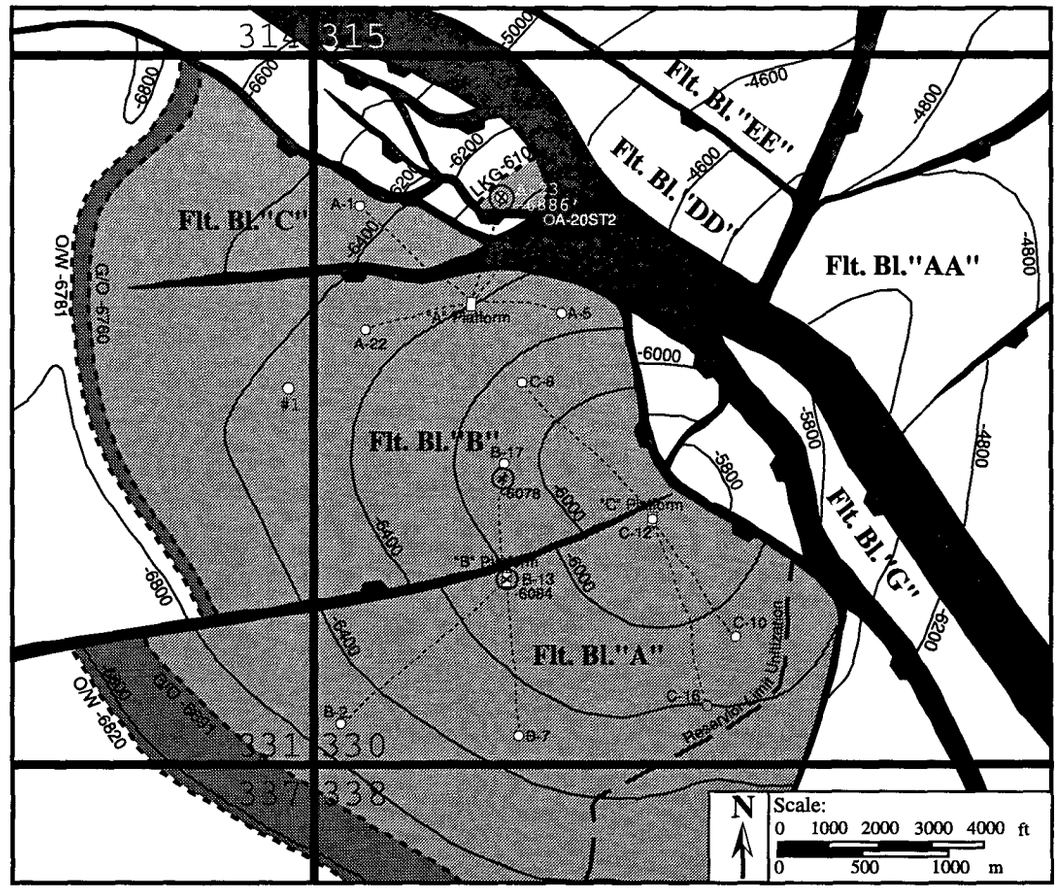

Figure 5.4: Structure map of the JD sand. Depth contours are in feet SSTVD. Medium dashed lines display the interpreted fluid contacts (O/W: oil-water; G/O: gas-oil). The associated depth intervals in the reservoir filled with oil/gas are shown in dark/light gray. See Figure 5.1 for more details of how this structure map was generated.

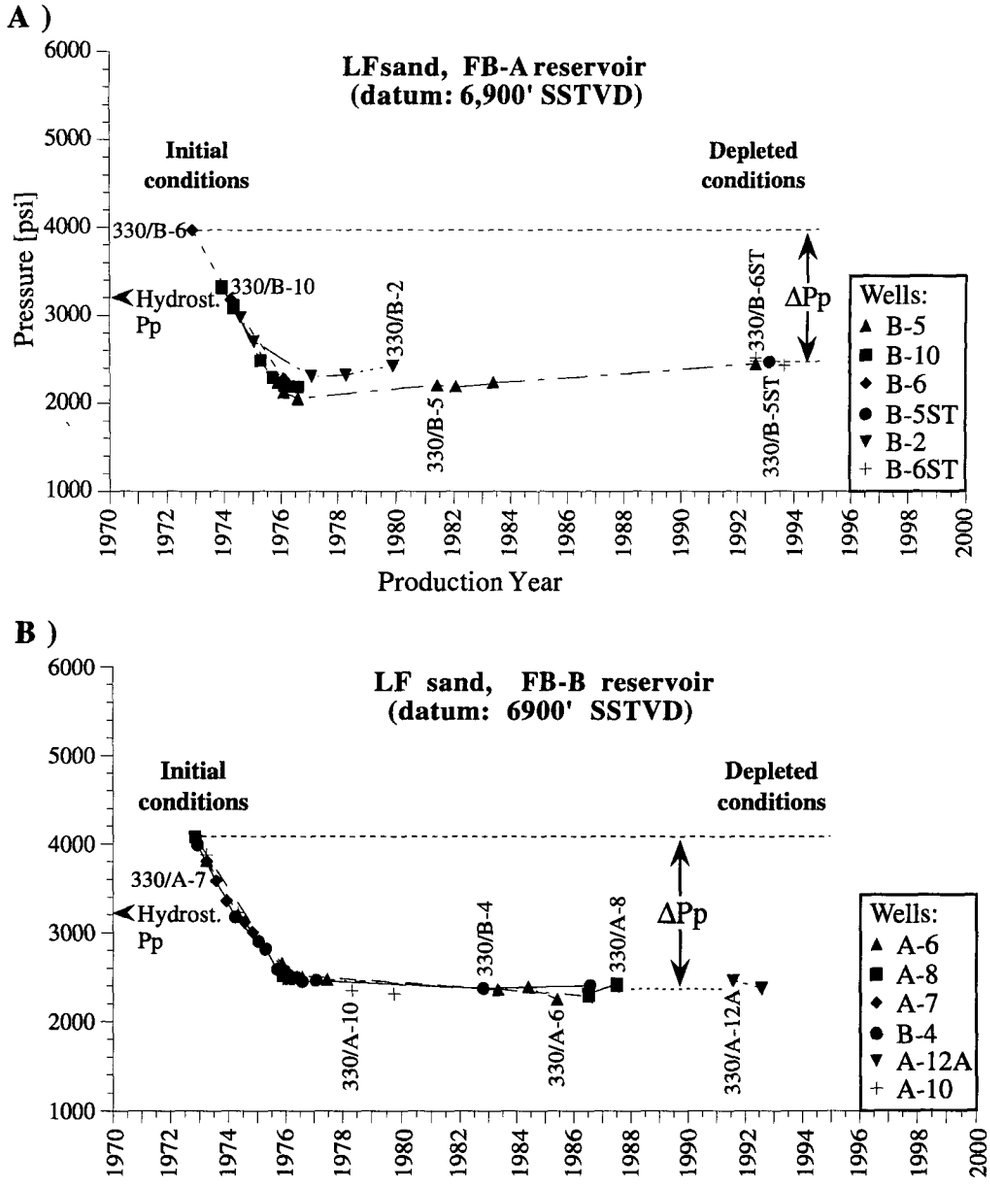

Figure 5.5: Pore pressure depletion in the LF sand, FB A and B. Both graphs are compiled with pressure surveys from 6 different wells (as labeled) and corrected to a datum of 6,900 ft. SSTVD. The change in pore pressure, ΔPp, is ~1,540 psi in FB-A and ~1,800 psi in FB-B. The reference hydrostatic pore pressure was calculated using an equivalent gradient of 0.465 psi/ft.

5.4.3 Depletion related stress changes

The pressure decline in both LF reservoirs implies that the load carried previously by the pore fluid is transferred to the sand matrix. The matrix of the LF sand apparently has sufficient stiffness to support the additional load, probably resulting from the relatively uniform cementation described above (Holland et al., 1992). It is likely that there is an

elastic pore compaction effect that is not recorded in the pressure data. As a consequence of this loading process, effective and differential stresses in both reservoir sands increase (Addis et al, 1996). For the reasons addressed in the introduction of this chapter and the issues discussed in chapter 3, it is of interest to analyze the stress path the LF reservoirs followed in response to the depletion. Since I have two stress tests available for the LF sand in FB-B at the initial and the depleted state of the reservoir (see chapter 3.4.3, Figure 3.8), I can determine its effective stress path as described by parameter A (Addis et al., 1996):

$$A = \frac{\Delta S_h}{\Delta P_p} \qquad \text{Eqn. 5.1}$$

Theoretically, the parameter A can vary between 0 and 1. Although Santarelli et al. (1998) argue that values of 0 and 1 for A have been observed in the North Sea, the compilation by Addis (1997) shows that A generally ranges between 0.2 ad 0.8. In the case of the LF/FB-B reservoir, A is to 0.81 (chapter 3.4.3), which is high but within the range reported by Addis (1997). As in Figure 3.9, Figure 5.6 displays in normalized S_h versus P_p space the stresspath for the LF FB-B reservoir. If μ was 0.4, pore pressure and stress conditions in the depleted LF sand would be in frictional equilibrium. Thus, production could be inducing fault slip.

However, I doubt that a very clean and uniformly cemented sand like the LF has low coefficients of friction. Laboratory measurements on sandstones revealed values for μ that are generally above 0.6 (Byerlee, 1978; Zoback and Healy, 1984). Furthermore, a few field studies on the state of stress in sedimentary formations (Zoback and Healy, 1984) also suggest higher shear strengths (i.e., $\mu \sim 0.6$ rather than 0.4). Therefore, I think a higher frictional value is more reasonable (i.e., $\mu = 0.6$). Hence, depletion of the LF sand increased the differential stress and brought the reservoir closer to frictional failure (because the stresspath is a little bit steeper than the line for frictional failure for $\mu = 0.6$) but it probably has not reached it.

The stress path can also be expressed in terms of the effective stress ratio K, which relates to A as follows (the derivation is shown in the appendix):

$$A = 1 - K = 1 - \frac{\Delta\sigma_h}{\Delta\sigma_v} \qquad \text{Eqn. 5.2}$$

Given A = 0.81 for the LF FB-B reservoir, K equals 0.19, which is rather low. Figure 5.7 displays the stress path in terms of K and illustrates how depletion drives the state of stress

away from the isotropic stress line leading to an increase in differential stresses. This process could eventually lead to shear failure.

Teufel et al. (1991) found a similar low values for K in the North Sea Ekofisk field. In contrast, uniaxial laboratory measurements on Ekofisk chalk revealed considerably higher K numbers (i.e., 0.4 - 0.5). Teufel et al. (1991) attribute this unequal change of effective stresses between field and laboratory to differences in boundary conditions. In laboratory measurements strict stress or strain boundary conditions can be achieved. In the field, however, combined stress-strain boundary conditions are very likely which result in rapidly increasing deviatoric stresses (perhaps because the reservoir rocks can deform more plastically).

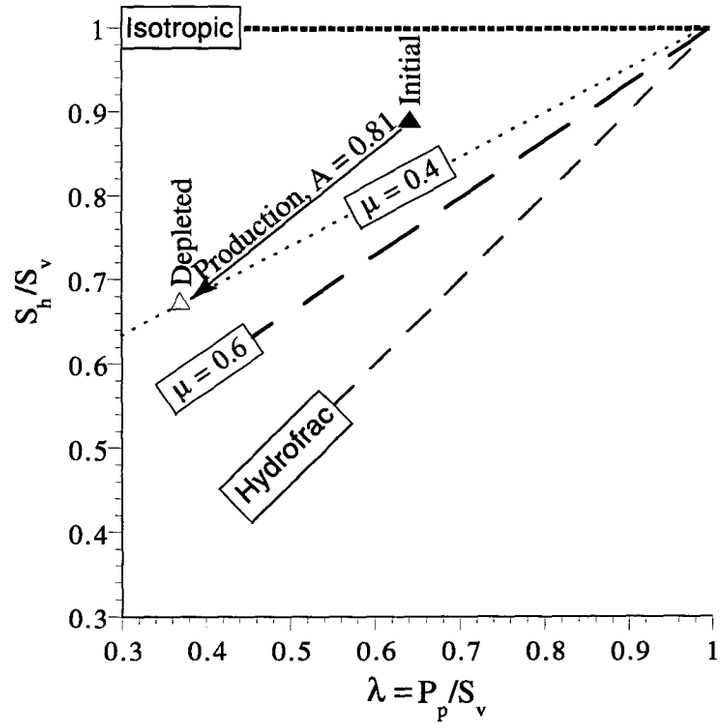

Figure 5.6: Normalized least principal stress versus normalized pore pressure. The diagram displays initial (black triangles) and depleted (open triangles) conditions of the LF FB-B reservoir. The arrow indicates the effective stress paths annotated by the value for the A parameter. Hydraulic fracturing, frictional failure for two coefficient of frictions (μ = 0.4 and 0.6), and the isotropic stress state are shown as dashed lines.

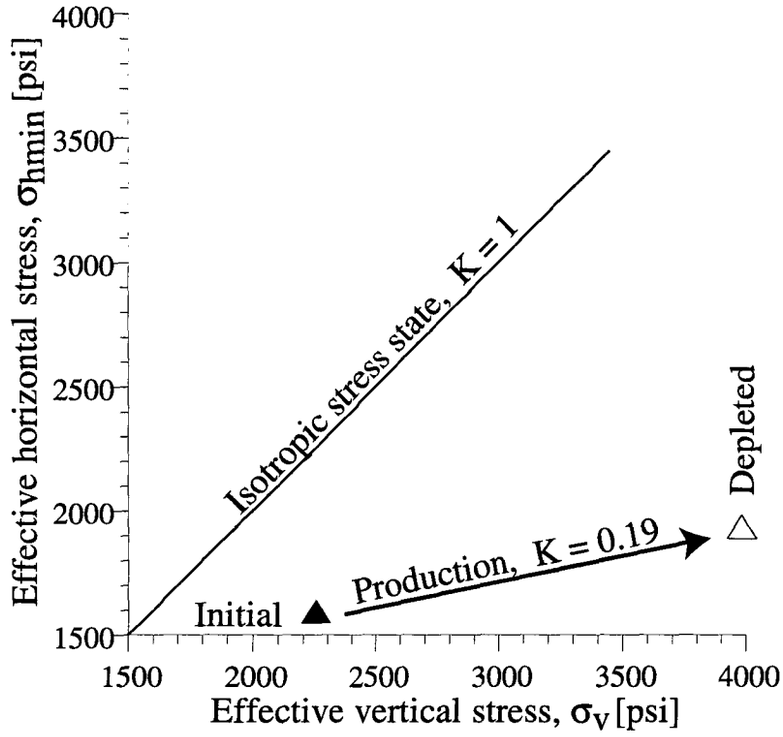

Figure 5.7: Diagram of effective vertical stress versus effective horizontal stress displaying the stress path of the LF FB-B reservoir in result of production related 1,800 psi depletion. The black and open triangle show initial and depleted states respectively. The arrow indicates the effective stress path annotated by the value for the effective stress ratio, K The isotropic stress path is shown as well.

5.5 Lentic sand

5.5.1 Overview

The Lentic-1 (or L-1) is stratigraphically the deepest reservoir in the SEI 330 field and lies well below 10,000 ft. SSTVD within the minibasin (see cross-section in Figure 1.4). It was deposited in an outer continental shelf to continental slope environment (Alexander and Flemings, 1995). The internal structure of this sand is complex, highly discontinuous, and its structural details are generally poorly understood because the quality of seismic reflection data deteriorates at this level.

The Lentic sand is relatively clean (not very different from shallower reservoir sands), very fine grained, and its thickness is quite variable but no more than 100 ft. However, the gamma ray log in Figure 5.2 exhibits rather thick, low permeability volumes of shale in the strata surrounding the Lentic. Laboratory analysis of Lentic core (C. Chang, pers. com.)

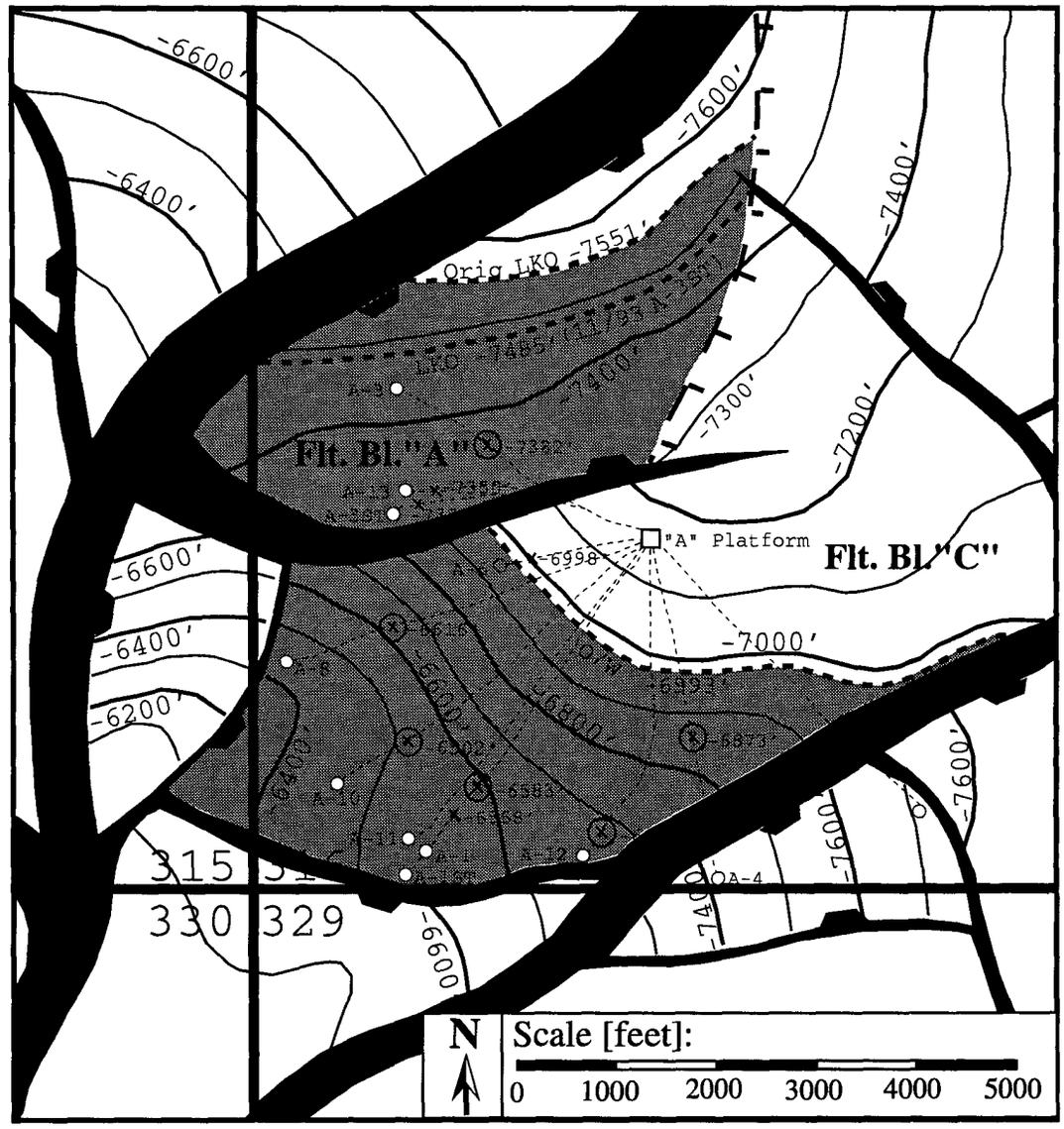

Figure 5.8: Structure map of the Lentic reservoir sand on the footwall side of the SEI 330 field. Depth contours are in feet SSTVD. Wellpaths of boreholes from which we obtained pore pressure and stress data were drilled from platform A in block 316 (small white square) and are shown as thin dashed lines with points of reservoir penetration (crosses along wellpaths). Thick dashed lines display interpreted fluid contacts in the individual fault blocks (O/W: oil-water; LKO: lowest known oil). The associated depth intervals in the two reservoirs filled with oil are shown in gray. Thick "T"-dashes in fault block A exhibit assumed permeability barriers. See Figure 5.1 for more details of how this structure map was generated.

indicate that although the sand is deeply buried, it is extremely undercompacted with almost no signs of cementation and experiences severe overpressures in-situ. This is likely to be a consequence of the rapid deposition and burial of thick shale sequences during basin

evolution and the associated insufficient sediment drainage (Holland et al., 1992; Alexander and Flemings, 1995). The resulting overpressured conditions are reflected in the sonic log in Figure 5.2, where the sand is found near the bottom of the well below the second velocity reversal.

I compiled pressure data from wells drilled on the footwall side in SEI block 316, where the sand lies above 7,000 ft. Figure 5.8 displays the dominant structural features in the southwest corner of SEI 330 block 316 and adjacent blocks. There are two NE-SW striking normal faults and subsidiary fault splays against which the Lentic sand abuts. A roughly E-W striking antithetic normal fault sub-compartmentalizes the sand into fault block A and fault block C. This antithetic normal fault does not entirely separate fault blocks A and C. Pennzoil geologists suggest complete closure and hydraulic decoupling between the two reservoirs is achieved by a permeability barrier (shown as thick "T"-dashes in Figure 5.8) further downdip to the east in fault block A.

5.5.2 Pressure history

The Lentic sand is an oil reservoir with minor amounts of gas. By February of 1995, production from the Lentic sand totalled at nearly 0.5 mbbls of water and oil and 0.1 mmcf of gas in FB-A. In FB-C, production was somewhat higher: almost 1.5 mbbls of liquids and 0.5 mmcf of gas. Figure 5.9 displays the pressure histories for both fault blocks A and C corresponding to this production. Pore pressures prior to depletion were 85% and 86% of the overburden for FBs A and C, respectively.

In FB-A (Figure 5.9A), I had pore pressure surveys from three wells. Initially, there was only one well, A-3, producing from this reservoir. After shut-in in 1993, because production had become uneconomical, two more wells came into production: the A-3ST in 1994 and the A-13 in 1995. The corresponding pressure history displays an initial pore pressure decline by about 1,400 psi over the first 5 1/2 years of production. After the A-3 had been shut-in, the pressure suddenly rose by about 1,750 psi (indicated in the figure) to nearly 6,200 psi (measured in the A-3ST; black square), which is higher than the initial pore pressure value. At this point, the A-3ST was fracture completed and the pore pressure measurement taken during this process (about 12 days after the pressure survey; open square with cross) confirmed the high pore pressure in the reservoir. Subsequently, the pressure dropped sharply to about 4,200 psi - a little bit lower than the last minimum (dashed line) - before it increased again.

In FB-C pressure surveys from 6 wells were available to monitor pore pressure during a production period of about 10 years (Figure 5.9B). The six pressure curves show non-uniform pressure depletion within the reservoir. The pore pressures in well A-4 remain high

and fluctuate about the initial value of about 5,400 psi (upper dashed line). Pressures in well A-1, in contrast, decline by about 1,100 psi to approximately 4,300 psi (lower dashed line) and then fluctuate around this value. In well A-8, the pressure sharply declines to the lower dashed line value (~4,300 psi) and then increases again by 400 psi. In well A-10, pressures decline to ~4,300 psi and then remain essentially constant. After fracture completion in 1994, well A-12 exhibits the same high initial pore pressures as measured in wells A-1 and A-4 about 10 years before; subsequently, the pressure declines significantly to about 3,700 psi.

The pore pressures in the six production wells of FB-C exhibit a compelling behavior: either they remain more or less unchanged at initial values (~5,400 psi) or decline to about 4,300 psi and then level off or increase again. I believe these peculiar trends bound by the two pore pressure values (dashed lines in Figure 5.9B) indicate the presence of a mechanism that increases and maintains high pore pressure. Furthermore, the non-uniform trend among the production wells suggests hydraulic compartmentalization on a sub-fault block scale (i.e., smaller than the structural resolution of the seismic data).

5.5.3 Mechanisms for maintaining high pore pressures

Figure 5.10 presents in a simple diagram illustrating the sources or mechanisms that I suggest are responsible for maintaining or recovering high pore pressures in the two Lentic reservoirs. Basically, there exist two types of sources: internal and external. External sources include fluid migration mechanisms such as active faulting and aquifer support; in addition there exist also capillary forces. The necessary condition to maintain or increase pore pressure in a reservoir is that the fluid volume produced from the reservoir has to be smaller or equal to the fluid volume migrated into the reservoir (i.e., $\Delta V_{in} \geq \Delta V_{prod}$). Internal pressure sources involve reservoir compaction (i.e., change of porosity). This compaction can either be elastic, viscous, or plastic. Elastic compaction results in an equal change of porosity volume to fluid production volume (i.e., $\Delta\Phi = \Delta V_{prod}$) if the reservoir pore pressure remains constant and there is no other mechanisms operating. Viscous creep or plastic compaction, in contrast, results also in a pore pressure increase, because the pore volume reduced can be larger than the fluid volume produced (i.e., $\Delta\Phi \geq \Delta V_{prod}$).

5.5.4 Laboratory measurements

In this section, I use data from laboratory measurements to complement the field data described above, and help explain the peculiar production induced pore pressure response in the two Lentic reservoirs. The measurements were made on plugs taken from a core of

well 316/A-12 (FB-C; Figure 5.8) that penetrates the Lentic sand. The plugs were subjected to uniaxial strain under drained and undrained conditions. For more details on test procedure and data acquisition refer to Chang and Zoback (1998). In the following, I discuss results from the evolving stress states in these plugs.

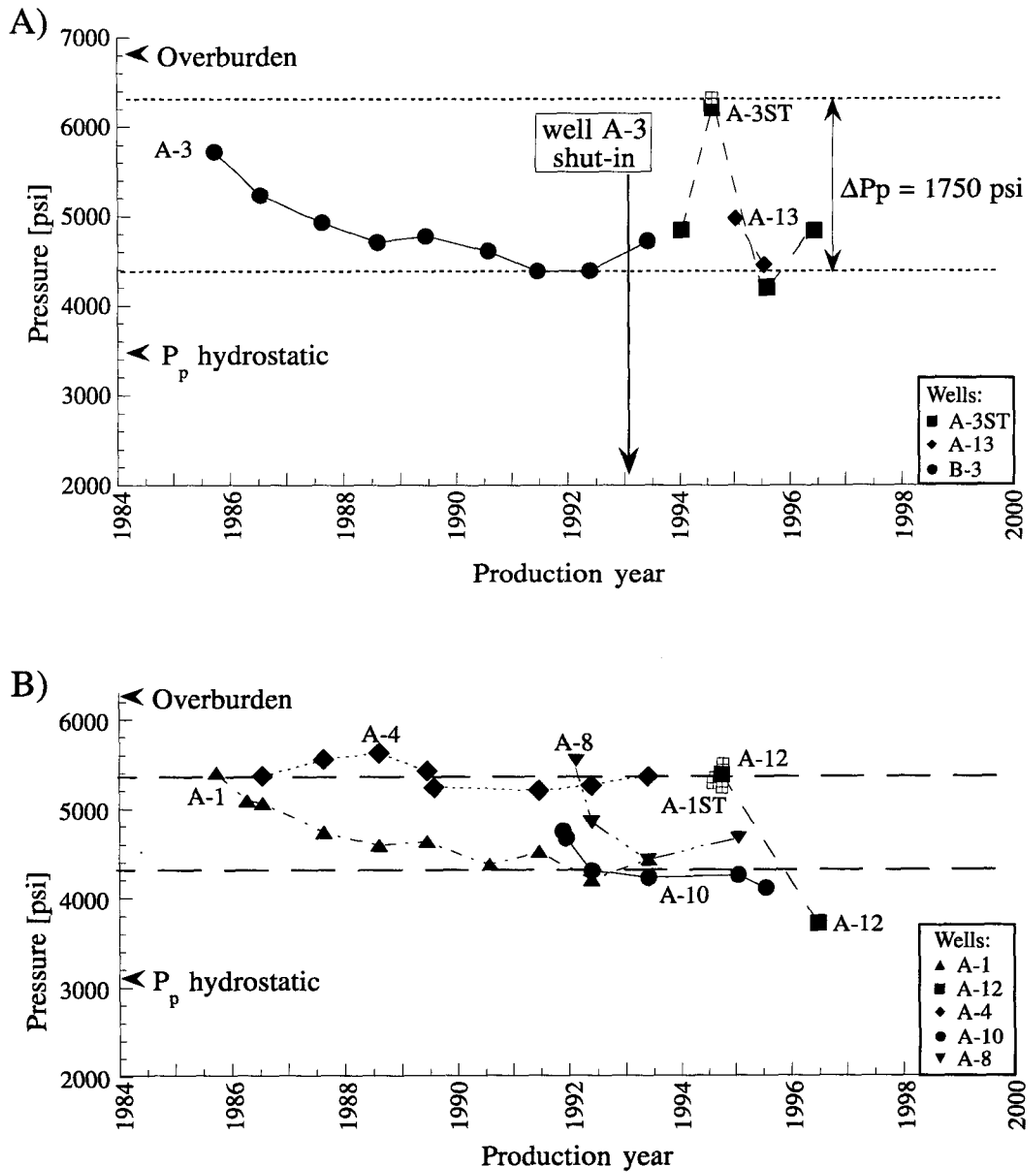

Figure 5.9: Pore pressure depletion in the Lentic sand, fault blocks A and C. The pressure data in FB-A were corrected to a datum of 7,400 ft. SSTVD and in FB-C to 6,800 ft. SSTVD. The open squares with crosses show pore pressures determined during fracture completions, while all other data (black symbols) come from repeated pressure surveys. The reference hydrostatic pore pressure was calculated using an equivalent gradient of 0.465 psi/ft.

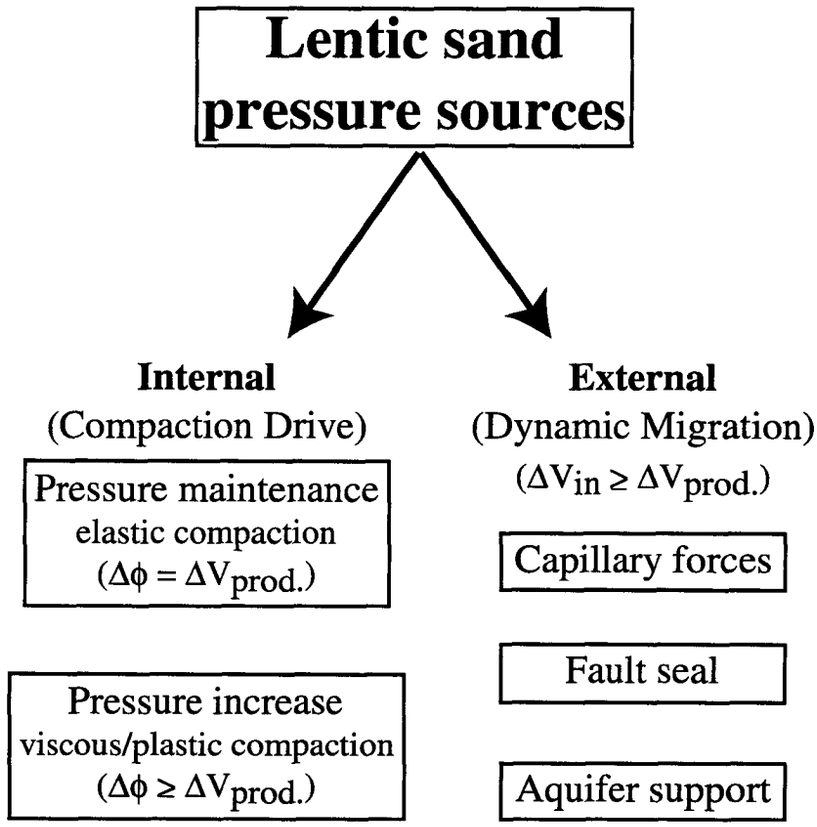

Figure 5.10: Diagram to visualize two types of sources potentially responsible for pore pressure maintenance or even increase in the Lentic sand. ($\Delta\Phi$: change of pore volume; ΔV_{prod}: volume of fluids produced; ΔV_{in}: volume of fluids migrated into the reservoir).

Undrained testing

The undrained tests were designed in an attempt to simulate qualitatively the production history in the Lentic sand, FB-A (Figure 5.8). The test procedures are explained in detail by Chang (1998). Reproduction of the reservoir pore pressure response (Figure 5.9A) in the lab can help to better understand the mechanics that accompany production in the highly overpressured and undercompacted Lentic sand.

Figure 5.11 shows the acquired data consisting of two curves: the differential load and the pore pressure. In a first step of the test, the differential stress on the sample was increased by raising the axial load and then held constant for the remainder of the experiment (step function loading). Even though not realistic, this process might simulate the initial burial of the reservoir under undrained conditions. The sample was then given sufficient time to achieve pore pressure equilibration imitating the initial in-situ conditions in the reservoir. In response to the step load, the pore pressure exhibits a strong increase

together with oscillations. After about 7 hours into the experiment, the oscillations cease and the pore pressure continues to rise monotonically. Pore pressure had equilibrated after 18 hours and production was simulated by opening a valve and "producing" a fraction of the pore fluid. The system was immediately shut-in again afterwards. This step simulates the actual production process. As a result of the drastic pore pressure drop, the load previously carried by the fluid is transferred to the sand matrix, which increases the differential stress on the grains. The response of the system following the simulated production shows that immediately after shut-in, the pore pressure starts to recover with time by increasing steadily for 17 hours until the experiment is terminated.

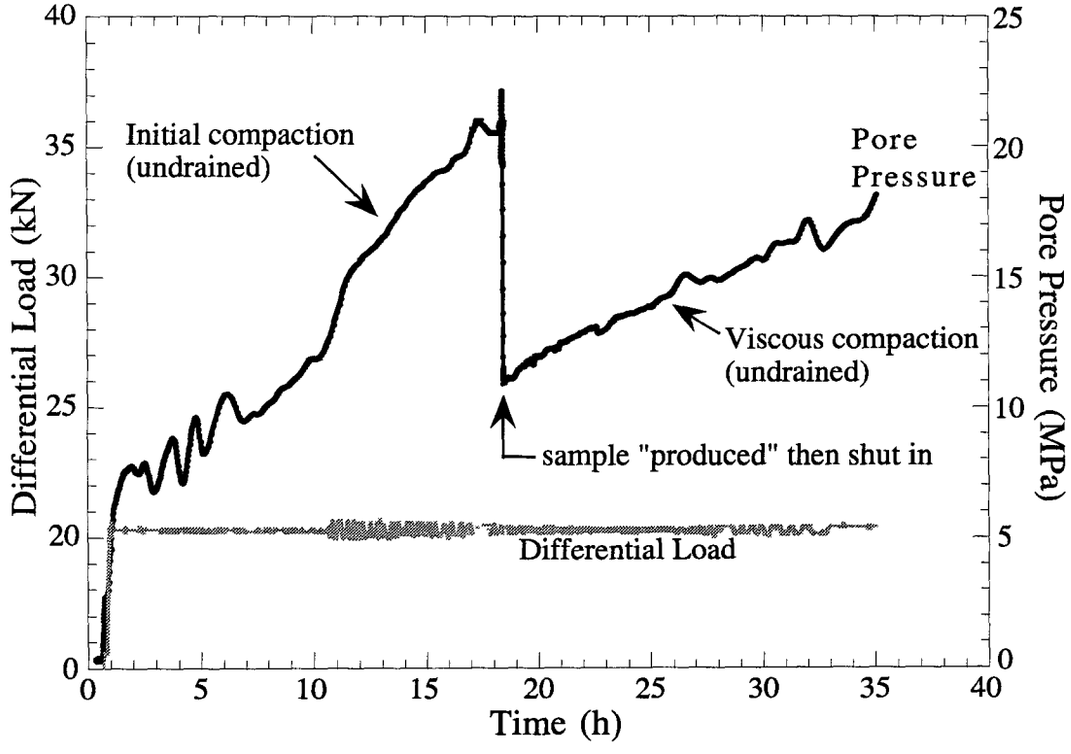

Figure 5.11: Differential load and pore pressure versus time for the undrained laboratory test on the Lentic sand.

This behavior confirms observations Chang and Zoback (1998) made in previous experiments on samples not only from the Lentic sand but also from the Wilmington Field, California, which is also unconsolidated. The Lentic sand is behaving in a visco-elastic fashion most likely due to the presence of small amounts of intergranular clay. Chang and Zoback (1998) modeled this behavior using a standard linear solid. The time dependent creep of grains allows for dissipation of excess differential stresses (i.e., stress relaxation)

imposed on the grains by additional load that the matrix is not capable to sustain. During this process, the pore volume is reduced and if the fluids cannot drain, pore pressure starts to increase. The result from this undrained loading experiment suggests that the pore pressure increase in the Lentic sand in FB-A after well A-3 was shut-in (Figure 5.9A) can be related to time dependent creep, stress relaxation, and associated pore volume reduction of the sediment matrix.

Drained testing

Figures 5.12 through 5.14 display the data from the drained test in ways that are frequently being used in soil mechanics: stress versus strain (Figure 5.12), effective mean versus differential stresses (Figure 5.13), and effective vertical versus effective horizontal stress (Figure 5.14) (Muir-Wood, 1991; Atkinson, 1993). Note that because this test was run under drained conditions, effective stresses equal total stresses. Unfortunately, meaningful porosity data accompanying the stress-strain measurements were not available. Consequently, I am not able to provide plots of porosity (or void ratio) versus mean effective stress - a potentially useful way to understand the mechanics of unconsolidated sediment compaction.

The stress versus strain graphs in Figure 5.12 indicate a strong compactional and non-linear elastic behavior of the Lentic sand. The general concave-up character (particularly reflected in Figure 5.12A) of the curves reflects virgin (i.e., initial) compaction of a weak, unconsolidated sediment (Atkinson, 1993). I consider the Lentic sand to be such a sediment, given the fact that it is extremely undercompacted (i.e., porosity ~35%) and shows essentially no signs of cementation. However, there also appear to be at least two yield points at which the sample has a local effective stress peak indicating a maximum sustainable load on the grains at that stage. The peaks are followed by short declines in effective stress which may indicate grain rearrangements accompanied by sudden volume change. Subsequently, effective stresses increase steeply which I interpret as periods of post-yield compaction resulting from steady volume change by continuous grain rearrangement (Jones, 1994).

Figure 5.13 displays the data from the same test in a graph of effective vertical versus effective horizontal stress which offers the possibility to look at the stress path. An important parameter in this regard is the effective stress ratio K_0 (i.e. effective horizontal versus effective vertical stress, σ_h/σ_v). It is considered a material constant for most uncemented sediments and describes the stress path under uniaxial strain conditions (which are relatively easy to achieve in the laboratory). For the Lentic sand, $K_0 = 0.38$, which is within the typical range for one-dimensional consolidation (i.e., virgin or initial

compaction) of an uncemented sand (Karig and Hou, 1992; Jones, 1994). The figure also exhibits local slope changes in response to the material yielding and sudden volume change. The local values show a significant increase in effective horizontal stress as a result of the yielding process. For a perfectly plastic yielding process (so called critical state) $d\sigma_h / d\sigma_v$ should approach 1. Subsequent to yielding, the material follows again the $K_0 = 0.38$ trend for initial compaction.

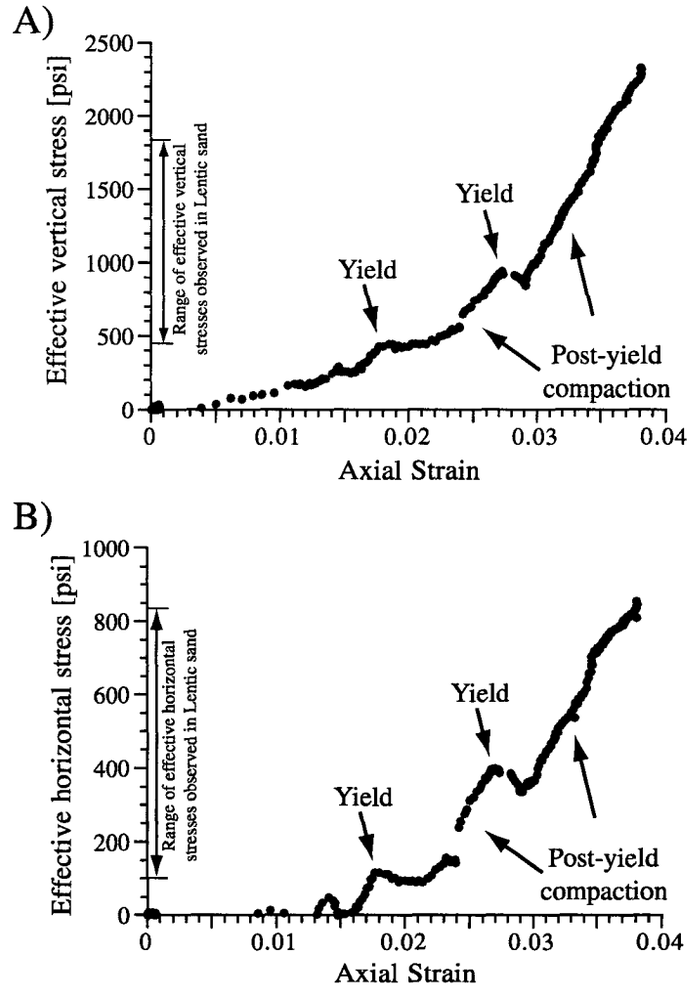

Figure 5.12: Stress versus strain in the L-1 sand FB-C measured in a specimen taken from the 316/A-12 core (Chang and Zoback, 1998). A: effective vertical stress versus strain; B: effective horizontal stress versus strain.

A third way to view the data is by plotting mean effective stress versus differential stress (Figure 5.14). This type of plot is usually called p-q plot in soil mechanics (e.g., Muir-Wood, 1991). The data exhibit a general trend (thin dashed line) that follows the virgin compaction stress path K_0 identified previously in Figure 5.13. At low effective

mean stresses (i.e., < 300 psi), the data plot slightly above this trend and may indicate some overconsolidation at stress states the Lentic sand experienced before. At effective mean stresses of ~300 psi and 1,300 psi, the plot reveals "flat spots" where the differential stress remains essentially constant. Again, these spots identify the yield points (arrows). The curved, dashed lines display the associated Roscoe surfaces (also called end-caps) and exhibit the state of sudden pore volume change and sediment compaction (Atkinson, 1993).

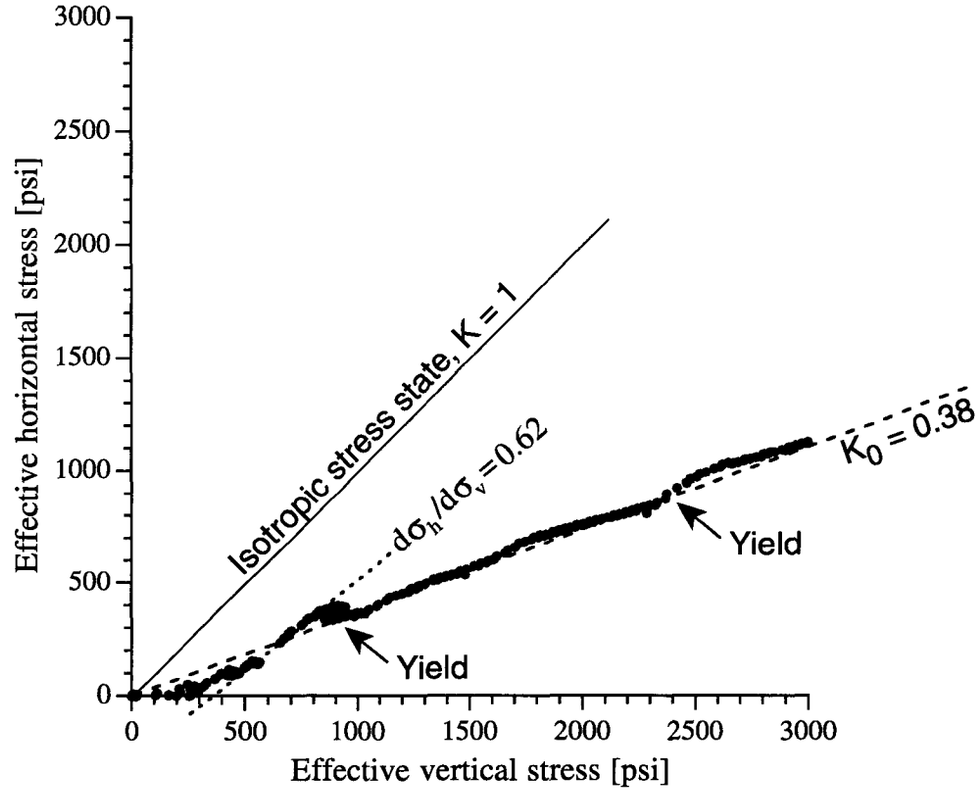

Figure 5.13: Effective horizontal versus effective vertical stress of the Lentic sand (well 316/A-12, FB-C; Figure 5.8). K_0 denotes the effective stress ratio. Local slope changes as a result yield are indicated by their $d\sigma_h/d\sigma_v$ value.

The gray squares in Figure 5.14 are the field measurements of pore pressure and stress for the two pore pressures that I specified as upper and lower bounds when viewing the pressure histories of the Lentic sand in FB-C (dashed lines in Figure 5.9B). They represent either the initial state (P_p = 5,400 psi) or a lower limit (P_p = 4,300 psi) to which three of the pressure curves (wells A-1, A-8, and A-10) appear to converge. The error bars were calculated from the uncertainties in pore pressure and stress measurements and variations (i.e., fluctuations) observed in Figure 5.9B around the two bounding values. The derivation of the state of stress from the field data, at the two given pore pressure values, is given in

the appendix to this chapter. It is interesting to observe that the depicted bounding field conditions plot either right at (P_p = 5,400 psi) or within the error range of (P_p = 4,300 psi) the identified yield points of the laboratory sample. This observation suggests that the observed plastic deformation in the laboratory may be able to explain the pressure history behavior seen in the field data. When fluid production depletes the reservoirs and induces loading, the Lentic sand in the field cannot sustain the increased differential stresses (i.e., > 1,200 psi). As a result, the sand follows a virgin compaction trend that is associated with grain rearrangements (rotations, reshuffling etc.) leading to continuous and at times even sudden loss of volume. These processes can either maintain or raise the pore pressure.

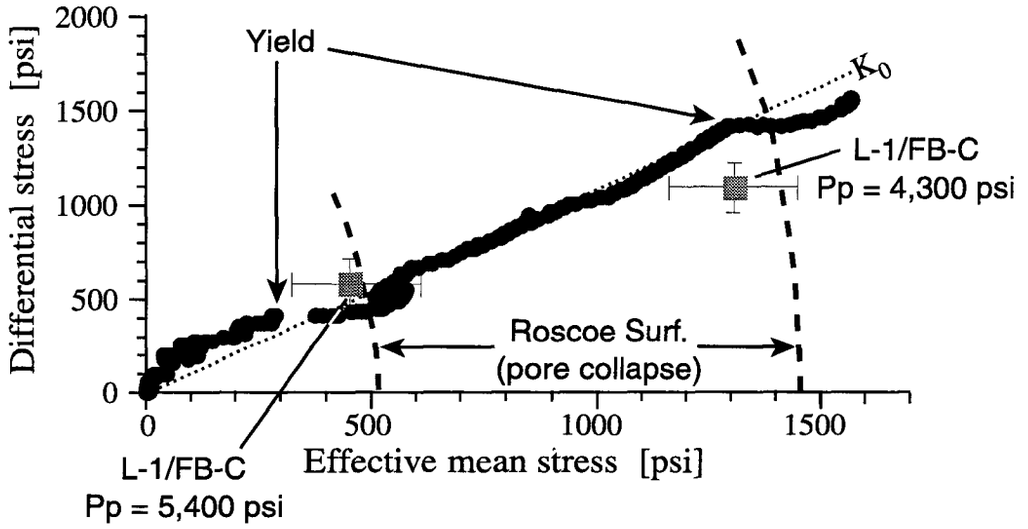

Figure 5.14: Effective mean versus differential stress of the Lentic sand (well 316/A-12, FB-C; Figure 5.8). Yield points are shown with arrows. The two dashed lines indicate the Roscoe surface at which pore collapse occurs. The dashed line following the general trend is the stress path K_0 as identified in Figure 5.12. The two gray squares with error bars exhibit two stress states in the Lentic sand, FB-C, corresponding with the two pore pressures identified in Figure 5.9B (dashed lines).

5.5.5 Implications

In-situ, the Lentic sand is highly overpressured and extremely undercompacted. This is a result of the undrained conditions the sand has been exposed to since it was deposited and burial began. The pore fluids never expelled from the system, hence, the sand never compacted or cemented, and is in a state of incipient failure as it was right after deposition. The pressure data from the field show that the sand grains cannot sustain shear stress higher than ~1,200 psi. The laboratory measurements provides evidence that in response to reservoir depletion and the resultant matrix loading, the reservoir responds in two ways: (i)

instantaneous virgin compaction and plastic deformation and (2) time dependent viscous creep and stress relaxation. Most probably, these two processes operate simultaneously in the reservoir reducing the pore volume. If fluids are being produced from the reservoirs, instantaneous effects such as compaction and pore volume reduction and time dependent viscous creep continuously accompany production. If production is shut-in, only viscous effects dissipate any excess differential stress. Because the sand is largely undrained the pore fluid pressure increases ($\Delta\Phi > \Delta V_{prod}$; Figure 5.10). These processes either maintain or even increase pore pressure if the change in porosity is equal or greater than the fluid volume produced from the reservoirs ($\Delta\Phi \geq \Delta V_{prod}$; Figure 5.10).

As a result of these findings, I suggest that the total strain (ε) in the reservoir induced by production can be written as the sum of the following three components:

$$\varepsilon = \varepsilon^e + \varepsilon^p + \varepsilon^\eta \qquad \text{Eqn. 5.3}$$

where ε^e, ε^p, and ε^η denote elastic, plastic, and viscous strain respectively. To give a quantitative example, I assume that the pore pressure increase (ΔP_p) of 1,750 psi in the sealed Lentic sand, FB-A, after shut-in (Figure 5.9A) is the result of pore volume reduction from the processes described above. The fluid strain in the undrained reservoir is:

$$\varepsilon^f = \frac{\Delta V}{V} = \frac{\Delta P_p}{K_f} = 0.024 \qquad \text{Eqn. 5.4}$$

where ΔV, V, and K_f denote change in volume, total volume, and the bulk modulus of the fluid respectively. Using a value of 0.5 GPa for K_f (Batzle and Wang, 1992), I obtain ε^f = 0.024. The elastic strain (ε^e) can be calculated in a similar fashion:

$$\varepsilon^e = \frac{\Delta V}{V} = \frac{\Delta \sigma_m}{K_s} = 0.0046 \qquad \text{Eqn. 5.5}$$

where $\Delta\sigma_m$ and K_s denote the change in mean effective stress and bulk modulus of the reservoir matrix respectively. I calculated $\Delta\sigma_m$ from the field data (= 1,085 psi = 7.5 MPa) taking the change in fluid pressure (ΔP_p) and a change in horizontal stress (poroelastic behavior with $\nu = 0.3$; Eqn. 3.2) into account. Chang and Zoback (1998) determined K_s for the Lentic sand to be 1.6 GPa. The resulting value for ε^e equals 0.0046, i.e. about 19% of ε^f. This simple calculation shows that within the assumptions made, a combination of

plastic and viscous deformation (ε^p and ε^η respectively) accounts for 80% of the total strain on the fluid (ε^f).

5.6 Discussion

The pore pressure histories in the three stratigraphic levels GA-2, LF, and Lentic exhibit marked differences. From shallow to deep, the SEI 330 field can be characterized as a system in which the reservoirs become increasingly overpressured and undercompacted. Because of the stratigraphic dissimilarity, individual sands show different pore pressure and sand compaction responses to hydrocarbon production. In Figure 5.15, I summarize in a diagram the differences in compaction behavior between the three stratigraphic levels. I schematically view each sand reservoir as being contained in a sealed box that is exposed to an overburden load (S_v) and has an outlet pipe with a valve for the pore fluids to drain (Figure 5.15 top).

The shallow GA-2 sand (Figure 5.15A) is well drained (open valve), hydrostatically pressured, and normally compacted. Compartmentalization does not exist at this level. As a result, production induces only minor pore pressure changes and no load change on the reservoir grains.

The intermediate LF sand (Figure 5.15B) is moderately overpressured, compartmentalized, and slightly undercompacted. Initially, the reservoir valve is closed and only production drains pore fluids out of the compartments. Production causes marked pressure declines and significantly raises the load on the reservoir grains. Because of uniform grain cementation, this increase in overburden load is well supported by the matrix, thereby increasing the differential stress and bringing the sand closer to frictional failure. It is very likely that linear elastic effects (elastic pore volume compaction) accompany the production process. However, this is not obvious from the pressure data.

The Lentic sand is severely overpressured and undercompacted showing essentially no intergranular cementation. Pressure histories demonstrate that the reservoirs are compartmentalized on a sub-fault block scale. Production induces very little change in pore pressure. Either pressures remain approximately at initial values or decrease somewhat and then increase again. After shut-in of a depleted reservoir pore pressure rises again. These observations indicate that the sands fails (i.e. yields) as it is being loaded during depletion. In response, it starts to follow a virgin compaction curve. This process is characterized by non-linear elastic effects such as plastic and viscous deformation and results in pore volume reduction and fluid compression (i.e., increasing the pressure). Elastic effects appear to play only a minor role.

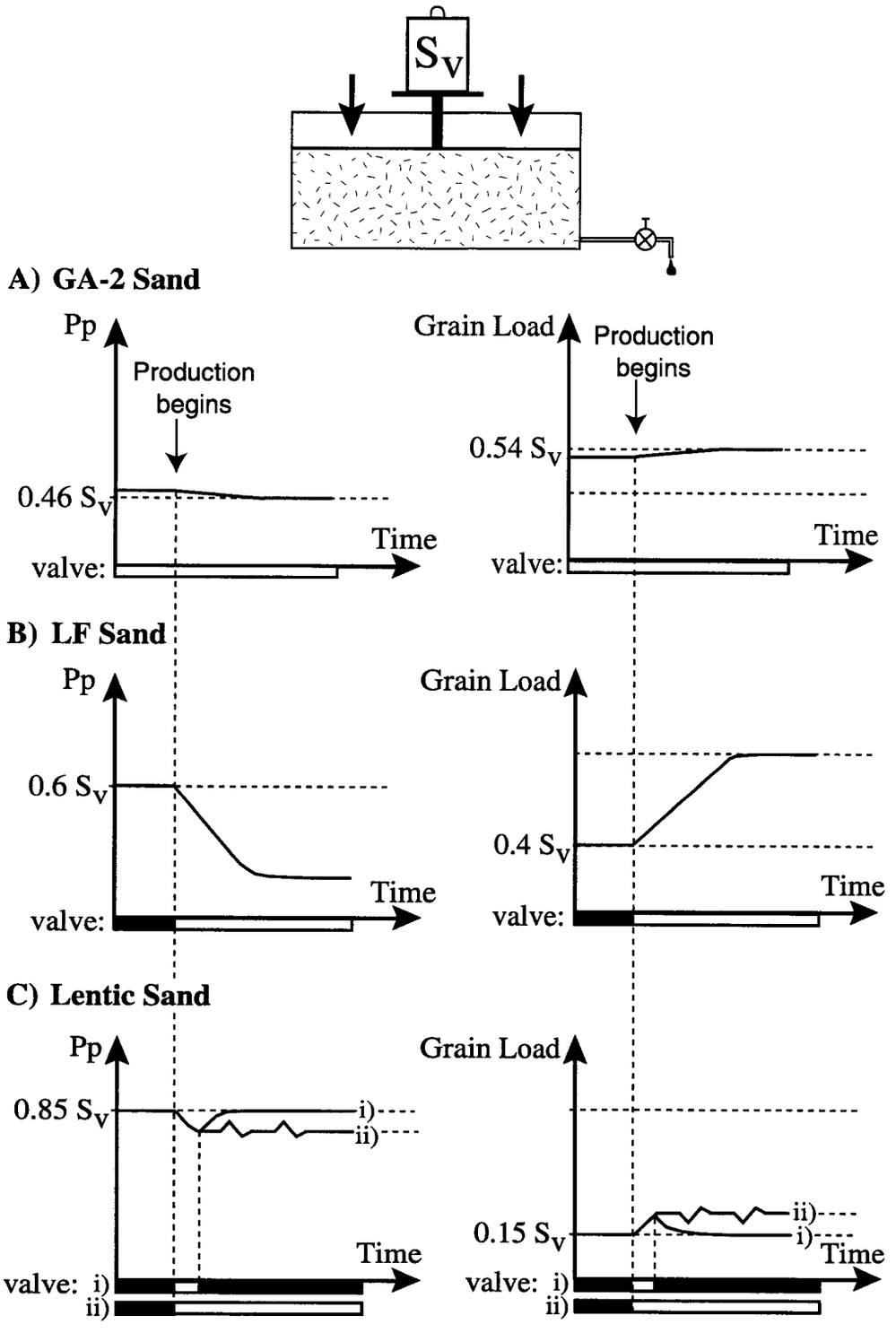

Figure 5.15: Schematic summary of pore pressure and grain load behavior in the three reservoirs sands GA-2 (A), LF (B), and Lentic (C). The valve shown in the top figure indicates drainage or production from the reservoirs. The valve indicator in the figures A) - C) below indicates black for a closed valve and white for an open valve. Notice, for the Lentic sand (C), there are two scenarios displayed (i and ii).

In figure 5.15C, I show two scenarios: (i) Pressure drop followed by an increase. This curve simulates the behavior observed in FB-A (Figure 5.9A), where after production shut-in viscous relaxation dissipates differential stresses in the matrix and raises the pore pressure. In this case, the valve is open only during a short production period. (ii) Pressure drop followed by fluctuations around a constant value. This curve imitates the behavior observed in FB-C (Figure 5.9B) representing virgin compaction and yielding during production. In this scenario, the valve is closed up to production begin and then remains open. Curve (ii) could also be shown without the initial pressure drop to acknowledge the pressure response in well A-4 (Figure 5.9B).

The pore pressure evolution in FB-C (Figure 5.9B) and the associated plastic behavior at equivalent effective stress levels as observed in the laboratory indicate a progression from one yield point to the other. Perhaps these yield points indicate as equilibrium states in the reservoir that is governed by viscous and plastic deformation. This is an intriguing observation, which may have broader implications. Numerous studies have shown that the crust when comprised of crystalline rocks is in frictional equilibrium (e.g., Zoback and Healy, 1984, 1992; Brudy et al., 1997). These rocks are well consolidated and sustain significant shear stresses (and stress is "locked-in" to the rock). Poorly consolidated and overpressured Lentic-type sediments from the Gulf of Mexico, however, appear to behave differently in the sense that they do not follow Mohr-Coulomb theory (see chapter 3). In terms of rheology, these sands and shales are quite different because they cannot sustain large differential stresses (they "flow"). It would be very interesting to test whether other sedimentary basins around the world that are also characterized by soft sediments due to rapid deposition and burial behave in a similar fashion. Perhaps, this would allow to establish states of equilibria for crustal rocks and sediments as a function of rheology (i.e., cemented versus unconsolidated).

5.7 Conclusions

The production related pressure transients exhibit different behaviors for reservoirs at different stratigraphic levels. Shallow sands (i.e., GA-2) are at hydrostatic conditions and appear to be well drained and normally compacted. At intermediate stratigraphic levels, reservoirs (i.e., LF) are undercompacted and moderately overpressured. With production, pore pressures decline significantly suggesting that the sand grains can support the additional, induced differential stresses. The change in horizontal stress with changing pore pressure indicates a value for the stress path parameter A of 0.81. This value is high but has been observed in other fields around the world (e.g., Ekofisk) and can be explained by

combined stress-strain boundary conditions. Multiple wells that penetrated the LF sand exhibit uniform pressure transients within the same fault block. I interpret this as evidence for a hydraulically continuous compartment. The deep Lentic (or L-1) sand is severely undercompacted and overpressured. Non-uniform pressure transients within the same fault block indicate sub-compartmentalization. During production pore pressures in the Lentic sand either maintain their initial values or decrease and then increase again. Laboratory measurements indicate that both plastic and viscous mechanisms operate at in-situ effective stress levels. Upon production, the reservoir matrix follows a virgin compaction stress path with occasional events of sudden pore volume collapse. Following production shut-in, the sand exhibits a steady pore pressure recovery that can be explained by viscous stress relaxation and associated pore volume reduction.

5.8 Acknowledgments

I would like to thank Pennzoil, Shell, Texaco, and Chevron for generously providing the data used in this analysis. Peter B. Flemings and Beth B. Stump provided invaluable help and suggestions during the preparation and revision of this manuscript. Gilbert Palafox and Carl Chang conducted the laboratory experiments on the Lentic sand and provided the resulting data. This project is funded by the Gas Research Institute under contract number 5095-260-3558 and the Stanford Rock and Borehole Geophysics (SRB) Consortium.

5.9 Appendix

5.9.1 Relation between effective stress path (A) and stress ratio (K)

The effective stress ratio can expressed as:

$$K = \frac{\Delta\sigma_h}{\Delta\sigma_v} = \frac{(S^d{}_h - P^d{}_p) - (S^i{}_h - P^i{}_p)}{(S^d{}_v - P^d{}_p) - (S^i{}_v - P^i{}_p)} \qquad \text{Eqn. 5.A1}$$

where superscripts d and i refer to depleted and initial states respectively. Assuming that the total vertical stress is constant during production, equation 5.A1 reduces to:

$$K = \frac{S^d{}_h - S^i{}_h + P^i{}_p - P^d{}_p}{P^i{}_p - P^d{}_p} = \frac{\Delta S_h - \Delta P_p}{-\Delta P_p} = 1 - \frac{\Delta S_h}{\Delta P_p} = 1 - A \qquad \text{Eqn. 5.A2}$$

5.9.2 Derivation of the state of stress in the Lentic sand, FB-C

The upper pore pressure value reflects the initial conditions (i.e., P_p = 5,400 psi; Figure 5.9B). Pore pressure measurements taken during four fracture completions carried out in 1994 in the Lentic sand show approximately the same pore pressure as the initial value (Figure 5.9B). Thus, I used the average least principal stress values obtained from the minifracs as representative for the state of stress at initial conditions (Table A1).

For the lower bound pore pressure value, I had to account for the pore pressure decline in the reservoir (i.e., ΔP_p = 1,100 psi). I assumed that this change in pore pressure is accompanied by a change in the state of stress. Chang and Zoback (1998) determined in laboratory measurements an average Poisson's ratio (ν) for the Lentic sand of 0.31. Using the poroelastic model for uniaxial conditions (chapter 3, equation 3.1), I calculated the change of stress (ΔS_h) with the change of pore pressure (ΔP_p) (Table A1).

TABLE A1:

Pp [psi]	**SSTVD [feet]**	**Sv [psi]**	**ΔP_p [psi]**	**ΔS_h (ν=0.31) [psi]**	**S_{hmin} (ave.) [psi]**	**σ_{mean} [psi]**	**σ_{mean} error [psi]**	**σ_{diff} [psi]**	**σ_{diff} error [psi]**
5,400	6,800	6,250	0	0	5,652	451	295	598	250
4,300			1,110	506	5,146	1,214		1,104	

CHAPTER 6

STRESS, PORE PRESSURE, AND DYNAMICALLY CONSTRAINED HYDROCARBON COLUMNS IN THE SOUTH EUGENE ISLAND 330 FIELD, GULF OF MEXICO

This chapter will be submitted this month (August 1998) to the American Association of Petroleum Geologists Bulletin with Beth B. Stump, Peter B. Flemings, and Mark D. Zoback as co-authors.

6.1 Abstract

Hydrocarbon phase pressures at the peak of two severely overpressured reservoirs in the South Eugene Island 330 field, Gulf of Mexico, converge on the minimum principle stress of the bounding caprock. I interpret the system is dynamically constrained by the stress field present through either fault slip or hydraulic fracturing. In two fault blocks of a shallower, moderately overpressured reservoir sand, hydrocarbon phase pressures are within a range of critical pore pressure values for slip to occur on the bounding growth faults. I interpret that pore pressures in this system are also dynamically controlled by the critical value for slip to occur on the bounding growth faults. I introduce a dynamic capacity model to describe a critical reservoir pore pressure value that corresponds to either the sealing capacity of the fault against which the sand abuts or the pressure required to hydraulically fracture the overlying shale or fault. This critical pore pressure is a function of the state of stress in the overlying shale and the pore pressure in the sand. I require that the reservoir pore pressure at the top of the structure is greater than in the overlying shale. The four remaining reservoirs studied in the field exhibit reservoir pressures well below critical values for dynamic failure and are, therefore, considered static. All reservoirs that are dynamically constrained are characterized by short oil columns, whereas the reservoirs with static conditions have very long gas and oil columns.

6.2 Introduction

A number of young and rapidly formed sedimentary basins exist around the world in which significant amounts of hydrocarbons have migrated considerable vertical distances through thick sequences of low permeability shale (e.g., offshore Nigeria, offshore Gulf of Mexico, offshore South-East Asia; Nehring, 1991; Holland et al., 1992; Grauls and Baleix, 1994). In this paper, I introduce a conceptual model, that I call the dynamic capacity model, to formalize two dynamic mechanisms (hydraulic fracturing and flow along active shear fractures) by which hydrocarbon migration in these sedimentary basins may occur by enhanced fracture permeability. For both of these dynamic mechanisms fluid flow is governed by fracture permeability and to quantify them precise knowledge of in-situ state of stress and pore pressures conditions is required.

Faults have long been known to act as conduits for fluid flow (see review by Hickman et al., 1995). Hooper (1991) raised the possibility that in many hydrocarbon reservoirs faults may seal or conduct fluids at different times (or space) along the same fault plane. In the past, it was argued that the sealing or non-sealing capacity of a fault is dependent only

upon the capillary properties of the fault gauge zone or the caprock (e.g., Smith, 1966) and leakage (i.e., fluid migration) is largely dominated by Darcian flow within the matrix. However, in the limit, if permeabilities are very low and capillary entry pressures become extremely high (e.g., shales) different mechanisms must provide enhanced permeability for fluids to migrate efficiently. Watts (1987) argues that in this scenario seal failure may occur by hydraulic fracturing. More recently, numerous publications have given the issue of fracture permeability controlling hydrocarbon entrapment and migration more importance. Leach (1993a-c) argues that hydrocarbons in South Louisiana Tertiary sediments have migrated vertically along faults by means of periodic hydraulic fracturing. Gaarenstrom et al. (1993) recognized more explicitly that faults control pressure distribution and compartmentalization in the Central North Sea. Similarly, Grauls and Baleix (1994) attributed efficient transfer of liquid hydrocarbons in a sedimentary in South-East Asia to the presence of faults and fractures. These publications specifically argue that stress is an important factor for fluid flow and point toward the importance that knowledge of the in-situ state of stress is vital for a fundamental understanding of distribution and prediction of pore pressures in sedimentary basins. However, they all presume that natural hydraulic fracturing is the dominant mechanisms for providing the necessary fracture permeability. In this scenario, pore pressures are required to be as high as the least principal stress in the overlying strata (Nur and Walder, 1990).

Alternatively, fracture permeability can also be enhanced by shear failure along active faults. Sibson (1992) proposed episodic fluid flow along rupturing faults associated with vein deposits in a "fault-valve" fashion. Barton et al. (1995) present strong evidence from wells drilled in crystalline rock to argue that faults, which are optimally oriented for shear failure (i.e., critically stressed), have increased permeability and conduct fluids. Non-critically stressed faults, in contrast, do not provide fluid migration pathways. Ingram and Urai (1997) argue in a general sense that this mechanisms may also be operative in sedimentary basins and, more specifically, Engelder and Leftwich (1997) propose it for fluid migration in the oil and gas fields of South Texas.

With the dynamic capacity model introduced in this paper, I further investigate both dynamic mechanisms (hydraulic fracturing and failure along shear fractures) to find out whether reservoir pore pressures, hydrocarbon columns, and fluid flow could be controlled by fracture permeability in a state of dynamic equilibrium with the ambient state of stress. To know if either of the two mechanisms are operative accurate knowledge of the state of stress and pore pressure conditions is needed in both shale units and sand reservoirs. I outline the required in-situ conditions for each mechanism and carefully test the model in eight reservoirs of the South Eugene Island (SEI) 330 field, Gulf of Mexico. Pore pressures

and hydrocarbon column heights in moderately and severely overpressured reservoirs of the SEI 330 field appear to be limited by the stress field present.

6.3 Dynamically constrained hydrocarbons

Figures 6.1A through C summarize three possible hydrocarbon migration scenarios by establishing relationships between reservoir sand pore pressures and in-situ state of stress in the ambient shales. Two of the mechanisms discussed (Figures 6.1A and B) are dynamic (i.e., involve sudden failure of the sealing cap rock) while the third one is static (Figure 6.1C). Mohr circles characterize the stresses in the caprock at the point where the sand is juxtaposed against shale and possibly a bounding fault. A necessary condition for either of the two dynamic mechanisms (Figures 6.1A and B) to be operative is for the pore pressure in the sand to be higher than in the overlying shales because it is the pressure in the underlying sands that has to induce failure in the shale for fluid flow to occur.

Areas undergoing rapid sedimentation like the Gulf of Mexico are often characterized by a normal faulting environment where the overburden is the maximum principal stress (i.e., $Shmin \leq SHmax \leq Sv$). In such areas the pore pressures in compacting shales are generally expected to be higher than in adjacent sands units because of their low permeability and relatively poor drainage during compaction. However, there have also been models published predicting the contrary (i.e., pore pressures in sands are higher than in adjacent shales) under appropriate circumstances. The so-called centroid is such a model in which at the top of a tilting, water-filled, sand-layer higher pore pressures develop than in adjacent, impermeable shales. This phenomenon is achieved by structural relief that induces differential sediment loading. The centroid model was first introduced by Dickinson (1953) and further elaborated on by England (1987) and Traugott and Heppard (1994), who coined its name. Stump et al. (in prep.) describe and quantify this model and apply it to the sedimentary sequences of the SEI 330 field.

The dynamic capacity model is a modified version of the centroid model. I not only consider relative values of pore pressures in sands and adjacent shale units but also takes into account the ambient state of stress in the shales that might control dynamic mechanisms for fluid migration and accumulation. There are two important differences between the centroid model and the dynamic capacity model. First, the centroid model focuses on a water filled sand lens or the water phase pressure in a sand sense. In the dynamic capacity model I consider the pore pressure as measured in the reservoir (P_p^{ss}) regardless of whether it is the water or a hydrocarbon phase. Hence, P_p^{ss} at the top of the structure accounts not only for the pressure difference between sand and shale due to

structural relief (as prescribed by the centroid model) but also for the hydrocarbon buoyancy effect. As a result, the pressure difference between sand and shale is even greater. Second, I consider dynamic mechanisms for fluid flow. These mechanisms allows me to establish bounds for the maximum column heights supported by the system since it is the sealing capacity of the overlaying caprock or the fault against which the reservoir abuts that controls a critical pore pressure in the sand.

Figures 6.1A and B exhibit a state of dynamic equilibrium in which the pore pressure in the sand (P_p^{ss}) has reached a maximum possible value. I call this maximum pressure value the dynamic capacity of the reservoir (P_p^{crit}). Beyond this critical pore pressure, failure would occur allowing fluids to escape. In Figure 6.1A this mechanism is hydraulic fracturing (e.g., Hubbert and Willis, 1957; Nur and Walder, 1990) where the pore pressure has to overcome the least principal stress in the shale (S_{hmin}^{sh}) for the seal to breach the cap rock. The second dynamic fluid flow mechanisms is by frictional failure along optimally oriented, pre-existing faults when the shear stress resolved along the fault overcomes its frictional resistance and the fault slips (Figure 6.1B). For this mechanism, the critical pore pressure in the sand is not required to be as high as the least principal stress in the overlying shale ($P_p^{crit} < S_{hmin}^{sh}$). Shear failure has been associated with dilatancy (pore-volume increase due to the formation of microcracks) resultant permeability increase and fluid expulsion along fault zones (e.g., Makurat, 1985; Antonellini and Aydin, 1994). Also, geometric irregularities along the fault plane tend to cause areas of opening at the time the fault slips.

The third scenario (Figure 6.1C) shows pore pressures that are considerably lower than the critical value P_p^{crit} and I consider these reservoirs not to be filled to their dynamic capacity. The sand pore pressure can be greater or less than that of the bounding shale, because the reservoir is in a relatively static state not involving any dynamic failure mechanisms. In this case the sand could still be filling, it could be leaking or the column height could be spill point controlled.

I illustrate the dynamic capacity model in the light of a sand reservoir that is filling over time with oil or gas until the hydrocarbon column has reached a specific height (Figure 6.2). The maximum column the reservoir sand can support depends on (i) the initial water phase pressure in the reservoir, (ii) the mechanisms by which fluids migrate, and (iii) the density of the hydrocarbon phase. When the reservoir sand has a low initial water phase pore pressure a large hydrocarbon column can accumulate before the dynamic capacity (i.e., P_p^{crit}) is reached (Figure 6.2A). When the reservoir sand has a high initial water phase pore pressure the dynamic reservoir capacity is reached at a much earlier time (t_2; assuming equal filling rates) and a significantly smaller hydrocarbon column develops (Figure 6.2B).

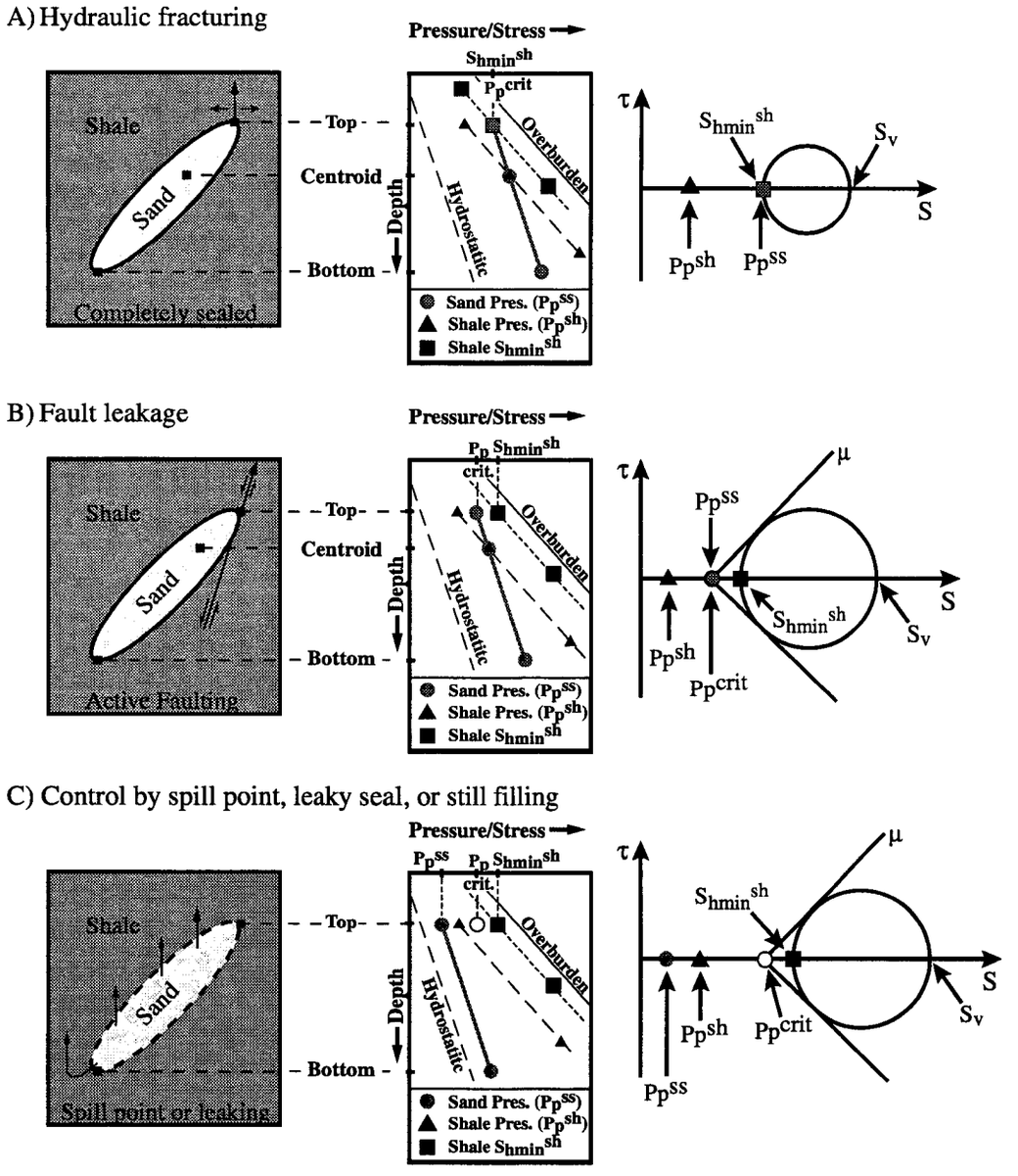

Figure 6.1: The dynamic capacity model. Left: tilting sand lens that is filled surrounded by shales. Middle: pore pressures and stresses as a function of depth for this reservoir system. Shale pressures (P_p^{sh}, black triangle) follow the lithostatic gradient (i.e., overburden) recording undrained conditions. Sand pressures (P_p^{ss}) record hydraulic communication and have the pressure gradient of the fluid phase. The centroid is the depth at which the shale pore pressure (P_p^{sh}) equals the sand pore pressure (P_p^{ss}) (Traugott and Heppard, 1994). Right: Mohr diagrams illustrate relative pore pressures and stress conditions at the top of the sand lens (i.e., the sand-shale interface). Total stresses are plotted and S_v denotes the overburden stress. A) Migration by hydraulic fracturing. $P_p^{ss} > P_p^{sh}$ and equals the least principal stress in the shale (S_{hmin}^{sh}). B) Migration by fault leakage. $P_p^{ss} > P_p^{sh}$ and equals the critical pore pressure (P_p^{crit}) for which the reservoir bounding fault starts to slip (indicated by the Coulomb friction line

touching the Mohr circle for a coefficient of friction of μ). Notice, in contrast to case (A), P_p^{crit} is lower than S_{hmin}^{sh}; yet, P_p^{ss} is at dynamic capacity. C) Migration controlled by a spill point or leaky seal. $P_p^{ss} < P_p^{crit}$ (i.e., not in dynamic equilibrium) and can either be above or below P_p^{sh}.

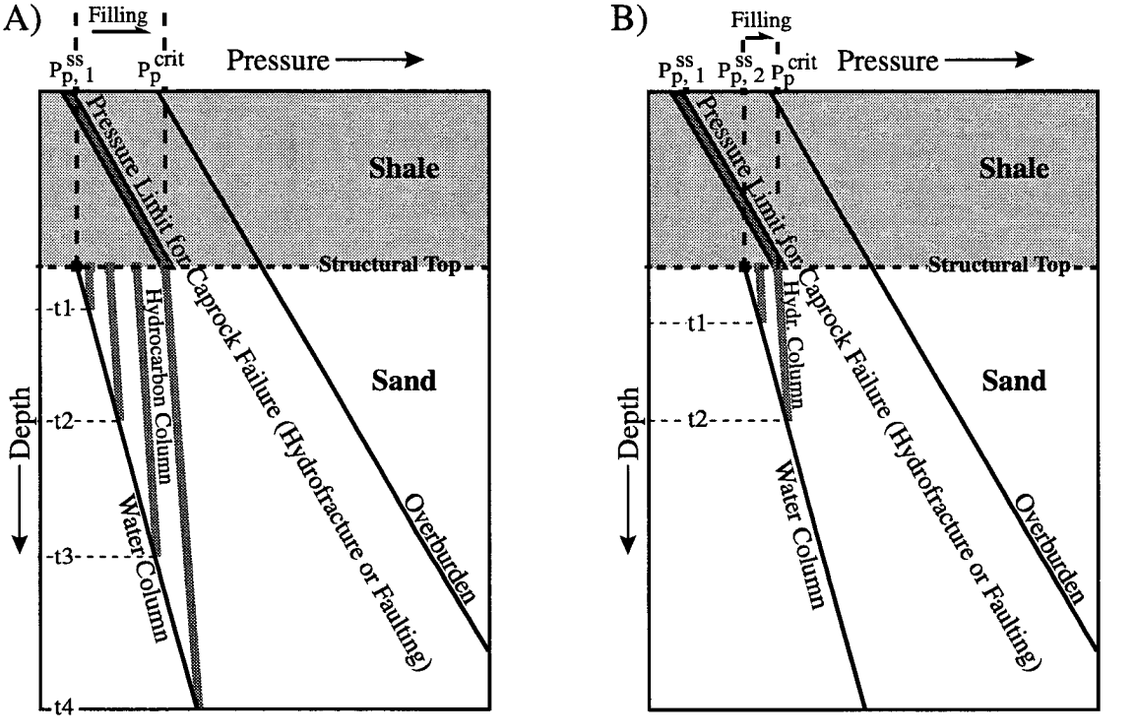

Figure 6.2: Conceptual model of filling of a sand reservoir with hydrocarbons (gray columns) as a function of initial water pressure (black) and time. The critical pore pressure (i.e., P_p^{crit}; wide gray line) is the maximum capacity of the reservoir where dynamic fluid flow mechanisms are invoked (hydraulic fracturing or fluid flow along active faults). A) Initially low reservoir water phase pore pressure, $P_p^{ss}{}_1$, allows development of a large hydrocarbon column over time (t_1 through t_4) before dynamic capacity (P_p^{crit}) is reached. B) Initially high reservoir water phase pore pressure ($P_p^{ss}{}_2 > P_p^{ss}{}_1$) allows only a small hydrocarbon column to accumulate and dynamic equilibrium (P_p^{crit}) is reached at an earlier time (t_2).

Since P_p^{crit} has to be equal to S_{hmin}^{sh} for hydraulic fracturing to occur the resulting hydrocarbon column is largest in this case as opposed to fluid flow along active faults, for which a smaller column accumulates because $P_p^{crit} < S_{hmin}^{sh}$. Conversely, if the reservoir has not reached its dynamic capacity because the observed hydrocarbon column is small and not in dynamic equilibrium, I can conclude that the reservoir is either still filling or has a spill point (i.e., statically controlled fluid flow).

Thus, I believe hydrocarbon column heights are potentially controlled by the state of stress at the reservoir-fault contact in a manner that when the pore pressure at the top of the sand (P_p^{ss}) reaches the value required for the fault to fail in the shale (P_p^{crit}) either by slip (Figure 6.1B) or by hydraulic fracturing (Figure 6.1A) an episode of fluid flow occurs. In this scenario, the reservoir has reached its maximum hydrocarbon column and is at dynamic capacity (i.e., the hydrocarbon column in the reservoir is in dynamic equilibrium with the state of stress in the overlying shale caprock).

6.4 The South Eugene Island 330 Field

6.4.1 Overview and data

I apply the dynamic capacity concept outlined above to the SEI 330 field.This field is a large hydrocarbon producing area in the Gulf of Mexico located about 160 km offshore Louisiana (Holland et al., 1990) (Figure 6.3A). Since 1972 over 250 million bbl (barrels) of liquid oil and 1.2 Tcf (trillion cubic feet) of gas have been produced (Schuhmacher, 1993) from over 25 different sands layers segmented by shales and normal faults into at least 100 structurally or stratigraphically distinct reservoirs (Figure 6.3B). The hydrocarbons produced from this thermally immature field are older than the reservoirs and are believed to have migrated vertically over significant distances (Holland et al., 1990).

This giant oil and gas field is a Plio-Pleistocene age salt-withdrawal minibasin bounded to the north and east by a regional (down to the south) growth fault system and to the south by an antithetic fault system (Alexander and Flemings, 1995). Beneath the OI sands the stratigraphy is largely shale dominated, and from the OI sands upward it is more sand-dominated. Pressures are closely tied to this stratigraphic architecture. In the shale-prone region, beneath the OI sands, severe overpressuring occurs. Because the pressures follow these stratigraphic surfaces, and because there is significant offset across the growth fault at this depth, overpressures are much deeper in the hanging wall than in the footwall (Gordon and Flemings, 1998).

Structure maps based on 3-D seismic and wireline data (provided by Pennzoil, the operator of blocks 330 ad 316) enabled me to analyze eight reservoirs from three different sands in five separate fault blocks. The three different sands are the Lentic (footwall, fault blocks A and C), the OI-1 (minibasin, fault blocks A, B, C, and E), and the JD (minibasin, fault blocks A and B) (Figures 6.3A and B) (see Alexander and Flemings, 1995, and Holland

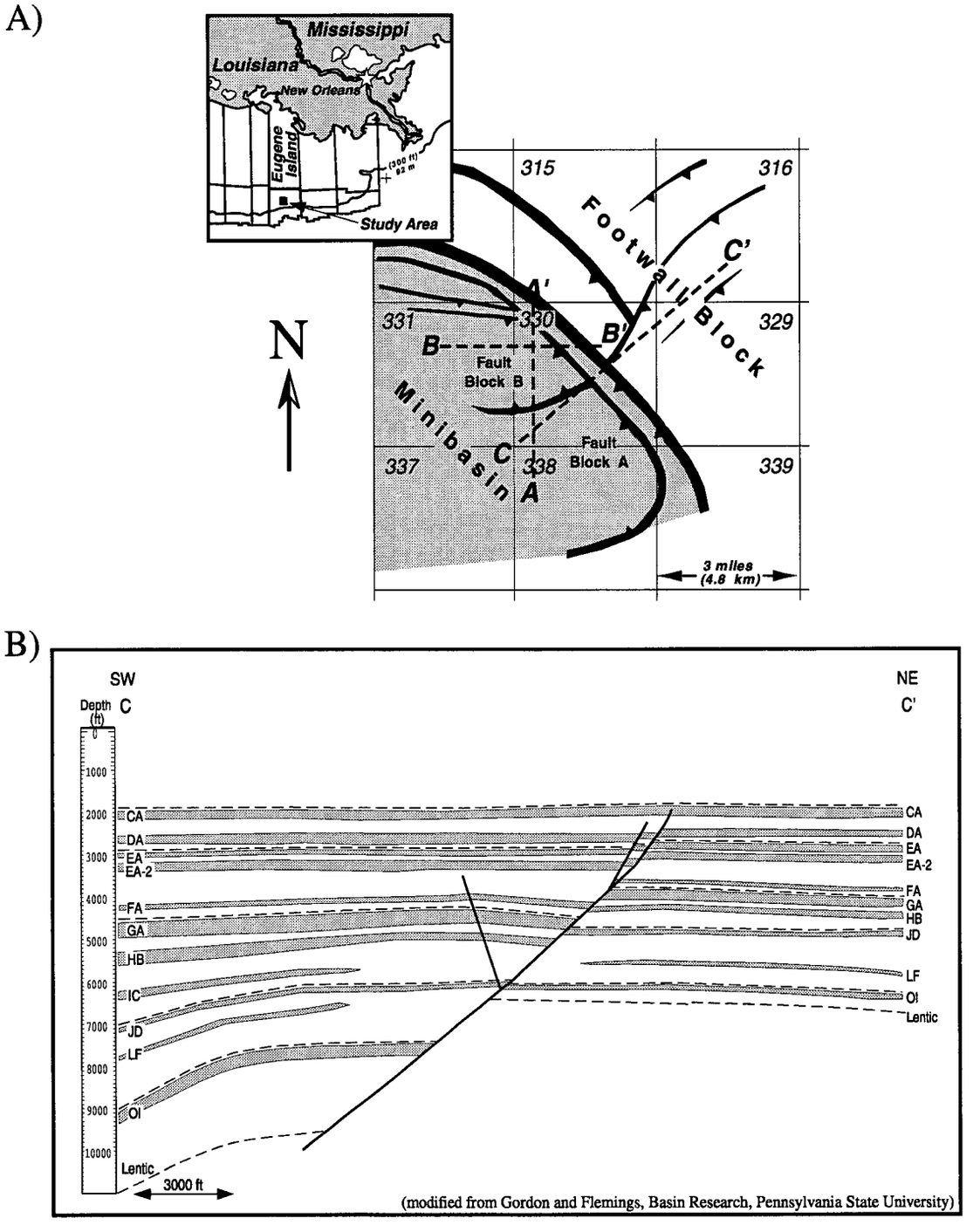

Figure 6.3: A) Basemap of the SEI 330 field outlining the minibasin and the footwall separated by the basin bounding growth fault system. The dashed line C-C' marks the transect of the cross-section in (B). Cross-sections along transects A-A' and B-B' are shown in Figures 6.10 and 6.11, respectively. B) Cross-section through the SEI 330 field along transect C-C' shown in A. Reservoir sands are displayed in gray labeled accordingly with their names; dashed lines are the corresponding flooding surfaces (modified from Gordon and Flemings, Basin Research, Pennsylvania State Univ.).

et al., 1992, for detailed discussion). I determined the depths of the structural highs in each of the 8 reservoirs from the structure maps and associated column heights using additional information on fluid contact levels (i.e., oil-water and gas-oil contacts). The data extracted from these maps are summarized in Table A1. The reservoir tops of the stratigraphically highest sand (the JD) shale out, while the structurally highest points of the deeper sand reservoirs (OI-1 and Lentic) abut against growth faults.

To determine in-situ pressure and stress, I used a data base consisting of downhole measurements from nearly 50 wells (provided by Pennzoil, Texaco, and Shell). These measurements include repeated pressure surveys (including in-situ temperature and oil gravity values), sonic logs, and leak-off tests (LOTs) and formation integrity tests (FITs) (Finkbeiner et al., 1996). I used the earliest pressure records in the reservoir sands to get the pore pressure conditions prior to production while the reservoir was still in an undepleted state (Table A2). Shale pressures (P_p^{sh}) were calculated from a porosity-effective stress method based on sonic log data (Hart et al., 1995; Stump and Flemings, 1997; Stump et al. 1998). For each fault block a pressure value was determined for any sonic log that penetrated the shales bounding the reservoirs (Table A3). A linear regression was fit to the data in each fault block to estimate the pressure within the caprock (Table A5). The minimum principal stress in the caprock (S_{hmin}^{sh}) was determined based on LOT and FIT measurements (Table A4). In contrast to LOTs, FITs do not hydraulically fracture the formation, hence, they generally present a lower bound for the minimum principal stress (Gaarenstrom et al., 1993). I linearly regressed the data to extrapolate S_{hmin}^{sh} on the structural high (Table A5).

Given pore pressures at some level within the reservoir sand, I calculated fluid densities and extrapolated the reservoir pressures to the structural tops. Some reservoirs have both oil and gas columns. In this case, I calculated the pressure using the oil gradient in the oil column between oil-water and gas-oil contacts and the gas gradient above the gas-oil contact to the top of the sand. I followed the approach of Batzle and Wang (1992) to obtain the live oil density (i.e., with the maximum gas dissolved) based on the in-situ reservoir temperature and API number of the oil. Oil gradients range from 0.2 psi/ft (= 4.52 MPa/km) to 0.34 psi/ft (= 7.68 MPa/km) (Table A2). I assumed a constant gradient of 0.1 psi/ft (= 2.26 MPa/km) for the gas gradient which is a reasonable assumption as verified from calculation of gas densities along structures using PVT data. The resulting fluid columns heights and pressures are then simply obtained by calculating the depth intervals from the fluid contacts (e.g., water-oil or oil-gas) to the top of the structure and using the respective fluid gradients (Tables A1 and A5).

The overburden stress (S_V) was derived by integrating density logs to account for undercompacted and highly overpressured sediments. The average density values from integration at the depths of interest resulted in gradients for all wells that range between 0.92 psi/ft and 0.93 psi/ft (Table A5). These values are significantly lower than the often assumed constant gradient of 1 psi/ft.

6.4.2 Characterization of pore pressure and stress conditions

The three sands investigated in this study (Lentic, OI-1, and JD sands; Figure 6.3B) cap three depositional cycles in the SEI 330 field and exhibit characteristic pore pressure and stress conditions. For each reservoir from these three stratigraphic layers I carefully examine pore pressures at their structural tops, in-situ stress of the overlying shale caps, and hydrocarbon column heights. This information is summarized in Tables A1 through A5. Subsequently, I analyze our results in view of the dynamic capacity model presented above.

First, I calculate the critical pore pressure value (P_p^{crit}) based on Coulomb frictional failure theory:

$$P_p^{crit} = \frac{S_{hmin}^{sh} - f(\mu)S_v}{1 - f(\mu)} \qquad \text{Eqn. 6.1}$$

where $f(\mu) = [\sqrt{\mu^2 + 1} + \mu]^{-2}$ and μ the coefficient of friction. I calculate an upper and lower bound for P_p^{crit} using two different values for μ that seem reasonable for the SEI 330 field: (i) $\mu = 0.3$ (lower bound) and (ii) $\mu = 0.6$ (upper bound) (Table A6). The lower μ bound results from laboratory experiments with clay under undrained conditions (e.g., Wang et al. 1979, 1980; Wood, 1990). The upper bound, in contrast, is a typical value found in field measurements in many areas around the world (e.g., see reviews in Zoback and Healy, 1984, 1992; Brudy et al., 1997). Second, I compare the pore pressure at the top of each reservoir sand to the range of P_p^{crit} values and draw some implications about fluid flow and the observed hydrocarbon column heights in each of the eight reservoirs. To evaluate how close the hydrocarbon column is to dynamic failure in a reservoir, I introduce a new parameter, the dynamic capacity stress ratio (C_{dyn}):

$$C_{dyn} = \frac{S_{hmin}^{sh} - P_p^{ss}}{S_v - P_p^{ss}} \qquad \text{Eqn. 6.2}$$

C_{dyn} resembles the effective stress ratio $K = (S_{hmin}{}^{sh} - P_p{}^{sh})/(S_v - P_p{}^{sh})$ for shales. K has been given substantial attention in the literature (e.g., Pilkington, 1978; Traugott, 1997) since it describes the fracture gradient, an important parameter for drilling operations. However, there is one important difference between K and C_{dyn}: for the dynamic capacity concept the driving parameter to invoke dynamic failure in the overlying shales is the critical pore pressure in the sand reservoir ($P_p{}^{crit}$). Therefore, with C_{dyn} I consider the reservoir pore pressure at the top of the structure ($P_p{}^{ss}$) and the least principal stress in the shale ($S_{hmin}{}^{sh}$). In case of hydraulic fracturing (Figure 6.1A), $P_p{}^{crit} = S_{hmin}{}^{sh}$ and hence, $C_{dyn} = 0$. In case of fluid flow along active faults (Figure 6.1B), $P_p{}^{crit} < S_{hmin}{}^{sh}$ and, hence, $C_{dyn} \neq 0$ depends upon the coefficient of friction, μ. Given μ=0.3 and μ=0.6 (upper and lower bound) I display the C_{dyn} values for each reservoir in Table A5. For comparison, Table A5 lists also the corresponding K values in the overlying shales. Table A6 shows the critical C_{dyn} values ($C_{dyn}{}^{crit}$) evaluated using $P_p{}^{crit}$ for μ=0.3 and μ=0.6 for which the bounding faults would slip.

6.4.3 The Lentic sand

The Lentic sand is the deepest reservoir sand in the SEI 330 field. It was deposited in an outer continental shelf to continental slope environment (Alexander and Flemings, 1995). Pore pressures prior to depletion are around 90% of the overburden. The data used for our study come from SEI 330 block 316 - the footwall side - of the minibasin bounding growth fault system (Figure 6.3A). There are two NE-SW striking normal faults and subsidiary fault splays against which the Lentic sand abuts (Figure 6.4). A roughly E-W striking antithetic normal fault sub-compartmentalizes the sand into fault block A and fault block C. This antithetic normal fault does not entirely separate fault blocks A and C. Pennzoil geologists suggest complete closure and hydraulic decoupling between the two reservoirs is achieved by an apparent permeability barrier (shown as thick "T"-dashes in Figure 6.4) further downdip to the east in fault block A. The Lentic sand has 500 ft. to 900 ft. of structural relief within each fault block (Figure 6.4). The highest points of the reservoirs abut the normal faults near the southern lease boundary. In fault block A, I used the 'lowest known oil' level as the oil-water contact to calculate the oil column. In both fault blocks, oil columns are less than 600 ft. (Table A1, Figures 6.5C and D).

Least principal stress magnitudes ($S_{hmin}{}^{sh}$) in the shales are derived from three different types of measurements conducted in the immediate vicinity of the Lentic sand (Table A4). The FIT and hydraulic fracture were carried out on the footwall side in block 330 just to the southwest of the area shown in Figure 6.4. The LOT comes from well 316/A-12 in fault block C (Figure 6.4). The hydraulic fracture test from well 330/A-20ST (Flemings et al,

1996) should accurately reflect the state of stress in the shale just above the Lentic sand. The state of stress in the shale on top of the Lentic sand obtained by a linear fit through the given data points suggests a near isotropic stress state (i.e., $S_{hmin}^{sh} \sim S_v$).

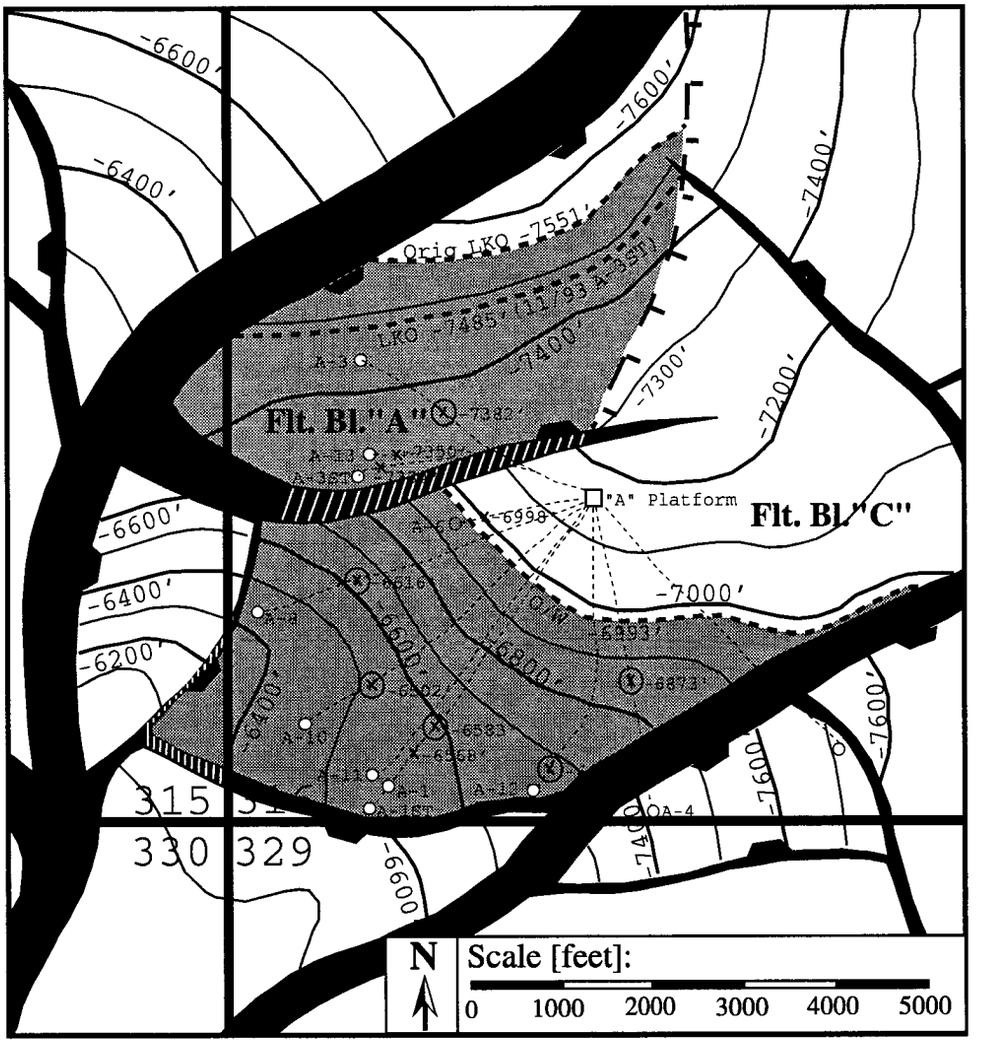

Figure 6.4: Structure map of the Lentic reservoir sand showing dominant structural features in the southwest corner of SEI 330 block 316 and adjacent blocks. Depth contours are in feet SSTVD (sub-sea true vertical depth). Wellpaths are displayed as thin dashed lines with points of reservoir penetration (crosses along wellpaths). Thick dashed lines display interpreted fluid contacts in the individual fault blocks (O/W: oil-water; LKO: lowest known oil). The associated depth intervals in the two reservoirs filled with oil are shown in gray. Thick "T"-dashes in fault block A exhibit assumed permeability barriers. The hatched fault segments (white) indicate potential slip areas along which fluids could migrate (see text). This structure map was generated by Pennzoil based on 3-D seismic and log data. The normal faults are vertical projections of the fault plane onto the Lentic horizon; the downthrown side of the fault is marked by black ticks.

Pore pressures in the Lentic sand reach greater than 90% of the overburden stress ($0.92 < \lambda_{ss} < 0.96$; Tables A2 and A5, Figure 6.5B). Water phase pore pressures at an equivalent depth do not match between fault blocks A and C indicating compartmentalization (Figure 6.5C). In footwall block C, P_p^{ss} at the top of the structure is within approximately 0.69 MPa to 1.38 MPa (= 100 psi to 200 psi) of the least principal stress in the shale (S_{hmin}^{sh}) (Figures 6.5A and B). The pore pressure at the top of the reservoir in footwall block A is also high but only within 1.82 MPa (= 264 psi) of P_p^{crit} for $\mu = 0.3$ and within 2.97 MPa (= 430 psi) of S_{hmin}^{sh} (Figures 6.5B and 6.6).

Stump et al. (in prep.) derived shale pore pressures in three wells just above the Lentic sand (Table A3). The shale is also highly overpressured ($\lambda_{sh} = P_p^{sh}/S_v$ ranges from 0.81 to 0.83, Table A3). However, the magnitudes are less than in the sands (i.e., $\lambda_{sh} < \lambda_{ss}$) indicating that pore pressures in the sand reservoirs below are about 9% higher (Figure 6.5C). As stated above, this is a necessary requirement for dynamic capacity mechanisms to operate in the reservoirs because it is the reservoir pore pressure that drives the overlying shale to failure.

As a result of the high overpressure in the shale, the near isotropic stress state, and low effective stresses, K is rather high (~0.9; Table A5). This is recorded in Figure 6.6 by the fact that the shale stress gradient line is 90% of the distance between the shale pressure and the overburden. This trend is typical for severely overpressured and undrained sediments of the Gulf Coast and has been reported in numerous publications (e.g., Althaus, 1977; Pilkington, 1978). Since overpressures at the top of the Lentic reservoirs are even more severe (i.e., P_p^{ss} is close to S_{hmin}^{sh}), I would expect C_{dyn} to approach zero or C_{dyn}^{crit} (Table A6) to indicate the proximity to dynamic failure. However, I find that C_{dyn} rather scatters between 0.46 and 0.76 (Table A5). Since the differential stress ($Sv - S_{hmin}^{sh}$) is so close to zero, the variations in P_p^{ss} are responsible for the significant scatter in C_{dyn}. Therefore, the proximity of the oil columns to dynamic failure in this case is quite difficult to assess using C_{dyn}.

However, it is clear from Figures 6.5A and B and Figure 6.6 that the pore pressures are close to both hydraulic fracturing and fault slip. In view of the dynamic capacity model, I find that the pore pressures in both fault blocks are not only near or within the lower and upper bound of P_p^{crit} but also approach the hydraulic fracture limit (Table A6) suggesting near dynamic failure conditions (i.e., slip along active faults as well as hydraulic fracturing) (Figures 6.5A, 6.5B, and 6.6).

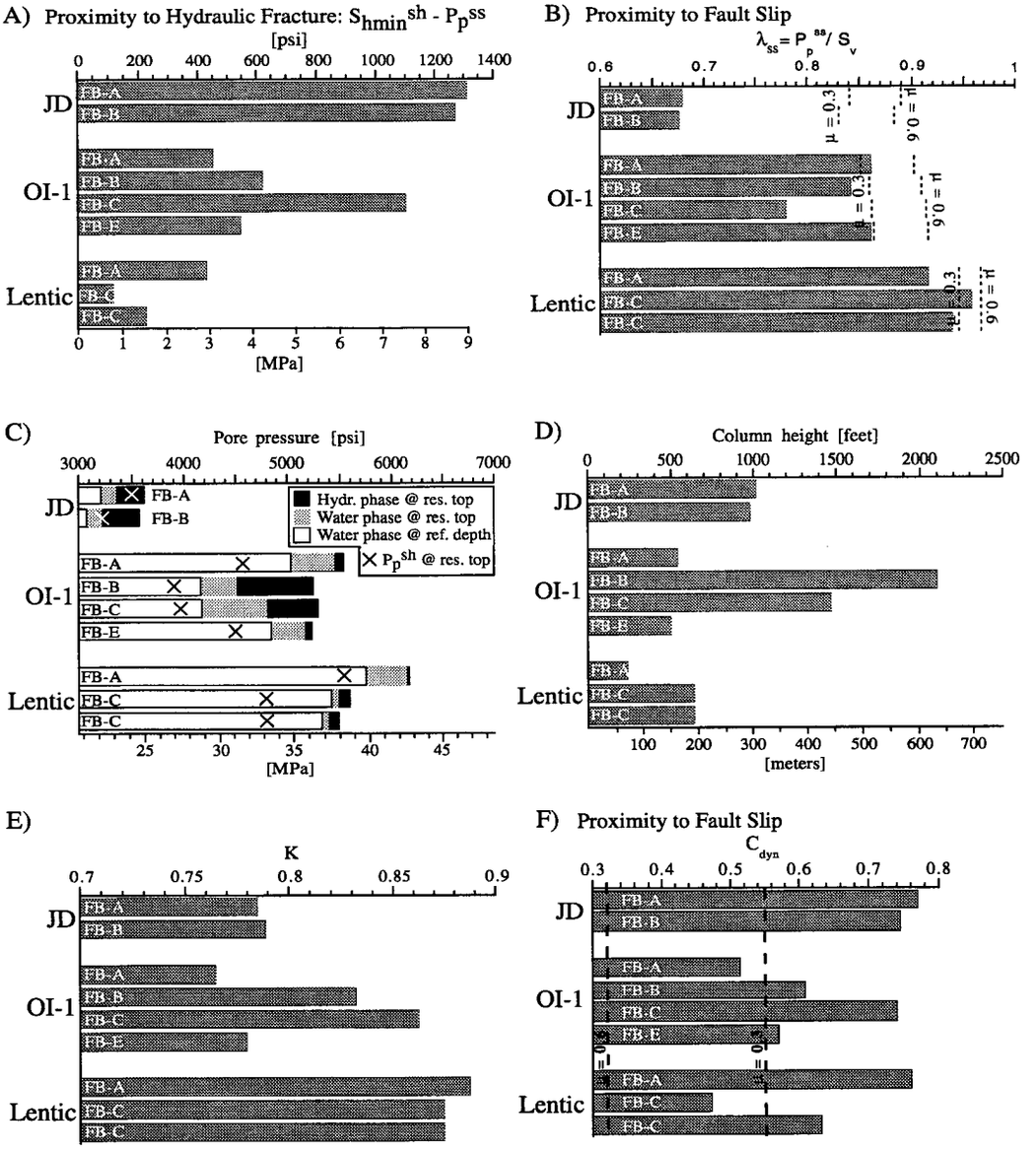

Figure 6.5: In-situ pore pressure and stress conditions at the top of the eight reservoirs in three SEI 330 sands. The abscissa displays the three sands in stratigraphic sequence. A: Tendency for hydraulic fracturing indicated by the difference between least principal stress in the shale (S_{hmin}^{sh}) and reservoir pore pressure (P_p^{ss}) to display the tendency for hydraulic fracturing. B: Tendency for fault slip shown as normalized reservoir pore pressures λ_{ss}. The dashed lines indicate lower and upper bound of critical pore pressures (P_p^{crit}) within the range of coefficients of friction (μ) between 0.3 and 0.6 respectively. C: Hydrocarbon (black column) and water (gray column) phase pore pressure at top of the reservoirs. The difference between both indicates hydrocarbon column height. The white column displays the water phase pore pressure at a sand specific reference datum (i.e., JD: 5,500'; OI-1: 6,000'; Lentic: 6,500' SSTVD). The cross shows the shale pressure (P_p^{sh}) at the top of the reservoirs. D: Column heights for hydrocarbon phases. E: Effective stress ratio K of the shale

caprock at the reservoir-cap interface. F: Dynamic capacity stress ratio, C_{dyn}, as defined with equation (2) to display the tendency for fault slip. The two dashed lines indicate the two critical C_{dyn} values evaluated using P_p^{crit} for both $\mu = 0.3$ and $\mu = 0.6$.

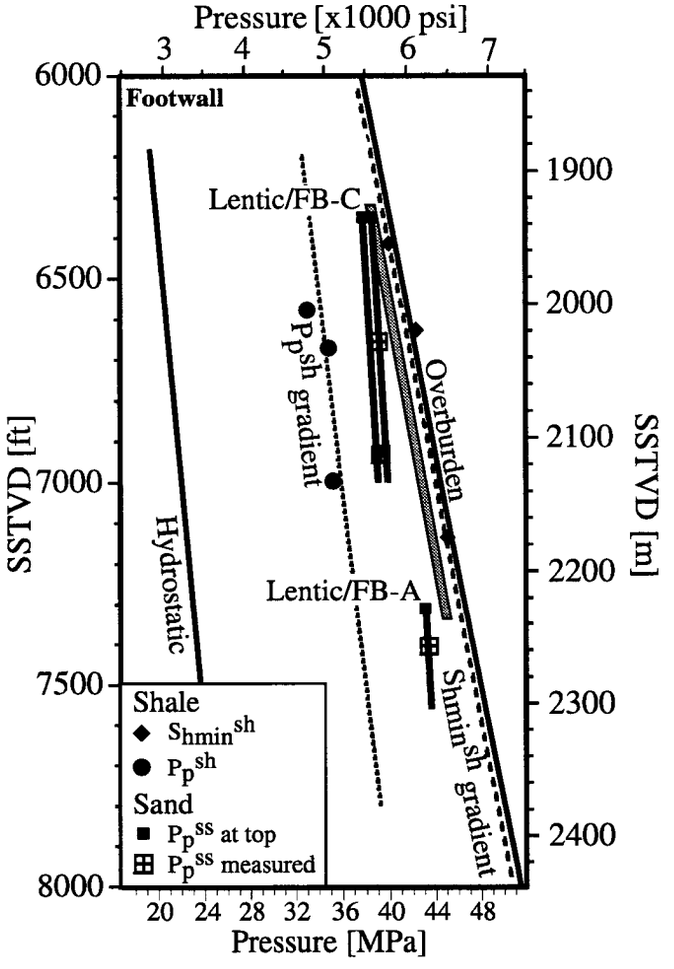

Figure 6.6: Pressure and stress state of the Lentic sand (located in Figure 6.4). Least principal stresses in shales (S_{hmin}^{sh}) are from leak-off tests (LOT) and formation integrity tests (FIT). I also display shale pore pressures (P_p^{sh}) (calculated using the porosity-effective stress method (Hart et al., 1995; Stump et al., 1998)) and reservoir pore pressures (P_p^{ss}). The black squares represent P_p^{ss} at the top of each sand (black for oil phase, gray for gas phase) calculated by using live oil gradients (Table A2). Solid lines represent hydrostatic and lithostatic gradients and the dashed lines are linearly regressed gradients for P_p^{sh} and S_{hmin}^{sh}. The gray area paralleling the shale pore pressure and overburden trends indicates the range of critical pore pressures (for $0.3 < \mu < 0.6$; equation 1) for which the caprock reaches its frictional limit, the reservoir bounding fault slips, and the reservoir is at dynamic capacity.

6.4.4 The OI-1 sand

The OI reservoirs are among the most productive in the EI-330 field and were deposited near the shelf margin of the ancestral Mississippi delta system - a much shallower environment than the Lentic sand (Figure 6.3B) (Holland et al., 1992). The OI sequence is comprised of four individual sand cycles that are separated by transgressive shales (Alexander and Flemings, 1995). I focus our analysis on the reservoirs of the uppermost sand, the OI-1. The OI-1 is bounded by a concave shaped, predominantly NW-SE striking sequence of normal faults that constitute the main basin bounding growth fault system in the SEI 330 field (Figure 6.7). On the downthrown side within the minibasin, several approximately E-W striking normal faults subdivide the system into at least 5 different fault blocks that are sequentially labeled "A" through "E". The offset along these normal faults is approximately of 100 ft. (antithetic and subsidiary faults) to 800 ft. (main basin bounding growth fault) (Figure 6.7).

Fault blocks A, D, and E exhibit small oil columns (dark gray) of between 500 ft. and 550 ft. In contrast, the total column heights in B and C are quite large (2,100 ft. and 1,500 ft. respectively) and characterized by long gas (light gray) and relatively short oil columns (Table A1, Figure 6.7). The OI-1 is moderately to severely overpressured with λ_{ss} varying from 0.77 to 0.83 (Table A2, Figures 6.5B and 6.8B).

There are significant differences in the hydrocarbon phase pressures and the water phase pressures in the different OI-1 reservoirs. The hydrocarbon phase pressure at the top of the structures in fault blocks B, C, and E are apparently equal whereas the oil phase pressure at the top of fault block A is significantly higher (Figure 6.5C, black bars). This is true even though the column heights are much larger in fault blocks B and C and the structural tops in fault blocks B, C, and E are at different depths (Table A1). Furthermore, if I look at the water pressure at an equivalent depth, I see that there are sharp differences (Figure 6.5C, white bars). Pressures in fault blocks B and C are 500 to 700 psi lower than in fault blocks A and E.

Predicted shale pore pressures (P_p^{sh}) as derived from the linear regressions exhibit moderate overpressures (λ_{sh} ranges from 0.69 to 0.76,Tables A3 and A5). In all cases, at the peak of the structure, the shale pressure is less than the sand pressure (this is a necessary prerequisite for the dynamic capacity model). Furthermore, shale pressures mirror the water phase pressures recorded in the sand. At a given depth shale pressures are lower in fault blocks B and C than in fault blocks A and E (Figure 6.5C).

The least principal stress in the shale (S_{hmin}^{sh}) lies approximately 80% of the distance between the shale pressure (P_p^{sh}) and the overburden (S_v) (Figures 6.8A-D) which corresponds to a stress ratio K of around 0.8 (Figure 6.5E). This trend is well established

in fault blocks A and B where multiple stress measurements were made in the vicinity of the OI-1 horizon. The S_{hmin}^{sh} trend is largely inferred in the adjacent fault blocks C and E because there is only one LOT available (Table A4).

In all fault blocks, hydrocarbon phase pore pressures at the peak of the OI-1 structure are lower than the least principal stress in the shale (i.e., the difference between S_{hmin}^{sh} and P_p^{ss} is not zero, Figure 6.5A). Consequently, the reservoirs are not at hydraulic fracturing conditions (Figure 6.1A). However, the OI-1 reservoir in fault blocks A and E are clearly within or at the window of critical pore pressures for frictional failure indicating dynamic equilibrium (Figures 6.5B, 6.8A, and 6.8D). The reservoir pore pressure in fault blocks B and C, in contrast, are below the P_p^{crit} window (Figures 6.5B, 6.8B, and 6.8C) suggesting they are not dynamically controlled.

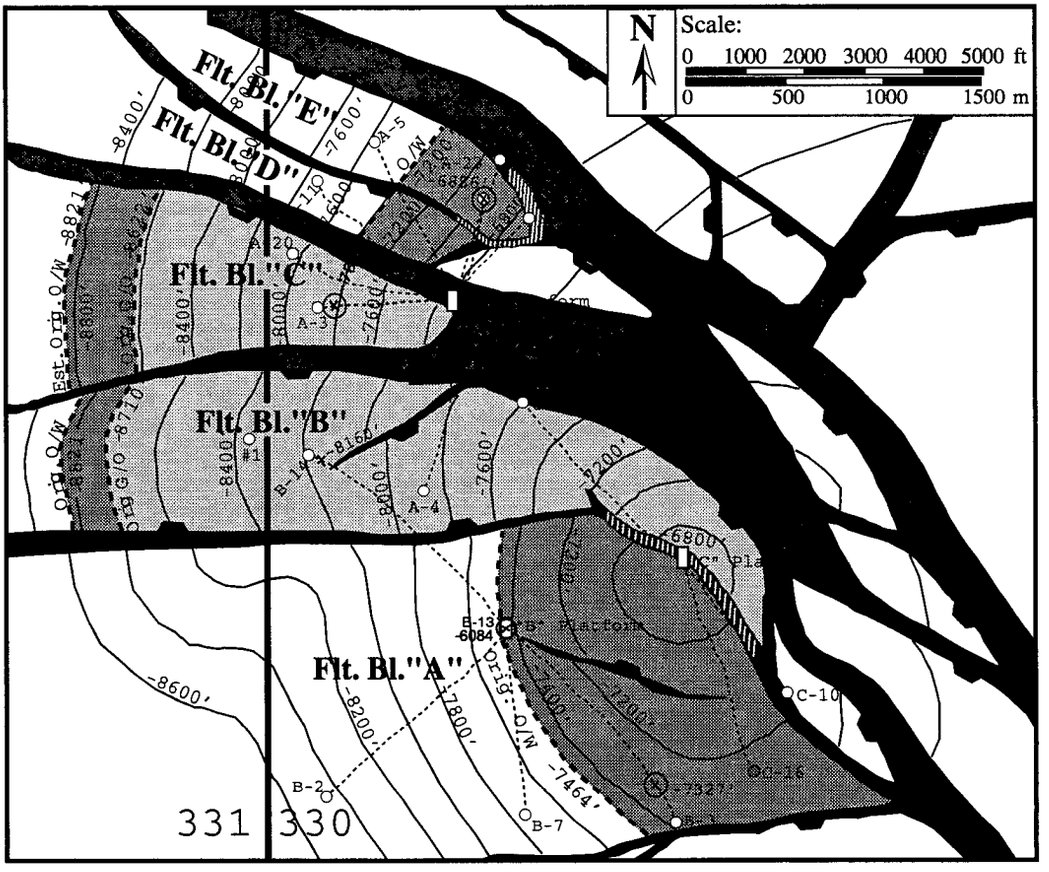

Figure 6.7: Structure map of the OI-1 reservoir sand for fault block 330 and parts of adjacent fault block 331. Depth contours are in feet SSTVD. Wellpaths are shown as thin dashed lines with points of reservoir penetration (crosses along wellpaths). Thick dashed lines display interpreted fluid contacts in the individual fault blocks (O/W: oil-water; G/W: gas-water; LKO: lowest known oil). The depth intervals filled with oil and gas are shown in dark ad light gray, respectively. The hatched fault segments (white) indicate potential slip areas along which fluids could migrate. Figure 6.4 caption describes how this map was generated.

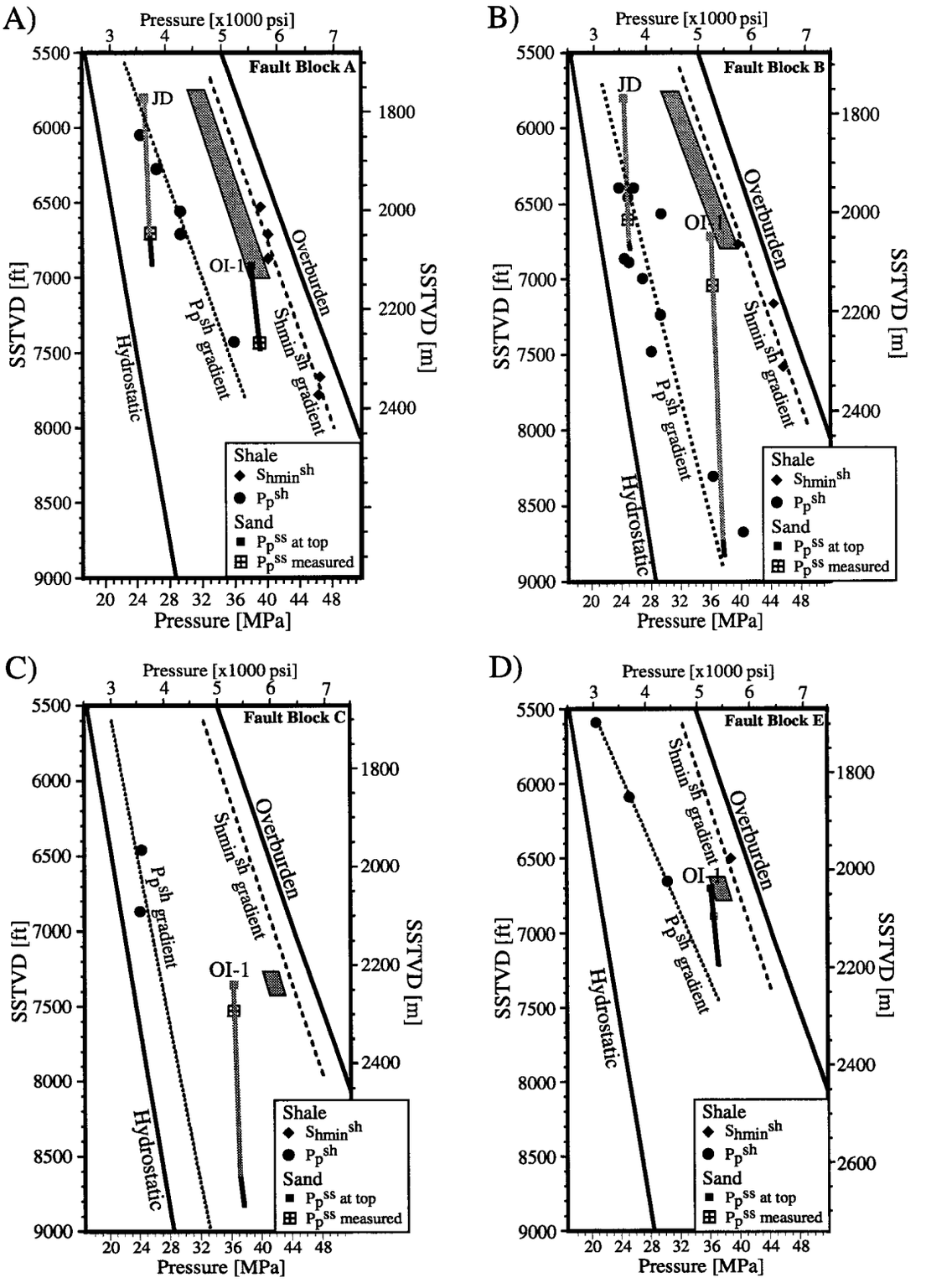

Figure 6.8: Pressure and stress state of the OI-1 (located in Figure 6.7) and JD (located in Figure 6.9) sands in minibasins fault blocks A (A), B (B), C (C), and E (D). Refer to Figure 6.6 caption for more details.

In the OI-1, I also identify an interesting correspondence between aquifer pore pressures and column heights. Low shale and sand aquifer pressures are associated with large hydrocarbon columns (fault blocks B and C), whereas fault blocks A and E exhibit relatively high aquifer pressures and short oil columns. Figures 6.2A and B provide an explanation for this scenario. In environments of high initial aquifer pressures, the difference between P_p^{crit} and P_p^{ss} is small, the reservoir supports less buoyant hydrocarbon phases, and P_p^{crit} can be reached much quicker (Figure 6.2A). Conversely, if initial aquifer pressures are relatively low, the difference between P_p^{crit} and P_p^{ss} is large, the reservoir supports a long hydrocarbon column (i.e., oil and gas), and P_p^{crit} could be reached at a later time (Figure 6.2B).

The fact that such drastic differences in sand and shale pore pressures can exist in adjacent fault blocks of the same sand (i.e., the OI-1) is very interesting but also quite puzzling. Since water phase pore pressures in fault blocks B and C are similar, they are hydraulically connected to the same aquifer but decoupled from fault blocks A and E as inferred from the large pressure contrast. Because the shale pressures adjacent to the OI-1 reservoirs show similar contrasts, the same mechanisms operating in the sands probably also affected the shales. I believe, therefore, that during burial and structural evolution of the OI-1 sand a very effective compartmentalization process allowed hydraulic decoupling of the aquifer in these fault blocks and substantial different aquifer pore pressure regimes to develop. Pressure compartmentalization in sedimentary basins as observed in the OI-1 sand is described with numerous case studies by Powley (1990) and Hunt (1990).

Both effective stress ratios K and C_{dyn} are quite variable on top of the OI-1 (Table A5, Figures 6.5E and F). These variations are the result of variations in both shale and reservoir pore pressures rather than differential stresses (i.e., Sv - S_{hmin}^{sh}), which are quite constant throughout the OI-1. K ranges from 0.78 to 0.86. The variations in C_{dyn} range from 0.51 to 0.74. The C_{dyn} values in fault blocks A and E are close to the lower C_{dyn}^{crit} bound (0.55) for μ = 0.3 (Table A5) and also indicate the proximity to dynamic failure of the corresponding hydrocarbon columns. In fault blocks B and C, C_{dyn} is quite high (0.61 and 0.74) supporting the observation that the corresponding hydrocarbon columns are not close to dynamic failure.

6.4.5 The JD sand

The JD sand is the youngest and shallowest sand considered in this study (Figure 6.3B). It constitutes the top level of a 4th order depositional cycle (i.e., top level) of four separate sands (MG through JD; Figure 6.3B) that were deposited in a proximal deltaic environment (Alexander and Flemings, 1995). The JD is structurally less complex than the deeper OI-1

or Lentic (Figure 6.9). The main structural feature is the NW-SE striking basin bounding growth fault system. On the downthrown side (i.e., minibasin), two more or less E-W striking antithetic normal faults subdivide the sand into three distinct fault blocks. In this paper, I focus on fault blocks A and B.

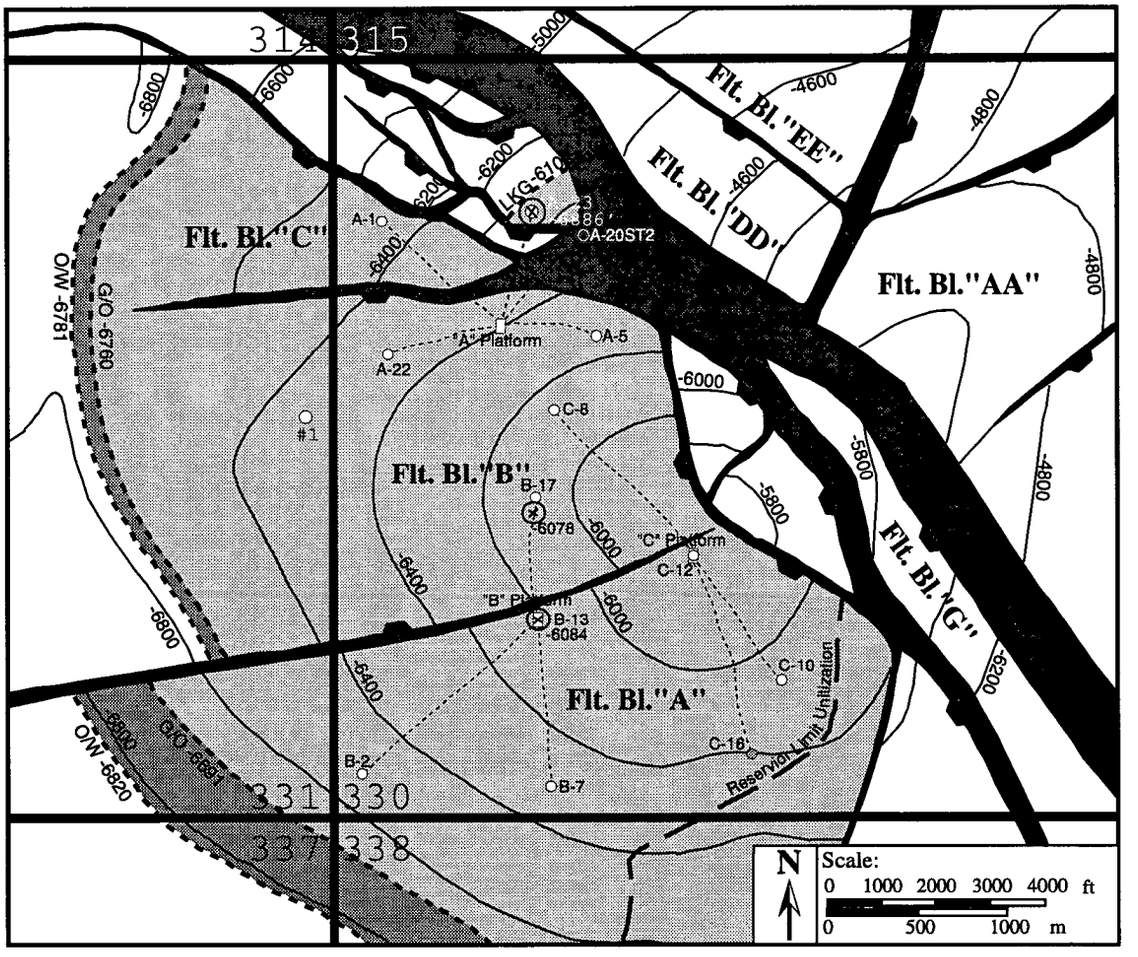

Figure 6.9: Structure map of the JD reservoir sand for fault block 330 and parts of adjacent fault blocks 331, 337, and 337. Depth contours are in feet SSTVD. Wellpaths are shown as thin dashed lines with points of reservoir penetration (crosses along wellpaths). Thick dashed lines display interpreted fluid contacts in the individual fault blocks (O/W: oil-water; G/W: gas-water). The depth intervals filled with oil and gas are shown in dark ad light gray, respectively. Figure 6.4 caption describes how this map was generated.

In both fault blocks A and B the JD has relatively large gas columns (891 ft. and 960 ft. respectively) and short oil columns (129 ft. and 21 ft. respectively; Table A1, Figures 6.8A and B). Initial reservoir pore pressures indicate soft overpressures (λ_{ss} = 0.66 and 0.61; Tables A2 and A5, Figure 6.5). At an equivalent depth, water phase pressures are equal to within 120 psi (Figure 6.5C). Pore pressures in the shales (P_p^{sh}) adjacent to the JD generally

compare with the pore pressures in the reservoirs (Table A3, Figures 6.8A and B). The λ_{sh} values at the top of the JD (obtained by fitting a linear trend through the provided P_p^{sh} data) are slightly lower than in the reservoir just below (λ_{sh} = 0.61 and 0.66 versus λ_{ss} = 0.68; Table A5, Figures 6.8A and B).

Since no LOT were run in the shales adjacent to the JD sand, I did not have any direct measurements of least principal stress magnitude available. In order to obtain S_{hmin}^{sh} values for the shales adjacent to the structural top of the sand reservoirs, I used linear regressions to extrapolate upward from deeper LOTs and FITs (Table A4). In fault block A, I used a LOT carried out near the MG sand (Figure 6.8A) and in fault block B a FIT conducted near the LF sand (Figure 6.8B). These tests came form within the same depositional cycle and follow more or less the same trend as the LOTs and FITs from the deeper OI-1 sand.

The reservoir pore pressures in the two JD reservoirs are similar and, therefore, in hydraulic communication across the normal fault separating the fault blocks (Figures 6.8A and B). Despite the long hydrocarbon columns and the associated large buoyancy effects, pore pressures are significantly lower than the range of critical pore pressures for dynamic capacity (Table A5, Figure 6.5B).

The effective stress ratios K and C_{dyn} are comparable in both fault blocks. In comparison to the deeper levels, K is lower than near the OI-1 and Lentic, while C_{dyn} is higher. In fault block A, K = 0.78 and C_{dyn} = 0.77 and in fault block B K = 0.79 and C_{dyn} = 0.74 (Table A5 and Figures 6.5E and F). These values reflect the similar pore pressure conditions in both sands and shales and indicate that the hydrocarbon columns in the reservoirs are currently not at failure conditions (Table A6, Figures 6.8A and B).

6.5 Discussion and implications

The ranges of critical pore pressure represent the crucial point for the dynamic capacity model because they indicate the points of dynamic equilibrium for which failure and fluid migration would occur (either the reservoir bounding faults slip or the caprocks hydraulically fracture) and, hence, limit the maximum column height (i.e., pore pressure) in a reservoir. I summarize and display all critical information pertaining to the eight reservoirs in Table A5 and Figure 6.5 respectively. In view of the dynamic capacity model I utilize these results in this section to infer the specific mechanisms responsible for the observed hydrocarbon column heights (i.e., pore pressure) and migration in each reservoir.

In the Lentic footwall sand the state of stress is nearly isotropic and differential stresses are very small. As a result, it is difficult to discern between the two dynamic mechanisms

hydraulic fracturing (Figure 6.1A) or slippage along reservoir bounding faults (Figure 6.1B). Because reservoir pressures in both Lentic fault blocks A and C are very high and close to or within the range of P_p^{crit}, both mechanisms can be invoked in order to explain the observed column heights. Thus, the Lentic reservoir appears to have reached its dynamic capacity, the oil columns are at maximum height, and a dynamic fluid flow mechanism appears to be operating, but it is not clear which. Any further increase in pore pressure would cause either the reservoir bounding fault to slip or hydraulic fracturing to occur to release the excess pressure. The hatched segments along the faults in Figure 6.4 are the areas along which I could envision potential fault slip and hydrocarbon migration. Finkbeiner and Zoback (1998) identified these same faults as potentially active structures controlling the local stress field based on the observation of borehole breakouts near the Lentic level. Furthermore, I observe rather small oil columns. Following our discussion for Figure 6.2B, initial water phase pressures (i.e., before the sand started filling with oil and gas) in the two reservoirs were quite high as well allowing only limited volumes of hydrocarbons to accumulate before critical pore pressures are reached and failure occurs. I illustrate this idea in Figure 6.5C, where the difference between the water (gray) and hydrocarbon (black) phase pore pressures indicates the pressure induced by the buoyant hydrocarbon columns. This difference is rather small in case of the Lentic sand.

The OI-1 sand within the minibasin shows two interesting things: (i) Fault blocks A and E (Figures 6.5, 6.8A, and 6.8D) exhibit relatively high pressures at their tops and short oil columns. Pore pressures are either well within or just about to reach dynamic equilibrium. This indicates the two reservoirs are at their dynamic capacity (i.e., the oil columns have reached their maximum height) as controlled by the ambient state of stress and dynamic mechanisms for hydrocarbon migration and accumulation are operating today in this part of the reservoir. The hatched segments along the faults in Figure 6.7 are the areas along which I could envision potential fault slip and hydrocarbon migration. Finkbeiner and Zoback (1998) identified these same faults as potentially active structures controlling the local stress field based on the observation of borehole breakouts. Again, initial aquifer pore pressure conditions were quite high in the past, allowing only relatively small amounts of oil to accumulate, thus limiting the oil column height at present (Figures 6.2B and 6.5C). (ii) In fault blocks B and C, the columns are much longer and pore pressures are (just) below dynamic equilibrium. Pore pressure data suggest that fault block B is in hydraulic communication with C (Figure 6.5C). I believe, the columns in fault blocks B and C are static and controlled by the presence of a spill point (i.e. leakage below dynamic capacity is reached). In fact, this spill point exists downdip and to the west in fault block C and is approximately equivalent to the mapped oil-water contact implying that hydrocarbons can

migrate westward into the 331 structure (Figure 6.7) (Rowan et al., in press).The long oil and gas columns in these two fault blocks (B and C) reflect relatively low initial pore pressures in the past. allowing for large oil and gas columns to develop (Figures 6.2A and 6.5C).

In the JD sand, the hydrocarbons are not in dynamic equilibrium. That is, the pressure and stress relations are such that neither the cap-rock seems ready to hydrofrac nor do the bounding faults seem ready to slip (Figures 6.5, 6.8A, and 6.8B). Thus, neither dynamic mechanism can be invoked to explain the observed column heights in this sand and I consider them as being static. In other words, viewed dynamically, the reservoirs have not reached their dynamic capacities and there could be more oil and gas being stored in each of these sands than is observed. The JD sand is also spill point controlled. It is located to the south and west out of the structure (Rowan et al., in press). This spill point would allow fluids to migrate westward into SEI block 331. Because fault blocks A and B are hydraulically connected, the column height in fault block A is also limited by this spill point. Initial pore pressures in the JD sand were relatively low allowing long hydrocarbon columns to develop (Figures 6.2A and 6.5C).

Our preferred interpretation is that the hydrocarbon columns are dynamically constrained today. In the Lentic horizon, pressures and stresses are so close that I cannot differentiate whether flow is controlled by frictional failure or hydrofracture. However, at the OI-1 level, it is clear that two reservoir bocks do not reach hydrofracture conditions but are within a window where frictional failure may be occurring. I do recognize that a second interpretation is plausible. Namely, those reservoirs with pressures below the hydrofracture condition are not dynamically constrained by the stress field today. It is possible leaking is occurring by cross-fault flow today or as the system evolved (Aexander and Handshy, 1998). It is also possible the system was once at fracture limit and subsequently pressure have dissipated.

Another possibility is that reservoirs with sub-critical pore pressures (and long hydrocarbon columns) might have been filled to dynamic capacity (i.e., critical pressures) in the past and then either bled off at a later stage or when the stresses increased with burial no further filling (i.e. pressure increase) occurred. As a consequence, pore pressures were driven away from their critical values and are below failure today. Even though there is no direct evidence to test these concepts in the SEI 330 field, especially the latter point is interesting to consider because for the past 1 Ma the SEI 330 minibasin is believed to be relatively inactive (the sub-basin salt has entirely withdrawn and only very little sediments are currently being deposited). As a result, only small amounts of deformation have occurred at very shallow levels (i.e. in the hydrostatically pressured zone above the

reservoirs I studied) accommodating sediment compaction and compaction driven fluid flow (Alexander and Flemings, 1995). At greater depth (i.e. below the JD level), however, deformation has essentially stalled along the basin bounding growth faults, which favors the concept of faults currently acting as seals rather than conduits inhibiting fluid flow and reservoir filling. Obviously, this idea does not work for the Lentic sand which is close to dynamic capacity since the least principal effective stress is almost zero.

Based on the dynamic capacity model, the cross-sections in Figures 6.10 and 6.11 (see transects in Figure 6.3) summarize our view of current hydrocarbon migration in the SEI 330 field. The deep Lentic sand (here shown on the minibasin side in Figure 6.10) experiences severe overpressures close to the minimum principal stresses in the overlying shales. From these deep levels, hydrocarbons migrate upward into the OI sands by hydraulic fracturing (indicated as "Migration Mech. I" in the figure) or along the basin bounding growth fault (indicated as "Migration Mech. II" in the figure). Depending on the minibasin fault block, the OI-1 sand above offers two possibilities for fluid flow: (i) in fault blocks A, D, and E (Figure 6.10) pressures are sufficiently high to cause the reservoir bounding faults to slip and to provide valves and pathways for hydrocarbons to migrate further up (indicated as "Migration Mech. II" in the figure). (ii) in fault blocks B and C (Figures 6.10 and 6.11), however, the reservoir pore pressures are below dynamic equilibrium and column heights appear to be spill point controlled (indicated as "Migration Mech. III" in the two figures). All shallower sands (i.e., the JD cycle and above; Figures 6.10 and 6.11) exhibit pore pressures far from dynamic equilibrium. I believe that fluids either simply leak out of these sands driven by their own buoyancy or the sands communicate hydraulically across faults due to small offsets along these structures (indicated as "Migration Mech. III" in the figures).

6.6 Conclusions

I introduced the dynamic capacity model to describe two dynamic mechanisms that may control hydrocarbon migration and column heights by enhancing fracture permeability I applied this conceptual model to eight sand reservoirs from three depositional cycles (Lentic, OI-1, and JD) in the South Eugene Island 330 field. Analysis of pore pressure and stress data from vertical and deviated wells into these reservoirs show highly variable pore pressures and least principal stresses. Hydrocarbon column heights appear to be controlled by different mechanisms in different parts of the reservoir suggesting varying mechanisms for fluid flow. In the deepest, severely overpressured Lentic sand, pore pressures are close to the least principal stress indicating that either natural hydraulic fracturing or fluid flow

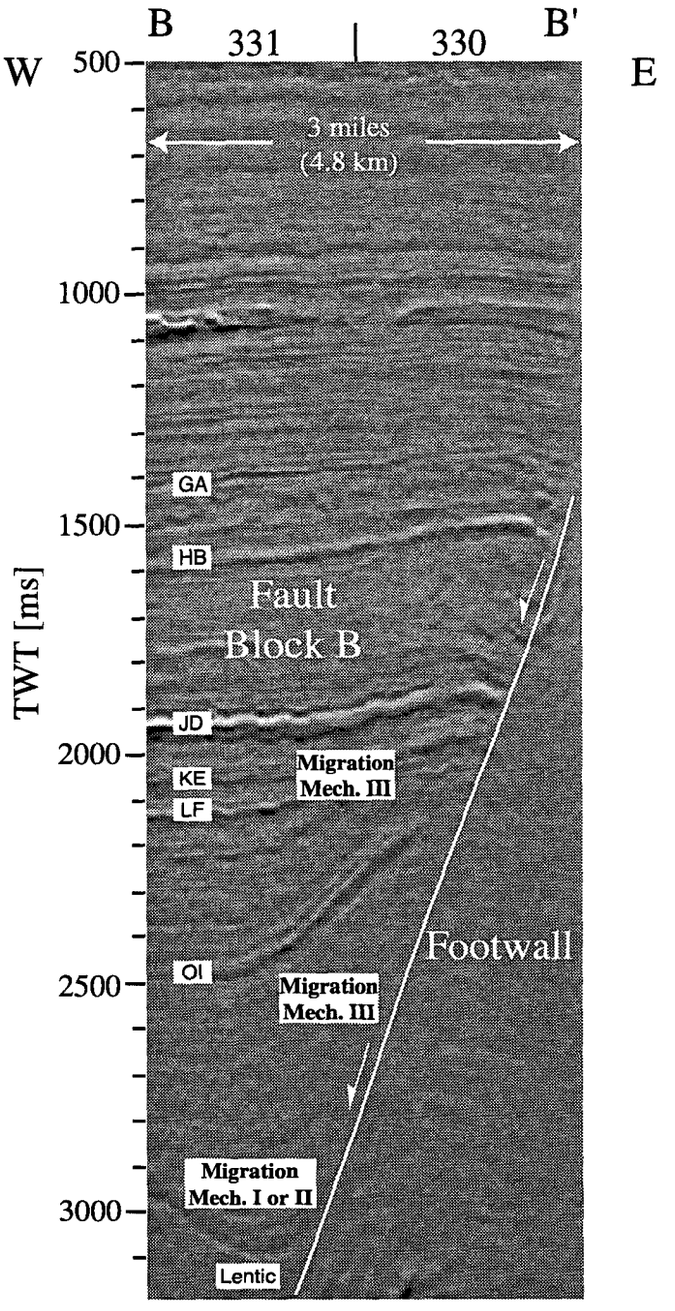

Figure 6.10: Cross-section along transect B-B' (Figure 6.3A). This cross-section was generated from 3-D seismic surveys. Positive high amplitudes are shown in black, negative high amplitudes are white. Various reservoir sands are shown within SEI 330 fault block B. The white normal fault displays the main basin bounding growth fault (Figure 6.3A). "Migration mech. I", "Migration mech. II", and "Migration mech. III" refer to fluid flow by hydraulic fracturing (Figure 6.1A), active faulting (Figure 6.1B) and spill point or leakage (Figure 6.1C), respectively. TWT is two-way travel time.

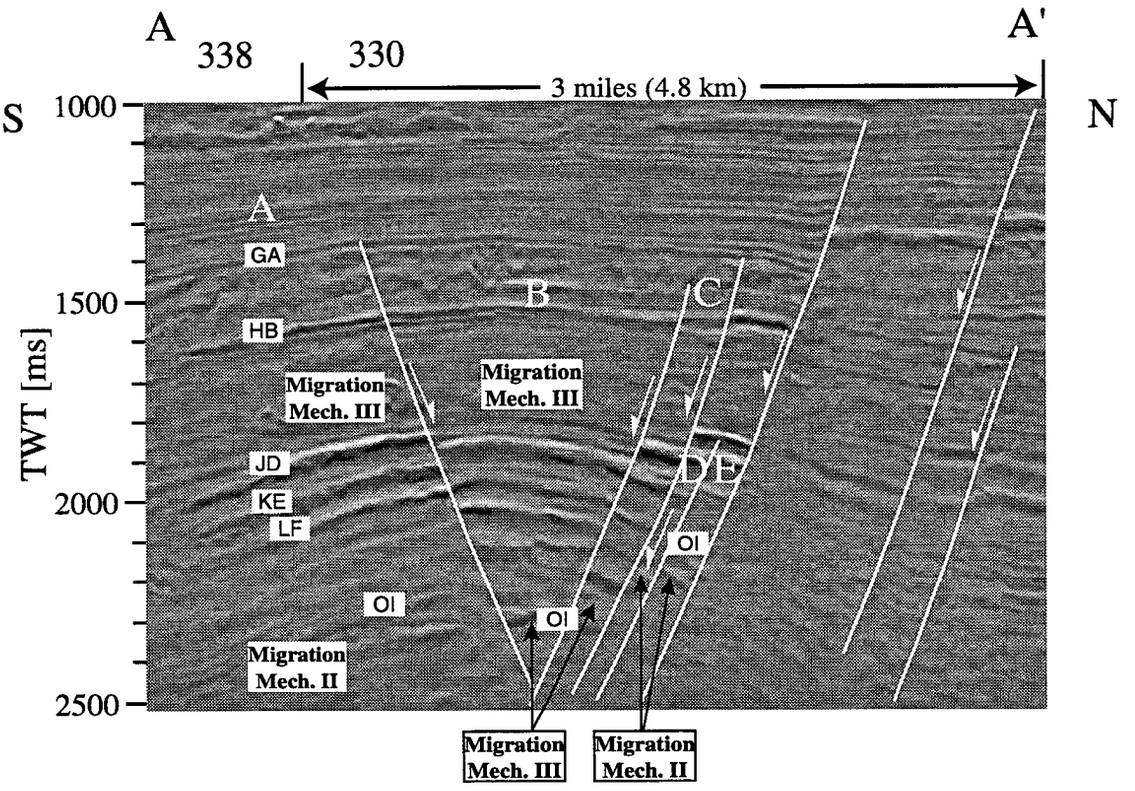

Figure 6.11: Cross-section along transect A-A' showing fault blocks A through E of the minibasin side (Figure 6.3A). Refer to Figure 6.10 caption for more detail.

along active faults may occur. The moderately overpressured OI-1 sand indicates two interesting points: (i) the oil columns in fault blocks A and E are short and exhibit high pressures close to the values expected for dynamic controls on column heights. Thus, I believe that the OI-1 sand in these two reservoir compartments is at dynamic capacity today and that column heights are controlled by active faulting along the reservoir bounding growth faults (i.e., pore pressures and fluid flow are controlled by the pressure at which fault slip and allow hydrocarbons to migrate). (ii) The OI-1 reservoirs in fault blocks B and C exhibit very long hydrocarbon columns and pressures are below dynamic equilibrium. There is good evidence that this sand is spill point controlled and hydrocarbons can escape into the westward structure of the OI-1. Pore pressures in the slightly overpressured JD sand are well below critical values for dynamic fluid flow even for low coefficients of friction. I suggest that either the sands are in a state of being filled, or the hydrocarbon accumulation is controlled by spill points or leaky seals, or the reservoirs were at dynamic capacity in the past and subsequent stalling of basin activity drove pore pressures away from the critical, dynamic value.

6.7 Acknowledgments

This research is financed by the Gas Research Institute under contract no. 5095-260-3558 and the Stanford Rock and Borehole Geophysics (SRB) consortium. Richard Parker of the Gas Research Institute provided valuable support for this project. Martin Traugott of Amoco helped me with many useful comments and suggestions. I would like to thank Pennzoil, Shell, and Texaco for generously providing the data used in this analysis.

6.8 Nomenclature

Parameter	Description	Units
C_{dyn}	Dynamic capacity stress ratio	unitless
C_{dyn}^{crit}	Dynamic capacity stress ratio at critical pore pressure (P_p^{crit})	unitless
FIT	Formation integrity test	n/a
K	Shale effective stress ratio	unitless
λ^{sh}	Normalized shale pressure [P_p^{sh}/S_v]	unitless
λ^{ss}	Normalized reservoir pressure [P_p^{ss}/S_v]	unitless
LOT	Leak-off test	n/a
Migration Mech. I	Fluid migration by hydraulic fracturing (Figure 1A)	n/a
Migration Mech. II	Fluid migration by frictional failure along active faults (Figure 1B)	n/a
Migration Mech. III	Fluid migration by leakage or spill point (Figure 1B)	n/a
P_p^{crit}	Critical hydrocarbon phase reservoir pore pressure	psi
P_p^{sh}	Shale pore pressure	psi
P_p^{sh} gradient	Shale pore pressure gradient from linear regression	psi/ft
P_p^{ss}	Hydrocarbon phase pore pressure in the reservoir	psi
$P_p^{ss},_1$	Hydrocarbon phase reservoir pore pressure at time 1	psi
$P_p^{ss},_2$	Hydrocarbon phase reservoir pore pressure at time 2 (time 2 > time 1)	psi
S_{hmin}^{sh}	Minimum principal horizontal stress in shale	psi
S_{hmin}^{sh} gradient	Shale minimum principal stress gradient from linear regression	psi/ft
S_{hmin}^{sh}/S_v	Normalized minimum principal stress in shale	unitless
S_{Hmax}	Maximum principal horizontal stress	psi
SSTVD	Sub-sea true vertical depth	feet
S_v	Overburden (vertical principal stress)	psi

6.9 Appendix

Table A1

Table A1:Fluid contact levels and column heights in the SEI 330 reservoirs studied. This information was extracted from structural maps shown in Figures 4, 7, and 9.

Reservoir Sand	Fault Block	Top of structure, SSTVD [ft]	Oil-water contact, SSTVD[ft]	Gas-oil contact, SSTVD [ft]	Oil column [ft]	Gas column [ft]
Lentic	Footwall, FB-A	7310	7551	n/a	175	n/a
	Footwall, FB-C	6350	6993	n/a	643	n/a
OI-1	A	6920	7464	n/a	544	n/a
	B	6720	8821	8710	111	1990
	C	7350	8821	8622	199	1272
	E	6700	7200	n/a	500	n/a
JD	A	5800	6820	6691	129	891
	B	5800	6781	6760	21	960

Table A2

Table A2: Initial sand pore pressures and corresponding live oil densities in the SEI 330 reservoirs studied. Pore pressure is normalized by the overburden ($\lambda_{ss}=P_p^{ss}/S_v$). The paths for the wells indicated are displayed in Figures 4, 7, and 9. Pore pressures come from pressure surveys, The live oil gradient was calculated following the approach by Batzle ad Wang (1992). The overburden was calculated by integrating density logs (provided by Pennzoil and Texaco).

Reservoir sand	Fault block	Well	SSTVD [ft]	Sand P_p [psi]	$\lambda_{ss} = P_p^{ss}/S_v$	Live oil gradient [psi/ft]
Lentic	Footwall, FB-A	316/A-3ST	7403	6205	0.90	0.34
	Footwall, FB-C	316/A-4	6931	5665	0.89	0.30
		316/A-8	6655	5684	0.93	0.30
OI-1	A	330/B-3	7434	5689	0.83	0.29
	B	330/B-14	7043	5283	0.81	0.25
	C	330/A-3	7527	5313	0.77	0.32
	E	330/A-23	6890	5363	0.83	0.32
JD	A	330/B-13	6138	3724	0.66	0.32
	B	330/B-17	6606	3656	0.61	0.32

Table A3

Table A3: Pore pressures in shales adjacent to the SEI 330 reservoirs studied. Pore pressure is normalized by the overburden (λsh=Ppsh/Sv). Shale pore pressures were calculated using the porosity-effective stress method based on sonic log data (Hart et al., 1995; Stump and Flemings, 1997; Stump et al., 1998). The paths for the wells indicated are displayed in Figures 4, 7, and 9. The overburden was calculated by integrating density logs (provided by Pennzoil and Texaco).

Closest sand	Fault block	Well	SSTVD [ft]	P_p^{sh} [psi]	$\lambda_{ss} = P_p^{sh}/S_v$
Lentic	Footwall	316/A-1	6562	4881	0.81
		316/A-6	6996	5263	0.82
		316/A-12	6673	5123	0.83
OI-1	A	330/B-13	7425	5224	0.76
	B	331/#1	8301	5279	0.69
		331/A-4	8673	5831	0.72
	C	n/a	n/a	n/a	n/a
	E	330/A-20ST	6666	4450	0.72
JD	A	330/B-13	6050	3560	0.64
		338/#5	6699	4252	0.64
	B	330/A-20ST2	6389	3465	0.59
		330/A-22	6460	3630	0.61
		331/#1	6401	3773	0.64
	C	n/a	n/a	n/a	n/a
	E	330/A-23	6090	3756	0.66

Table A4

Fault block	Well	SSTVD [ft]	Type	Closest sand	S_{hmin}^{sh} [psi]	S_{hmin}^{sh}/S_v
A	330/B-2	7776	FIT	OI-1	6755	0.94
	330/B-7	7667	LOT	OI-1	6783	0.95
	330/C-10	6717	LOT	OI-1	5847	0.94
	330/C-12	6535	LOT	MG-3	5690	0.94
	330/C-16	6877	FIT	OI-1	5802	0.91
B	330/A-11	7585	FIT	OI-1	6591	0.94
	330/A-5	6769	FIT	LF	5748	0.92
	330/C-8	7159	LOT	OI-1	6414	0.97
C	n/a	n/a	n/a	n/a	n/a	n/a
E	330/A-6ST	6500	LOT	OI-1	5660	0.94
Footwall	316/A-12	6408	FIT	Lentic	5787	0.98
	330/#9	6627	LOT		6175	1.01
	330/A-20ST	7134	Hydrofrac		6494	0.99

Table A5

Table A5: Pore pressures, stresses, dynamic capacity ratio C_{dyn} (calculated using equation 2), and shale effective stress ratio ($K = (S_{hmin}{}^{sh} - P_p{}^{sh})/(S_v - P_p{}^{sh})$) at the top of the SEI 330 reservoirs studied. The top of the structures are the same as in Table 1. We calculated the overburden by integrating density logs (provided by Pennzoil and Texaco). Sand pore pressures ($P_p{}^{ss}$) were derived using live oil densities following the approach by Batzle ad Wang (1992) and, where necessary, gas gradients of 0.1 psi/ft. We calculated least principal stresses ($S_{hmin}{}^{sh}$) and pore pressures ($P_p{}^{sh}$) values and gradients in shales by linearly regressing the values listed in Tables 3 and 4 in each individual fault block.

Fault block	Sand	Sand top SSTVD [ft]	S_v [psi]	$P_p{}^{ss}$ [psi]	λ^{ss}	$S_{hmin}{}^{sh}$ [psi]	$S_{hmin}{}^{sh}$ gradient [psi/ft]	C_{dyn}	$P_p{}^{sh}$ [psi]	$P_p{}^{sh}$ gradient [psi/ft]	λ^{sh}	K
A	JD	5800	5329	3623	0.68	4936	0.94	0.77	3500	0.95	0.66	0.78
	OI-1	6920	6428	5540	0.86	5992		0.51	4574		0.71	0.76
B	JD	5800	5283	3575	0.68	4848	1.02	0.74	3222	0.75	0.61	0.79
	OI-1	6720	6167	5205	0.84	5790		0.61	3912		0.63	0.83
C	OI-1	7350	6785	5295	0.78	6398	1.02	0.74	3969	0.54	0.58	0.86
E	OI-1	6700	6149	5302	0.86	5785	1.02	0.57	4497	1.24	0.73	0.78
Footwall	L-1, FB-A	7310	6739	6174	0.92	6604	0.93	0.76	5535	0.58	0.82	0.89
	L-1, FB-C	6350	5847	5597	0.96	5716		0.47	4801			0.87
				5491	0.94			0.63				

Table A6

Table A6: Critical reservoir pore pressures (P_p^{crit}, calculated with equation 1) and critical effective stress ratios for dynamic capacity (C_{dyn}^{crit}, calculated with equation 2 using P_p^{crit}) at the top of the SEI 330 reservoirs studied.

Fault block	Reservoir sand	Top of structure SSTVD [ft]	P_p^{crit} [psi] ($\mu = 0.3$)	C_{dyn}^{crit} ($\mu = 0.3$)	P_p^{crit} [psi] ($\mu = 0.6$)	C_{dyn}^{crit} ($\mu = 0.6$)
A	JD	5800	4452	0.55	4756	0.32
	OI-1	6920	5452		5786	
B	JD	5800	4307		4640	
	OI-1	6720	5322		5612	
C	OI-1	7350	5916		6221	
E	OI-1	6700	5336		5612	
Footwall	L-1, FB-A	7310	6438		6540	
	L-1, FB-C	6350	5554		5655	

REFERENCES

Aadnoy, B.S., and Larsen, 1987, Method for fracture gradient prediction for vertical and inclined boreholes: Society of Petroleum Engineers, SPE 16695.

Aadony, B.S., 1990, In-situ stress direction from borehole fracture traces: Jounral of Petroleum Science and Engineering, v. 4, p. 143-153.

Addis, M.A., Last, N.C., Yassir, N.A., 1996, Estimation of horizontal stresses at depth in faulted regions and their relationship to pore pressure variations: SPE Formation Evaluation Journal, March 1996, p. 11-18.

Addis, M.A., 1997, Reservoir depletion and its effect on wellbore stability evaluation: Int. J. Rock Mech. & Min. Sci, v.34, no. 3-4, paper no. 004.

Agricola, G., 1556, De Re Metallica. Translated by H.C. and L.H. Hoover, 1950, Dover, Mineola N.Y., 638 p.

Alexander, L.L. and Flemings, P.B., 1995, Geologic evolution of a Plio-Pleistocene salt withdrawal minibasin: Eugene Island block 330, offshore Louisiana: American Association of Petroleum Geologists Bulletin, v.79, 1737-1756.

Alexander, L.L., and Handshy, J.W.,1998, Fluid flow in a faulted reservoir system: fault trap analysis for the block 330 field in Eugene Island, south addition, offshore Louisiana: American Association of Petroleum Geologists Bulletin, v. 82, p. 387-411.

Althaus, V.E., 1977, A new model for fracture gradient: Journal of Canadian Petroleum Technology, April - June, 98-108.

Anderson, E.M., 1937, The dynamics of sheet intrusion: Proc. R. Soc. Edinburgh, v. 58, p. 242.

Anderson, R.A., Ingram, D.S., and Zanier, A.M., 1973, Determining fracture pressure gradients from well logs: Journal of Petroleum Technology, November, 1259-1268.

Anderson, R.N., Flemings, P.B., Losh, S., Austin, J., Woodhams, R., and the GBRN team, 1995, In-situ properties of a major Gulf of Mexico growth fault: Oil and Gas Journal, June 6th, 97-102.

Antonellini, M., and Aydin, A., 1994, Effect of faulting on fluid flow in porous sandstones: American Association of Petroleum Geologists, v. 78, p. 355-377.

Atkinson, J., 1993, The mechanics of soils and foundations:McGraw-Hill Book Company, 337 p.

Barton, C.A, L. G. Tesler, and M.D. Zoback, 1991, Interactive image analysis of borehole televiewer data, *in*, I. Palaz and S.K. Sengupta, eds., Automated pattern analysis in petroleum exploration: Springer Verlag, p. 223 - 248.

Barton, C.A, and M.D. Zoback, 1992, Self-similar distribution and properties of macro-

scopic fractures at depth in crystalline rock in the Cajon Pass scientific drill hole: Journal of Geophysical Research, v. 97, p. 5181-5200.

Barton, C.A. and M.D. Zoback, 1994, Stress perturbations associated with active faults penetrated by boreholes: possible evidence for near complete stress drop and a new technique for stress magnitude measurement: Journal of Geophysical Research, v.99, p. 9373 - 9390.

Barton, C.A., Zoback, M.D., and Moos, D, 1995, Fluid flow along potentially active faults in crystalline rock: Geology, v.23, 683-686.

Barton, C.A., Moos, D., and Zoback, M.D., 1997, In-situ stress measurements can help define local variations in fracture hydraulic conductivity at shallow depth: The Leading Edge, November, p. 1653-1656.

Batzle, M., and Wang, Z., 1992, Seismic properties of pore fluids: Geophysics, v.57, 1396-1408.

Behl, R.J., and R.E. Garrison, 1994, The origin of Chert in the Monterey Formation of California (USA): Proc. 29th Int'l. Geol. Congr., part C, p. 101-132.

Bell, J.S. and D.I. Gough, 1979, Northeast-southwest compressive stress in Alberta: Evidence from oil wells: Earth and Planetary Science Letters, v.45, p. 475-482.

Borgerud, L., and Svare, E., 1995, In-situ stress field on the Norwegian margin, 620-670 north. Workshop on Rock Stresses in the North Sea, Trondheim, Norway, Feb. 13-14 (1995).

Bowers, G.L., 1994, Pore-Pressure Estimation From Velocity Data: Accounting for Overpressure Mechanisms Besides Undercompaction: IADC/SPE Drilling Conference, p. 515-530.

Breckels, I.M. and van Eekelen, H.A.M., 1981, Relationship between horizontal stress and depth in sedimentary basins: Society of Petroleum Engineers, SPE 10336.

Brennan, R.M. and Annis, M.R., 1984, A new fracture gradient prediction technique that shows good results in Gulf of Mexico abnormal pressure: Society of Petroleum Engineers, SPE 13210.

Brudy, M., and Zoback, M.D., 1993, Compressive and tensile failure of boreholes arbitrarily-inclined to principal stress axes: Application to the KTB boreholes, Germany: Int. J. Rock Mech. Min. Sci., v. 30, p. 1035-1038.

Brudy, M., Zoback, M.D., Fuchs, K., Rummel, F., Baumgaertner, J., 1997, Estimation of the complete stress tensor to 8 km depth in the KTB scientific drill holes: Implications for crustal strength: Journal of Geophysical Research, v. 102, p. 18,452-18,475.

Brudy, M., 1998, Determination of the state of stress by analysis of drilling-induced fractures - results from the northern North Sea: paper SPE 47236 presented at the 1998 SPE

Annual Technical Conference and Exhibition, Trondheim, Jul. 8-10.

Byerlee, J.D., 1978, Friction of rocks: Pure and Applied Geophysics, v.116, 615-629.

Chang, C.T., Zoback, M.D., Moos, D., in press, Anelasticity and dispersion: Int. J. Rock Mech. & Min. Sci., v.34, 3-4, Paper No. 048.

Chang, C.T., 1998, Time dependent viso-elastic behavior of unconsolidated sands, PhD Dissertation, Stanford University.

Chang, C.T., and Zoback, M.D., 1998, The role of viscous rheology in the state of stress of unconsolidated sands: paper SPE 47401 presented at the 1998 SPE Annual Technical Conference and Exhibition, Trondheim, Jul. 8-10.

Christiansen, R.L., and R.S. Yeats, 1992, Post-Laramide geology of the U.S. Cordilleran region, *in*, B.C. Burchfiel, P.W. Lipman, and M.L. Zoback, eds, The Cordilleran orogen: conterminous U.S.: The Geology of North America, v. G-3, p. 261-406.

Christman, S.A., 1973, Offshore fracture gradients: Journal of Petroleum Technology, August, 910-914.

Cooper, G.A., 1994, Directional drilling, Scientific American, v. 270, p.56-61.

Crain, W.E., W.E. Mero, and D. Patterson, 1985, Geology of the Point Arguello discovery: American Association of Petroleum Geologists Bulletin, v. 69, p. 537-545.

Daines, S.R., 1982, Prediction of fracture pressures for wildcat wells: Journal of Petroleum Technology, April 1982, p. 863.

Dickinson, G., 1953, Geological aspects of abnormal reservoir pressures in Gulf Coast Louisiana: Bulletin of the American Association of Petroleum Geologists, v. 37, p. 410-432.

Dudley II, J.W., Myers, M.T., Shew, R.D., and Arasteh, M.M., 1994, Measuring compaction and compressibilities in unconsolidated reservoir materials via time-scaling creep: Eurock '94, Balkema, Rotterdam, 45-54.

Dunham, J.B., 1987, Guide to coastal outcrops of the Monterey Formation of western Santa Barbara county, California: Field Trip Guide, Pacific Section SEPM, 35 p.

Economides, M.J., and Nolte, K.G., 1989, Reservoir stimulation: Prentice Hall, Englewood Cliffs, New Jersey 07632.

Engebretson, D.C., A. Cox, and R.G. Gordon, 1985, Relative motions between oceanic and continental plates in the Pacific Basin: Geological Society of America Special Paper, no. 206, 59 p.

Engelder, T. and Fischer, M.P., 1994, Influence of poroelastic behavior on the magnitude of minimum horizontal stress, Sh, in overpressured parts of sedimentary basins: Geology, v.22, 949-952.

Engelder, T., and Leftwich, J.T., 1997, A pore pressure limit in overpressured South Texas

oil and gas fields: in Surdam, R.C., ed, Seals, Traps, and the petroleum system: American Association of Petroleum Geologists Memoir, v.67, p. 255-267.

England, W.A., MacKenzie, A.S., Mann, D.M., and Quigley, T.M., 1987, The movement and entrapment of petroleum fluids in the subsurface: Journal of the Geological Society, London, v. 144, p. 327-347.

Fejerskov, M., 1994, Breakout interpretation in 7 wells near the Troll Field, on the east flank of the northern Viking Graben: Integrated Basin Studies, Dynamics of Norwegian Margin, Topic 1.3, Regional Stress Field, report #4, 20 p.

Fejerskov, M., 1995, Criteria for breakout identification based on 4-arm oriented caliper logs: Integrated Basin Studies, Dynamics of Norwegian Margin, Topic 1.3, Regional Stress Field, report #2, 17 p.

Finkbeiner, T., Stump, B.B., Zoback, M.D., Flemings, P.B., 1996, Pressure, overburden, and minimum horizontal stress in Eugene Island Block 330, offshore Gulf of Mexico: Gas Research Institute, Topical Report 96/0285, 30 p.

Flemings, P.B., Zoback, M.D., Bishop, B.A., Anderson, R.N., 1996, State of stress in the Pathfinder well: in Anderson, R.N., Billeaud, L.B., Flemings, P.B., Losh, S., Whelan, J., and the GBRN team, eds., Results of the Pathfinder drilling program into a major growth fault: Joy Allen, LDEO Press, p. 548-615.

Flemings, P.B., Alexander, L.L., and Anderson, R.N., in preparation, The plumbing of a Plio-Pleistocene growth fault: the Eugene Island Block 330 field.

Flemings, P.B., Finkbeiner, T., Zoback, M.D., Stump, B.B., Dugan, B., in prep., Pressure, minimum principal stress, and column height in the Eugene Island 330 field: a case study of two reservoirs.

Gaarenstroom, L., Tromp, R.A.J., de Jong, M.C., and Brandenburg, A.M., 1993, Overpressures in the Central North Sea: implications for trap integrity and drilling safety, in Parker, J.R., ed., Petroleum Geology of Northwest Europe: Proceedings of the 4th Conference, 1305-1313.

Gephart, J.W., and D.W. Forsyth, 1984, An improved method for determining the regional stress tensor using earthquake focal mechanism data: application to the San Fernando earthquake sequence: Journal of Geophysical Research, v. 89, p. 9305-9320.

Gephart, J.W., 1990, Stress and the direction of slip on fault planes: Tectonics, v. 9, p. 845-858.

Gordon, D.S., and Flemings, P.B., 1998, Generation of overpressure and compaction-driven fluid flow in a Plio-Pleistocene growth-faulted basin, Eugene Island 330, offshore Louisiana: Basin Research, v. 10, p. 177-196.

Graham, S.A., and L.A. Williams, 1985, Tectonic, depositional, and diagenetic history of

Monterey Formation (Miocene), central San Joaquin basin, California: American Association of Petroleum Geologists Bulletin, v. 69, p. 385-411.

Grauls, D.J., and Baleix, J.M., 1994, Role of overpressures and in-situ stresses in fault-controlled hydrocarbon migration: a case study: Marine and Petroleum Geology, v.11, 734-742.

Gross, M.R., 1993, The origin and spacing of cross joints: examples from the Monterey Formation, Santa Barbara Coastline, California: Journal of Structural Geology, vol. 15, p. 737-751.

Gross, M.R., 1995, Fracture partitioning: failure mode as a function of lithology in the Monterey Formation of coastal California: Geological Society of America Bulletin, v. 107, p. 779-792.

Gross, M.R., and T. Engelder, 1995, Strain accommodated by brittle failure in adjacent units of the Monterey Formation, U.S.A.: scale effects and evidence for uniform displacement boundary conditions: Journal of Structural Geology, v. 17, p. 1303-1318.

Hart, B.S., Flemings, P.B., and Deshpande, A., 1995, Porosity and Pressure: Role of Compaction Disequilibrium in the Development of Geopressures in a Gulf Coast Pleistocene Basin: Geology, v. 23, p. 45-48.

Hickman, S., Sibson, R., and Bruhn, R., 1995, Introduction to special section: Mechanical involvement of fluids in faulting: Journal of Geophysical Research, v. 100, p. 12,831-12,840.

Holbrook, P.W., Maggiori, D.A., and Hensley, R., 1995, Real-time pore pressure and fracture pressure determination in all sedimentary lithologies: Society of Petroleum Engineers Formation Evaluation, December, 215-222.

Holland, D.S., Nunan, W.E., Lammlein, D.R., and Woodhams, R.L., 1980, Eugene Island Block 330 field, offshore Louisiana: *in* Halbouty, M.T., ed., Giant oil and gas fields of the decade: 1968-1978: American Association of Petroleum Geologists Memoir 30, p. 253-280.

Holland, D.S., Leedy, J.B., and Lammlein, D.R., 1992, Eugene Island Block 330 field - USA, offshore Louisiana: in Beaumont, E.A. and Foster, N.H., eds., Structural traps III, tectonic fold and fault traps: American Association of Petroleum Geologists, Treatise of Petroleum Geology Atlas of Oil and Gas Fields, 103-143.

Hooper, E.C.D., 1991, Fluid migration along growth faults in compacting sediments: Journal of Petroleum Geology, v. 14(2), p. 161-180.

Hubbert, M.K., 1953, Entrapment of petroleum under hydrodynamic conditions: American Association of Petroleum Geologist Bulletin, v. 37, p. 19540-2026.

Hubbert, M.K., and Willis, D.G., 1957, Mechanics of hydraulic fracturing: Journal of Pe-

troleum Technology, v.9, 153-168.

Hubbert, M.K., and Rubey, W.W., 1959, Role of fluid pressure in mechanics of overthrust faulting: Geological Society of America Bulletin, v. 70, p. 115-205.

Hunt, J.M., 1990, Generation and migration of petroleum from abnormally pressured fluid compartments: American Association of Petroleum Geologist Bulletin, v. 74, p. 1-12.

Ingram, G.M., and Urai, J.L., 1997, Top seal leakage through faults and fractures: the role of mudrock properties: Proceedings of the Geological Society Conference on "Mudrocks at the Basin Scale: Properties, Controls, and Behaviour", 28-29 January, 30p.

Isaacs, C.M., 1984, Geology and physical properties of the Monterey Formation, California: Society of Petroleum Engineers, no. 12733, p. 83-96.

Jackson, P.A., and R.S. Yeats, 1982, Structural evolution of Carpinteria Basin, western Transverse Ranges, California: American Association of Petroleum Geologists Bulletin, v.66, p. 805-829.

Jaeger, J.C., and N.G.W. Cook, 1979, Fundamentals of rock mechanics (third edition): New York, Chapman and Hall, p.28-30.

Jennings, C.W., 1975, Fault map of California with locations of volcanoes, thermal springs and thermal wells: California Division of Mines and Geology, 1 map, scale 1:750,000.

Jones, M., 1994, Mechanical principles of sediment deformation: *in* Maltman, A., ed., The geologic deformation of sediments,Chapman & Hall, p. 37-71.

Karig, D.E., and Hou, G., 1992, High-stress consolidation experiments and their geologic implications: Journal of Geophysical Research, v. 97, p. 289-300.

Karig, D.E., 1996, Uniaxial reconsolidation test o porous sediments: mudstones from site 897: in Whitmarsh, R.B., Sawywe, D.S., Klaus, A., and Mason, D.G., eds., Proc. ODP Sci. Results, v.149, p. 363-373.

Leach, W.G., 1993, New exploration enhancements in S Louisiana Tertary sediments: Oil and Gas Journal, Mar. 15, p. 83-87.

Leach, W.G., 1993, Fluid migration, HC cocentration in South Louisiana Tertiary sands: Oil and Gas Journal, Mar. 1, p. 71-74.

Leach, W.G., 1993, Maximum hydrocarbon window determination in South Louisiana: Oil and Gas Journal, Mar. 29, p. 81-84.

Lockner, D.A., 1995, Rock failure: in American Geophysical Union, A handbook of physical constants, American Geophysical Union Reference Shelf 3, 127-147.

Long, J.C.S., K. Karasaki, A. Davey, J. Peterson, M. Landsfeld, J. Kemeny, and S. Martel, 1991, An inverse approach to the construction of fracture hydrology models conditioned by geophysical data: Int. Rock Mech. Min. Sci. & Geomech. Abst., v. 28, p. 121-

142.

Losh, S., in press, Oil migration in a major growth fault: structural analysis of the Pathfinder core, South Eugene Island Block 330, offshore Louisiana.

Makurat, A.N., 1985, The effect of shear displacement on the permeability of natural rough joints, in Hydrogeology of rocks of low permeability: International Association of Hydrogeologists Memoir 17, p. 99-106.

Mardia, K.V., 1972, Statistics of directional data: Department of Mathematical Statistics, Hull, England, Academic Press, London.

Mastin, L., 1988, Effect of borehole deviation on breakout orientations: Journal of Geophysical Research, v. 93, p. 9187-9195.

Matthews, W.R. and Kelly, J., 1967, How to predict formation pressure and fracture gradient: The Oil and Gas Journal, February 20, 92-106.

Moos, D., and Zoback,M.D., 1990, Utilization of observations of wellbore failure to constrain the orientation and magnitude of crustal stresses: application to continental, deep sea drilling project, and ocean drilling program boreholes: Journal of Geophysical Research, **95**, 9,305-9,325.

Mount, V.S. and J. Suppe, 1987, State of stress near the San Andreas fault: Implications for wrench Tectonism: Geology, v. 15, p. 1143-1146.

Muir-Wood, D.M., 1991, Soil behaviour and critical state soil mechanics: Cambridge University Press.

Namson, J. and T.L. Davis, 1990, Late Cenozoic fold and thrust belt of the southern Coast Ranges and Santa Maria Basin, California: American Association of Petroleum Geologists Bulletin, v. 74, p. 467-492.

Narr, W., 1991, Fracture density in the deep subsurface: techniques with application to Point Arguello oil field: American Association of Petroleum Geologists Bulletin, v. 75, p. 1300-1323.

Nehring, R., 1991, Oil and gas resources: *in* Salvador, A., ed., The gulf of Mexico Basin: Decade of North American Geology, Geological Society of America, v. J, p. 445-494.

Nicholson, C., C.C. Sorlien, T. Atwater, J.C. Crowell, and B.P. Luyendyk, 1994, Microplate capture rotation of the western Transverse Ranges, and initiation of the San Andreas transform as a low-angle fault system: Geology, v. 22, p. 491-495.

Nur, A.M., and Walder, J., 1990, Time-dependent hydraulics of the Earth's crust. In: Geophysics Study Committee, National Research Council, 1990, The role of fluids in crustal processes. National Academy Press, 113-127.

Page, B., 1981, The southern Coast Ranges, *in*, Ernst, W.G., ed., The geotectonic development of California: Englewood Cliffs, New Jersey, Prentice-Hall, p. 329-417.

Peska, P., and Zoback, M.D., 1995, Compressive and tensile failure of inclined wellbores and determination of in-situ stress and rock strength: Journal of Geophysical Research, v.100, no. 12, p.791.

Pilkington, P.E., 1978, Fracture gradient estimates in Tertiary basins: Petroleum Engineer International, May, 138-148.

Pisciotto, K.A., and R.E. Garrison, 1981, Lithofacies and depositional environments of the Monterey Formation, California, *in*, Garrison, R.E., and R.G. Douglas, eds., The Monterey Formation and related siliceous rocks of California: Pacific Section of the Society of Economic Paleontologists and Mineralogists symposium volume, p. 97-122.

Plumb, R.A. and J.W. Cox, 1987, Stress directions in eastern North America determined to 4.5 km from borehole elongation measurements: Journal of Geophysical Research, v. 92, p. 4805-4816.

Plumb, R.A., and Hickman, S.H., 1985, Stress-induced borehole elongation: a comparison between the four arm dipmeter and the borehole televiewer in the Auburn geothermal well: Journal of Geophysical Research, v.90, no.5, p. 513.

Powley, D.E., 1990, Pressures and hydrogeology in petroleum basins: Earth-Science Reviews, v. 29, p. 215-226.

Reasenberg, P.A., and D. Oppenheimer, 1985, FPFIT, FPPLOT, and FPPAGE: FORTRAN computer programs for calculating and displaying earthquake fault-plane solutions: U.S. Geological Survey Open-File Report 85 - 739.

Rowan, M.G., Hart, B.S., Nelson, S., Flemings, P.B., and Trudgill, B.D., in press, Three-dimensional geometry and evolution of a salt-related growth-fault array: Eugene Island 330 field, offshore Louisiana, Gulf of Mexico: Mar. Pet. Geol.

Sadler, R.K., 1990, The relationship of lithology and tectonics to fracturing in the Monterey Formation, Point Arguello Field, offshore California, *in*, Keller, M.A. and McGowen, M.K., eds, 1990, Miocene and Oligocene petroleum reservoirs of the Santa Maria and Santa Barbara - Ventura basins, California: Soc. Econ. Paleon. Min. Workshop, no. 14, p. 245-269.

Salz, L.B., 1977, Relationship Between Fracture Propagation Pressure and Pore Pressure: Society of Petroleum Engineers of AIME.

Santarelli, F.J., Tronvoll, J.T., Svennekjaer, M., Skeie, H., Henriksen, R., Bratli, R.K., 1998, Reservoir stress path: the depletiona and the rebound: paper SPE 47350 presented at the 1998 SPE Annual Technical Conference and Exhibition, Trondheim, Jul. 8-10.

Schlumberger, 1986, Dipmeter Interpretation, Fundamentals: Schlumberger Limited, New York, 76 p.

Schuhmacher, D., 1993, Eugene Island Block 330 field, offshore Louisiana: geochemical evidence for active hydrocarbon recharging (abs.): AAPG Annual Convention Program, p. 179.

Segall, P., and Fitzgerald, S., in press, A note on induced stress changes in hydrocarbon and geothermal reservoirs.

Shamir, G., and M.D. Zoback, 1992, Stress orientation profile to 3.5 km depth near the San Andreas Fault at Cajon Pass, California: Journal of Geophysical Research, v.97, p. 5059-5080.

Sibson, R.H., 1992, Implications of fault-valve behavior for rupture nucleation and recurrence: Tectonophysics, v. 211, p. 283-293.

Smith, D.A., 1966, Theoretical considerations of sealing and non-sealing faults: American Association of Petroleum Geologists Bulletin, v. 50, p. 363-374.

Spencer,J.W., Cates, M.E., and Thompson, D.D., 1994, Frame moduli of unconsolidated sands and sandstones: Geophysics, v.59, 1352-1361.

Stearns, D.W., and M. Friedman, 1972, Reservoirs in fractured rock, *in*: Stratigraphic oil and gas fields - classification, exploration methods, and case histories: American Association of Petroleum Geologists Memoir, v. 16, p. 82-106.

Stump, B.B., Flemings, P.B., Finkbeiner, T., Zoback, M.D., in preparation, Pressure differences between overpressured sands and bounding shales of the Eugene Island 330 field (offshore Louisiana, U.S.A.) with implications for fluid flow induced by sediment loading.

Taylor, D.B. and Smith, T.K., 1970, Improving fracture gradients estimates in offshore drilling: The Oil and Gas Journal, April 13, 67-72.

Tennysson, M.E., W.R. Beeman, and S.B. Urban, 1994, Preliminary digital geologic map of the Santa Maria 30' X 60' quadrangle, California, in Arc/Info, with exploration well locations and subsurface formation depths: U.S. Geological Survey, Open File Report 94-25.

Teufel, L.W., Rhett, D.W., and Farrell, H.E., 1991, Effect of reservoir depletion and pore pressure drawdown on in-situ stress and deformation in the Ekofisk Field, North Sea: Rock Mechanics as a Multidisciplinary Science, Roegiers (ed.), Balkema, Rotterdam, p. 63.

Terzaghi, K., Die Theorie der hydrodynamischen Spannungserscheinungen und ihr erdbautechnisches Anwendungsgebiet: Proc. Int. Appl. Mech. Delft, p. 288-294.

Traugott, M.O., and Heppard, P.D., 1994, Prediction of pore pressure before and after drilling - taking the risk out of drilling overpressured prospects: American Association of Petroleum Geologists Hedberg Research Conference, Abnormal Pressures in Hydro-

carbon Environments, Golden Colorado, June 8-10.

Traugott, M.O., 1997, Pore/fracture pressure determinations in deep water: Deepwater Technology, August 1997, p. 68-70.

Vernik L., and Zoback, M.D., 1992, Estimation of maximum horizontal principal stress magnitude from stress-induced wellbore breakouts in the Cajon Pass scientific research borehole: Journal of Geophysical Research, **97**, 5,109-5,119.

Wang, C.Y., Mao, N., and Wu, F.T., 1979, The mechanical property of montmorillonite clay at high pressure and implication on fault behavior: Geophysical Research Letters, v. 6, p. 476-478.

Wang, C.Y., Mao, N., and Wu, F.T., 1980, Mechanical properties of clays at high pressures: Journal of Geophysical Research, v. 85, p. 1,462-1,468.

Watts, N.L., 1987, Theoretical aspects of cap-rock and fault seals for single- and two phase hydrocarbon columns: Marine and Petroleum Geology, v.4, 274-307.

Wiprut, D.J., and Zoback, M.D., 1998, High horizontal stress in the visund field, Norwegian North Sea: consequences for borehole stability and sand production: paper SPE 47244 presented at the 1998 SPE Annual Technical Conference and Exhibition, Trondheim, Jul. 8-10.

Yassir, N.A., and Bell, J.S., 1994, Relationship between pore pressure, stresses, and present-day geodynamics in the Scotian Shelf, offshore Eastern Canada: American Association of Petroleum Geologists, **78**. 1,863-1,880.

Yassir, N.A., and Bell, J.S., 1996, Abnormally high fluid pressures and associated porosities and stress regimes in sedimentary basins: SPE Formation Evaluation, March 1996, p. 5-10.

Yassir, N.A., and Zerwer, A., 1997, Stress regimes in the Gulf Coast, offshore Louisiana: data from well-bore breakout analysis: American Association of Petroleum Geologists Bulletin, v. 81, p. 293.

Zemanek, J., E.E. Glenn, L.J. Norton, and R.L. Caldwell, 1970, Formation evaluation by inspection with the borehole televiewer: Geophysics, v. 35, p. 254-269.

Zerwer, A., and Yassir, N.A., 1994, Borehole breakout interpretation in the Gulf Coast, offshore Louisiana: *in* Nelson and Laubach, eds., Rock Mechanics, Balkema, Rotterdam, p. 225-232.

Zheng, Z., J. Kemeny, and N.G. Cook, 1989, Analysis of borehole breakouts: Journal of Geophysical Research, v.94, p. 7171-7182.

Zoback, M.L., and M.D. Zoback, 1980, State of stress in the conterminous U.S.: Journal of Geophysical Research, v.85, p. 6113-6156.

Zoback, M.D, and Healy, J.H., 1984, Friction, faulting, and in-situ stress: Annales Geo-

physicae, v.2, p. 689-698.

Zoback, M.D, and Healy, J.H., 1992, In situ stress measurements to 3.5 km depth in the Cajon Pass scientific borehole: implications for the mechanics of crustal faulting: Journal of Geophysical Research, v. 97, p. 5,039-5,057.

Zoback, M.D., D. Moss, L. Mastin, and R.N. Anderson, 1985, Wellbore breakouts and in situ stress: Journal of Geophysical Research, v.90, p. 5523-5530.

Zoback, M.D., M.L. Zoback, V.S. Mount, J. Suppe, J.P. Eaton, J.H. Healy, D Oppenheimer, P. Reasenberg, L. Jones, C.B. Raleigh, I.G. Wong, O. Scotti, C. Wentworth, 1987, New evidence on the state of stress of the San Andreas fault system: Science, v.238, p. 1105-1111.

Zoback, M.L., and 28 others, 1989, Global patterns of intraplate stresses; a status report on the world stress map project of the International Lithosphere Program: Nature, v.341, p. 291-298.

Zoback, M.D., and M.L. Zoback, 1991, Tectonic stress field of North America and relative plate motions in D.B. Slemmons, E.R. Engdahl, M.D. Zoback, and D.D. Blackwell, eds., Neotectonics of North America: Geological Society of America, Decade Map Volume, p. 339 - 366.

Zoback, M.D., and Peska, P., 1995, In-situ stress and rock strength in the GBRN/DOE Pathfinder well, South Eugene Island, Gulf of Mexico: Journal of Petroleum Engineers, p. 582.